Additive Manufacturing of Soft Polysiloxane-based Bio-structures with Heterogeneous Properties

by

Farzad Liravi

A thesis
presented to the University of Waterloo
in fulfillment of the
thesis requirement for the degree of
Doctor of Philosophy
in
Mechanical and Mechatronics Engineering

Waterloo, Ontario, Canada, 2018

Examining Committee Membership

The following served on the Examining Committee for this thesis. The decision of the Examining Committee is by majority vote.

External Examiner: Daniel Therriault
Professor
Dept. of Mechanical Engineering
Polytechnique Montreal

Supervisor: Ehsan Toyserkani
Professor
Dept. of Mechanical and Mechatronics Engineering
University of Waterloo

Internal Member: Hyock Ju Kwon
Associate Professor
Dept. of Mechanical and Mechatronics Engineering
University of Waterloo

Internal Member: Mihaela Vlasea
Assistant Professor
Dept. of Mechanical and Mechatronics Engineering
University of Waterloo

Internal-External Member: Boxin Zhao
Associate Professor
Dept. of Chemical Engineering
University of Waterloo

Author's Declaration

This thesis consists of materials all of which I authored or co-authored: See the Statement of Contributions included in the thesis. This is a true copy of the thesis, including any required final revisions, as accepted by the examiners.

I understand that my thesis may be made electronically available to the public.

Statement of Contributions

I would like to acknowledge my co-authors who contributed to the research described in this thesis:

- Prof. Ehsan Toyserkani: Supervision of the research, providing the original idea for the current thesis, editing and reviewing papers, providing experimental facilities.
- Prof. Mihaela Vlasea: Guiding the research work in the area of powder bed binder jetting of silicone, brainstorming, providing experimental facilities.
- Prof. Leonardo Simon: Guiding the project of curing kinetics of silicone polymer, providing experimental facilities.
- Dr. Mehrnaz Salarian: Running the CT scanning experiments and analyzing the nano-CT data.
- Dr. Charles Dal Castel: Running the FTIR spectroscopy experiments and analyzing the results.
- Robin Darleux: Helping in running the experiments for material extrusion of silicone and finite element modeling of the extrusion process.

Abstract

This thesis is concerned with the development of novel additive manufacturing (AM) systems and methodologies for high speed fabrication of complex material-graded silicone structures with controllable internal features consistently. To this end, two AM systems were developed, each pertaining to a specific phase of silicone rubber.

The first system integrates material extrusion and material jetting AM systems. This system is designed to process the paste-like silicone rubbers at high viscosity levels ($>$ 400,000 $mPa.s$ at 10 s^{-1}). In this system, the outer frame of each layer is made by extruding a highly uniform silicone strand at 5 mm/s printhead velocity. Once the perimeter is laid down on the substrate or the previous layer, a piezoelectric-based printhead with a translational speed of over 100 mm/s covers the internal section of layer by depositing uniform droplets of silicone at predefined locations. The printing parameters for both extrusion and jetting techniques were tuned using statistical optimization tools in order to minimize the surface waviness of printed parts. The optimized surface waviness values obtained are 8 μm and 3 μm for jetting and extrusion, respectively. Moreover, parts with solid density of over 99% and mechanical performance similar to the bulk material were manufactured by tailoring the rheology of silicone ink.

A combination of powder-bed binder-jetting (PBBJ) system and micro-dispensing material extrusion form the second hybrid AM system. The three-dimensional (3D) shape forming of silicone powder is made possible for the first time using this system. The tomography results for the fabricated parts reveal a porous structure ($\sim$ 8% porosity). This AM process is introduced as a the proof-of-concept. The porosity of structures can be tuned by improving the silicone binder delivery method so that binder droplets with pico-liter volumes can be dispensed.

The characterization techniques used for materials and additively manufactured parts include confocal-laser profilometry for investigating the surface quality of printed parts, differential scanning calorimetry (DSC) for investigating the curing mechanism of heat-curable silicone inks, Fourier transform infrared (FTIR) spectroscopy for controlling the curing kinetics and surface cohesion of UV-curable silicones, dynamic mechanical analysis (DMA) tests for tuning the rheological properties of silicone inks under different shear stresses, rheometry for establishing the viscosity threshold for jetting of silicone inks at different temperatures, scanning electron microscopy (SEM), particle size analysis, and powder rheometry for establishing guidelines for the size, shape, cohesiveness, flow, and shear stress resistance of silicone powders, uniaxial tensile test, tearing test, and durometry for identifying the mechanical characteristics of 3D printed parts, and computed-tomography (CT) scanning for quantifying the porosity of parts.

The systems and fabrication methods introduced in this research, with high commercialization readiness levels, were concluded to have great impact on the manufacturing of functionally-graded complex bio-structures. This has been validated through high speed fabrication of multiple heterogeneous bio-structures. Moreover, the proposed techniques can be used for the fabrication of other silicone-based products.

Acknowledgements

The realization of this research work would have not been possible without the help and support of several people, to whom I wish to express my gratitude.

I would like to express my deepest gratitude to my supervisor, Prof. Ehsan Toyserkani, for his guidance, caring, and patience through the completion of the work. I am mostly grateful for his friendship and persistent help during my graduate studies at the University of Waterloo.

I hereby acknowledge my thesis examining committee members, Prof. Daniel Therriault from Polytechnique Montreal, Prof. Mihaela Vlasea, Prof. Hyock Ju Kwon, and Prof. Boxin Zhao from the University of Waterloo for taking time to review my thesis and provide their valuable and constructive insights.

It would have not been possible to finish this work without the guidance and support of Prof. Leonardo Simon and Prof. Pu Chen from the University of Waterloo, Mark Barfoot, Laurie Wilfong, James Hinebaugh from Expanse Microtechnologies Inc., Peter Kaminski and Johnathan Titone from Nordson EFD, Remi Thiria from Elkem Silicones, and Joy Spandler from Airboss of America.

I am also very grateful to all my colleagues at MSAM laboratory for their friendship and assistance.

Finally and most importantly, I would like to thank my parents for their endless support and encouragement.

Dedication

To my family.

Table of Contents

List of Tables

List of Figures

List of Abbreviations

2D two-dimensional 36

3D three-dimensional 3

adj MS adjusted mean of squares 43

ADSA-P axisymmetric drop shape analysis profile 32

ALE arbitrary Lagrangian-Eulerian 40

AM additive manufacturing 1

ANOVA analysis of variance 43

CAD computer-aided design 8

CB carbon black 11

CCD central composite design 57

CFD computational fluid dynamics 40

CNC computer numerical control 8

CT computed tomography 8

DEA dielectric elastomer actuator 16

DF degree(s) of freedom 43

DoE design of experiments 29

FDM fused deposition modeling 8

FEM finite element modeling 28, 29

FRE freeform reversible embedding 10

HTV high temperature vulcanized 17

LED light-emitting diode 36

LOPP low one-photon polymerization 14

MEMS microelectromechanical systems 40

NPP normal probability plot xxv, 174

PBBJ powder-bed binder-jetting 3, 9, 24, 97

PDMS polydimethylsiloxane 12

PI photoinitiator 14

PPJ piezoelectric-pneumatic jetting 16, 58

RSM response surface methodology 43

RTV room temperature vulcanized 21

SLA stereolithography 8

SLS selective laser sintering 8

SS sum of squares 32

List of Symbols

a characteristics of length 57

CT close time of nozzle 58, 64–67, 69, 78, 176–179, 182–184, 187

Θ_c contact angle 18, 32, 33, 166

CyT cycle time of nozzle xxi, 59, 64, 66, 78, 176–179

c capillary constant 32

DD diameter difference 104, 105, 115, 191, 193

ρ density 32, 40, 57, 164, 165

D diameter of the nozzle 58, 99, 101

δ Dirac delta function 165

ϵ_f elongation at break 19, 21, 91, 93, 96, 122, 195

ϵ thickness of transition layer in level-set method 165

F_f friction between fluid and internal wall of nozzle 28, 166

Fr dispensing frequency 101, 104, 105, 115, 121, 191–193

Γ reinitialization factor in level-set method 165

g acceleration of gravity 32, 165

w half of the maximum width of the droplet 47, 49, 51, 54, 56

H height of printed pattern 28, 99, 101, 104, 105, 115

h' the height of the droplet created on the substrate 47, 51, 54

h_z length of the tapered zone of nozzle 28

h the distance between the nozzle tip and the lowest point of the pendant droplet 47, 49, 51, 54, 56, 191, 193

I identity matrix 165

ID inner diameter 104, 105, 115, 191, 193

K coefficient of power law 58

L length of the nozzle 58

G'' loss modulus 18, 19, 22, 77, 84, 88, 96

LT layer thickness 101, 104, 105, 115, 121, 191–193

N normal to the interface 165

OD outer diameter 104, 105

Oh Ohnesorge number 57, 58

OT open time of nozzle xxi, 59, 64, 66, 78, 176–179

ϕ level set-function 164

P pressure 28, 32, 35, 37, 39, 40, 43, 46, 56, 58, 64, 66, 78, 106, 165, 169, 172, 173, 176–179

PT pulse time of nozzle 58, 64–67, 69, 78, 176–179, 182–184, 187

Q_{pne} jetting rate due to pneumatic force 58

Q_{pzt} jetting rate due to the piezoelectric force 58

R_1 principal radius of curvature 32

R_2 principal radius of curvature 32

λ relaxation factor in Carreau-Yasuda model 30, 31

R_s internal radius of nozzle 28

RW raster width 40, 46, 65, 70, 82, 172, 173, 188

β slip length 166

n slope of the power law region 30, 31, 58

G' storage modulus 18, 19, 22, 77, 84, 88, 96

$Str\%$ stroke 58, 64–67, 78, 176–179, 182–184

F_{st} surface tension force 165

γ surface tension 18, 28, 32, 57, 165

T_s tear strength 19, 21, 23, 91, 96, 122, 195

T temperature 64, 66, 78, 176–179

σ_f tensile strength 19, 21, 23, 91, 93, 96, 122, 195

t time 33, 41

a width of transition in Carreau-Yasuda model 30

v velocity 28, 35, 37, 39, 40, 43, 56, 64–66, 70, 78, 169, 172, 173, 176–179, 188

ν_n normal component of velcoity field 164

ν velcoity field 164, 165

μ dynamic viscosity 28, 30, 40, 57, 164, 165

V pulsed voltage 58, 64–67, 78, 176–179, 182–184

W_q root mean square of surface waviness 36, 39, 40, 43–46, 56, 63–65, 70, 74, 168, 172, 188

W_{avg} average value of width measured over a line xxii, 36, 39, 43–45, 63, 67, 68, 70, 168, 169, 176–178, 182

W_d width of the deposited fluid 28

WD working distance 35, 37, 39, 40, 43, 46, 56, 64, 66, 78, 82, 169, 172, 173, 176–179

$W_{s.d.}$ standard deviation of width measured over a line (uniformity) 36, 39, 43–45, 63, 168, 169, 176–178

σ_y shear yield stress 84

Chapter 1

Introduction

1.1 Overview

Silicone is a biocompatible material with unique properties that make it suitable for fabrication of biomedical and medical devices. Silicones are inert polymers that are composed of the metalloid, silicon (Si), as well as other elements like carbon, hydrogen, oxygen etc. Walter Noll defines it as "an organosilicon polymer in which the silicon atoms are bound to each other through oxygen atoms, the silicon valences not taken up by oxygen being saturated by at least one organic group [1]". Unique properties of silicone such as thermal stability, strength, flexibility, biocompatibility, and biodurability can be traced back to this organic-inorganic molecular structure.

Silicone has been used for a variety of medical applications since its initial commercialization in 1946, mainly owing to its biocompatibility and thermal stability. Different forms of silicone have been used for the production of different classes of implants including orthopedic [2, 3], stomach [4], heart valve [5], cranio-maxillo-facial [6], and mammary [7]. Medical-grade silicones are also used in phantoms, pharmaceuticals, drug delivery devices, lubricating injection devices etc. To be considered medical-grade, a silicone is required to pass certain tests such as histopathology cultures and common biocompatibility tests before being used in contact with human tissue. Luria has reported different applications of this class of silicone in a comprehensive review [8].

The numerous biomedical applications of silicone highlight the importance of an efficient manufacturing method that enables fabricating multi-scale functionally-graded structures from this material. Recent research findings in the area of manufacturing of silicone products suggest that additive manufacturing (AM) can be used to achieve this goal. AM is a general term used to describe a family of manufacturing technologies that fabricate a solid structure layer-by-layer through deposition, polymerization, melting, sintering, or binding of materials. By eliminating the expensive and time-consuming tooling step, removing any limits in the design of products, and enabling the control of the properties of every voxel of the structure, AM has provided the manufacturing industry with unprecedented flexibility. On the other hand, in the new trend of digitization of manufacturing, known as industry 4.0, AM is depicted as the main fabrication method for the end-user products. To realize the smart manufacturing fully, it is crucial to investigate the AM of novel functional materials. Silicone is one of these new materials.

1.2 Motivation

Conventional methods for the production of silicone structures (e.g. molding, soft lithography, and their derivatives. [9–15]) have a number of limitations and disadvantages such as their inability to fabricate highly complex and integrated structures. To better understand the limitations of conventional silicone manufacturing techniques and their consequences in biomedical area, the fabrication of silicone prostheses is considered in the following.

The loss of a body organ and its associated function can cause psychological disorders in patients, and can lead to their social isolation [16, 17]. Depending on the type and severity of the body function loss, approaches such as physiotherapy, corrective surgeries, and the use of prosthetics and/or orthotic devices may be adopted. In many cases, the use of a reversible prosthetic restoration is the preferred option. This highlights the importance of realistic-appearing prostheses, especially for those used to correct cranio-maxillo-facial trauma [18–20], in helping patients to move forward in their recovery process.

Conventional prostheses production methods are costly and time consuming, and the patients must be physically present for most of the design and manufacturing steps. The production process also requires high technical experience [21, 22]. In addition, the process of making an impression of the defect can cause patient discomfort. For example, for the production of a nasal prosthesis, the airway may need to be covered for a long period of time. Also, the impression materials, e.g., plaster, are heavy and may cause distortion to the underlying tissue, potentially resulting in a mismatch between the produced prosthesis and the morphology of the defect area [23]. In some patients with infectious disease, makeing an impression using direct contact techniques is impossible [24]. Moreover, the prostheses need to be replaced after some time (from a few months to a few years) due to the changes in their color and physical properties, requiring the patient to undergo this tedious process multiple times. Despite all their shortcomings, these conventional techniques are still being practiced in most of the prosthetics centers [25].

To address these shortcomings, research on the direct AM of silicone as an alternative method with higher design flexibility has gained momentum from both academia and industry in the last few years. In case of the prosthesis production, silicone AM can increase the products accuracy, decrease the patients consultation time and discomfort during the impression-taking step of casting, and lower the dependency of final quality on the clinicians skills. More generally, AM of silicone can positively impact the medical/biomedical sector through:

- High speed production of functionally-graded silicone structures by varying the properties of every building unit.
- Converting the passive silicone objects to smart structures by embedding materials responsive to external signals.
- Fabricating micro-scale silicone patterns which cannot be achieved by conventional molding techniques.

Motivated by the research gap in this field, we have investigated the feasibility of AM of silicone in two different phases (high viscous fluid and powder). For viscous silicone paste (400,000 $mPa.s$ at 10 s^{-1}), we were able to jet uniform droplets of silicone at a high frequency due to the considerable shear energy produced by piezoelectric-actuated changes in the volume of the fluid reservoir at an unprecedented printing velocity of 100 mm/s and printing resolution of 500 - 600 μm. This method is the first reliable system for fast fabrication of viscous thermosets. In another method, the silicone powder scaffold is three-dimensional (3D) printed in a powder-bed binder-jetting (PBBJ) system followed by the dispensing of a liquid silicone binder to encapsulate the silicone particles and produce a soft elastomer object upon thermal curing. This method makes the fabrication of porous 3D structures made from silicone powder possible for the first time.

1.3 Thesis Objectives

The objective of this thesis is “developing high speed AM systems and methods for the fabrication of heterogeneous silicone structures”. The target speed is at least three times the translational speed of extrusion-based printheads (> 60 mm/s). On the other hand, the shape forming of structures where different sections are made of three different materials (at least one silicone polymer) as well as internally porous silicone parts are the heterogeneity levels pursued in this research. To this end, the following tasks were undertaken:

- Development of a hybrid multi-nozzle AM system composed of material extrusion and material jetting for processing highly viscous silicone pastes.
- Optimization of printing parameters for material extrusion and material jetting for highly viscous silicone pastes.
- Elimination of the quality flaws in material jetting system for highly viscous silicone pastes through developing a novel trajectory pattern.
- Optimizing the rheological properties of highly viscous silicone pastes for material jetting.
- Mechanical characterization of silicone parts fabricated via material jetting.
- Development of a hybrid AM system composed of material extrusion and powder-bed binder-jetting for processing of silicone powder.
- Characterization of internal features of parts fabricated via powder-bed binder-jetting.

1.4 Thesis Outline

This thesis includes 7 chapters. Chapter 1 outlines the problem definition, motivation, and objectives of the present research. The related literature on the state-of-the-art silicone AM systems and tailoring silicone properties for AM is reviewed in Chapter 2. The feasibility of AM of viscous silicone pastes is investigated in Chapter 3 using material extrusion technology, and in Chapter 4 using material jetting technology. The printing parameters are optimized for both systems using statistical analysis tools. The rheological properties of silicone are tuned in Chapter 5 in order to control the level of porosity within the structure, and in turn reduce the difference between mechanical properties of the AM-made parts and the bulk material. Chapter 6 introduces a novel method for fabrication of porous silicone structures from silicone powder. In Chapter 7, conclusions and future work are outlined. Chapters 2 – 6 are adapted from author's published work or manuscripts submitted for publication as following:

Chapter 2:

- Liravi, F., & Toyserkani, E. (2018). Additive manufacturing of silicone structures: review and prospective. (under review – journal of Additive Manufacturing)

Chapter 3:

- Liravi, F., Darleux, R., & Toyserkani, E. (2015). Nozzle dispensing additive manufacturing of polysiloxane: dimensional control. International Journal of Rapid Manufacturing, 5(1), 20-43. [26]
- Liravi, F., Darleux, R., & Toyserkani, E. (2017). Additive manufacturing of 3D structures with non-Newtonian highly viscous fluids: Finite element modeling and experimental validation. Additive Manufacturing, 13, 113-123. [27]

Chapter 4:

- Liravi, F., & Toyserkani, E. (2018). A hybrid additive manufacturing method for the fabrication of silicone bio-structures: 3D printing optimization and surface characterization. Materials & Design, 138, 46-61. [28]

Chapter 5:

- Liravi, F., Salarian, M., Dal Castle, C., Simon, L., & Toyserkani, E. (2018). High speed additive manufacturing of heterogeneous silicone bio-structures: mechanical characterization and trajectory planning. (under review – journal of Materials & Design)

Chapter 6:

- Liravi, F., & Vlasea, M. (2018). Powder bed binder jetting additive manufacturing of silicone structures. Additive Manufacturing, 21, 112-124. [29]

The content of these publications have been slightly modified to fit within the scope of this thesis. The license agreements are provided in Letter of Copyright Permission section .

Chapter 2

Background and Literature Review

2.1 Silicone

Silicones are synthetic polymers consisting of an inorganic silicon-oxygen (Si – O) backbone and organic groups attached to silicon atoms. Hence they inherit the inertness of inorganic materials as well as the softness and other structural features of macromolecules [1, 30]. Stable Si – O – Si structures are the basis for the generation of silicones. The covalent Si – O bonds, however, are not completely single bonded. They demonstrate a partial double-bonded behavior. The Si atoms are saturated with at least one radical organic group such as methyl ($-\ CH_3$), ethyl ($-\ C_2H_5$), and phenyl ($-\ C_6H_5$) and their remaining valences will be saturated with oxygen. The general formula of silicone is $R_nSiO_{\frac{4-n}{2}}$, $n = 1, 2, 3$. Figure 2.1 shows possible silicone structural units.

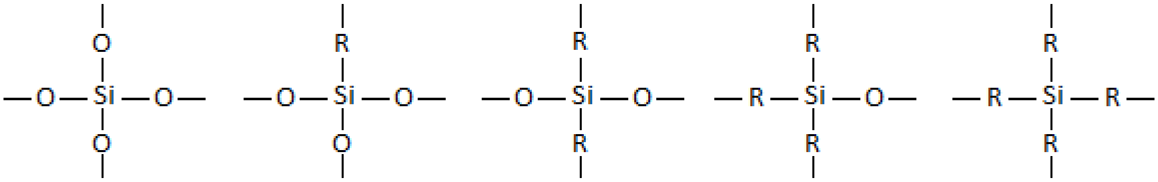

Figure 2.1: Silicone structural units. Adapted from [1]

The great chemical, physical, and surface properties of silicone can be justified through their chemical structure at molecular level including relatively long and flexible Si – O and Si – C bonds, repetitive arrangement of silicon and oxygen atoms in the polymer chain, arrangement and type of the organic substituents, and the low intermolecular forces between organic groups. Longer backbone bonds and larger bond angles in addition to the alternation of Si – O – Si and O – Si – O bond angles along the silicone backbone result in more flexible structures. This highly flexible structure is the reason of silicones' low glass transition temperature, low melting point, and small viscosity-temperature slope. Long and flexible Si – O and Si – C bonds allow a freedom of rotation with an almost zero rotation energy compared to 14 KJ/mol rotation about C – C bonds [31]. Hence molecules can adopt the lowest energy configuration at interfaces resulting in the reduction of surface tension [32]. The explained chemical structure makes silicone retain their physical and chemical properties when exposed to elevated temperatures and also increases their oxidative resistance.

The Si – O is also a polar covalent bond with partially ionic properties. This property is a result of relatively large difference in electronegativity of silicon and oxygen atoms (1.8 and 3.5, respectively). The 1.7 difference in electronegativity causes a 37 to 51% ionic character for siloxane backbone [32]. This covalent bond is not a complete strong σ bond, but a combination of different linkages including σ and π. The partial ionic and partial double bond character of the siloxane are responsible for the strength of this polymer.

The organic groups in silicone have low intensity interactions with each other. These interactions between organic groups have a direct influence on surface properties of silicone. As a result, the type of organic group along with the flexibility of backbone chain can determine the surface tension, water repellency, wetting, and spreading properties of silicone [32, 33]. The combination of chemical inertness, thermal stability, hydrophobicity, and low surface activity of silicones make them a biocompatible polymer suited for biomedical applications [31, 34].

2.2 Manufacturing of Silicone Bio-structures

Eggbeer et al. (2012) have evaluated AM against conventional silicone production methods, and identified its superiority for prosthesis production in terms of the quality of final products [35]. They categorized silicone-based AM processes used to create maxillo-facial prosthetics as: (1) indirect AM of silicone; (2) direct AM of silicone. The same categorization is used throughout this thesis. In the indirect AM of prosthetics, casts are first 3D printed (mostly from thermoplastics) followed by the conventional casting of silicone bio-structure. Indirect approaches eliminate the need for the patient to be present during the manufacturing [12, 36]. The successful applications of indirect AM for the fabrication of prosthetics used in maxillodental surgeries have also been reported by several researchers [37–39]; however, the indirect use of AM does not have a significant effect on the total production time. Another disadvantage in manufacturing of shaped silicone parts using both conventional and indirect AM techniques is their inability in production of structures with variable property profiles such as a nasal prosthesis with different mechanical properties at its different sections [40]. Hence, researchers suggested the direct use of AM for the printing of elastomeric biomaterials [21, 35]. Although most of the recently introduced methods are not designed for the manufacturing of bio-structures, it is valuable to review them in order to identify the specifications of a viable AM process for medical-grade viscous silicones.

2.3 Indirect Additive Manufacturing of Silicone

One of the first attempts to eliminate the drawbacks associated with the conventional manufacturing of soft tissue prostheses involved the introduction of computer-aided design (CAD) packages, non-contact morphological measurement systems such as computed tomography (CT) scanning [41], and computer numerical control (CNC) systems. Chen et al. (1997) pointed out the distress induced by the conventional plaster-cast to the patient and proposed the production of a wax model based on the CT scan data using a CNC machine. Tsuiji et al. (2004) suggested the fabrication of facial prostheses by direct milling of the silicone rubber blocks [24].

In the early part of the millennium, researchers tried to incorporate AM techniques into prosthetic production methods. The indirect AM of silicone changes the fabrication of prostheses in the following manner: (1) Data acquisition of the target part can be achieved using CT scan, (2) the virtual reconstruction of the part and designing of the mold can be done using CAD systems, (3) and the mold can be fabricated using AM [42]. Different AM methods such as stereolithography (SLA) [43], selective laser sintering (SLS) [44], fused deposition modeling (FDM) [25], and material jetting [45, 46] have been employed by researchers for the production of both positive and negative molds for prosthetics. For instance, FDM-based 3D printers have been used to fabricate molds for a functional artificial heart [47] and a mitral valve [48]. In an alternative method, Palousek et al. (2014) proposed the fabrication of a prototype of the target part using AM and then using the prototype to produce the mold [36].

The indirect application of AM in the prostheses production has decreased the turn around time and cost of the process, provided a more flexible workflow, eliminated long patient consultations, and most importantly manufactured more realistic prostheses which can increase the patients satisfaction and speed up their rehabilitation. However, in these processes, the extra steps of mold design and casting increases the production time. On the other hand, in a thorough review of AM-based prosthesis production techniques, Bibb et al. (2010) demonstrated that the conventional AM technologies, despite their potential effectiveness are not specifically designed to meet the needs of the prosthetics industry, and novel and/or modified AM technologies are needed to process biomaterials used in this field [49]. The application of AM in the prosthesis production can only be sufficient and worthy of clinical use only if the silicone is printed directly, and the prosthesis is produced without the use of a mold [41].

2.4 Direct Additive Manufacturing of Silicone

2.4.1 Adding Silicone in the Post-Processing Step

Eggbeer et al. (2012) proposed the first direct application of AM for the production of a nasal prosthesis using an acrylate-based material, TangoPlus (Stratasys, Minnesota, United States), in a commercial material jetting AM system (PolyJet). The fabricated body was wrapped over by a thin pliable silicone sheet [35]. Their experiment showed that the additively manufactured prosthesis has the same level of appearance quality as a similar nasal prosthesis made using the conventional molding technique. The direct AM method could improve the prostheses manufacturing process flow by potentially reducing the patients required consultation time. However, the mechanical properties of the substitute polymer were not similar to those of a medical-grade silicone. The poor mechanical properties of TangoPlus (tensile strength of $\sim 1\ kN$ and tear strength of $\sim 0.8\ N/mm$) limit the application of this method in reality, as a prosthesis made using this material is susceptible to pre-mature tearing when used on a daily basis. The research did, however, point out the limitations of conventional AM methods for handling the viscous soft materials and showed the benefits of developing a manufacturing system for this class of materials.

The UK-based Company Fripp Design and Research and Zardawi et al. (2013) developed a different method for the direct fabrication of a prosthesis body from a material other than silicone. Their methodology was based on the PBBJ AM, in which the prosthesis is made from the starch powder and an aqueous binder, then the 3D printed part is infiltrated with the biocompatible silicone under different pressure conditions [50, 51]. Similar to the method presented by Eggbeer et al. [35], producing the prosthesis body from starch led to a decrease in the durability of prosthesis. These alternative materials are not as resistant to weathering conditions as silicones, resulting in the degradation of their mechanical properties and color fade over time. The advantage of the method introduced by Zardawi et al. is an advanced color-match system and the jetting of colorful binders based on the patients skin tone resulting in the production of a fully-colored prosthesis body. Fig. 2.2(a) shows a nasal prosthesis made using this technique. The binding effect of silicone is demonstrated in Fig. 2.2(b-c).

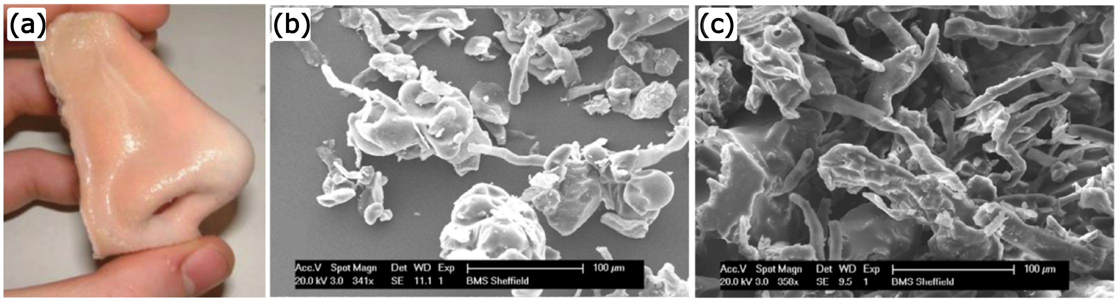

Figure 2.2: (a) Silicone-infiltrated structure made of starch powder using powder-bed binder-jetting technique; SEM of starch particles (b) before silicone infiltration and (c) after silicone infiltration. (b-c) (adapted from [52]).

2.4.2 Using Silicone as the Main Material

Since the early 2010s, researchers have been trying to directly print silicone using different AM methods such as SLA, material extrusion (e.g., nozzle dispensing and freeform reversible embedding (FRE)), and material jetting. A few companies have also started to modify these techniques in order to customize them for silicone indicating the existence of the market potential for 3D printed silicone parts.

Material Extrusion

Compared to other AM technologies, nozzle dispensing systems are well-suited for the deposition of a wide range of fluids, from low viscous liquids to thick pastes (up to 6×10^7 $mPa.s$ viscosity with a shear-thinning behavior) [53–55]. In comparison, the maximum material viscosities suggested for SLA and drop-on-demand inkjet printing processes are in the range of 300 - 5000 mPa.s [56, 57] and 10 - 100 mPa.s [53, 57, 58], respectively. This capability of material extrusion systems in deposition of viscous pastes is important due to: (1) the high shape-retention capability of viscous polymers, and (2) the high flexibility and resilience resulted from highly viscous silicones (> 10,000 mPa.s) with longer polymer chains [55]. Different dispensing mechanisms are being used to push fluids through a nozzle in material extrusion systems with pressure-actuated (pneumatic) and mechanical dispensing systems being the most popular [59]. The flow of material in these systems has been numerically modeled for the viscous moisture-curable silicone by Jin et al. (2015) [60].

Material extrusion AM was used by Mannoor et al. (2013) to print silicone, biological hydrogel, and conductive polymers to produce the scaffold of a bionic ear to be cultured *in vitro* in order to grow the cartilage tissue [61]. Their work was the first attempt to apply AM in the fabrication of functional prosthetics. The promising results of this research showed the vital role AM could play in the production of a new generation of prosthetics. The printed bionic ear is showed in Fig. 2.3(a-c). A micro-syringe dispensing technique used by Duoss et al. (2014) for the production of porous silicone structures with controllable mechanical properties was the first successful example of direct AM of silicone [62]. Moreover, they showed that this technique is able to dispense polymers with a viscosity as high as 10^6 $mPa.s$ with reliable quality. Duoss et al. also showed that obtaining designed mechanical properties is possible with the extrusion-based AM of silicone as they were able to control the compression and shear strength of the printed structures by modifying their porosity and micro-structures [62]. This capability of extrusion AM can be used to produce smart prosthetics with heterogeneous and controllable properties compared to the passive structures produced via molding. Samples of vascular networks fabricated via material extrusion are shown in Fig. 2.3(d-f). Material extrusion technique has also been employed by other researchers to 3D print silicone-based structures for tissue engineering [63, 64], drug-delivery devices [65], stretchable electronics [66], sensing skin [67], actuators [68], foams [69], and membranes with designed properties [70–72].

In most of the abovementioned research, thermal-curable silicones were used as the raw material. Porter et al. (2017) investigated the feasibility of extruding UV-curable strands of low viscous silicone (7×10^4 $mPa.s$ at 10 s^{-1}) followed by *in-situ* curing [73]. This method involves complications during the print such as nozzle clogging and deflection of silicone stream from the cured previous layers before reaching the substrate due to repulsive silicone surface charges. Porter et al. have suggested addition of 0.15 - 1 wt.% carbon black (CB) to the silicone which eliminates the electrostatic repulsion, and at the same time reduces the reflection of UV by previously laid silicone which is the main cause of nozzle clogging. In their research, the controlling factor in the amount of CB additive is its effect on the reduction of silicone UV curing depth.

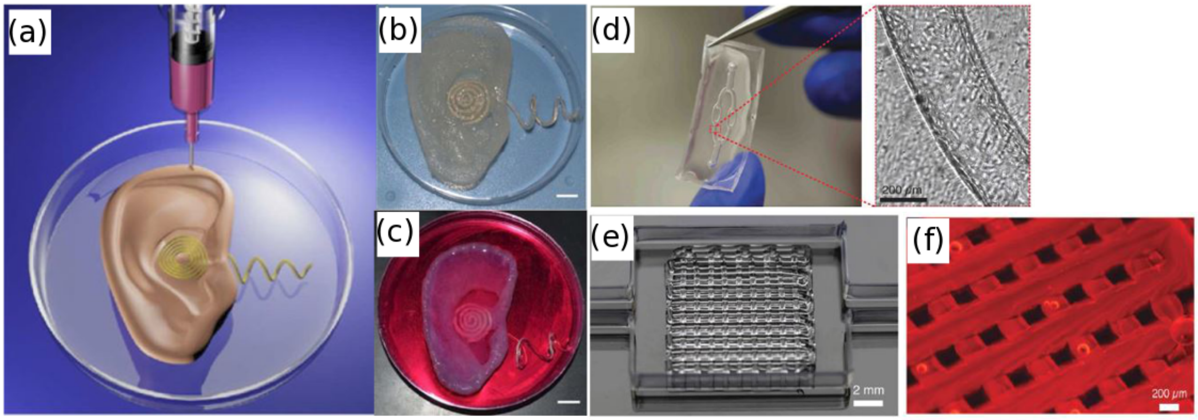

Figure 2.3: (a) Schematic view of the extrusion AM setup for printing of the bionic ear, (b) 3D printed ear, (c) in vitro culture of the 3D printed bionic ear for the cartilage tissue growth, (b-c) scale bars: 1 cm.(a-c) (adapted with permission from [61]. Copyright (2013) American Chemical Society); Images of (d) 2D and (e) 3D embedded silicone vascular networks fabricated by material extrusion AM, (f) Fluorescent image of the 3D vascular network after perfusion with a water soluble fluorescent dye demonstrates performance of the interconnected channels, (d-f) (adapted with permission from [63]. Copyright (2014) John Wiley and Sons).

Freeform Reversible Embedding

FRE can be considered as a variety of material extrusion AM. Hinton et al. (2016) have developed a method based on FRE for AM of polydimethylsiloxane (PDMS) [74]. In this method, a vat of hydrophilic Bingham plastic acts as a support structure under low stress while the hydrophobic PDMS is extruded inside the vat. This technique, although only suitable for the extrusion of low viscous silicones (e.g. $3000 - 4000\ mPa.s$), is extremely useful for the fabrication of hollow structures and continuous freeforming. This method resolves the issue of maintaining the shape of printed structures during the long curing time required by heat- or moisture- curable silicones by providing a support structure which does not have an adverse effect on the surface of the features, and is easily removed using a chemo-mechanical process. Fig. 2.4(a-c) demonstrates the procedure of FRE AM of silicone and some of the printed parts. The width of the FRE printed PDMS linear features, height of the printed lines, and the printhead velocity were reported as 140 μm – 400 μm (depending on the nozzle size), 100 μm, and 20 mm/s, respectively. The main drawback of this method, as reported by the original authors, is the need for the pressure to be induced by the deposition of upper layers to make sure the layers completely adhere to each other. The lack of such a pressure in the XY direction prevents the lateral adhesion.

O'Bryan et al. (2017) improved the quality and resolution of the silicone parts made using the FRE technique by replacing the aqueous supporting environment with an oil-based micro-organogel support material [75]. The similar oil-based nature of the silicone and the proposed micro-organogel facilitates the adhesion of printed silicone features both laterally and vertically. Moreover, it was found that increasing the viscosity of silicone resulted in the ability to print 30 μm wide features. The reported surface roughness of 150 nm demonstrates the ability of this 3D printing technique to fabricate the very smooth surfaces required for biomedical applications. Another advantage of this technique is its compatibility with UV-curable silicone, enabling the use of a material that will decrease the manufacturing time.

A slightly different FRE method was proposed by Fripp Design Ltd. for the AM of two part silicones [76]. In their commercial 3D printer, PICSIMA, the vat is filled with the base of a two-part silicone, and the curing agent is extruded through a nozzle inside the vat. Upon extrusion of the curing agent, the silicone solidifies and a 3D object is fabricated layer-by-layer. The major advantage of PICSIMA over other FRE-based techniques is the use of different commercially available silicones with a wide viscosity range as the raw materials that facilitates the fabrication of different bio-structures. Moreover, by controlling the concentration of curing agent or using multiple nozzles, this technique has the potential to fabricate functionally-graded structures with heterogeneous properties.

Vat Photopolymerization

Femmer et al. (2014) introduced the first application of a vat photopolymerization system for 3D printing of functional microfluidic PDMS membranes [77]. They have used the commercial SLA system from EnvisionTEC (MI, USA) equipped with a digital micro-mirror device for this purpose.

As mentioned before, in vat photopolymerization machines, the viscosity of resin should be low enough to make sure a thin layer of fresh photopolymer with uniform surface is generated for printing of the next layer. To address this issue, Kim et al. (2016), modified SLA method for the fabrication of viscous soft materials [78, 79]. Although this technique is still in its initial phase, it could have a positive impact on the 3D printing of soft materials upon further improvements. Similar to regular SLA, the 3D structure is created by laser curing of the photopolymer inside the vat instead of its surface. In their proposed approach, there is no movement in the resin vat; this creates a hydrostatic environment which acts as a support structure. This support-free fabrication technique requires a sophisticated optics

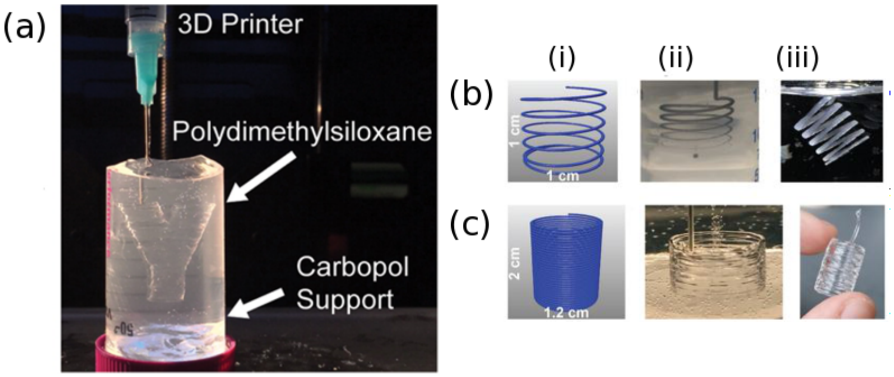

Figure 2.4: (a) The FRE setup for fabrication of silicone structures in Carbopol support vat. Samples of printed silicone structures with FRE system: (b) helix, (c) Cylindrical tube. (b-i) The toolpath for the helix, (b-ii) FRE printing of the helix structure, (b-iii) Helix after removal and cleaning, (c-i) The toolpath for the cylindrical tube, (c-ii) FRE printing of the cylindrical tube, (c-iii) The tube after removal and cleaning. (a-c) (adapted from [74]).

and low power UV curing system, known as low one-photon polymerization (LOPP), to control the light intensity. Also, the curing should only happen at the laser focal point. Hence, the properties of the photoinitiator (PI) used in the polymer should be evaluated to coordinate with the UV exposure set up. Although the reported resolution of this technique, $1 - 2\ mm$, is not comparable to other silicone 3D printing methods, it could be enhanced by improving the preliminary two-tier model developed for LOPP [80] as has been done for the other photopolymers used in the SLA process [81]. Details of this AM system are shown in Fig. 2.5(a-c). The image of the printed parts shows a high degree of discrepancy between the cylindrical CAD models and the printed pillars. The hydrostatic environment required for the 3D printing in this technique eliminates the problem of the flow of viscous materials during the print, however, the viscosity limit for the silicones compatible with this method is yet to be determined as highly viscous paste-like silicones cannot be easily poured into a resin vat. Moreover, degassing the silicone vat to produce a uniform media free of air-trapped areas would be challenging.

The Folchs research group at the University of Washington is also working on the fabrication of microfluidic devices for biotechnology applications by developing an SLA system customized for PDMS [82].

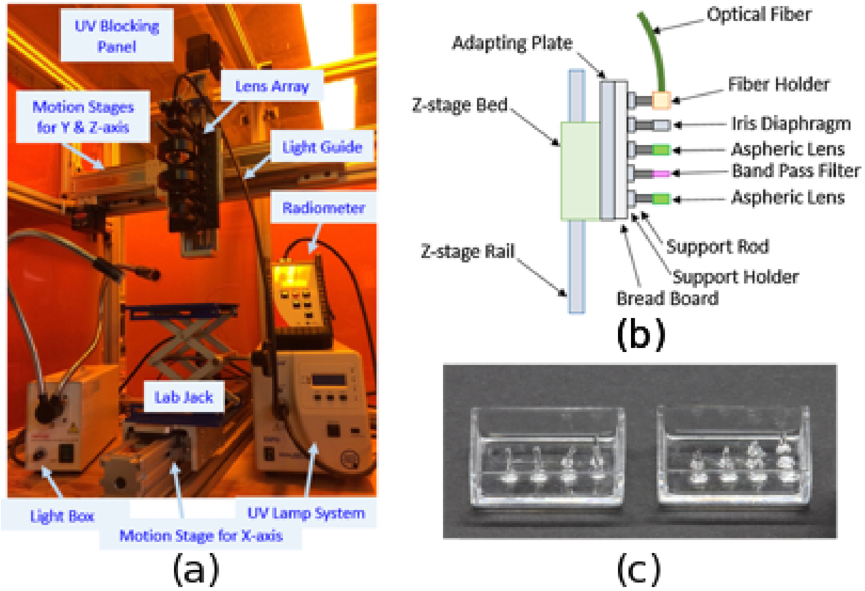

Figure 2.5: (a) The vat Photopolymerization setup for hydrostatic support-free AM of silicone structures, (b) The schematic view of the lens array used for the low one photon absorption polymerization, (c) The 3D printed silicone cylinders at multiple UV laser powers, (a-c) (adapted with permission from [78]. Copyright (2016) Elsevier).

Material Jetting

The flexible UV-curable elastomers TangoPlus and TangoBlack were introduced by Stratasys to be used in their Connex 3D printer family, and later were used on J750 PolyJet 3D printers. These systems have been widely used by researchers to produce soft elastic objects. For example, inspired by the spider leg, Han et al. (2017) 3D printed a finger [83], and Mohammed et al. fabricated material-graded ear and nose prostheses, both from TangoPlus [84]. Even though, PolyJet with a vertical resolution of 14 μm is capable of producing high quality digital colorful parts, it can only be used with the commercial materials that Stratasys provides. These materials lack the sufficient mechanical properties for special applications. Moreover, these commercial UV-curable elastomers are no replacement for silicone in terms of the biocompatibility and biodurability. However, this technique with an established multi-color printing technology already in place can provide a robust solution to the 3D printing of silicone, provided that the printheads are modified based on the rheological properties of the viscous elastomers, and the properties of raw materials used in the system are tunable [85].

Reitelshofer et al. (2016) proposed a multi-nozzle AM method for the production of stacked dielectric elastomer actuator (DEA) made of silicone and graphene using aerosol jetting [86]. Two aerosol streams containing two parts of a silicone were generated using a pneumatic atomizer. The two streams were combined in a chamber before being transferred to the nozzle and then printed on a substrate. This method can produce silicone layers with a thickness as low as 10 μm. However, in practice its application is limited by the maximum compatible viscosity (5 $mPa.s$ for ultrasonic atomizer and 1000 $mPa.s$ for pneumatic atomizer) as well as the manufacturing speed ($5 - 10$ mm/s). The viscosity of the sample silicone used in their research is less than 2000 $mPa.s$, and the ink was heated up to meet the viscosity requirement.

McCoul et al. (2017) demonstrated the possibility of fabrication of very fine silicone membranes (2 - 4 μm) with minimum surface waviness for multiple commercial silicones using piezoelectric drop-on-demand inkjet printing [87]. In these systems, applying a controllable square voltage signal flexes the piezoelectric ceramic behind the ink reservoir and in doing so jets a droplet of ink out of the nozzle. Fabrication of functional DEAs at a printhead speed of 50 mm/s has been showcased in this study; however, the inability of the proposed system in jetting of the electrodes as well as its incompatibility with intermediate to high viscous inks (> 40 $mPa.s$) are limiting factors in rapid AM of complex 3D structures with tunable mechanical properties

Yang et al. (2013) have investigated the possibility of printing silicones with different viscosities using material jetting systems with dual piezoelectric-pneumatic jetting (PPJ) mechanism [88]. The results of their work show that material jetting methods are promising for printing of different Newtonian and non-Newtonian silicones with viscosities as high as 100,000 $mPa.s$. However, droplet formation and jetting procedure in this method should be controlled and the printing quality should be optimized. Foerster et al. (2017) have also used this technique to fabricate porous silicone structures [89]. Similar PPJ system for jetting of viscous pastes at a velocity above 100 mm/s has been employed by Wacker Chemie for silicone AM [57]. Unlike regular inkjet printheads which can only handle fluids with a maximum viscosity of 40 $mPa.s$, these piezoelectric/pneumatic systems can generate enough force to even jet pastes with 1,000,000 $mPa.s$ viscosity.

2.5 Silicone Development for Additive Manufacturing

The main challenge in the development of materials for biomedical applications is their chemical, structural and mechanical biocompatibility [90]. As mentioned in Section 2.1 The biocompatibility and biodurability of silicone can be justified through its chemical structure at molecular level including the relatively long and flexible Si − O and Si − C bonds, the repetitive arrangement of silicon and oxygen atoms in the polymer chain, the arrangement and type of organic substituents, and the low intermolecular forces between the organic groups [31, 32]. However, the currently available silicones should be improved on three fronts for biomedical AM applications: (1) curing mechanism; (2) rheological properties and printability; (3) mechanical performance. Even though the development of silicone customized for AM is as important as the development of an AM system compatible for use with viscous non-Newtonian polymers, little research has been conducted in this area.

2.5.1 Curing System

The silicones reviewed in Section 2.4.2 were mostly two-part high temperature vulcanized (HTV) polymers. The HTV silicones need a few minutes to a few hours to at least be partially cured. This partial curing is necessary to allow the previously laid layers to tolerate the forces induced by the weight of upper printed layers. This slow polymerization rate increases the printing time required, if each silicone layer is to be cured after printing. Transferring the 3D printed structure to the oven after printing each layer also seems prohibitively cumbersome and reduces the printed part's accuracy. On the other hand, curing the silicone after printing multiple layers can result in losing the structural fidelity of the sample due to the weight of upper layers. Other difficulties associated with the heat-curable silicones such as the fast gelation time, short range of heat transfer when the heat beds are used, and potential for geometrical deformation have been pointed out in the study of Morrow et al. (2017) [91]. Therefore, the UV-curable silicones with the curing rate in the order of a few seconds can be a suitable replacement for both material extrusion and material jetting methods. Some silicone manufacturers such as Momentive, Novagard, Wacker, Elkem Silicones, and Shin-Etsu are already producing different types of UV-curable silicones. Some researchers have also started to develop their own UV-curable silicones or tune the commercially available ones for their AM systems.

Femmer et al. developed a UV curable silicone requiring 12 s irradiation at 440 nm UV for 100 μm features to be cured for the production of separation barriers [77]. The controlling factor in their research is the gas permeability of the silicone. Their silicone was used in a vat photopolymerization system. A sample of the functional 3D printed membrane made from this silicone and its curing mechanism are shown in Fig. 2.6(a) and Fig. 2.6(b), respectively. Another UV-curable silicone targeted for vat photopolymerization processes was introduced by In et al. (2017) [92]. This silicone is a composition of commercially available UV curable silicone (Momentive), a silicone thinner (to adjust the viscosity of the precursor), de-ionized water, and hydrophilic silicone. The results of their research showed that by adding water to the combination of UV-curable and hydrophilic silicone, the curing time could be decreased (Fig. 2.6(c)). The optimized curing time reached was approximately 20 *s*; however, this would need to be further reduced to be appropriate for 3D printing applications. The target of the research in [92] was manufacturing of solid phantoms for medical imaging.

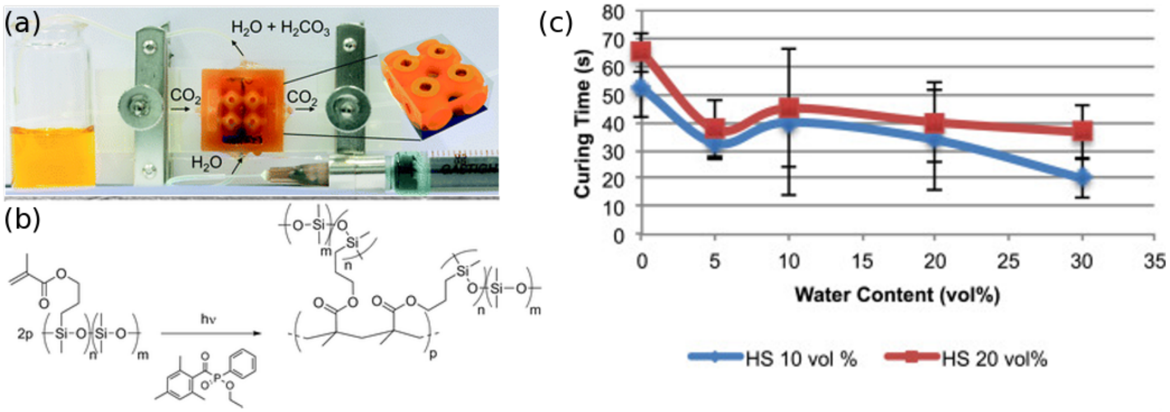

Figure 2.6: (a) Additively manufactured membrane made from the tuned UV-curable silicone. The change in the color of pH indicator from blue to yellow shows the permeability of CO_2 gas; (b) The photopolymerization process at molecular level in the developed silicone ink. (a-b) (adapted with permission from [77]. Copyright (2014) Royal Society of Chemistry). (c) Decrease in the curing time of UV-curable silicone by increasing the water content for inks with 10 vol.% and 20 vol.% hydrophilic silicone (HS). (adapted with permission from [92]. Copyright (2017) Elsevier).

2.5.2 Rheological Properties and Printability

The rheological properties of viscous silicones are important factors in the determination of their flow, droplet formation, and interaction with the surface. The effect of parameters such as viscosity, viscoelasticity, contact angle (Θ_c), surface tension (γ), interfacial energy, storage modulus (G'), loss modulus (G''), and capillary action, as well as the effect of fillers and additives on the extrusion, jetting, and flow of the viscous silicones should be comprehensively investigated.

Controlling the viscoelastic properties of silicone for material extrusion by optimizing the mixing ratio of low and high molecular weight silicones was used in the work of Robinson et al. (2015) [67]. Based on their work, an ink containing 60 wt.% high molecular weight silicone and 40% low molecular weight silicone showed a solid-like response at low shear stress region to make sure it will not slump after extrusion and retain its geometrical fidelity. Similarly, the effect of silica fillers on the rheological properties of PDMS and its extrusion quality was studied by Lv et al. (2017) [93]. The results of their research show that adding a controlled amount of filler (15 – 20%) can create a solid-like paste with G' slightly above the G'', that is not so viscous that it cannot be extruded. Fig. 2.7(a-b) shows the changes in the viscosity and dynamic moduli by varying the weight percentage of filler. Similar shear-thinning behavior was reported by addition of 10 - 20 wt.% of treated silica to poly(diphenylsiloxane-dimethylsiloxane) copolymer (PDMS–co–PDPS) by Durban et al. (2017) [94]. The adoption of these approaches for developing customized silicone for AM assures the flow of silicone ink under the regular shearing at the nozzle while preventing the collapse of printed features.

Roh et al. (2017) developed a three-phase silicone ink customized for material extrusion [95]. Their developed ink consists of micro-particles of cured silicone, liquid silicone precursor, and water. In their technique, suspensions of cured silicone particles are covered with liquid silicone resulting in the formation of capillary bridges, which in turn produce a gel-like printable elastic ink. This procedure has been illustrated in Fig. 2.7(e). This porous silicone ink can be printed both in air or inside aqueous environment, meaning it can be used for *in vivo* 3D printing applications. The presence of cured silicone particles, however, may limit the resolution of the printed line features. Fig. 2.7(f) shows that adding a small amount of liquid silicone (2 vol.%) to create capillary bridges changes the viscoelastic properties of PDMS drastically. The cross-linked capillary suspension with G' higher than G'' acts as an elastic paste. Thus, another mechanism for controlling the flowability and shape-retention of the silicone inks was introduced through this research.

2.5.3 Mechanical Performance

The mechanical characterization of elastomers including silicone has been extensively studied [96–102]. Silicones used in biomedical applications should generally demonstrate high tear strength (T_s), tensile strength (σ_f), and elongation at break (ϵ_f). Moreover, their hardness should be tuned for each application. For instance, in the case of the prosthetics, resilience, high elongation, and soft skin-like properties are necessary as they are usually removed for sleep and adhered to the skin when awake. This repetitive wearing/removing should be possible without the risk of damaging the prosthesis. Aziz et al. (2003) have investigated the mechanical properties of some commercial silicones used in prosthetics industry [103] (see Table 2.1), and pointed out the need for improvement in mechanical

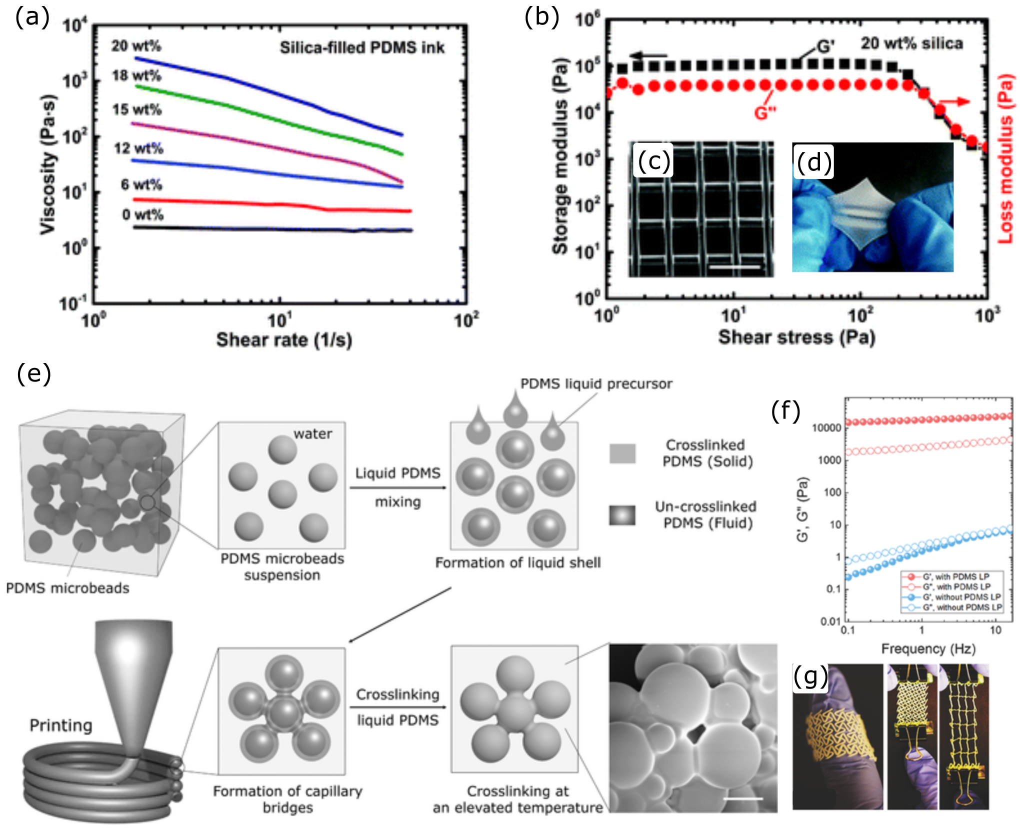

Figure 2.7: (a) The effect of silica on the viscosity of silicone; (b) 20% silica filler results in storage modulus greater than loss modulus for printing of porous parts with high shape retention; (c-d) sample of the 3D printed membrane; (c) The scale bar is 1 mm.(d) The 3D printed membrane under stretching. (a-d) (Adapted with permission from [95]. Copyright (2017) Royal Society of Chemistry). (e) The process of formation of capillary bridges; (f) The effect of capillary bridges on the storage and loss moduli of the PDMS; (g) A sample of flexible 3D printed structure from the capillary suspensions. (e-g) (Adapted with permission from [93]. Copyright (2017) Wiley and Sons).

and surface properties of currently available silicones. The shortcomings of current commercially available silicones and UV-curable elastomers in terms of their mechanical and optical properties have also been well explained by Patel et al. (2017) [85].

Table 2.1: Mechanical properties of commercial silicones.

Property	Suggested Range
σ_f $[MPa]$	5.5 – 8
T_s $[kN/m]$	5 – 17
ϵ_f [%]	500 – 1200
Hardness [I.R.H.D.]	16 – 25

Ozbolat et al. (2017) have reported decreased level of air entrapment inside the silicone structures made using extrusion-based AM compared to molded structures resulting in the improvement of mechanical properties of AM-made silicone parts [104]. Based on their work, 1.5 - 4 % reduction in the porosity of silicone parts has showed an increase of up to 2-fold for σ_f and ϵ_f for the parts with a printing path aligned with the uniaxial tensile test direction. Negligible difference in the stiffness of AM-made and bulk silicone has been reported in [73] as well.

Jindal et al. (2016 & 2017) proposed modifications to the PDMS structure to make it compatible with extrusion-based AM for maxillofacial prosthetics [105, 106]. They proposed an optimum combination of PDMS, catalyst, filler, and cross-linker to obtain the mechanical properties of commercial silicones typically used for the fabrications of facial prosthetics. The focus of their study was the development of a two-part room temperature vulcanized (RTV) silicone that undergoes a fast cure once extruded. In their study, Jindal et al. came to four conclusions about the effects of different components on silicone's mechanical properties. First, The combination of long (L) and short/medium (S/M) polymer chains (70% L – 30% S/M) improved mechanical properties. The short chains produced excessive local cross-links between the long chains resulting in higher tensile and tear strengths while the long chains maintained the elastomeric behavior of the substance. Second, increasing the amount of short/medium polymer chains (50% L - 50% S/M) resulted in a more brittle material, however, the hardness could be increased to up to 30 (Shore A). Third, increasing the amount of filler improved all mechanical properties, however, samples with more than 20 wt.% of filler were difficult to mix due to their high viscosity. 5 wt.% appeared to be the optimum amount of cross-linker. Fourth, higher concentrations of cross-linker increased the brittleness of the samples and reduced their flexibility [105]. The experimental results are summarized in Table 2.2. Once the optimum mechanical properties (3.5 ± 0.6 MPa for σ_f, 8.5 ± 0.7 kN/m for T_s, and 24.3 ± 0.5 Shore A hardness) were achieved, they modified the curing system from an HTV to an RTV. The final silicone ink could be cured in less than 1 minutes at room temperature after mixing the cross-linker and catalyst parts. In order to prevent slumping after extrusion, thixotropic agents were added to the silicone ink to increase its viscosity. This, however, resulted in a decrease in tear and tensile strength which was compensated for by addition of filler [106].

By taking advantage of the effect of crosslink density on the hardness and flexibility of polymers, Durban et al. developed silicones with a wide range of hardness from 10 to 70 (Shore A) tailored for material extrusion AM [94]. In their work, dihydrid chain extenders and short-chain vinyl-terminated PDMS have been used for decreasing and increasing of the crosslink density, respectively.

Foerster et al. demonstrated the effect of the cellular structures on the viscoelastic behavior of silicone parts fabricated via PPJ [89]. Based on their work, a higher level of porosity reduces both shear and loss moduli of the AM-made sample drastically, resulting in a less stiff structure; however, the highly porous structure showed a more thermally stable behavior for both G' and G'' at 25 - 120 °C.

2.6 Discussion

The review of studies conducted on silicone AM showed that further work on development of AM systems and materials must be carried out. Table 2.3 summarizes 3D printing parameters such as lateral and vertical resolutions and printing speed, as well as the type of silicone used in the research work reported since 2013. Although not all parameters were reported in all papers, comparing the available results provides a clear understanding of the status of silicone AM research and highlights where there is room for improvement.

In material extrusion and FRE methods, the lateral resolution (i.e., the width of the printed linear features in XY plane) is adjusted by the amount of back pressure, nozzle velocity, inner diameter of the nozzle, and the stand-off distance between the nozzle tip and the substrate [104]. The latter is not applicable to the FRE where the period of elastic recovery and the interfacial interactions between the two phases affect the resolution [75]. Yuk et al. (2017) have extensively investigated the relationship between the nozzle velocity and stand-off distance to the pattern and dimensions of printed strands based on the viscoelastic properties of silicone [107]. The rheological properties of the silicone polymer also impact the lateral resolution of printed features if not cured *in-situ*. The silicone should be viscous enough so that it does not slump and is able to maintain its geometrical fidelity after being printed [105], and at the same time should demonstrate a shear-thinning behavior so that its viscosity is low enough for extrusion at the shear rate

Table 2.2: The mechanical properties of different combinations of PDMS chains with 5% cross-linker (adapted with permission from [105]. Copyright (2016) Elsevier).

	Long Chains (%)	Medium Chains (%)	Short Chains (%)	Avg. Mol. W. (kDa)	Hardness (Shore A)	σ_f (MPa)	T_s (kN/m)
Composition A	70	20	10	29.4	24.3 (± 0.47)	3.52 (± 0.66)	8.48 (± 0.72)
Composition B	60	30	10	26.4	23.2 (± 0.37)	2.21 (± 0.54)	5.42 (± 1.61)
Composition C	60	20	20	25.7	24.7 (± 0.47)	2.79 (± 0.31)	5.87 (± 1.50)
Composition D	50	20	30	22	28.5 (± 0.76)	1.46 (± 0.29)	1.27 (± 0.36)

the ink experiences in the orifice. The minimum sufficient width reported so far is 30 μm by O'bryan et al. obtained by increasing the viscosity of the silicone ink and eliminating the interactions between the silicone surface and the support structure [75]. Femmer et al. reported printing 100 μm features, demonstrating the potential of vat photopolymerization techniques for the production of high resolution silicone parts [77]. This can be achieved by modeling the curing mechanism of the silicone while being exposed to UV light. The LOPP system introduced by Kim et al. has the maximum achieved raster width of 1 – 2 mm at the proof-of-concept stage.

Most researchers have not measured and reported the vertical resolution, and/or layer thickness, which controls the surface waviness and the general aesthetic aspects of the 3D printed objects. This property is controlled by the nozzle to the substrate off-set, the thickness of uncured layers of photopolymer, or the rheological properties of the ink for the extrusion, vat photopolymerization, and jetting systems, respectively. The minimum value reported for the vertical resolution is 2 μm (McCoul et al.) achieved by inkjet printing.

Generally, the speed of 3D printing is measured by the volume of material which is laid down, fused, or bound per unit of time. This important parameter has not been reported in most of the reviewed research work; however, the translational speed of printheads which has direct correlations with the 3D printing speed will be discussed in the following.

The nozzle speeds for material extrusion and FRE techniques are very similar. Depending on the pressure value, this speed in material extrusion can vary between 1 – 20 mm/s. The printhead speed for the aerosol jetting system reported by Reitelshofer et al. is 5 mm/s as well. The slow velocity of the mentioned methods can drastically reduce their adoption for clinical and industrial applications.

Up to now, drop-on-demand jetting systems has shown the highest velocity at around 100 mm/s. Unless systems capable of fabricating a 2D plane instantly, such as DMD-based SLA or PBBJ, were employed for the production of silicone parts, jetting systems remain the fastest for the fabrication of highly viscous polymers such as silicone.

This review of sparse research in the area of silicone customization for AM shows the need for improvement in the polymerization mechanism of silicones, as well as their rheological and mechanical properties in parallel to the system development.

Considering long production time as the main hindrance to industrial adoption of AM in general, heat-curable silicones with the minimum gelation time of 5 min should be replaced with irradiation-curable systems in order to make silicone AM more attractive at a commercial level. Current trials investigating the development of UV-curable silicones have been limited to the vat photopolymerization techniques. In the future, UV-curable silicones should be developed for material extrusion and jetting systems as well. The instantaneous curing, lack of surface tackiness after photopolymerization, long working hours under visible light, and biocompatibility will be key factors in development of such materials. A holistic study of the effects of silicone's rheological properties on its flow, extrusion, and jettability needs to be performed as well so that the behaviour of these non-Newtonian viscous fluids can be predicted and controlled. Tuning the mechanical properties of UV-curable silicone with optimized rheological properties is also necessary. Finally, the mechanical performance of the parts manufactured using any of the reviewed AM methods should be tested and compared to that of bulk materials.

2.7 Conclusion

The review showed that the feasibility of silicone AM in a PBBJ process has not been investigated before. Material extrusion and FRE methods can already shape form fully functional and complex structures, however, at a low speed. Among all, material jetting and DMD-based vat photopolymerization techniques seem to be able to provide solutions to the AM of silicone with a high throughput. For material jetting, improvements in three aspects of resolution, scalability, and multi-color printing are necessary. For the vat photopolymerization, the current challenge is design and development of affordable mask-projection laser-optical systems to build structures in the middle of polymer reservoir without crosslinking the voxels that are not going to be a part of the final shape. Complemented with customization of silicone properties for different AM processes, 3D printing might become the new standard approach for manufacturing of bio-structures.

Table 2.3: Comparison of the 3D printing features for the silicone AM techniques

AM Method	Authors / Company	Publication Year	Lateral Resolution (μm)	Vertical Resolution (μm)	Printing Speed (mm/s)	Curing System	Viscosity ($mPa.s$)
Material Extrusion	Mannor et al.	2013	*	*	*	*	*
	Duoss et al.	2014	100-610	*	1-20	HTV	*
	Liravi et al.	2015	250-300	100	5-10	UV	40,000
	Schmalzer et al.	2016	*	*	*	HTV	*
Freeform Reversible Embedding	Hinton et al.	2016	140-400	100	20	HTV/Moisture	3,000-4,000
	O'bryan et al.	2017	30-700		2-10	UV	
	Fripp Design Ltd.	2016	*	*	*	RTV	*
Vat Photopolymerization	Femmer et al.	2014	100-400	*	*	UV	*
	Kim et al.	2016	*	1000-2000	*	UV	*
Material Jetting	Reitelshofer et al.	2016	*	30	5	HTV	2,000
	Liravi et al.	2017	500-600	300	100	UV	40,000
	Wacker Chemie AG (ACEO)	2015	*	*	*	UV	*

* Not reported

Chapter 3

Additive Manufacturing of Silicone via Material Extrusion

3.1 Introduction

Material extrusion is one of the seven classes of AM, based on the ASTM F 2792-12a standard [108]. Nozzle dispensing is one of the techniques used under this class of AM that has gained attention from academia and industry due to its emerging applications in different areas from electronics [109–111] and microsystems packaging [112] to tissue engineering [113, 114]. This technology has been reported to be the most widely used method in bio-manufacturing and life sciences [55, 115]. Material extrusion includes a wide range of different AM processes, and different definitions have been proposed for it. However, all of these definitions enumerate the following characteristics: (1) the ability to produce 3D objects; (2) the ability to manufacture on planar and non-planar surfaces; (3) the ability to process a wide range of materials including metals, polymers, ceramics, biomaterials etc.; and (4) the ability to fabricate structures at different dimensional scales from nano- to millimeter [112].

This flow-based manufacturing method produces 3D structures by depositing a continuous stream of the material onto a surface using a robotically controlled nozzle [59, 116]. The movement of nozzle in the z-direction and depositing a new layer of fluid on top of the previous layers and/or support structures makes the manufacturing of a 3D structure possible [53]. The deposited fluid turns into solid after dispensing by cooling, photo-curing, or solvent evaporation [59].

Different dispensing mechanisms are being used to push the fluids through a nozzle in a nozzle dispensing system with pressure-actuated (pneumatic) and mechanical dispensing systems being the most popular [59]. In pressure-actuated nozzles, a time-controlled compressed air is used to activate the deposition process. Simple mechanism of these nozzles along with their easy operation and maintenance are the reasons for their widespread adoption for in-house developed AM systems. Mechanical dispensing systems use either a screw-based or a positive-displacement mechanism which generate the required force for deposition by rotation of a stepper motor or linear displacement of a piston, respectively [55]. Although mechanical dispensing systems provide better control for low volume feed rates of fluids, they have a maximum force limit which will constrain their application in dispensing of highly viscous materials [53, 55]. As a result, among prevalent AM technologies, pressure-actuated nozzle dispensing system is more suited for the fabrication of 3D structures from viscous materials [54].

Vozzi et al. (2002) introduced the driving pressure produced by the compressed air (P), polymer surface tension (γ), and the friction between the fluid and the internal nozzle wall (F_f) as the main forces that determine the flow of viscous materials in these systems [117]. In this dynamic fluid model, width of the deposited fluid (W_d) can be calculated from the internal radius of the nozzle (R_s), viscosity of fluid (μ), printing velocity (v), height of the printed pattern (H), length of the tapered zone of the nozzle (h_z), and air pressure (P) using Eq. 3.1. These significant forces are depicted in Fig. 3.1. Based on this work, an analytical model was developed to relate the injection process and dimensional parameters of the extrusion-based system [118]. In this two-tier model, first model estimates the flow of fluid through the nozzle and the second one predicts the dimensional parameters of the extruded fluid based on the results of first model. These models, however, assume that the material has a low viscosity, the fluid is Newtonian, and the flow is laminar throughout the dispensing system. These assumptions are not valid for injection of medical-grade silicones that are mostly non-Newtonian fluids with paste-like behavior. As a result, alternative methods such as statistical experimental design and finite element modeling (FEM) can be adopted to control the dimensional accuracy and surface quality of the deposition for different materials. Multiple research groups have used similar statistical analysis tools to improve the quality of their additively manufactured parts [119–121].

$$W_d = \frac{\pi R_s P}{8 \mu V h h_z} \tag{3.1}$$

The feasibility of direct additive manufacturing of highly viscous silicone using material extrusion technique is evaluated in this chapter; moreover, the influence of process

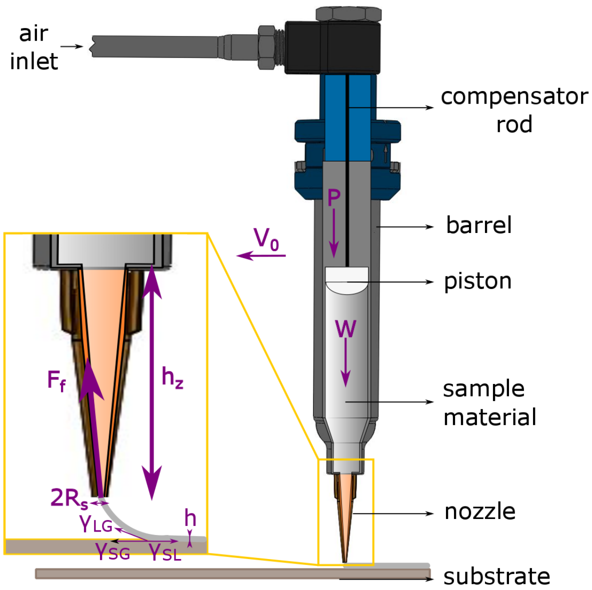

Figure 3.1: Influential forces in fluid dispensing: compressed air (P), polymer surface tension (γ), the friction between the fluid and the internal nozzle wall (F_f), and the weight of fluid (W). The width of the deposited fluid can be calculated from the internal radius of the nozzle (R_s), viscosity of fluid (μ), printing velocity (V_0), height of the printed pattern (h), length of the tapered zone of the nozzle (h_z).

parameters on the dimensional accuracy of printed silicone lines and the surface quality of printed silicone planes is investigated. To this end, different statistical techniques have been adopted. To conduct an initial investigation, design of experiments (DoE) has been used, followed by the response optimization to obtain the target dimensions using desirability function approach. In order to relate the significant parameters, an empirical mathematical model has been presented. The results of this study assure uniform and precise printing of highly viscous silicone which can be used as a basis for the fabrication of three-dimensional shapes using material extrusion technique. The surface properties of printed structures can also be controlled resulting in the fabrication of implants with desired surface texture that can eliminate the complications after the surgery. In other words, prosthetic implants with desired smoothness can be produced using this technique. The effects of surface properties of implants on their acceptance by body have been studied by different researchers [122, 123].

Finally, in order to predict the dimensions of extruded features, a FEM of the dispensing of highly viscous silicone is presented. The modeling results are experimentally validated by comparing the simulated injection flow profile with that of the real process. The model is proved to be accurate in predication of the dispensing profile and the geometry of injected fluids.

3.2 Materials and Methods

3.2.1 Silicone

Commercial biocompatible silicone (RTV 800 – 400, Novagard Solutions, OH, USA) was used as-received for optimizing the extrusion process in this study. Similar silicone with lower viscosity (RTV 800 – 620, Novagard Solutions, OH, USA) was used to model the dispensing procedure. These two polymers are UV-curable, and contain the photoinitiator Irgacure TPO-L (BASF Corporation, MI, USA) which is sensitive to the long wavelength UV light (less than 500 nm).

Viscosity Measurement

The viscosity of RTV 800 – 620 was measured using a rotational viscometer (High Shear CAP-2000+, Brookfield, MA, USA). The experimental results (Fig. 3.2) demonstrate the shear thinning behavior of this polymer. Experimental results plotted in semi-logarithmic scale can be modeled using Carreau-Yasudas model (Eq. 3.2).

where μ is the dynamic viscosity, μ_0 is the initial value of viscosity, μ_∞ is the infinite value of viscosity (mostly zero), λ is the relaxation factor and represents the time after which the transition to non-Newtonian region happens, a is the width of transition (non-Newtonian) region, and n is the slope of the power-law region. Parameters μ_0 and μ_∞ can be measured from the experimental data. Parameter a is considered to be 2. The values of λ and n are estimated by fitting a curve to the experimental data using the least square curve fit algorithm of MATLAB. The Carreau parameters are presented in Table 3.1.

$$\mu - \mu_\infty = (\mu_0 - \mu_\infty)(1 + (\lambda\gamma)^a)^{\frac{n-1}{a}} \tag{3.2}$$

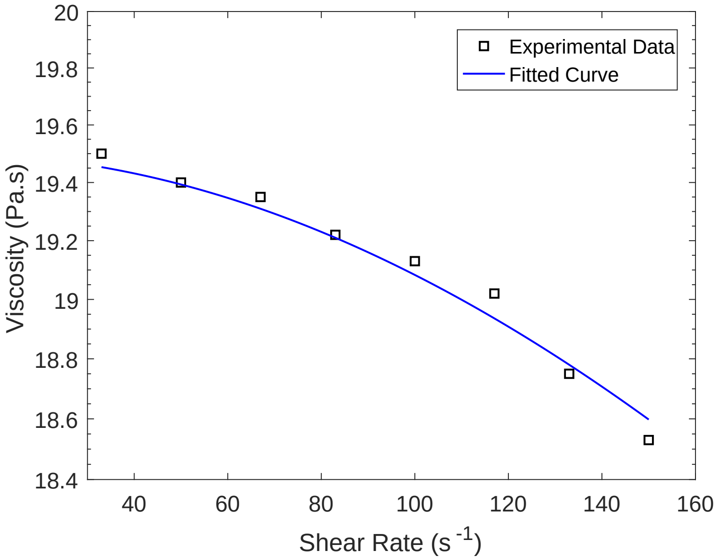

Figure 3.2: Viscosity vs. shear rate for silicone RTV 800 – 620.

Table 3.1: Rheological parameters of silicone RTV 800 – 620

μ_0 (Pa.s)	μ_∞ (Pa.s)	λ (s)	n
19.9	0	0.0016	0.79

Surface tension measurement

Measurement of the surface tension of silicone (RTV 800 – 620) was carried out using an in-house developed instrument designed based on axisymmetric drop shape analysis profile (ADSA-P) technique. The details of development of this instrument can be found in [124]. The calculation of surface tension value is made by fitting the geometrical dimensions and profile of the pendant droplet to those obtained from Young-Laplace equation of capillary throughout the injection (Eq. 3.3):

$$\Delta P = \gamma(\frac{1}{R_1} + \frac{1}{R_2}) \tag{3.3}$$

where ΔP denotes the pressure difference across the surface, γ denotes the surface tension, R_1 and R_2 are the principal radii of curvature. Images of the pendant droplet are captured during the injection and sum of squares (SS) of the normal distance between the experimental and theoretical points are minimized in ADSA-P method. After fitting the best curve to the profile of droplet, the software calculates volume, surface area, and surface tension of the droplet. This process is continued until a steady-state value for the surface tension is reached [125]. Fig. 3.3 shows the pendant silicone drop and the fitted Laplace curve. The density of silicone (0.87 g/cm^3 at 18 °C) is an input for calculating the surface tension which is plugged into the model by the following capillary constant:

$$c = \frac{\Delta\rho g}{\gamma} \tag{3.4}$$

where c is the capillary constant, $\Delta\rho$ is the difference between the densities of silicone and air, and g is the acceleration of gravity [26]. The value of silicone/air surface tension measured with this technique is approximately 18.9 mN/m, which is very similar to the values reported in the literature for other silicone polymers [126, 127].

Contact angle measurement

The measurement of contact angle (Θ_c) between silicone (RTV 800 – 620) and glass slide and that of the silicone and plastic nozzle tip was carried out using the captured photos of the fluid (Fig. 3.4). The open source image processing software ImageJ was used for this purpose. As contact angle of silicone on the glass substrate varies with time, the value of contact angle was measured at 1 s time intervals and a regression model (Fig. 3.5) was fit to model its changes over time. Different values of Θ_c can be found in Table 3.2. Figure 3.5 shows samples of Θ_c measurement on different surfaces.

Figure 3.3: Silicone drop image captured using ADSA-P technique.

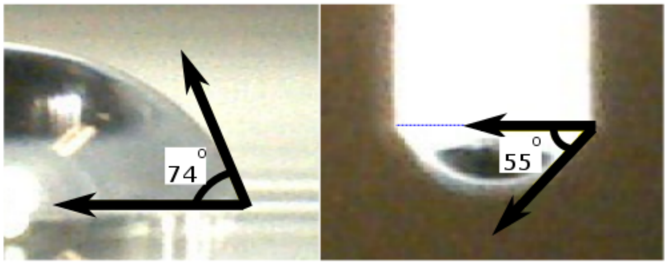

Figure 3.4: Contact angle between (a) silicone droplet and glass slide, (b) silicone and plastic nozzle tip.

Table 3.2: Contact angle between silicone and glass substrate vs. time.

t (s)	4	5	6	7	8	9	10
Θ_c (rad)	2.25	1.9	1.73	1.47	1.48	1.45	1.29

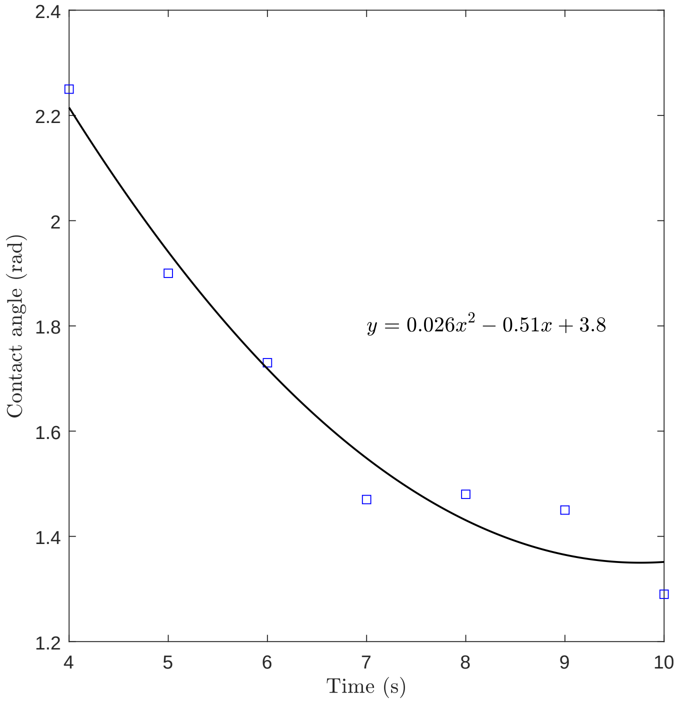

Figure 3.5: Fitted curve to the variations in the value of contact angle of silicone and glass substrate.

3.2.2 Experimental Setup

A pressure-actuated printhead has been used in our 3D printer. In this type of printhead, the time-controlled compressed air is used to activate the deposition process. The first step in AM of silicone products using material extrusion is developing a CAD model of the part. Then, the part will be fabricated layer-by-layer by direct deposition of silicone from a nozzle. The deposition process can be done using pneumatic or piezoelectric actuators. Another nozzle needs to be used to fabricate sacrificial support structures. For this study, an in-house-developed pneumatic micro-syringe deposition system that uses an air-powered dispenser (Ultimus$^{\mathrm{TM}}$ V high precision dispenser, Nordson, OH, USA) is used and proved to be able to inject highly-viscous silicone consistently [128]. The additive manufacturing set up is shown in Fig. 3.6.

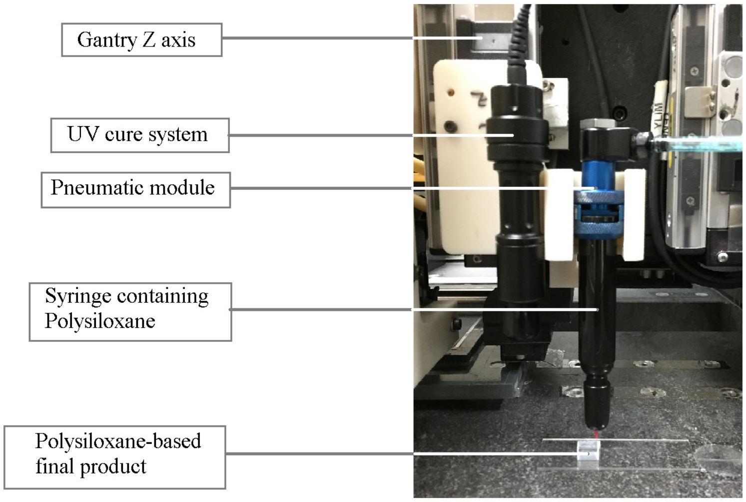

Figure 3.6: Components of the micro-syringe nozzle dispensing system.

3.2.3 Sample Preparation and Profilometry

The material extrusion technique was used to produce 1 cm straight silicone line features (RTV $800-400$). Pressure (P), printing velocity (v), and working distance (WD) (distance between the substrate and nozzle tip) were the process parameters that have been changed to print different samples. Before printing, the microscope slides used as substrate were washed with acetone and dried. Immediately after printing, silicone lines were cured with UV lamp for 10 s and left overnight to make sure that the full polymerization has happened.

Dimensional properties of lines: average width (W_{avg}), uniformity ($W_{s.d.}$), and surface waviness (W_{avg}) were investigated using two-dimensional (2D) and 3D images produced by means of a 3D optical profilometer (UP series, Rtec Instruments, USA). The optical profilometer scans the printed silicone-based line patterns using a white light-emitting diode (LED) light source with a sub-micrometer vertical resolution. The scanning area has a dimension of 1 $mm \times 1$ mm. High resolution 2D images were used to calculate width of samples at five different locations as shown in Fig. 3.7(a). A 250 μm precision dispensing tip (Smoothflow tapered tip, Nordson Corporation, OH, USA) was used to print sample lines. The average of five values is considered as the average width of that sample and their standard deviation is considered as the measure of uniformity. In order to quantify the surface quality, the surface profile of sample at aforementioned five locations was obtained and, the difference between the highest peak and lowest dip for every plot was calculated and averaged out. The lower this value, the higher the surface quality will be. Figure 3.7(b) shows a sample of surface profile. Figures 3.8(a-d) shows the difference in the uniformity of width for some of the samples. Excessive pressure and low printing velocity create wide lines (Fig.3.8(a)). Figures 3.8(a-b) are products of suitable combination of process parameter values and have produced finer lines; however, the difference in their surface quality is obvious. Figure 3.8(d) shows failure in printing of a uniform line, mostly due to the large working distance or high printing velocity. Different level sets of process parameters result in different surface qualities. 3D images shown in Fig. 3.8(e-f) demonstrate this difference in the quality of surfaces. The printed line in Fig. 3.8(e) has a non-uniform surface with lots of fluctuations in one side. On the other hand, Fig. 3.8(f) shows a smooth surface with lower roughness.

In order to optimize the surface quality of the 3D plane features [1], a layer of 1 $cm \times 1$ cm silicone square was made on a silicon wafer. The 3D image of each sample was captured using an optical/laser profilometer (VK-X250, Keyence, Japan) at 100× magnification. The root mean square of surface waviness (W_q) at the filter cut-off wavelength of 0.08 mm was selected as a measure of the surface quality. Waviness is described as the uneven features that are repeated periodically on the surface at longer intervals compared to the roughness. The profile data was collected over 31 lines. The waviness was measured for each line, and their average was used as the final surface quality value. Figure 3.9 shows a sample of the waviness measurement and the surface profile.

---

[1] The experimental results related to the surface quality of planes are adapted from author's published work [28].

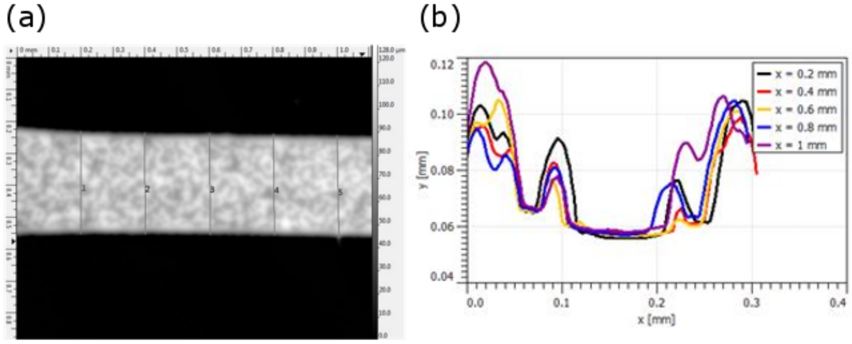

Figure 3.7: (a) Sample width five locations is measured. Average and standard deviation of five values are used as measures of sample width and uniformity, respectively; (b) Surface profile is used to calculate the difference between the highest peak and lowest dip as a measure of surface quality.

3.2.4 Time-lapse Imaging

A calibrated digital Microscope (Dino Lite, AnMo Electronics Corporation, Taiwan) was used to capture the geometry and location of the silicone (RTV $800-620$) flow at predefined time intervals during the dispensing process. The microscope was fixed on its holder at the distance of 10 mm from the nozzle tip with a magnification of 42×. Images of the dispensing process captured with digital microscope were used to validate the FEM results. The software DinoCapture was used to measure the geometrical and flow parameters.

3.2.5 Experimental Designs

An experimental procedure was designed to find the optimum treatment combination of the process parameters (P, v, and WD) to achieve the minimum line width without any significant reduction in the surface quality and uniformity. A review on the scientific background of DoE is provided in A.1. Two replicates of the experiment were conducted to capture the variance in the process with higher accuracy and two center points were chosen to study the curvature as well. The number of replicates was determined using power and sample size for 2-level factorial designs. As a result a 2-level full factorial experiment with 2 replicates and 2 center points was designed which resulted in 18 runs. It would have been possible to choose a resolution III design with 10 runs, but this design confounds main factors and second order interactions which will make it difficult to find

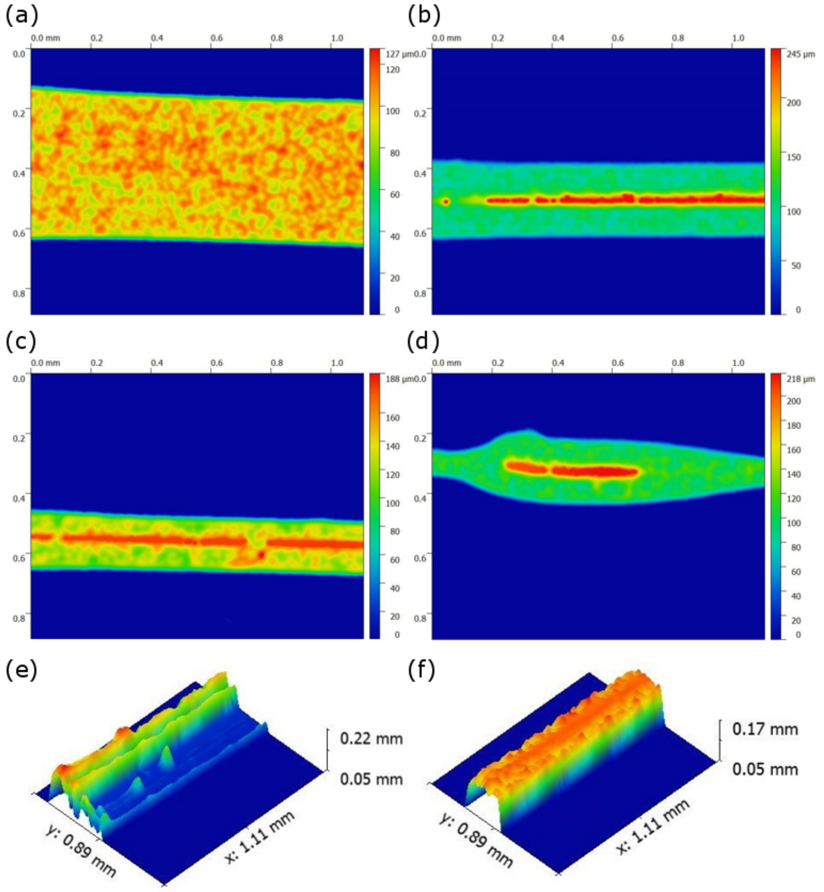

Figure 3.8: (a-d)2D Profilometry results showing different width and uniformity variations of lines extruded using RTV 800 – 400 silicone based on changes in the process parameters, (a) $P = 200\ kPa$, $V = 5\ mm/s$, $WD = 0.5\ mm$, (b) $P = 150\ kPa$, $V = 7.5\ mm/s$, $WD = 0.35\ mm$, (c) $P = 100\ kPa$, $V = 5\ mm/s$, $WD = 0.2\ mm$, (d) P = 100 kPa, $V = 5\ mm/s$, $WD = 0.5\ mm$; (e-f) 3D Profilometry results showing different surface profiles based on changes in process parameters, (e) $P = 200\ kPa$, $V = 5\ mm/s$, $WD = 0.5\ mm$, (f) $P = 150\ kPa$, $V = 7.5\ mm/s$, $WD = 0.35\ mm$.

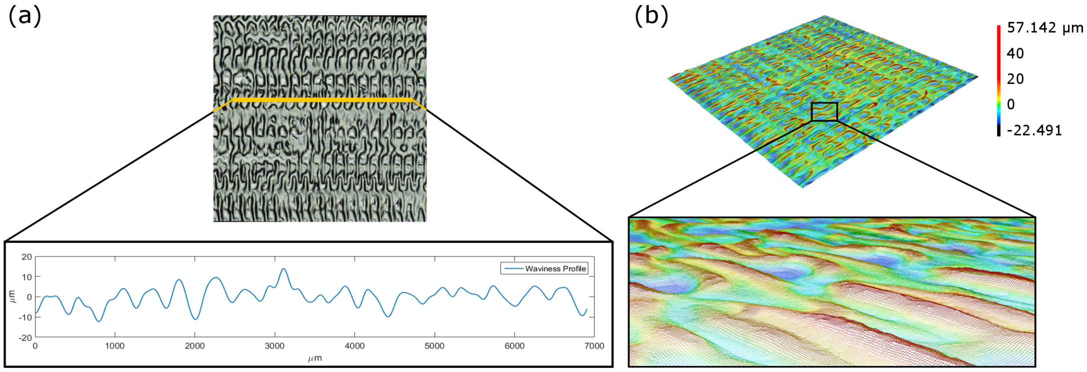

Figure 3.9: Sample of surface characterization for the RTV 800 – 400 silicone plane features: (a) the optical and laser image of the printed sample and the waviness profile obtained at the cut-off wavelength of 0.08 *mm* over the scanning length, (b) 3D profile of the printed plane.

the significant factors. The experimental factors and levels for initial 2^3 factorial design are shown in Table 3.3.

At final stage, all responses were optimized simultaneously considering all the process parameters using the desirability function method. The details of this technique are provided in A.2. In the simultaneous optimization, the importance of W_{avg} and $W_{s.d.}$ are considered three times and twice the W_q, respectively. The quality of the 3D printed products is highly dependent on the resolution of single lines that are the building units of every layer [129]. The less the width of the line features, the higher the quality of final structure. Consequently, the highest priority has been assigned to W_{avg} in the optimization process. On the other hand, the surface quality can be improved in the post-processing. Hence it gets lower weight in the optimization algorithm [130–132]. $W_{s.d.}$ is of a mid-level importance compared to the two other parameters.

Table 3.3: Levels of process parameters for optimization of line features in material extrusion technique for silicone RTV 800 – 400.

Experimental Factors	Low (–1)	Center (0)	High (+1)
P (kPa)	100	150	200
v (mm/s)	5	7.5	10
WD (mm)	0.2	0.35	0.5

Similar experimental design was conducted to optimize the surface quality of the 3D layers (planes) printed via material extrusion. A 2^4 full factorial design with one center point was designed and replicated twice. The parameters under study are same as those investigated for the line features in addition to the RW. These four screening factors and their lower and higher levels are shown in Table 3.4. The resulting 34 treatment combinations were printed in a completely randomized order. W_q was measured for each sample as explained in Section 3.2.3.

Table 3.4: Six Influential factors and their treatment levels for the material extrusion of plane features.

Factors	Low Level (–1)	High Level (+1)
RW (mm)	0.1	0.2
v (mm/s)	10	20
WD (mm)	0.1	0.15
P (kPa)	150	200

3.2.6 Numerical Modeling

Different numerical methods have been proposed to simulate the motion of the interface of two immiscible fluids. These methods can be classified into three groups of Lagrangian, Eulerian, and arbitrary Lagrangian-Eulerian (ALE) methods [133]. In this chapter, Level-set method, an Eulerian method, is employed to simulate the dispensing of silicone using transient Navier-Stokes equations. The level-set method is explained in details in A.3. 2D and 3D finite element algorithms which are able to solve full non-linear Navier-Stokes equations for predicting the emerging and evolution of droplet of a Newtonian fluid have been developed by Wilkes et al. (1999) for the first time [134]. The equations governing the fluid flow in nozzle dispensing systems are provided in A.4.

A time-dependant two-phase laminar flow interface was chosen in COMSOL multiphysics 5.1. This interface is a part of both computational fluid dynamics (CFD) and microelectromechanical systems (MEMS) modules. The designed 2D axisymmetric geometry is presented in Fig. 3.10(a). Parts I and II represent the inner geometry of the tapered nozzle tip and air, respectively. The two fluids are distinguished by defining two different initial values for parts I and II. Air has been called from the COMSOL material library and silicone has been custom defined. The density of silicone (ρ) was set as a constant value and its viscosity (μ) was defined using the Carreau model parameters, listed in Table 3.1.

The inner diameter of the nozzle and its distance from the substrate are shown in the Fig. 3.10(a) as well. The gap between the nozzle tip and air represents the plastic wall of the nozzle tip, and is modeled to prevent numerical errors at the initial phase of dispensing. Only the tapered part of the nozzle is modeled as the pressure gradient in the cylindrical upper part of nozzle and throughout the barrel is negligible [118].

The boundaries are marked in Fig. 3.10(a) with letters **a-g**. Boundary **a** is defined as pressure inlet. Pressure is applied to this boundary using the following equation:

$$P_{air}[step(t[\frac{1}{s}]) - step(t[\frac{1}{s}] - t)] \tag{3.5}$$

where P_{air} is the amount of pressure and t is the total time the pressure is activated. Function *step* is used to avoid inconsistent initial condition when pressure is applied and removed. This step function smooths the transition of the value of pressure from zero to P_{air} at time 0 and from P_{air} to 0 at time t. Boundary **b** is a no-slip wall and covers the wall of barrel. Boundary **c** models the microscope slide substrate as a wetted wall with contact angle presented in Fig. 3.4. The slip length is suggested to be equal to the average length of mesh. Boundary **d** represents the inlet of air with pressure zero. The initial interface of two fluids is defined in boundary **e**. Even at the highest vacuum pressure of the dispensing system (4.48 kPa), oozing of silicone creates a semi-spherical droplet before the printing, boundary **e** shows this aggregation of material at nozzle tip. Boundary **f** is a no-slip wall, and boundary **g** models the wetted wall with contact angle of 55°.

The effect of weight was considered by defining gravity for the entire geometry. In order to complete the design of FEM, the surface tension of silicone was introduced to the model as a user defined parameter. Considering the dependency of the quality of the results on the meshing, mesh independency analysis was done and a triangular mesh with 0.012 mm and 0.084 mm as the minimum and maximum element sizes, respectively, was selected. Fig. 3.10(b) demonstrates the mesh elements.

3.3 Results and Discussion

3.3.1 Optimizing the Extrusion of Line Features

Factor Screening

Dimensional accuracy and surface quality of the silicone lines manufactured with extrusion technology depend on many factors including the printing velocity, pressure, working dis-

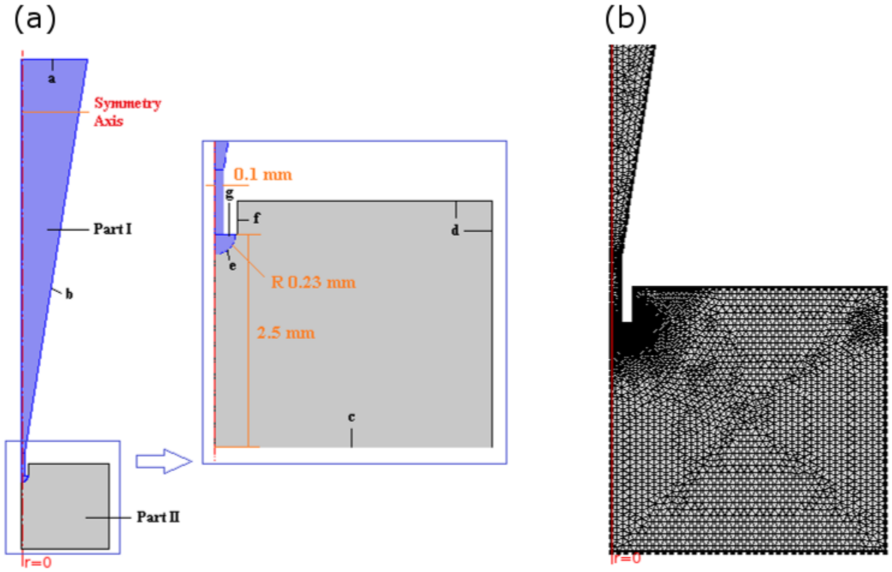

Figure 3.10: (a) Geometry and boundaries of the model: part I represents the silicone inside the nozzle tip, part II represents the air, r = 0 is the symmetry axis, **a** is pressure inlet, **b** is no-slip wall, **c** is wetted wall, **d** is air inlet, **e** is initial interface of fluids, **f** is no-slip wall, **g** is wetted wall; (b) Meshing: triangular mesh was chosen for both domains, mesh independency analysis resulted in an optimized value of 10938 mesh elements with minimum and maximum sizes of 0.012 mm and 0.084 mm, respectively.

tance, substrate preparation, curing time, environmental conditions, etc. It is not feasible to study all these factors as it will be extensively time consuming. The most important process parameters (P, WD, and v) have been selected as controlling factors for the dimensional accuracy of printed parts. The factor screening design is shown in Table B.1. As explained in section 3.2.5 a total of 18 silicone lines based on different factor level combinations were printed and their width, uniformity, and surface waviness were investigated using a 3D optical profilometer.

Figure B.1(a-d) shows the significant process parameters for three different responses in a normal plot of standardized effects. Significant factors are highlighted in red in these plots and are far from the line indicating a lower P-value. In Pareto chart (Fig. B.1(d)), factors with a maximum value located left to the 2.262 line are insignificant. All three main process parameters and the interaction $P \times v$ have a significant effect on W_{avg} at a 95% confidence level. For $W_{s.d.}$, only P and WD and their interaction are significant. None of the process parameters have a significant effect on W_q; however, the Pareto chart for the surface quality shows that v and the interaction $v \times WD$ have highest impacts on the final quality of the surface. After removing the insignificant process parameters and rerunning the model, process parameter coefficients in regression equation (β_i) were calculated. The coefficient values are shown in Table B.2. Table B.3 also presents analysis of variance (ANOVA) and summary of average width and uniformity models after removing insignificant parameters.

As seen in Table B.3, all the parameters have a p-value of less than 0.05 meaning they are significant. Table B.3 also presents degree(s) of freedom (DF) and other parameters required for ANOVA for significant factors. The last two parameters both are the measures of variation of different terms of model with the only difference being consideration of DF for calculation of adjusted mean of squares (adj MS). R-squared and adjusted R-squared show how close the observations (measurements) are to the fitted regression line. The values of R-squared and adjusted R-squared for both models are above 90% showing a very good regression fit. The p-value of center points show that the curvature is not significant for both models. It means that the response value follows a pure decreasing or increasing path as we increase one parameter from low level to high level. In other words, the response value at the center is not higher or lower than that of the low and high levels. As a result, the regression model (Eq. 3.5) and its coefficients presented in B.2 are enough to relate the influential factors and responses, and there is no need to use response surface methodology (RSM). RSM is a method to explore the relationship between process parameters in the optimized area if the curvature is significant. This method is usually followed by factor screening and response optimization.

In order to make sure the models are valid, analysis of residual plots is required. Different residual plots are displayed in Fig. B.2 for average width. The residual plots show that the normality and independence assumptions are valid. The normal plot however shows two outliers at the beginning and end of the data series. More investigations showed that the outliers are associated with severely non-uniform prints. The purpose of the study is to prevent the generation of such non-uniform lines. It seems that there is not enough evidence indicating those outliers are caused due to any other reason such as a change in the experiment environment, operator, or measurement equipment. Hence, the analysis was continued without removing the outliers. Same analyses may be extended to uniformity and surface quality residual plots. There seems to be a slight lack of homogeneity of variance which may have arisen from the slight errors in calculation of width average in image processing software (operator error) or insufficient number of samples, but it is not significant enough to require corrective actions like logarithmic or square root transformations.

Simultaneous Optimization of Responses

After screening the process parameters and calculating the regression coefficients, the response optimization was carried out in order to minimize the value of W_{avg}, $W_{s.d.}$ and W_q. The optimization was done simultaneously and the parameter levels are same as the levels presented in Table 3.7. Priority of the optimization was given to W_{avg} with an importance value of 3, followed by $W_{s.d.}$ and W_q with importance values of 2 and 1, respectively. Table 3.5 presents the summary of response optimization. The target values and upper limits were calculated automatically based on the results of factor screening. Table 3.6 shows the optimized level set that minimizes the responses based on the importance levels provided in Table 3.5. It can be inferred that the low level (-1) values for all three process parameters result in the narrowest silicone lines and best quality. The optimization result can be seen well in Fig. B.3. The level set combination -1, -1, -1 result is predicted to give the average width of 322.8 μm, standard deviation of 3.8 μm for five measures of width (uniformity), and a maximum of 43.5 μm difference in surface altitude over the measurement path (surface quality). Table 3.6 also presents 95% confidence and prediction intervals for every response. Mean of the population falls inside a 95% confidence interval. Also there is a 95% chance that the value of an observation falls within the range of a 95% prediction interval.

Table 3.5: Summary of response optimization.

Response	Goal	Target	Upper limit	Importance
W_{avg} (μm)	Min	42.4	870.6	3
$W_{s.d.}$ (μm)	Min	0.5	32.75	2
W_q (μm)	Min	8	290.3	1

Table 3.6: Response optimization predications.

Response	Fit	95% Confidence Interval	95% Prediction Interval
W_{avg} (μm)	322.9	(240.5, 405.2)	(154.1, 491.6)
$W_{s.d.}$ (μm)	3.78	(0.32, 7.24)	(-3.96, 11.51)
W_q (μm)	43.5	(-66.9, 154.0)	(-147.8, 234.9)

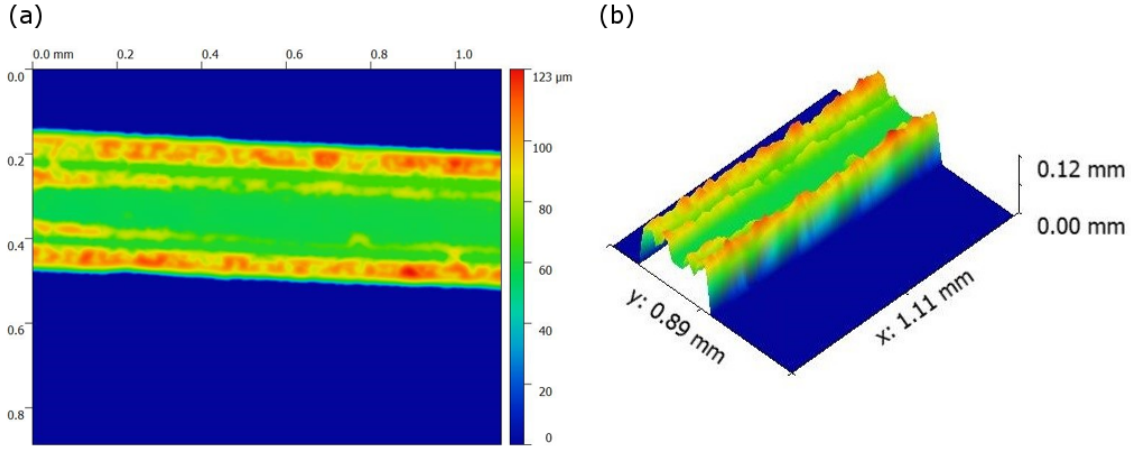

Figure 3.11: Profilometry results of the optimized line made from RTV 800 – 400 silicone at the 100 kPa pressure, 5 mm/s velocity, and 0.2 mm working distance: (a) 2D top view, (b) 3D view.

3.3.2 Optimizing the Extrusion of Plane Features

Table B.4 contains the results of the full factorial model for the extrusion of plane features. The factors P, RW, and WD, as well as the second order interactions of $P \times WD$ and $RW \times WD$ are determined to be significant in the initial ANOVA (Table B.5). After removing the insignificant factors, a reduced model with all significant factors was generated (Table B.6). Figures B.4, B.5, and B.6 do not show any deviations from the normal behavior for the residual plots which verifies the validity of underlying assumptions.

The plot of marginal means (Fig. 3.12) for both significant second order interactions $P \times WD$ and $RW \times WD$ reveal that at the low level of RW and high level of P, the amount of extruded silicone is large enough that the stand-off distance does not affect W_q. As a result, moving toward a very smooth surface in the optimization directions demonstrated in Fig. 3.13 can be achieved by increasing P and/or decreasing RW. The only constraint in this steepest descent method is jeopardizing the vertical resolution of the 3D printed parts by excessive increase in the pressure or designing a trajectory with very close printing roads. Thus, depending on the application and the internal structure of the target object, appropriate P and RW values can be selected based on the following regression model:

$$W_q = 5.685 - 1.914P + 2.21RW + 1.786D - 1.656PD + 1.459D \tag{3.6}$$

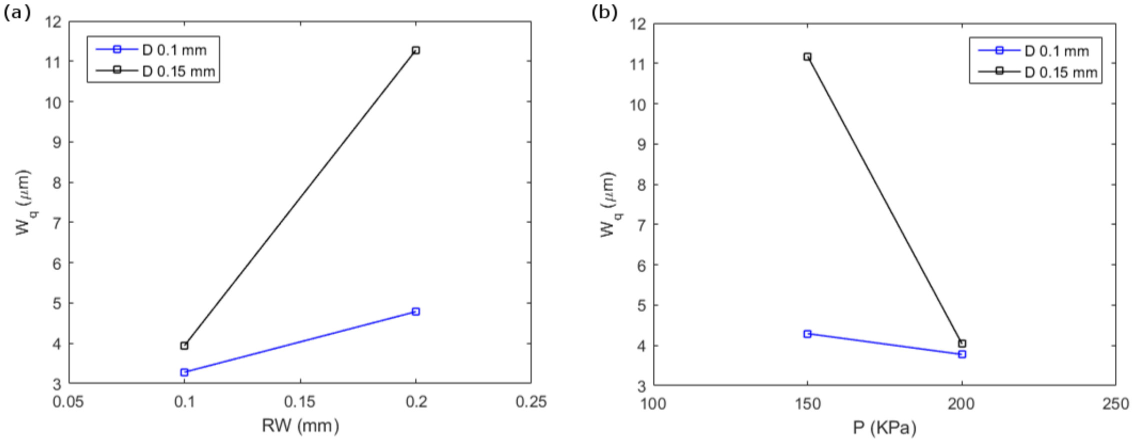

Figure 3.12: The plot of marginal means for the second order interactions (a) $RW \times WD$, (b) $P \times WD$.

Figure 3.14(a-c) shows the reduction in the W_q of the extruded plane features from 22 μm to 3 μm after conducting the DoE study.

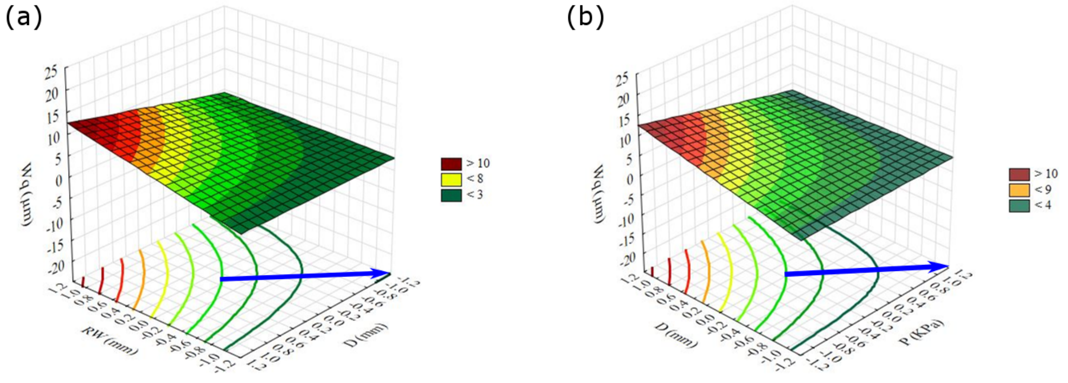

Figure 3.13: The contour plot and fitted response surface for (a) $RW \times WD$ and (b) $P \times WD$. The blue arrows indicate the optimization path. The color-coded values of W_q are shown in the legends.

3.3.3 Finite Element Model of Silicone Dispensing

The experimental and simulation results of three different scenarios: (a) $P_{air} = 100\ kPa$ for $3\ s$; (b) $P_{air} = 100\ kPa$ for $5\ s$; (c) $P_{air} = 150\ kPa$ for $3\ s$, were obtained. In order to investigate the validation of the finite element model, the following parameters were extracted from the model and measured experimentally at $1 - 10\ s$ time period with one second intervals: (1) the distance between the nozzle tip and the lowest point of the pendant droplet (h); (2) half of the maximum width of the droplet (w); (3) the height of the droplet created on the substrate (h'). Parameter 1 is to study the topology of the flow in terms of the relationship between time and location of the pendant drop. Parameters 2 and 3 represent the geometry of the droplet. These parameters are presented in Fig. 3.15. The measured parameters from the experiments and their corresponding model results are illustrated in Fig. 3.16(a-c), Fig. 3.17(a-c), and Fig. 3.18(a-b). The contour of the level-set model is considered as the geometrical boundary between the silicone flow and air.

Profile and Time of Flow

Figure 3.16(a-c) compares the distance of the lowest point of droplet to nozzle tip before the droplet is ruptured and separated from the nozzle for both the experimental trials and the finite element model. For three scenarios, the model and experimental values follow a similar increasing and decreasing trend. Moreover, the discrepancy between the

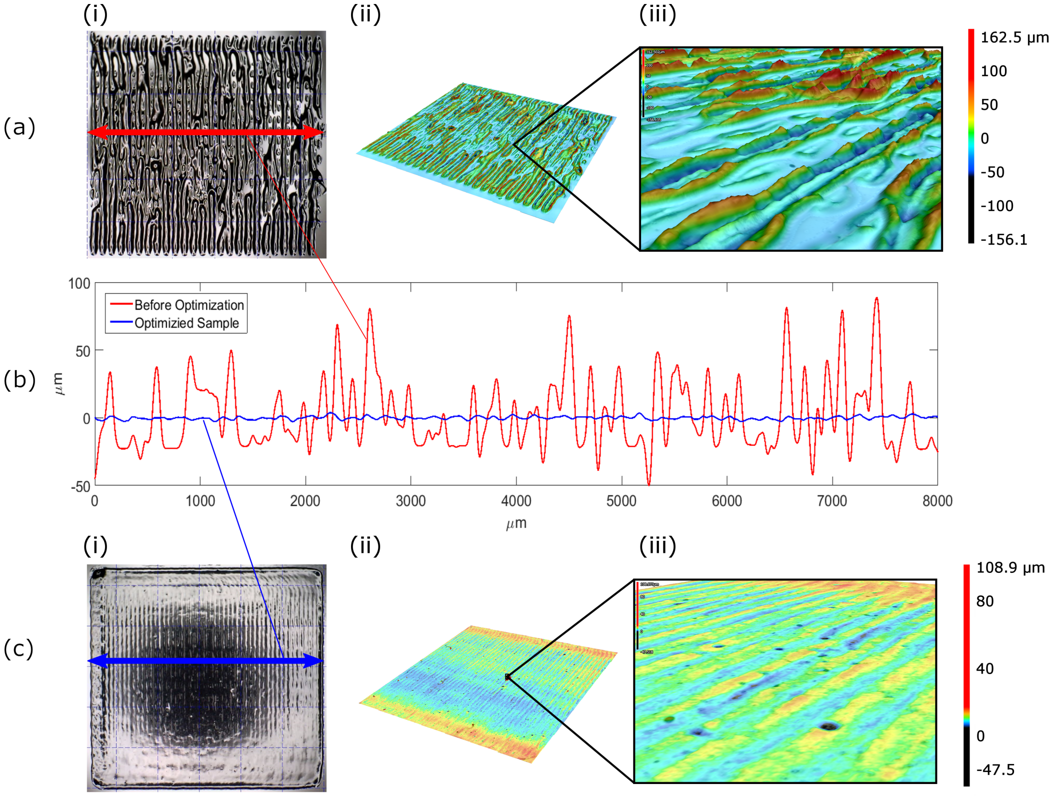

Figure 3.14: The optimization steps for extrusion of plane features: (a-i) a sample of the printed plane before the optimization showing periodic irregularities on the surface, (a-ii) the profilometry result for the plane before optimization with W_q of approximately 22 μm, (a-iii) the magnified view of the surface structure before optimization; (b) A comparison between the waviness profile for the printed planes before and after optimization along the identified scanning lines: (c-i) a sample of the printed plane after the optimization showing a smooth surface, (c-ii) The profilometry result for the plane after optimization with a W_q of approximately 3 μm, (c-iii) The magnified view of the surface structure after optimization.

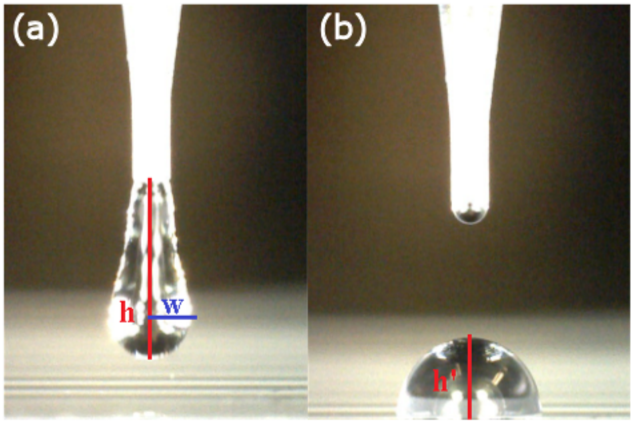

Figure 3.15: Selected parameters, h represents height of the pendant droplet, w represents maximum half width of both pendant droplet and droplet on substrate, and h' represents height of the droplet on substrate. Images of the flow were captured in pre-defined time intervals using a digital microscope.

experimental and simulation results is negligible. On average, there is a 3.8% difference between the predicted and experimental values for parameter h. Figure 3.19 compares the experimental and simulation results during the dispensing time for scenario b. By observing the results of Fig. 3.16(a), the importance of accuracy in the prediction of this parameter becomes clearer. This graph shows that applying 100 kPa air pressure for 3 s is not enough for the flow to reach the substrate. By changing the working distance of the nozzle, the suitable pressure can be selected that outputs the desired pattern width and prevents the creation of a dangling droplet. Fig. 3.16(b) and Fig. 3.16(c) show that the flow reaches the substrate at nearly the same time as in reality which verifies this claim. However, increasing the pressure increases the error between the experimental and model data. For example, in Fig. 3.16(c), the silicone flow under the air pressure of 150 kPa reaches the substrate after 2 s, however the simulation results show that there is an approximately 0.072 mm distance between them at this time.

Droplet Geometry

The main focus of this study was the prediction of the geometrical features of droplet (w and h), which in turn provide the width and height of the line patterns that produce a 3D structure in nozzle dispensing systems. Fig. 3.17(a-c) illustrates the difference between the actual w and its corresponding simulation. On average, there is 4.5%, 6.2%, and

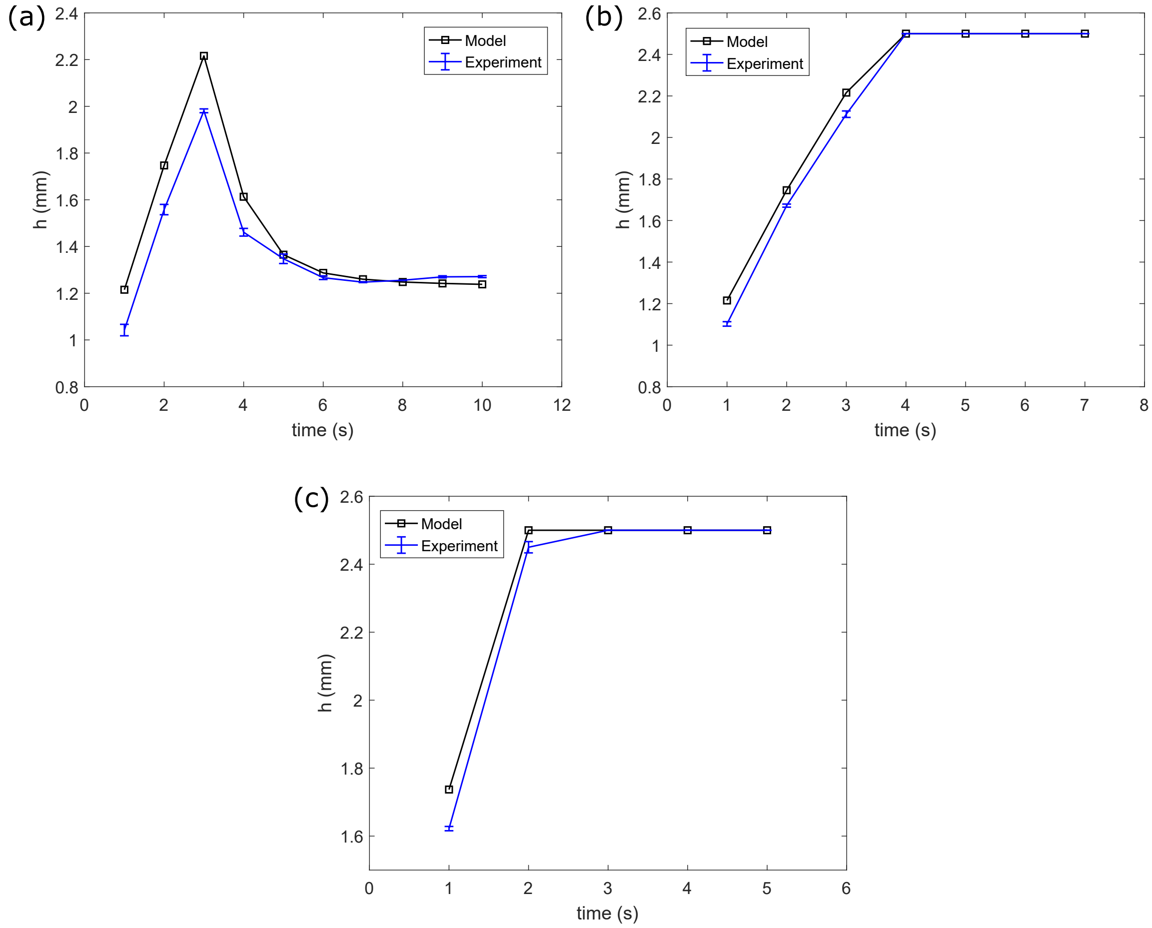

Figure 3.16: Distance between the nozzle tip and the lowest point of pendant droplet (h) vs. time for (a) $P_{air} = 100\ kPa$ for 3 seconds; (b) $P_{air} = 100\ kPa$ for 5 s; and (c) $P_{air} = 150$ kPa for 3 s. Experimental results are shown as error bars with average standard deviations of 0.04, 0.016, and 0.015 for scenarios a-c, respectively. All three graphs illustrate that the experimental and simulation data follow the same trend in terms of the topology of the flow. Also, the difference between the experimental and simulation data is more obvious as the air pressure increases. The difference between the experimental and simulation results is negligible (an average of 3.8%). In scenarios (b) and (c) the difference between the experimental and simulation results is zero after 4 and 3 s, respectively, which demonstrates the accuracy of the model in simulating the time at which the pendant droplet reaches the substrate.

12.9% difference between the simulated results and experimental values for scenarios a, b, and c, respectively. These relatively high difference values may arise from error in the measurement of experimental values and silicone parameters such as viscosity. Owing to the importance of the width of printed patterns, these percentage difference values should be considered as adjustment factors. As seen from the Fig. 3.16(b-c), the deviation between the models and experimental trials increases after the creation of the droplet ($t > 4\ s$), i.e., the model is more accurate in predicting the width of the pendant droplet. In Fig. 3.16(a), the droplet is not generated on the substrate due to insufficient time of activation of pressure. Hence, the pendant drop reaches to a stable point after 5 s without any significant changes in the width. Also the average deviation will increase as the pressure increases.

The graphs presented in Fig. 3.18(a-c) compare the height of the droplet on the surface (h') in the model and experiment. The results are plotted only for scenarios b and c, as no droplet is generated on the substrate in scenario a. Average percentage differences of 13.4% and 8.4% are measured for scenarios b and c, respectively. Although the difference values may seem considerable, the plots show that the difference between simulated and experimental values at the time when the droplet is separated from the nozzle tip (see Fig. 3.19 ($t = 8s$)) is the highest. By excluding the amount of difference at this point, the difference values are reduced to 7.5% and 5.6%, respectively.

Sensitivity Analysis on Viscosity

The sensitivity of the finite element model was evaluated by varying the value of silicone viscosity. The viscosity value calculated in section 2.1 (19.9 Pa.s) was chosen as the standard value and the model was run at ± 10%, ± 20%, and ± 30% deviations from this value. Table 3.7 shows the average deviations in the selected parameters after changing the value of viscosity. These changes for parameters h and w follow the same trend for all three scenarios. In other words, a 30% decline in the viscosity decreases the value of parameters the most; this change is reduced as the viscosity value gets closer to its standard value. Same analysis can be extended to the increase in viscosity. Parameter h' does not demonstrate an organized behavior. The main reason of the fluctuations in the average error for this parameter is the unpredictable and drastically different changes in the time and the location at which the droplet is ruptured and separated from the nozzle tip. Also, decreasing the value of viscosity usually has a higher effect on the parameters than increasing it. For example in scenario b, a 10% decline in viscosity yields a 5.9% reduction in the value of w, but the same amount of incline in viscosity only increases this parameter for 5%. It cannot be inferred that which parameter is more sensitive to the

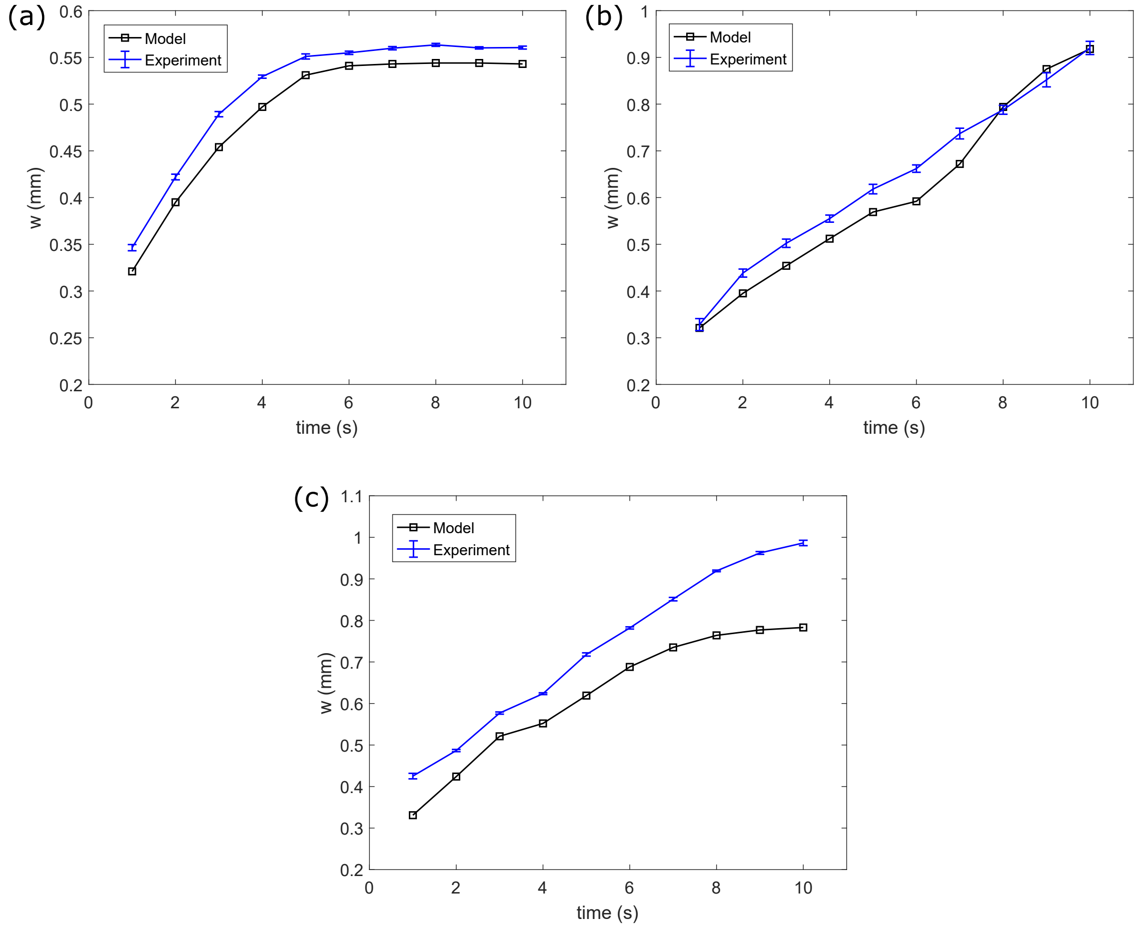

Figure 3.17: Half of the maximum width of droplet (w) vs. time for (a) $P_{air} = 100\ kPa$ for $3\ s$; (b) $P_{air} = 100\ kPa$ for $5\ s$; and (c) $P_{air} = 150\ kPa$ for $3\ s$. Experimental results are shown as error bars with average standard deviations of 0.007, 0.01, and 0.012 for scenarios a-c, respectively. All three graphs illustrate that the experimental and simulation results follow the same trend in terms of the topology of the flow; however, the difference between the results is considerable and the value of the difference needs to be taken into account in calculation of the width of the features.

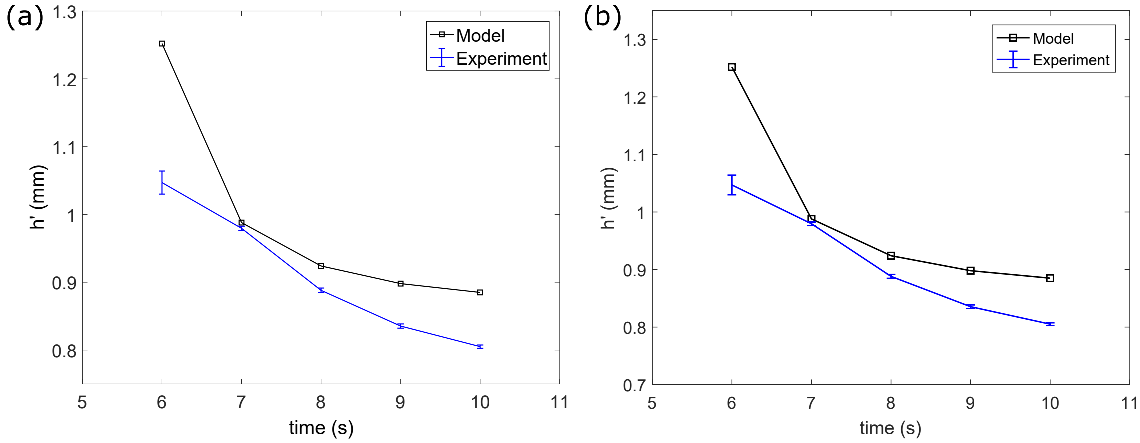

Figure 3.18: Height of droplet (h') vs. time for (a) $P_{air} = 100\ kPa$ for 5 s; and (b) $P_{air} = 150\ kPa$ for 3 s. Experimental results are shown as error bars with the average standard deviations of 0.016 and 0.02 for scenarios b-c, respectively. All two graphs illustrate that the experimental and simulation results follow the same trend in terms of the topology of the flow. The difference between experimental and simulation results at the time when the droplet is generated (separation of the droplet from the nozzle tip) for both cases is much higher than the rest of the dispensing process.

viscosity variations, however, it seems that the amount of time that a droplet is pendant from the nozzle may affect it. If we consider scenarios b and c as successful scenarios in which the droplet is formed on the substrate, then parameters w and h' are respectively the most sensitive and the least sensitive parameters to the changes of viscosity in these two scenarios.

Table 3.7: Effect of changes in viscosity on the location and the geometrical dimensions of silicone droplet dispensed through a nozzle with an inner diameter of 100 μm

Change in the value of viscosity		–30%	–20%	–10%	10%	20%	30%
		Average Error (mm)					
100 kPa – 3 s	h	–0.466 (–32.3%)	–0.394 (–27.3%)	–0.112 (–7.7%)	0.063 (+4.3%)	0.117 (+8.1%)	0.16 (+11.1%)
	w	–0.138 (–28%)	–0.098 (–20%)	–0.018 (–3.6%)	0.016 (+3.2%)	0.03 (+6%)	0.041 (+8.3%)
100 kPa – 5 s	h	–0.115 (–5.3%)	–0.115 (–5.3%)	–0.078 (–3.6%)	0.04 (+1.8%)	0.074 (+3.4%)	0.14 (+6.4%)
	w	–0.12 (–20.9%)	–0.073 (–12.7%)	–0.034 (–5.9%)	0.029 (+5%)	0.053 (+9.3%)	0.077 (+13.3%)
	h'	0.041 (+3.8%)	0.049 (+4.5%)	0.04 (+3.7%)	–0.094 (–8.7%)	–0.303 (–28.1%)	–0.374 (–34.6%)
150 kPa – 3 s	h	–0.118 (–5%)	–0.071 (–3%)	–0.025 (–1.1%)	0.02 (+0.9%)	0.069 (+2.9%)	0.107 (+4.6%)
	w	–0.123 (–19.8%)	–0.077 (–12.4%)	–0.034 (–5.5%)	0.031 (+5.1%)	0.06 (+9.7%)	0.086 (+13.9%)
	h'	–0.008 (–0.8%)	0.011 (+1.1%)	–0.003 (–0.3%)	–0.029 (–2.9%)	–0.18 (–18.2%)	–0.062 (–6.2%)

3.4 Summary

The optimization of line features study suggested that material extrusion technology is a promising method for additive manufacturing of highly viscous silicones. A 2^3 full factorial

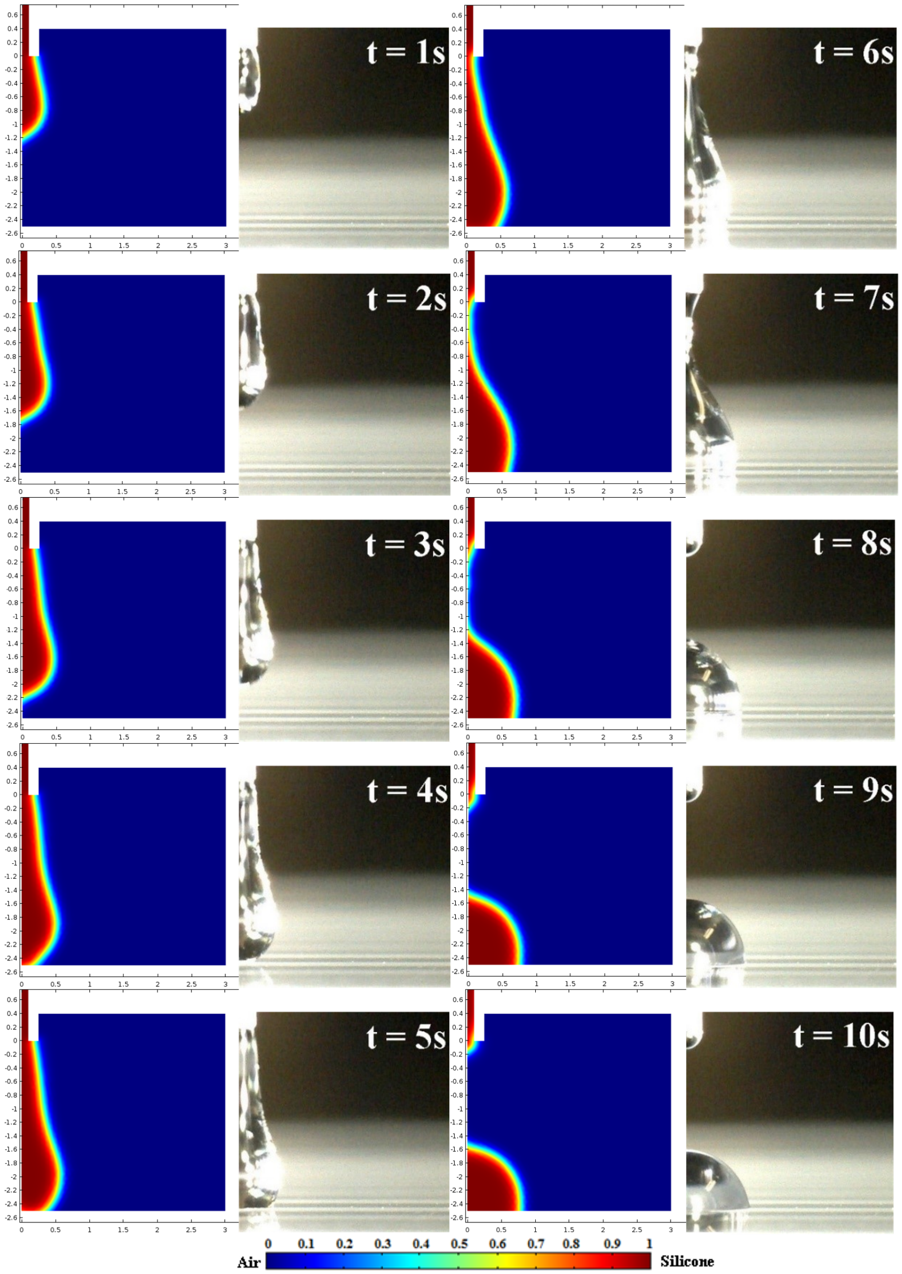

Figure 3.19: Comparison of the experimental trial and simulation for $P_{air} = 100\ kPa$ for $10\ s$. The green band represents the boundary between silicone and air (contour 0.5).

design were employed to screen the effect of P, v, and WD on the quality of the printed features. For the width of built samples, the effects of P, v, and their interaction were the influencing factors. P, WD, and their interaction also proved to affect uniformity of lines more than other factors. None of the factors were significant in the creation of rough surfaces at 95% level of confidence in the investigated parameter ranges. However, v and the interaction of v and WD show the highest effects on this response. Simultaneous response optimization was conducted to minimize all three responses. The level set treatment with $P = 100\ kPa$, $v = 5\ mm/s$, and $WD = 0.2\ mm$ is the optimum solution resulting in a highly uniform line with a width of 322.8 μm and high surface quality. Comprehensive statistical analyses were also conducted to optimize the printing quality of material extrusion system when printing 3D plane features. The results showed that when working with optimum parameter values, the lateral resolution will be 300 – 400 μm for the extrusion system. On the other hand, 3 – 4 μm was obtained for W_q for the 3D printed planes while printhead was moving at 5 mm/s speed.

A finite element model was also developed to simulate the dispensing of silicone in material extrusion system. The effects of two process parameters, air pressure and time of its application, on the flow and geometrical properties of droplet were investigated by conducting the experimental trials. The results of the experiments were used to validate the model. The experimental results of w of the droplets are on average 4.5%, 6.2%, and 12.9% higher than the results of simulation for 100 kPa – 3 s, 100 kPa – 5 s, and 150 kPa – 3 s scenarios, respectively. These values can be employed as adjustment factors for the prediction of the geometry of droplet and consequently the width of printed hairpin lines. On the other hand, the model predicts the location of the pendant droplet and its height on the substrate with dependable average accuracy tolerances of 3.8% and 6.5%, respectively. Hence, the model can be used to determine the suitable combination of pressure value, pressure time, and working distance that guarantees the flow reaches the substrate and spreads on it while maintaining the uniformity of the printed feature. The sensitivity of different parameters to the changes in viscosity of silicone was evaluated showing that this material property affects the width of droplet the most and its height the least. The average changes of 11.1% and 3.6% were calculated from scenarios b and c for w and h, respectively. Overall, the developed model demonstrates the capability of yielding accurate and consistent results in terms of the location and geometry of the flow of highly viscous fluids.

Chapter 4

Additive Manufacturing of Silicone via Material Jetting

4.1 Introduction

Material jetting is another class of AM that has been adopted to 3D print the low viscous silicone polymer before [86] at a printing velocity similar to material extrusion (5 mm/s). The review of previous research work reveals the lack of an AM system which is able to print high viscous silicones directly at a high throughput rate and with high quality. On the other hand, the shortcomings of conventional manufacturing methods (see Section 2.4) make the need for such a system clear. In this chapter, a material jetting technique that has been optimized using statistical tools to print uniform and smooth features from highly viscous silicone approximately 20 times faster than the current methods, is proposed. Statistical tools used in this work to optimize the printing quality (for line and plane features) include DoE, RSM, and central composite design (CCD).

The conventional material jetting system, formerly known as inkjet printing, is compatible with fluids having a maximum viscosity of 40 $mPa.s$. In these systems, fluids with a Ohnesorge number (Oh) between 0.1 and 1 (or $1 < Z < 10$ where $Z = Oh^{-1}$) are considered jettable. Ohnesorge number is calculated according to Eq. 4.1:

$$Oh = \frac{\mu}{(\gamma \rho a)^{1/2}} \tag{4.1}$$

where μ is the dynamic viscosity, γ is the surface tension of the fluid, ρ is the density, and a is a characteristics of the length. Medical-grade silicones with a minimum viscosity of approximately 25,000 $mPa.s$ have an Oh value greater than 1. As a result, this class of polymers are not printable via conventional material jetting.

The new generation of jetting printheads, however, is theoretically able to jet the droplets of fluids with a viscosity of up to 1,000,000 $mPa.s$ at a high frequency in a repeatable and precise manner [135]. The dual PPJ mechanism in these printheads can provide enough force to eject a droplet of the viscous paste with a volume in the order of pico-litre. Figure 4.1 demonstrates the jetting mechanism in these systems. A sample of the pulsed voltage (V) signal is shown in Fig. 4.1(a). In this printhead the valve is normally open, as a result, applying the actuation voltage (e.g. 95 V) moves the sealing ball downward and prevents the flow of fluid as it sits on the ceramic nozzle seat (Fig. 4.1(b)).; The drop of voltage to a certain stroke percentage ($Str\%$) results in the opening of the orifice, followed by filling of the orifice with the fluid due to the air back-pressure. The air pressure fills the orifice with the material (Fig. 4.1(c)).; Fig. 4.1(d) corresponds to the grey region of the plot showing the closing ramp. In this step, the voltage signal rises up to the closing voltage resulting in the downward movement of the sealing ball and jetting of one droplet. The valve remains closed until the beginning of a new cycle.

In this mechanism, the volume of jetted droplet is a function of both the reversed piezoelectric and the pneumatic forces. The amount of material jetted due to the reversed piezoelectric force is controlled by the orifice close time (CT), and that jetted due to the pneumatic force is controlled by the pulse time (PT) according to Eq. 4.2 [88]. The experimental results presented in the following sections confirm the significant effect of PT and CT parameters on the quality of printed lines.

$$V = Q_{pzt} \times CT + Q_{pne} \times PT \tag{4.2}$$

where Q_{pzt} is the jetting rate due to the piezoelectric force, and Q_{pne} is the jetting rate due to pneumatic force. Eq. 4.3 is used to calculate Q_{pne}.

$$Q_{pne} = (\frac{\pi D^3}{32})(\frac{4n}{3n+1})(\frac{D\Delta P}{4LK})^{\frac{1}{n}} \tag{4.3}$$

where n and K denote the power law constants of the fluid, D is the diameter of the orifice, L is the length of the nozzle, and ΔP is the pressure difference.

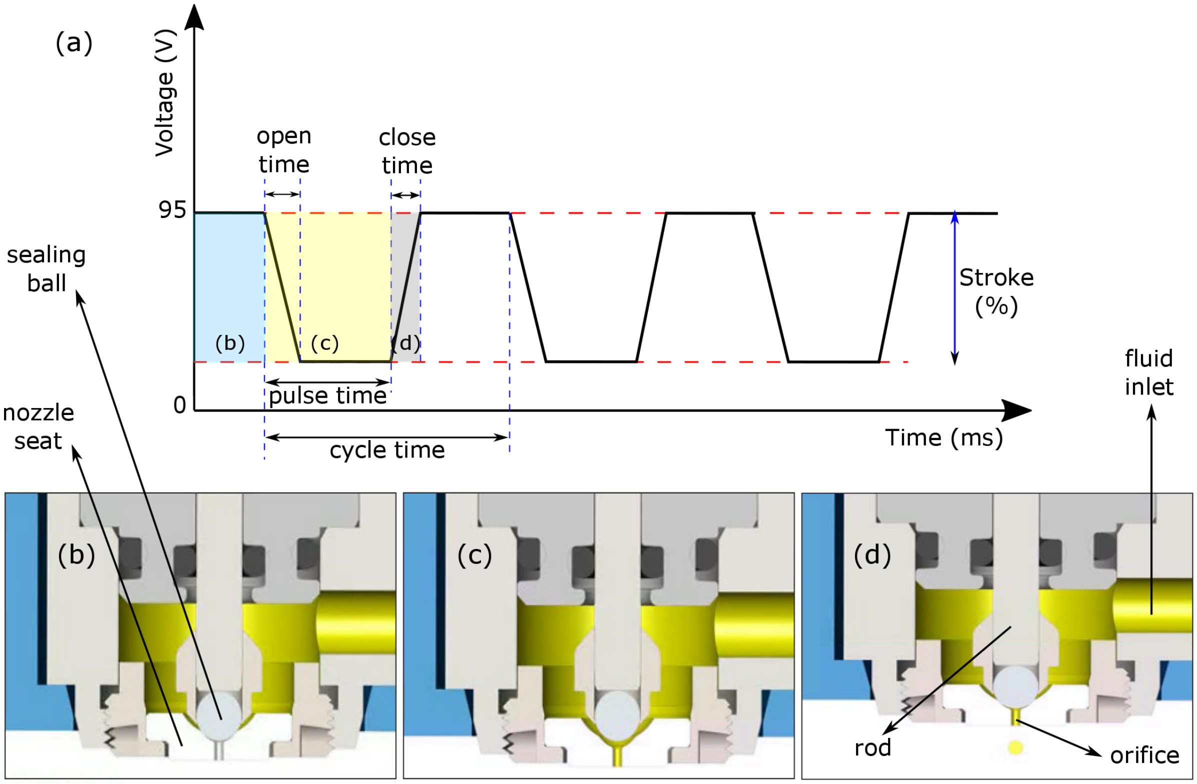

Figure 4.1: The working principle of the PPJ; (a) the plot shows the voltage signal sent to the piezoelectric stacks for three complete cycles, OT indicates how fast the valve is opened, CT indicates how fast the valve is closed, PT is the total time the valve is open, and the CyT is the total duration of one open/close cycle; (b) corresponds to the blue region of the plot showing the time duration that the valve is closed; (c) corresponds to the yellow region of the plot when the orifice is open and filled with the material; (d) corresponds to the grey region of the plot showing the closing ramp. ((b-d) adapted with permission from www.nordsonefd.com.

4.2 Materials and Methods

4.2.1 Experimental Setup

Figure 4.2 shows the in-house-developed hybrid AM system and its components. This system consists of three PPJ printheads (Pico Pulse, Nordson EFD, RI, USA), one solenoid-actuated material extrusion printhead (xQR41 MicroDot^{TM}, Nordson EFD, RI, USA), one pneumatic material extrusion printhead (Optimeter^{TM}, Nordson EFD, RI, USA), and a UV lamp (365 *nm*, Edmund Optics, NJ, USA). Three controlling units (Pico$^{®}$ Touch, Nordson EFD, RI, USA) actuate the piezoelectric stacks by sending out the voltage signals, and one controller (ValveMate^{TM} 9000, Nordson EFD, RI, USA) coordinates the air-pressure in the extrusion-based printheads. The 3-axis motion stage (E6V automated dispensing system, Nordson EFD, RI, USA) has been used to make the printing of 3D structures possible.

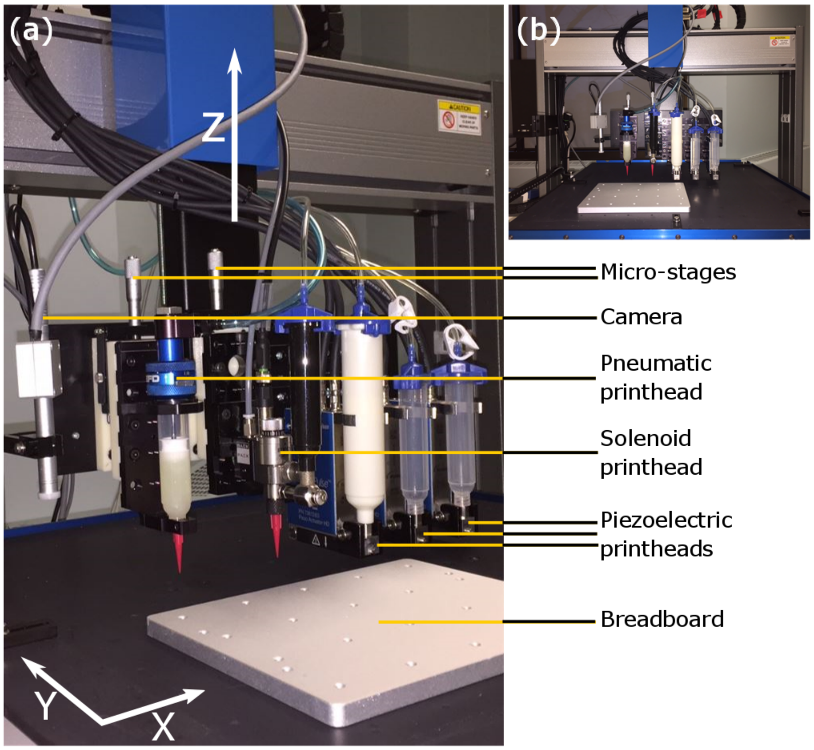

Figure 4.2: The overall view of the AM system: (a) main components; (b) front view.

4.2.2 Trajectory Design

Different area filling patterns have been used for the direct writing AM where rectilinear is the most prevalent. A common quality flaw in these techniques is the deposition of extra material where there is any change in the direction of movement as well as the start and stop points. The reason is the need for the reduction of printhead's speed to virtually zero when a point of direction change is approaching, followed by acceleration until the steady velocity is obtained [58]. If the deposition rate is not changed accordingly, more material will be dispensed at these points.

The PPJ method suffers from the overfilling phenomenon as well (Fig. 4.3(a-i)). To print lines with uniform width, the conventional rectilinear pattern was replaced by a custom pattern composed of separate parallel lines (Fig. 4.3(a-ii)). This led to eliminating the points of change in direction. Moreover, the delayed dispensing and early termination of dispensing [114] have been employed to reduce the effect of overfilling at the start and stop points of a line, respectively (Fig. 4.3(a-iii)). In other words, the printhead moves along the toolpath (which is a straight line) from the start point but the deposition is not started until it reaches a stable velocity (settling distance). Similarly, no deposition happens over a distance close to the end point where deceleration occurs (shutoff distance). To make sure the geometrical accuracy of the part is maintained, the trajectory lines are oversized to include the actual length of the line as well the settling and shutoff distances as shown in Fig. 4.3(b). The length of stabilization segments can be calculated based on the velocity and acceleration of gantry system.

To convert the digital 3D structures into the printing trajectory (G-code), the open source software Slic3r was used. The Slicer was modified slightly to include the custom pattern of parallel lines. The oversizing value is defined as a function of the width of perimeter lines through the pattern/perimeter overlap command of Slic3r. A text-processing python script was also developed that parses the G-code generated by Slic3r and translates it to the syntax compatible with our developed AM system. The lengths of settling and shutoff distance for each printhead are set in this script as well.

4.2.3 Silicone

The silicone described in Section 3.2.1 has been used in this research with a new PI, 2-Hydroxy-2-methyl propiophenone (3 *wt.*%).

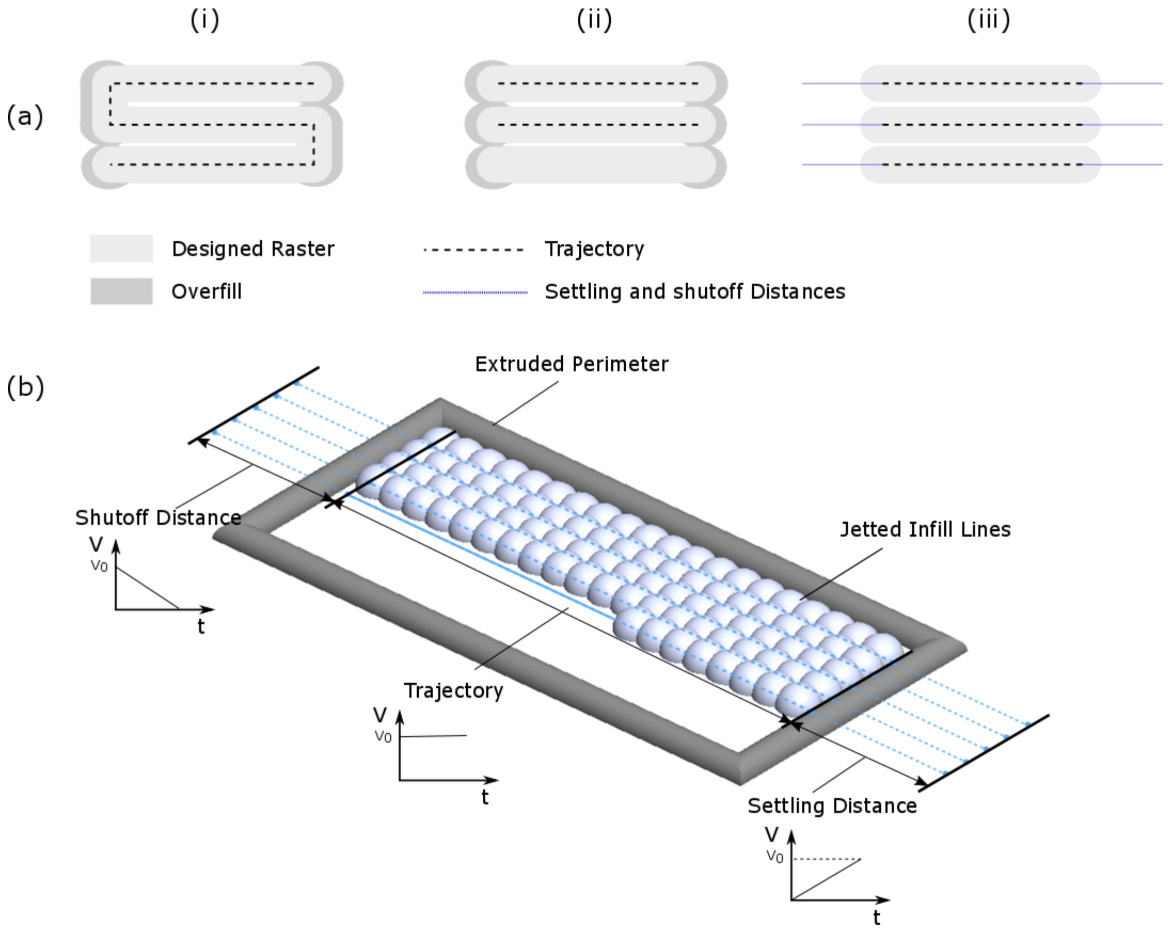

Figure 4.3: The effect of filling pattern on overfilling: (i) rectilinear, (ii) parallel lines, (iii) oversized parallel lines containing settling and shutoff distances. (b) The velocity plot for the printhead at different locations of trajectory.

4.2.4 Sample Preparation and Profilometry

In order to optimize the line features printed via PPJ system, 5 *cm* lines were jetted for each treatment combination. The process parameter values for each treatment at different optimization stages can be found in Appendix C. Images of the printed features were taken using a digital microscope (AM7915MZT, Dino-Lite, Taiwan), followed by measuring the lines width at five equally distant locations as shown in Fig. 4.4. This procedure was replicated at three different sections of the line. The average of the values for each line was used as the average width of feature (W_{avg}), and their standard deviation was used as a measure of the uniformity ($W_{s.d.}$). Each of these two values were used as the response at different stages of the experiment. For example, the initial factor screening phase should lead to finding the treatment combination which yields a uniform continuous line, hence, the standard deviation of the width values was used as the response at this phase. On the other hand, in the optimization and surface response method steps, the resolution was maximized by selecting the average width as the response.

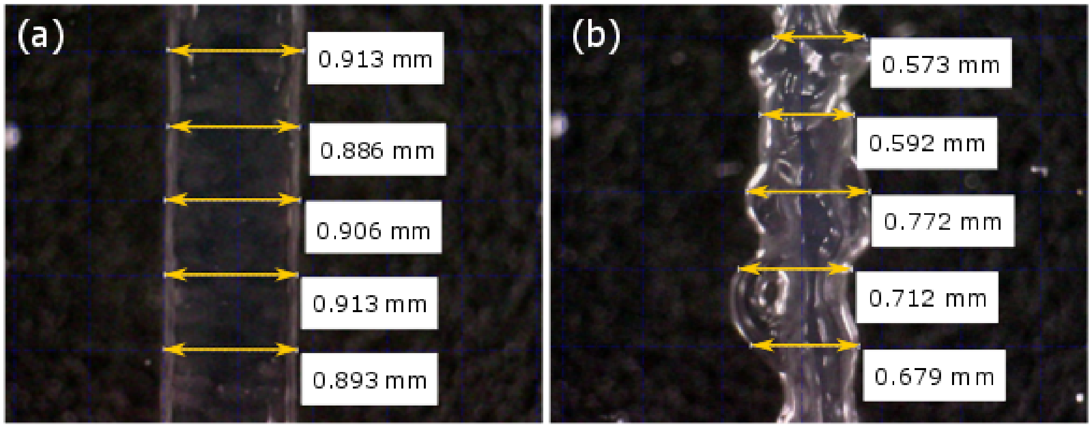

Figure 4.4: Samples of width measurement for the silicone line features; (a) uniform line with 0.012 *mm* standard deviation; (b) non-uniform line with 0.083 *mm* standard deviation.

In order to optimize the surface quality of the 3D plane features printed via material jetting technique, a layer of 1 *cm* × 1 *cm* silicone square was made on a silicon wafer according to each of the DoE treatments. The 3D image of each sample was captured using an optical/laser profilometer (VK-X250, Keyence, Japan) at 100× magnification. The root mean square of waviness (W_q) at the filter cut-off wavelength of 0.08 *mm* was selected as a measure of the surface quality. Waviness is the uneven features that are repeated periodically on the surface at longer intervals compared to the roughness. The profile data was collected over 31 lines. W_q was measured for each line and their average was used as the final surface quality value. Figure 3.9 shows a sample of the waviness measurement and the surface profile.

4.2.5 Experimental Designs

As explained in Section 3.1, the lack of analytical models explaining the flow of highly viscous non-Newtonian fluids justifies the need for the empirical models to relate the dimensional parameters of the printed building blocks (lines or beads) to the input parameters of the AM systems. Here, the statistical optimization tools (e.g., design of experiments) are used to create linear and quadratic empirical models to better understand these relationships.

Many factors control the quality and the printability in the PPJ mechanism. Ten influential factors were identified in the initial stage of working with the system. Table 4.1 shows these factors at their low and high levels. The significance of these working parameters was investigated using a $2^{10\text{-}5}{}_{\text{IV}}$ fractional factorial screening design. The statistically significant factors were further studied in a $3^{4\text{-}1}{}_{\text{IV}}$ fractional factorial design, and a linear regression model was fit to the collected data. RSM was adopted at the next step to move toward the optimized area [136]. Finally, a comprehensive non-linear regression model was formed based on the CCD. The experimental design has been carried out for a 100 μm nozzle.

Table 4.1: Influential factors and their treatment levels for the material jetting of line features.

Factors	Low Level (−1)	High Level (+1)
PT (ms)	0.37	0.43
CyT (ms)	3.5	4
T $(°C)$	90	100
V (V)	85	95
$Str\%$ (%)	80	90
OT (ms)	0.15	0.2
CT (ms)	0.15	0.2
v (mm/s)	50	60
WD (mm)	2	3
P (kPa)	500	600

In the next step, using the optimized values of printing parameters for the line features, a new design was formed to optimize the surface quality of the 3D plane features printed via PPJ. The raster width (RW) and printing velocity (v) were selected as the input factors and the root mean square of waviness (W_q) as the response. The high and low levels of the input factors are demonstrated in Table 4.2. Even though the optimized value of v is 60 mm/s for printing a single line, this factor was included in this study to investigate the possibility of speeding up the 3D printing process without increasing the surface waviness. To this end, a 2^2 full factorial design with two center points and one replication was formed.

Table 4.2: Influential factors and their treatment levels for the material jetting of plane features.

Factors	Low Level (-1)	High Level (+1)
RW (mm)	0.4	0.5
v (mm/s)	60	100

4.3 Results and Discussion

4.3.1 Optimizing the Jetting of Line Features

The details of factor screening design and the values measured for the dependent variables can be found in Table C.1. The DOE analysis for the measured width averages (Table C.2) shows that only four factors (PT, V, $Str\%$, and CT) are significant at 95% confidence level. The ANOVA results after removing insignificant factors are shown in Table C.3. All the remaining factors at the reduced model are significant; hence, they are accepted as the influential operating factors and will be investigated more in the future steps. Also, the residual plots (Figs. C.1, C.2, and C.3) show that the normality, independency, and variance consistency assumptions are valid.

After identifying the significant factors, a $3^{4\text{-}1}{}_{\text{IV}}$ fractional factorial design was formed to minimize the width of the printed line features. The values of insignificant factors were selected based on the results of the factor screening experiment. The goal is decreasing the value of standard deviation, hence, factors with a positive effect value were fixed at their low levels and vice versa. Table 4.3 shows the fixed values of insignificant factors. Table 4.4 shows the selected three levels for the significant factors.

Table 4.3: The values of insignificant factors for jetting of line features.

Factor	Effect	Level	Value
CyT (ms)	< 0	1	4
T $(°C)$	< 0	1	100
OT (ms)	< 0	1	0.2
v (mm/s)	< 0	1	60
WD (mm)	> 0	–1	2
P (kPa)	> 0	–1	500

Table 4.4: Three levels of significant factors for jetting of line features.

Factor	Low Level (–1)	Center (0)	High Level (+1)
PT (ms)	0.35	0.37	0.39
V (V)	93	95	97
$Str\%$ (%)	86	88	90
CT (ms)	0.15	0.17	0.19

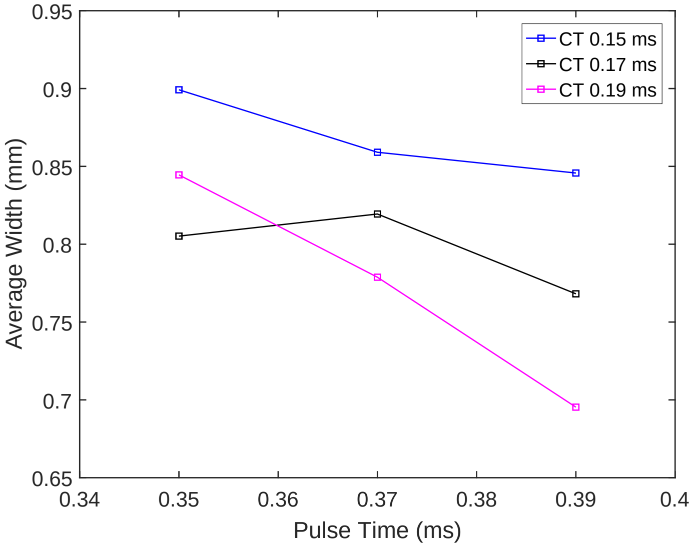

Figure 4.5: The plot of marginal means for the second order interaction $PT \times CT$. Setting both CT and PT factors at their higher levels results in the lowest average width for the jetted line features.

The details of $3^{4\text{-}1}{}_{\mathrm{IV}}$ fractional factorial design with one replication and two center points are demonstrated in Table C.4. The results of analysis of variance for this design (Table C.5) reveal that all four factors as well as the second order interaction of PT and CT are significant. Furthermore, none of the quadratic terms are significant in this experiment, i.e., there is no obvious curvature in the response surface at the investigating area. After reducing the model, no change was observed in the number of significant factors. The ANOVA results for the reduced model and the regression coefficients are presented in Tables C.6 and C.7, respectively.

The positive regression coefficients of the V and $Str\%$ indicate that the lower the values of these two parameters, the higher the printing resolution. Hence, it is recommended to set these two factors at their low levels. For the PT and CT parameters, their marginal mean plot will be investigated in order to decide on their optimized levels as their second order interaction ($PT \times CT$) is significant. The marginal mean plot for the PT vs. CT is depicted in Fig. 4.5. This plot shows that there is not much difference in the W_{avg} when CT is equal to or less than 0.17 ms, regardless of the value of PT. On the other hand, when CT is set at its higher level (0.19 ms), the response value will be decreased by increasing the PT. Based on the marginal mean plot, fixing both PT and CT on their high level yields the best result, i.e., the highest printing resolution in terms of the line features width. In the next step, this initial estimate of the optimum operating conditions will be used to move toward the minimum width. The analysis of the residuals (Figures C.4, C.5, and C.6) does not raise any concerns in terms of the validity of the model as all the assumptions, i.e., normality, variance consistency, and independence have been met.

The method of steepest descent was employed to move toward the area containing the minimum value as fast as possible. Fig. 4.6 contains two contour plots and the steepest descent path. The vertical and horizontal axes show the coded values for CT and PT, respectively. The values of these two parameters can only be changed in 0.01 ms steps. The contour plots show that the coded value of 1.5 (uncoded: 0.2 ms for CT and 0.4 ms for PT) result in a maximum decrease of approximately 100 μm in the average width of the features. As a result, this point (1.5 coded) was selected as the center of the CCD. Due to the limitations in the values that can be assigned to the CT and PT, only a CCD with face-centered axial point could be designed. The upper section of Fig. 4.6 shows the CCD as well as the fitted contour plot. It is observed from the plot that our first point has been accidently located inside the optimum area resulting an average width of less than 600 μm.

The degree of curvature seen in the contours reveals that the response surface is highly twisted and a second order regression equation is required to describe its behavior. The non-flat shape of the surface plot is illustrated in Fig. 4.7. The ANOVA results for the

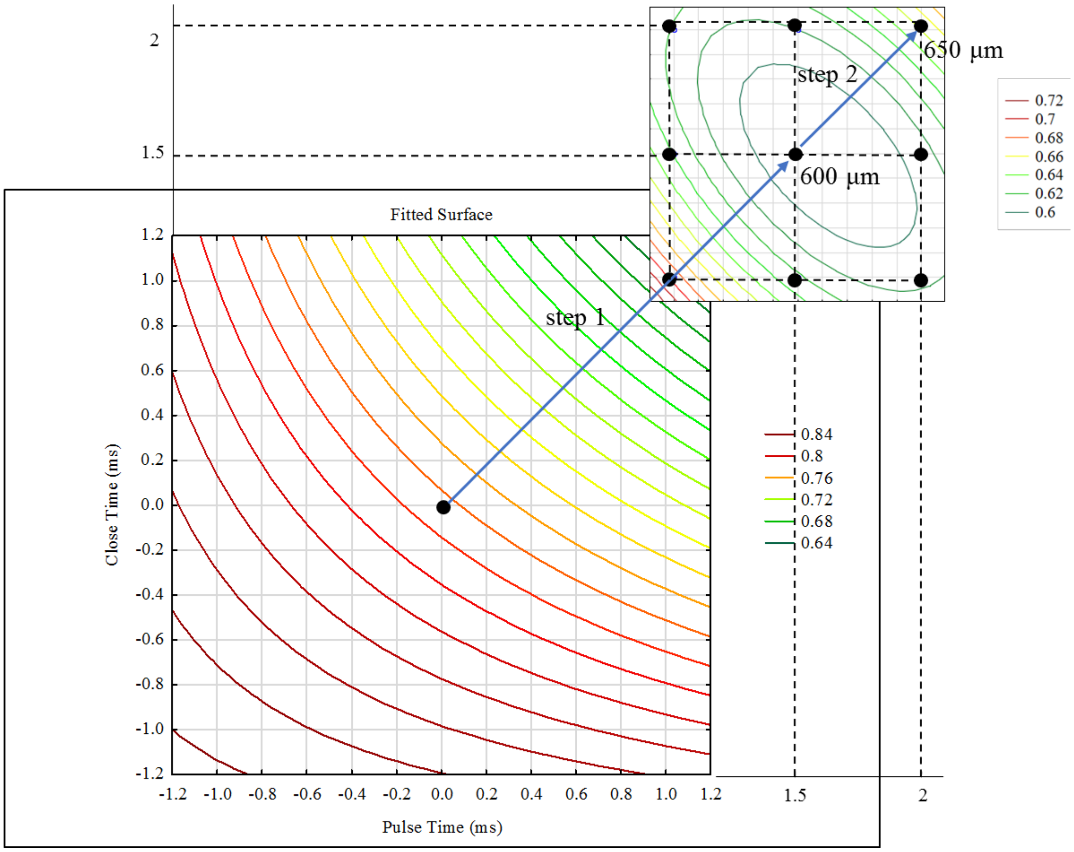

Figure 4.6: The fitted contour plots for the method of steepest descent. The first step corresponds to moving in the optimization direction (minimizing W_{avg}) from the center of the first contour plot so that the movement path is perpendicular to the contour lines. The optimum region is found after two steps, and a new contour plot is formed around it using central-composite design. The color-coded legend shows the values of W_{avg}

CCD are presented in Table C.8, which shows that only quadratic terms and second order interaction of the two factors are significant. However, due to the model hierarchy, the main effects cannot be eliminated. The regression coefficients are presented in Table C.9. The following quadratic model can be fit to the data at the optimum area:

$$W_{avg} = 0.593 - 0.012 \times PT + 0.025 \times PT^2 - 0.006 \times CT - 0.023 \times CT^2 + 0.027 PT \times CT \tag{4.4}$$

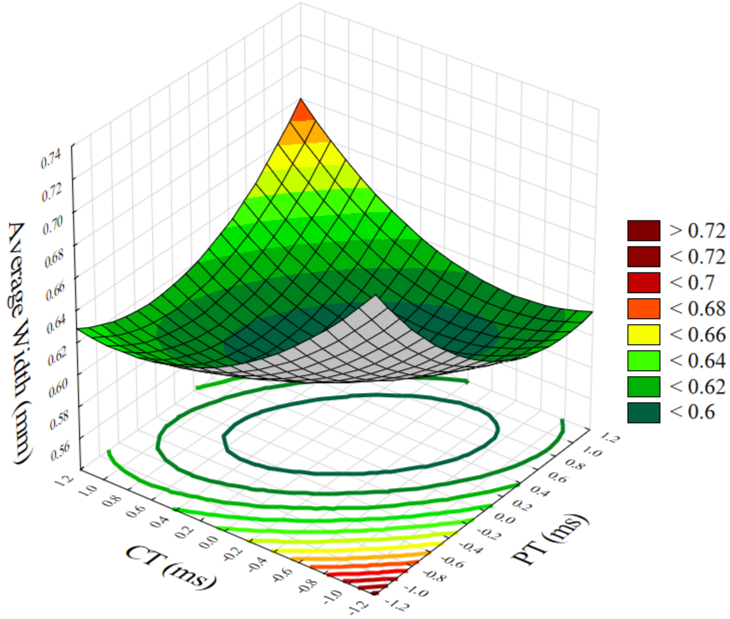

Figure 4.7: The fitted surface plot of the optimum zone. The convex shape of the surface plot assures the optimized point is not a local minimum at the selected parameter ranges.

The final results are compatible with the physical principles of PPJ systems. In these systems, the volume of jetted droplet is a function of both reversed piezoelectric and pneumatic forces. The amount of material jetted due to the reversed piezoelectric force is controlled by CT, and that jetted due to the pneumatic force is controlled by PT according to Eq. 4.1. The step-by-step improvement in the printing quality is illustrated in Fig. 4.8. A high degree of overspraying of satellite droplets with diameters as large as approximately 250 μm was observed in the screening step (Fig. 4.8(a)). By reaching the optimized set of factor levels, uniform lines with no overspraying were jetted (Fig. 4.8(b)). At this step, the average width of the lines was around 800 μm, and uniform hemispherical cross-sections were achieved. Further optimization of the process parameters using the response surface analysis technique reduced the lines width to approximately 580 μm with a high level of uniformity.

4.3.2 Optimization of Plane Features Jetting

The measured values can be found in Table C.10. Based on the residual plots (Figures C.7, C.8, and C.9), there is no concern in terms of the validity of analysis assumptions. The ANOVA results, shown in Table C.11, indicate that RW and v, as well as their second order interaction, are significant at 95% confidence level. However, v has a higher impact on W_q than the other two items. In order to find the path to optimized waviness value, the marginal means, contour, and surface plots were studied. All three plots indicate that increasing the velocity and decreasing the raster width will produce a lower surface waviness. Based on the regression coefficients presented in Table C.12, the following regression model can be fit to the experimental data:

$$W_q = 41.621 - 10.325V + 4.093RW + 4.301V \times RW \tag{4.5}$$

Setting the RW and v at their low and high levels, respectively, resulted in a smooth surface with approximately 22 μm of W_q. The possibility of improving the surface quality using the method of steepest ascent was investigated. From the results shown in Fig. 4.10, it can be concluded that jetting the solid planes with speed of 104 mm/s and raster width of 0.39 mm (Coded values of $+1.2$ for v and -1.2 for RW) yields the best surface quality with the average W_q of approximately 8.1 μm. The step-by-step minimization of the waviness for the jetted plane structures is illustrated in Fig. 4.11. The optimization process has reduced W_q from 40 μm (Fig. 4.11(a)) to 8 μm (Fig. 4.11).

4.3.3 Printing Quality and Hybrid AM Method

Comparing the optimization results conducted for the silicone extrusion and silicone jetting in Chapters 3 and 4, respectively, demonstrates that material extrusion results in higher resolution and better surface quality. W_{avg} of a line printed via extrusion is approximately 320 μm. The same parameter for a line printed based on the optimized jetting parameters is between 500 μm and 600 μm. These results are from a 250 μm tapered needle for the extrusion and a 100 μm nozzle for the jetting system. Printing lines with higher resolution

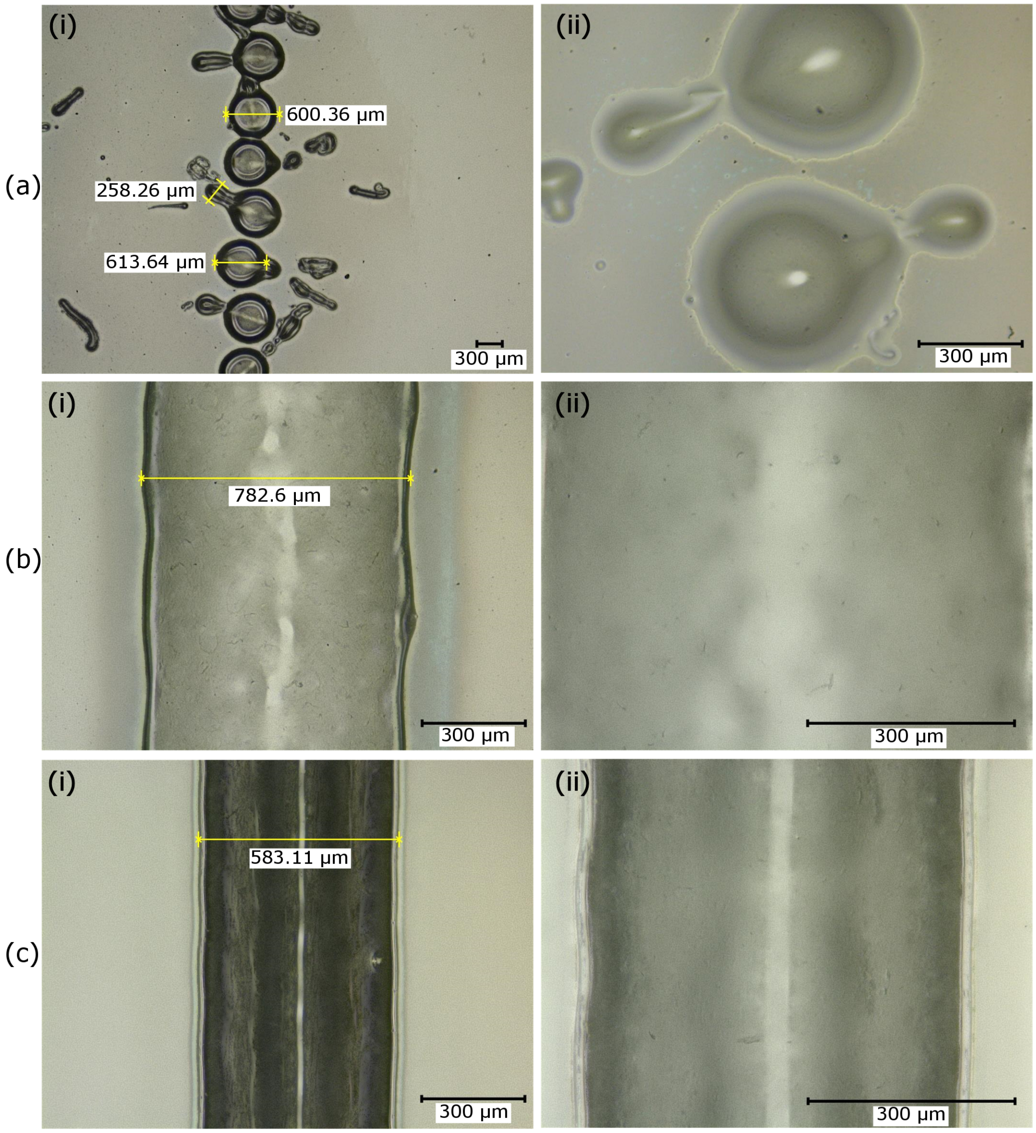

Figure 4.8: The optimization steps for jetting of line features; (a) Failed printed feature at factor screening steps, (a-i) 25×, (a-ii) 100×; (b) Continuous line feature after the optimization step, (b-i) 100×, (b-ii) 200×; (c) The line feature with improved resolution after response surface optimization, (c-i) 100×, (c-ii) 200×.

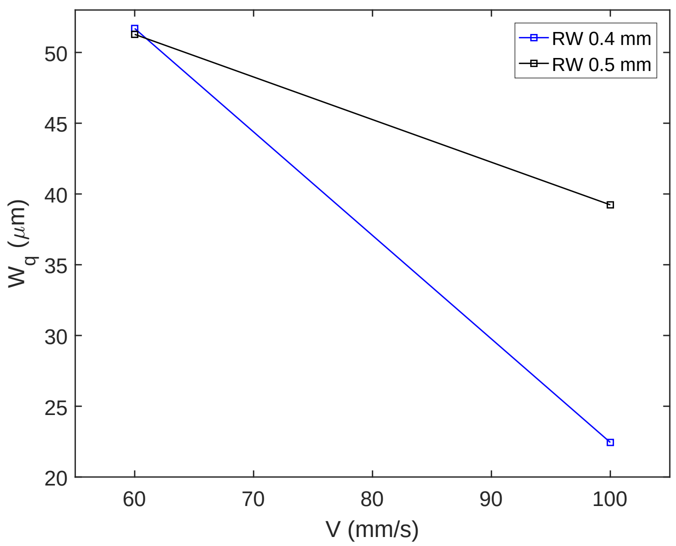

Figure 4.9: The plot of marginal means for the second order interactions $V \times RW$.

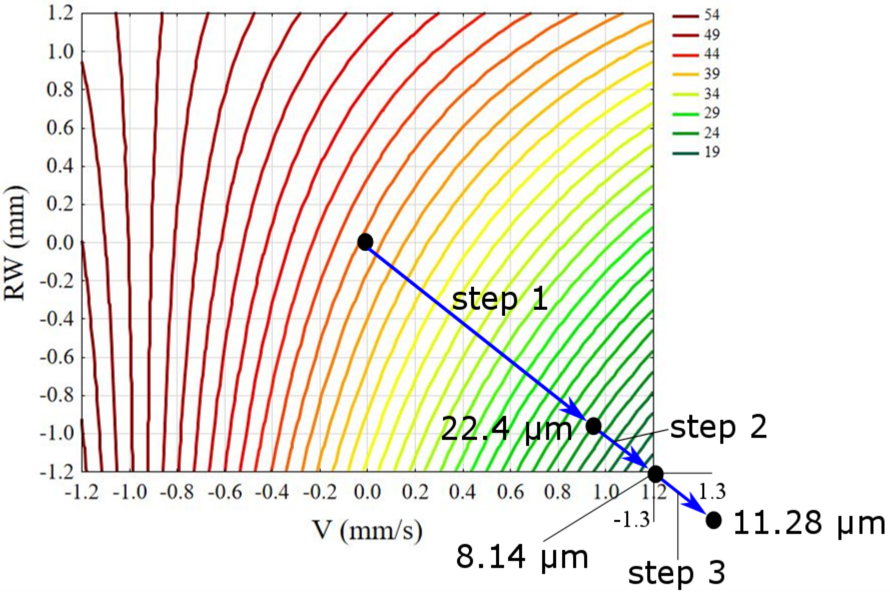

Figure 4.10: The fitted contour plot for the method of steepest descent. The first step corresponds to moving in the optimization direction (minimizing W_q) from the center of the contour plot so that the movement path is perpendicular to the contour lines. The color-coded legend shows the values of W_q

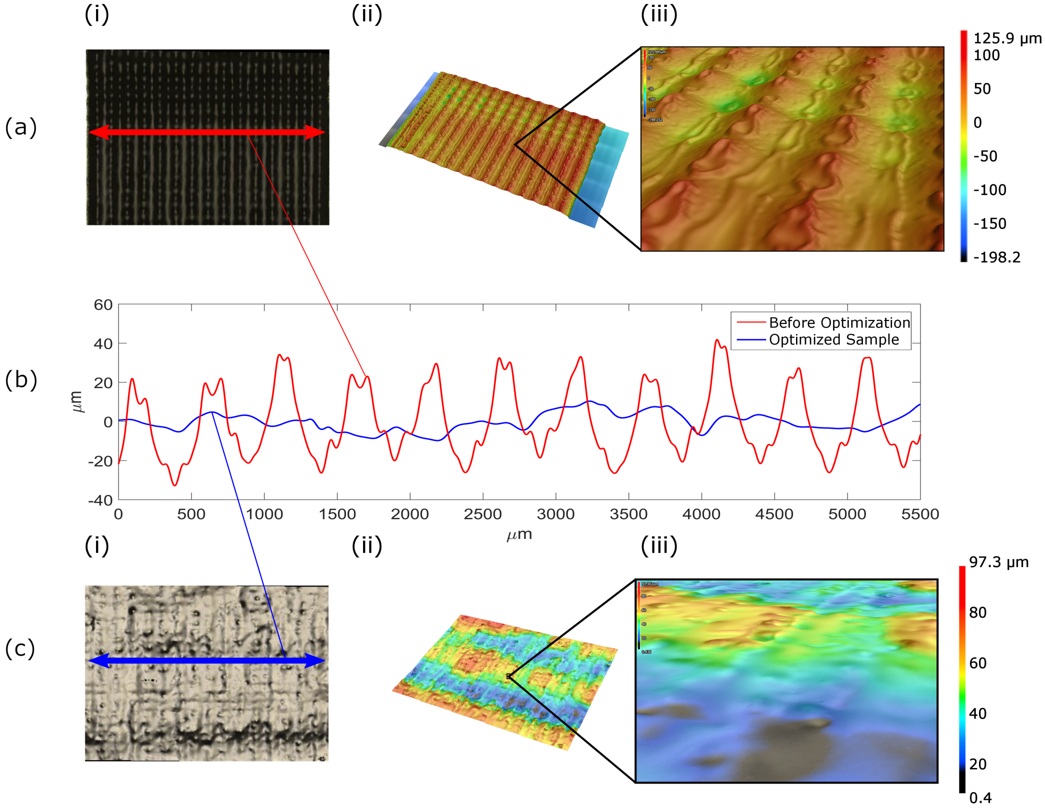

Figure 4.11: The optimization steps for jetting of plane features; (a-i) A sample of the printed plane before the optimization showing periodic irregularities on the surface,; (a-ii) The profilometry result (W_q of approximately 40 μm), (a-iii) The magnified view of the surface structure before optimization. (b) A comparison between the waviness profile for the printed planes before and after optimization along the identified scanning lines; (c-i) A sample of the printed plane after the optimization showing a smooth surface, (c-ii) The profilometry result (W_q of approximately 8 μm), (c-iii) The magnified view of the surface structure after optimization.

has been proven to be possible in the extrusion system with 100 μm nozzles. However, using 50 μm nozzle in the jetting system resulted in printing instability. In terms of the surface quality, W_q of the extruded plane features was measured to be 3 – 4 μm after the optimization study. However, an optimized jetted surface had a W_q of 8 – 10 μm with hollow spaces across its surface. The extruded lines were more uniform as well which makes the extrusion of pastes a better option for high quality 3D printed structures. However, the fact that the PPJ system can print a pattern at a velocity of 104 mm/s compared to 5 mm/s velocity of the extrusion system with only slightly inferior quality made us select it as the main printing method in our hybrid AM system.

In our proposed hybrid method, the outer frame (shell) of each layer is printed using the pneumatic material extrusion printhead. The PPJ printheads are used to print the infill patterns as well as the support structure at a fast rate. This new method takes advantages of both high velocity of the jetting system and the high quality of the extrusion system. This hybrid manufacturing model is illustrated in Fig. 4.12.

The optimization of the resolution and quality of the 3D printing building units at 1D and 2D levels results in the production of defect-free 3D structures. The proposed hybrid method is capable of printing structures 5 – 20 times faster than the material extrusion method; however, as the current printhead only jets the materials through one orifice, the high speed fabrication and characterization of 3D articles with considerable height to cross-section aspect ratio can be achieved through improving the process scalability by development of printheads that have hundreds of orifices and are capable of processing highly viscous polymers.

4.4 Summary

In this chapter, a novel hybrid AM method that combines material extrusion and material jetting techniques for the production of silicone-based bio-structures was introduced. This system takes advantage of the high printing quality of extrusion system as well as the high printing velocity of PJJ system. Comprehensive statistical analyses were conducted to (1) identify the working range of the input parameters for PJJ system; and (2) optimize the printing quality at 1D and 2D levels. The results showed that when working with optimum parameter values, the lateral resolution will be 500 – 600 μm. On the other hand, 8 – 10 μm was the optimized surface waviness value obtained for this process. These optimum values were reached when the jetting printhead was moving at 104 mm/s. The efficient implementation of the proposed method for fabrication of large 3D parts is feasible through development of printheads containing arrays of multiple orifices in the future.

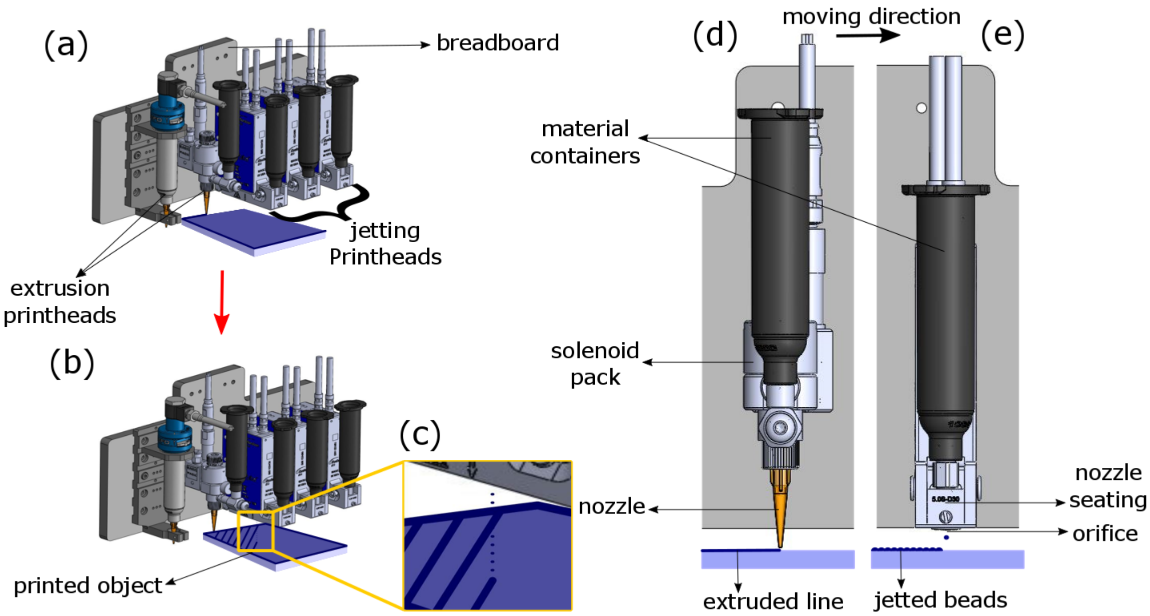

Figure 4.12: The working prininciple of the hybrid AM technique for printing of silicone; (a) The solenoid-controlled pneumatic printhead is forming the frame of a layer by extruding a continuous stream of silicone; (b) The PPJ printhead is filling the layer at a fast rate based on the program; (c) A magnified view of the PPJ of silicone showing the stream of droplets; (d) The front view of the material extrusion system; (e) The front view of the material jetting system demonstrating how the silicone beads form up a solid line.

Chapter 5

Mechanical Characteristics of Silicone Parts Made via Material Jetting

5.1 Introduction

To further optimize the PPJ technique for silicone AM, mechanical characteristics and internal structure of parts fabricated using this method should be investigated. Generally, most of the research in the area of mechanical characterization of AM-made silicone parts is related to material extrusion [94, 105, 106]. Regular thermal or piezoelectric inkjet printers are mostly used for the fabrication of films and patterns rather than a 3D structure. Consequently, the mechanical characterization for these drop-on-demand processes is mostly conducted at 2D level [137–139] including for silicone films [87]. Foerster et al. have investigated the effect of scaffolds porosity on the viscoelastic behavior of parts fabricated via PPJ [89]. Based on their work, lower solid density (more air voids) produces a less stiff structure by lowering the values of dynamic moduli. In this chapter, the effects of rheological properties of silicone ink on the internal porosity and tensile, tear resistance, and hardness of 3D parts made using PPJ is investigated for the first time. Decreasing the difference between mechanical characteristics of AM-made parts and the bulk silicone inks has been achieved by reducing the internal porosity of parts. Moreover, the crosslinking kinetics of inks has been studied to establish an in-situ curing policy for UV-curable silicone polymers.

5.2 Materials and methods

5.2.1 Ink Preparation

A viscous UV-curable silicone (800-400, Novagard, OH, USA), hereinafter known as silicone A, is diluted using a silicone with similar composition but lower viscosity (800-610, Novagard, OH, USA), hereinafter known as silicone B. To tailor the rheology of the 3D printing ink, silicone A and silicone B were blended at four different mixing ratios (A, 70A-30B, 50A-50B, 45A-55B by weight). The samples were mixed using a planetary centrifugal mixer (ARE 310, Thinky, Japan) at 2000 rpm for 30 min and defoamed at 2200 rpm for 15 min.

Rheological Characterization

The shear dynamic moduli (G' and G'') of silicone inks (A, 70A-30B, 50A-50B, 45A-55B) were measured in a stress sweep test using a rheometer (Bohlin CS) with a cone and plate (40 mm \4°) measuring system at room temperature. The stress sweep test was conducted in the shear stress range 1 - 500 Pa at a constant frequency of 1 Hz. The viscosity of A and 45A-55B inks was measured using a rheometer (RST-CPS-P, Brookfield Engineering, MA, USA). The tests were conducted for both inks at controlled temperatures 25 ± 0.01 °C and 100 ± 0.01 °C. The viscosity values were collected at 1 - 500 s^{-1} shear rate range using 25 mm \1° and 50 mm \1° cone and plate geometries for inks A and 45A-55B, respectively.

Fourier Transform Infrared Spectroscopy (FTIR)

The infrared spectra were recorded for silicones A and B with a microscope (Hyperion 1000, Bruker, MA, USA) equipped with a Mercury-Cadmium-Telluride (MCT) detector, attached to a FTIR spectrometer (Tensor 27, Bruker, MA, USA). The spectrometer is able to record up to 2 spectra per second at a resolution of 16 cm^{-1}. The sample was placed between two Potassium Bromide (KBr) disks, and placed in the microscope stage operating in transmission mode. The thickness of the sample was adjusted ($\sim$ 200 μm) in order to result in a spectrum with appropriated intensity. UV radiation was performed with a UV light curing system (OmniCure S2000, Excelitas Technologies, ON, Canada) through a 5 mm diameter lightguide, and the iris was adjusted to be 20% open. The end of the fiber optic was placed at 5 mm from the KBr disk at an angle of 90°. The intensity of the incident UV light measured by a radiometer (OmniCure R2000, Excelitas Technologies, ON, Canada) was 3.54 w/cm^2 at 5 mm working distance.

5.2.2 Experimental Setup

The silicone parts were made using the hybrid extrusion-PPJ AM system, as presented in Chapter 4. In this Chapter, however, to study the mechanical characteristics and porosity of parts made via the PPJ technique, the fabrication of layers shell with extrusion was eliminated, and both the shell and core were jetted. The printing parameters for each ink are provided in Table 5.1. For all the parts manufactured for mechanical characterization and porosity analysis in this research, 2000% pattern/perimeter overlap and 10 mm settling and shutoff distances were selected. The alternating printing angles of 0° and 90° were selected for successive layers to achieve a weave pattern.

Table 5.1: PPJ printing parameters for different silicone inks.

Printing Parameters	A	70A-30B	50A-50B	45A-55B
PT (ms)	0.4	0.4	0.4	0.4
CyT (ms)	4	6	10	12
T (C)	100	100	100	100
V (V)	85	85	120	120
$Str\%$ (%)	80	80	75	75
OT (ms)	0.2	0.2	0.2	0.2
CT (ms)	0.2	0.2	0.2	0.2
v (mm/s)	104	104	104	104
WD (mm)	2	2	2	2
P (kPa)	500	500	500	500

5.2.3 Mechanical Characterization

Tensile, tear resistance, and hardness tests were conducted in accordance with ASTM D412 (Die C), ASTM D624 (Die C), and ASTM D2240 guidelines, respectively. For preparing the cast specimens, plastic molds were 3D printed using a PolyJet system (J750, Stratasys, MN, USA). Silicones A and B have a dual irradiation-condensation curing mechanism. To make sure the full mechanical performance has been obtained, the samples were exposed to environment moisture for 7 days after UV curing. The tensile and tearing tests were conducted using a universal testing system (Tensometer 2000, Alpha Technologies, OH, USA) at velocity of 508 mm/min using a 1 kN load cell until failure was observed. The hardness of samples was measured based on their resistance to the indentation of a Shore 00 rigid ball using a handheld durometer (Shore S1, Shore Instruments-Instron, MA, USA).

5.2.4 Tomography and Porosity Analysis

To analyse the internal porosity of parts, 0.5 *cm* × 0.5 *cm* × 0.5 *cm* cubic samples were manufactured using PPJ system for inks A and 45A-55B. The tomography data was captured for these samples using a nano-CT scanner (Xradia 520 Versa 3D X-ray microscope, Zeiss, Germany). Cone beam X-rays were transmitted through the silicone specimens. Optimized scintillators converted the X-rays to photons in the visible light spectrum. It is then magnified using a 4× objective lens, and lastly detected by a charge-coupled detector (CCD). To allow the 3D reconstruction, the specimen was turned around 360°, and a series of 2D images were captured. The X-ray CT scanning conditions are presented in Table 5.2.

Advanced image processing and porosity analysis were performed using a visualization and image processing package (Dragonfly Pro v3.0, Object Research Systems Inc., QC, Canada). The reconstructed dataset was segmented into the base silicone material and air voids (pores) by using routine image processing steps, including greyscale thresholding and morphological operations. Furthermore, the binarized images were obtained to be subsequently used for acquiring quantitative information such as total volume and size distribution of pores. 3D image analysis software ImageJ was employed to measure the relative density that represents the distribution of porosity throughout the part. To this end, 2D projections of the binarized porous dataset was divided by a binary mask in which each pore was filled using the ImageJ plug-in Fill Holes.

Table 5.2: Parameters of CT measurements.

Parameters	
Source-to-detector distance (mm)	21.11
Voxel size (μm)	4.0001
Voltage (kV)	40.18
Power (W)	3
Current (μA)	74.62
Source filter	Air
Exposure time (s)	2.5
Optical magnification	4×
Camera binning	2
Number of projection	2001

5.2.5 Imaging

To visualize the slumping, droplets were jetted on a 5 cm linear pattern using inks A, 70A-30B, and 45A-55B based on the parameters of Table 5.1. The distance between the droplets was kept constant by jetting all the inks at similar frequency (83 Hz). For each ink, the printed lines were completely cured at 0, 10, 30, and 60 s after jetting. Images of the lines were captured after curing using a microscope (VK-X250, Keyence, Japan) at 50× magnification. The fractography study has been conducted by obtaining images of the tensile specimens at their failure surface using a scanning electron microscope (SEM) (Ultra Plus, Carl Zeiss AG, Germany).

5.2.6 Statistical Analysis

The differences between mechanical properties of AM-made and cast samples were evaluated using one-way ANOVA at 95% confidence level ($p < 0.05$).

5.3 Results and Discussion

5.3.1 Curing Policy

Commercially available silicones are crosslinked using three main chemical reactions as shown in Fig. 5.1: (1) platinum-catalyzed hydrosilylation between vinyl groups and Si−H bond; (2) thiol-ene click chemistry between vinyl group and thiol group; (3) condensation reaction of alkoxysilane [140]. Hydrosilylation is the most common silicone curing method, however, it is a slow process that requires high temperatures. Thiol-ene reactions are photoinitiated and very fast, however, crosslinking will not happen in areas not irradiated. Condensation of alkoxysilanes can be performed at room temperature but it requires several hours to cure properly.

In order to overcome the limitations of thio-ene crosslinked silanes, the material used in this work uses a dual-cure mechanism that combines the fast, UV activated, thiol-ene click chemistry with alcoxysilane functionality so unexposed fractions of the material can also be crosslinked via condensation [141]. The material is formulated with two prepolymers as presented in Fig. 5.2. The prepolymer A is a thiol and alkoxy functional polysiloxane while prepolymer B contains vinyl and alkoxy functionality. It is worth mentioning that the viscosity of the material increases with the degree of polymerization, n, of the prepolymers.

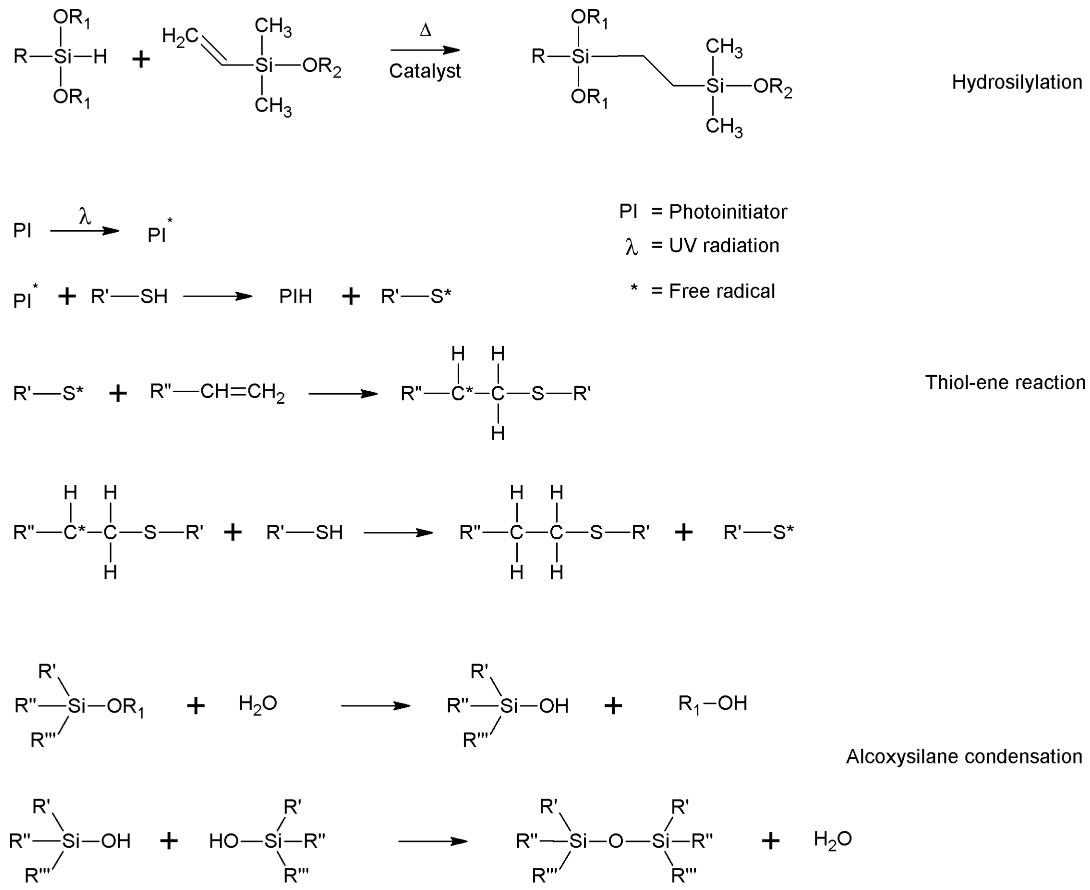

Figure 5.1: Crosslinking reaction mechanisms for silicone resins.

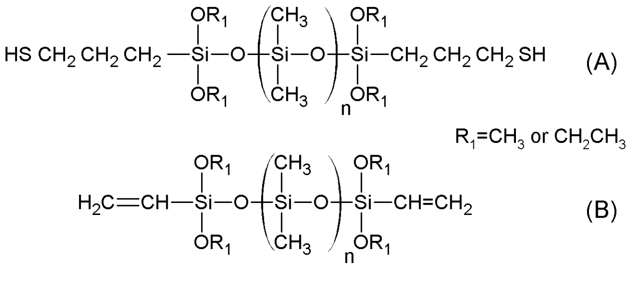

Figure 5.2: (a) structure of polyorganosiloxane with terminal mercapto and alkoxy functionality; (b) polyorganosiloxane with terminal vinyl and alkoxy functionality.

The characteristic vibrations of the functional groups from both polysiloxanes before crosslinking is presented in Fig. 5.3(a). The peak assignments were performed according to Tingaut et al. [142]. It is important to notice that the silicon groups showed very strong peaks while the thiol and vinyl terminal groups are a lot less intense. This is an indication of a high degree of polymerization of the prepolymers before the crosslinking reaction.

The intensity of the peak at 1673 cm^{-1}, corresponding to C=C stretching, was monitored as a function of the UV exposure time to study the development of the crosslinking reaction. As can be seen in Fig. 5.3(b-c), the intensity of the peak at 1673 cm^{-1} is reduced when the sample is exposed to UV light reaching a minimum after around 20 s. The reduction of the intensity of this peak is expected as the crosslinking reaction advanced, as demonstrated in the mechanism shown in Fig. 5.1. At the same time, the peak at 2500 cm^{-1}, corresponding to S–H stretching, was supposed to be reduced due to the reaction of S−H groups with C=C ones. However, due to the low intensity of the S−H peak, it was not possible to detect any significant change on this region.

Interestingly, the appearance of a peak at 1712 cm^{-1} is related to the oxidation of the polysiloxanes by the UV light in the presence of air, leading to formation of C=O groups that are associated with this region of the IR spectrum.

From the spectra, we applied a method derived on Beers law that was based on the ratio of the characteristic to reference absorbance peak. Changes in the area under peak of the band at 1673 cm^{-1} were calculated at different times to obtain the conversion and the results are shown in Fig. 5.4. The results showed that the viscosity of the sample has small effect on the polymerization reaction once both liquid and paste sample showed similar conversion plots, with complete conversion around 20 s. This makes designing a uniform curing policy for all inks (A, 70A-30B, 50A-50B, and 45A-55B) possible. An ideal curing mechanism for direct write AM will crosslink each layer after printing just enough to prevent the structural collapse or deformation due to the weight of upper layers while conserving the active surface to strengthen the cohesion of successive layers. Based on the conversion plots for silicones A and B (Fig. 5.4), the UV laser lightguide followed a trajectory pattern similar to that of the printhead with RW of 6 mm at WD of 5 mm so that each section of the printed layer with an approximate area of 25 mm^2 is exposed to UV light for 1 s. This corresponds to approximately 20% and 15% crosslinking for silicone A and silicone B, respectively. The curing was conducted after printing every two layer (longitudinal and transverse).

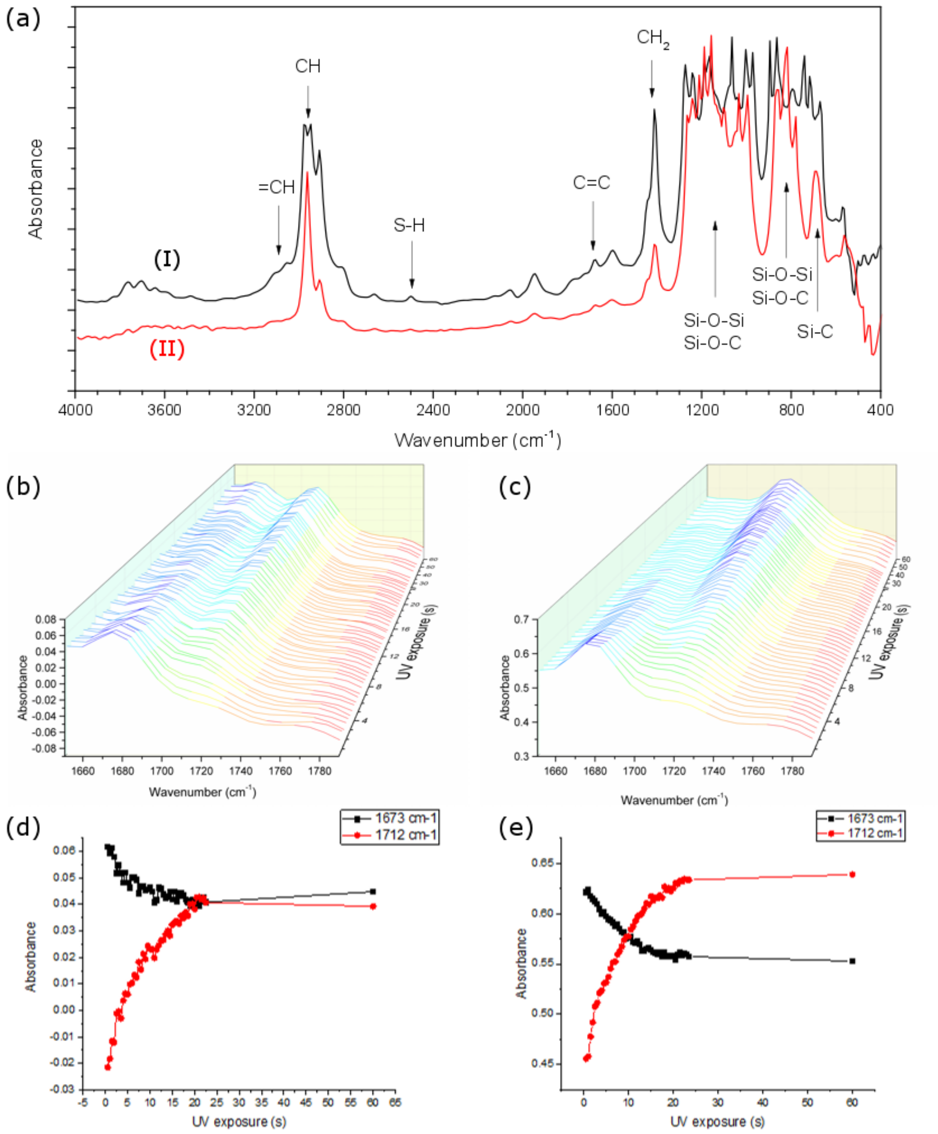

Figure 5.3: (a) FTIR absorbance spectra of (I) silicone A (II) silicone B; (b) FTIR spectra obtained at different UV exposure times for silicone A; (c) FTIR spectra obtained at different UV exposure times for silicone B; (d) . Evolution of peaks at 1673 and 1712 cm^{-1} for silicone A; (e) Evolution of peaks at 1673 and 1712 cm^{-1} for silicone B.

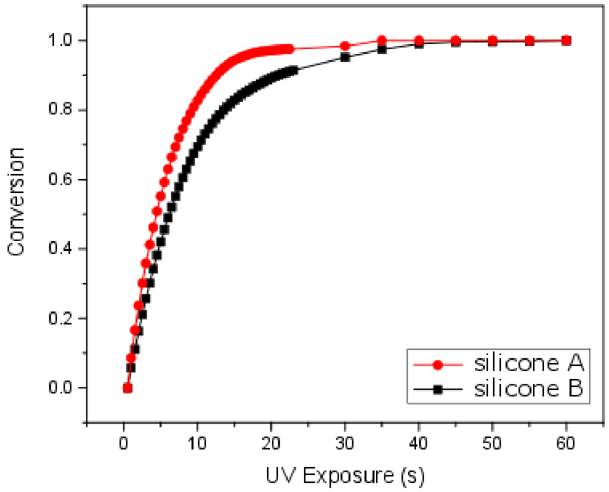

Figure 5.4: Conversion vs. time plots for silicones A and B.

5.3.2 Effects of Silicone Rheology on Internal Porosity of Parts

To investigate the shape retention properties of different blends of silicones A and B, the stress-sweep test was conducted (Fig. 5.5(a-d)). For pure silicone A, G' is more than G'' with a high shear yield stress (σ_y) of ~ 300 Pa, exhibiting a solid-like behavior (Fig. 5.5(a)). This difference between the dynamic moduli as well as the length of storage modulus plateau is decreased for 70A-30B ink (Fig. 5.5(b)). Similar trend is observed as the content of silicone B is increased (Fig. 5.5(c-d)). For 50A-50B ink, the value of G' is slightly higher than G'' in low shear stress region with the yield stress of ~ 15 Pa. By increasing the weight percentage of silicone B to slightly more than 50%, ink 45A-55B with the dominant fluid-like behavior was obtained (Fig. 5.5(d)). The slumping on the glass substrate over time is compared for different inks in Fig. E.1. This test shows the initiation of droplets coalescence for ink 45A-55B almost after deposition. Creation of non-parallel contact lines for ink 45A-55B after the droplets are fully merged is acceptable in our proposed hybrid extrusion-jetting method as both the external and internal perimeters are extruded using ink A in this method.

The viscosity plots for inks with dominant solid-like behavior (A) and dominant fluid-like behavior (45A-55B) at two different temperatures of 25 °C (room temperature) and 100 °C (maximum working temperature of printhead) are compared in Fig. 5.5(e-f). The plots show a highly shear-thinning behavior for ink A with a viscosity of 15×10^5 $mPa.s$

at shear rate of 1 s^{-1}. The high shear-thinning property causes a reduction in the viscosity to less than 2 × 10^5 at shear rate of 20 s^{-1}. Increasing the temperature to 100 °C results in a reduction in the viscosity of ink to 6 × 10^5 $mPa.s$ at 1 s^{-1}. This lower viscosity makes the jetting of droplets easier, as a result, 100 °C was selected as the printing temperature. Ink 45A-55B with the dominant amount of silicone B demonstrates similar shear-thinning behavior and lower viscosity. The value of viscosity for 45A-55B at 1 s^{-1} for this ink (3.7 × 10^4 $mPa.s$) is two orders of magnitude less than the viscosity of pure silicone. A. This value drops to 10^4 $mPa.s$ at shear rate of 20 s^{-1}. Similar to ink A, increasing the temperature results in the drastic reduction of viscosity (1.5 × 10^4 $mPa.s$ at shear rate of 1 s^{-1}). Similar viscosity reduction ratio from 25 °C to 100 °C temperatures (0.4) is observed at low shear rate region for both inks.

X-ray CT scanning was used to observe and quantify the internal porosity of samples manufactured using PPJ technique for inks A and 45A-55B. To obtain the finest resolution for the parts, voxel edge lengths of 4 μm were used. Figure 5.6[(a-i)-(b-i)] represent the 3D visualization of voids internal to the part at scanning resolution of 4 $\mu m/pixel$ in which pores are labelled by volume. Figure 5.6(a-i) shows that sample A consists of smaller number of pores while pores are dramatically larger compared to sample 45A-55B. This is also evident in the 2D slice rendering of pore distribution in XZ plane (Figure 5.6[(a-ii)-(b-ii)]).

These findings correlate well with the quantitative pore analysis from X-ray CT scans of the parts at 4 $\mu m/pixel$. As summarized in Table 5.3, the volume of the smallest detected pore is 512.08 μm^3 for both samples, and any objects (pores) smaller than 512.08 μm^3 were chosen to be noise, which corresponds to $(2 \times \text{voxel size})^3$ for the noise filtration. The volume of the largest detected pore for sample A is 2.34 × 10^8 μm^3. These large pores add up to the total pore volume of 13.1 × 10^8 μm^3 for sample A that is a considerable air void volume compared to 0.7 × 10^8 μm^3 for sample 45A-55B, and contributes to a much smaller relative density (89.17% for sample A vs. 99.65% for sample 45A-55B, respectively), while only 840 pores were detected for sample A vs. 3358 for sample 45A-55B.

Histogram of the pore volumes obtained at scanning resolution of 4 $\mu m/pixel$ associated with samples A and 45A-55B are exhibited in Fig. 5.7(a-b). As seen, pore volume peak is in the range of $10 \times 10^3 - 50 \times 10^3$ μm^3 for sample 45A-55B, while pore volume peak is remarkably shifted to $0.8 \times 10^6 - 10 \times 10^6$ μm^3 range for sample A. Slice-wise relative density calculation of parts at 4 $\mu m/pixel$ scan is shown in Fig. 5.7(c). Quantitative values for relative density are based on the analysis of each individual 2D cross section normal to the central axis. Therefore, the relative density of each tomography slice is calculated by the number of voxels that are identified as the solid phase compared to the total number of voxels identified as either solid or void within the boundary of the part. The lower average

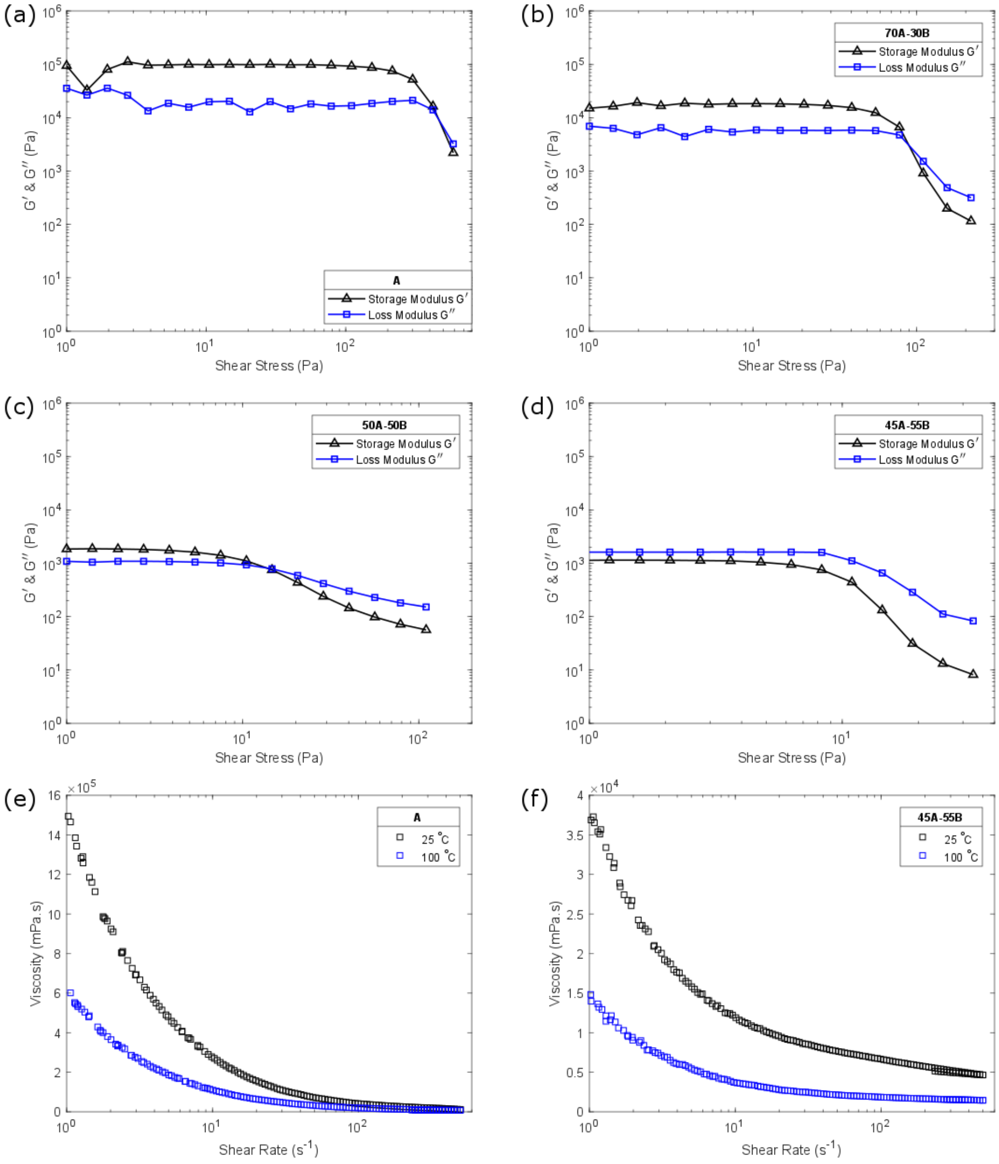

Figure 5.5: The stress-sweep results for (a) ink A, (b) ink 70A-30B, (c) ink 50A-50B, and (d) ink 45A-55B. The reduction in the solid-like behavior of inks is observed as the content of silicone B is increased. Shear-thinning Viscosity plots for (e) ink A and (f) ink 45A-55B at 25 °C and 100 °C. Elevated temperature reduces the viscosity value and facilitates the jetting process.

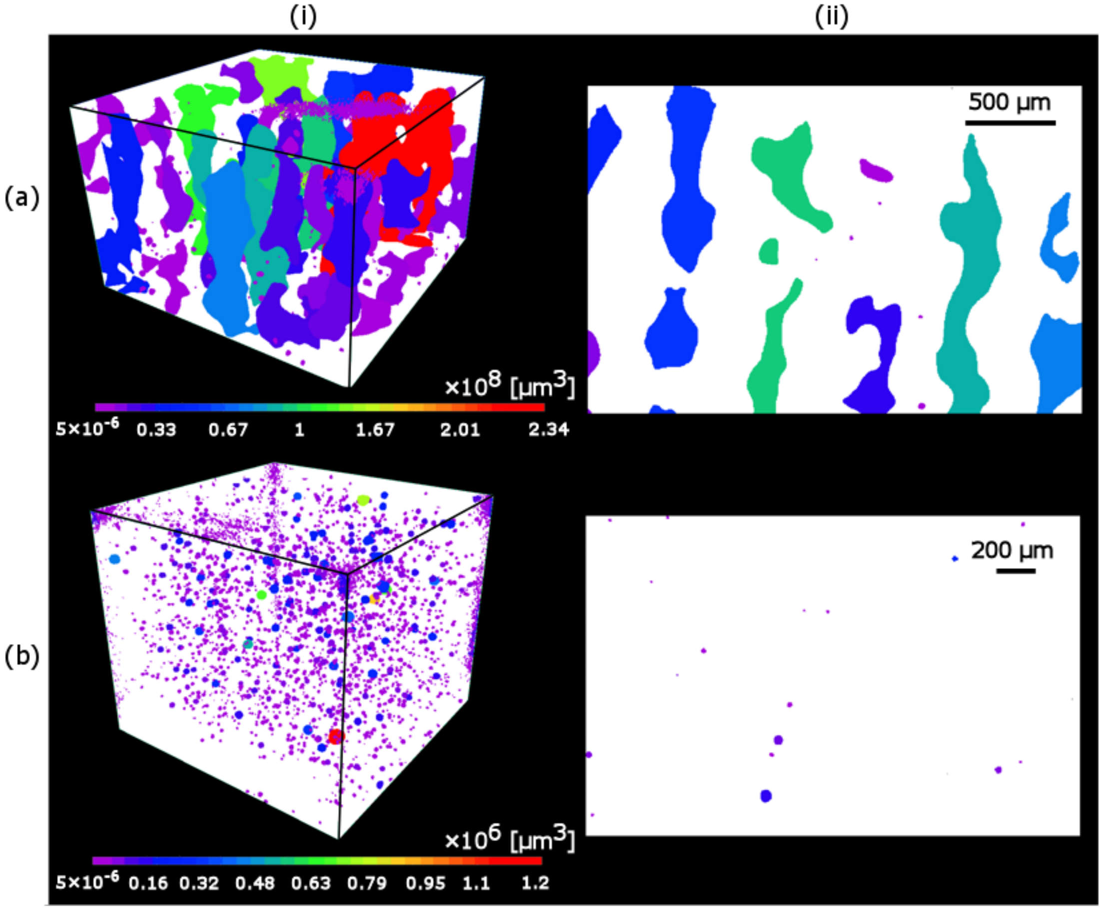

Figure 5.6: CT scan results for (a) sample A and (b) sample 45A-55B: (i) 3D rendering of porosities of parts at two scanning resolutions of 4 $\mu m/pixel$ showing the distribution of voids throughout the parts, (ii) 2D slice rendering of pore distribution in XZ plan.

Table 5.3: Summary of the tomography analysis results.

Parameter	A	45A-55B
Pore volume (voxels)	20541520	1104708
Pore volume (μm^3)	13×10^8	0.7×10^8
Number of detected pores	840	3358
Largest pore (μm^3)	2.3×10^8	18×10^5
Smallest detected pore (μm^3)	512.08	512.08
Relative density (%)	89.17	99.65

density for sample A (89.17%) is attributed to the existence of dominant large pores (0.8 $\times$ 10^6 – 300 $\times$ 10^6 μm^3), which mainly do not exist in sample 45A-55B.

For material extrusion techniques, the shape retention capability of the ink after deposition determines its final resolution and printing quality. Tuning the rheological properties of silicone ink to obtain a shear-thinning viscous polymer with solid-like behavior ($G' > G''$) that is extruded easily under the shear stress at the nozzle without slumping on the surface upon extrusion has been extensively investigated [67, 93–95, 104]. For successful AM of silicone using material jetting, however, a different rheological behavior is required, as in this technique, the building unit is a beaded line composed of adjacent droplets with a certain level of overlap as apposed to a uniform filament. In material extrusion or FDM techniques, air voids might be generated parallel to the printed filament. This difference is depicted in Fig. 5.8. This is the source of anisotropic mechanical properties and poor mechanical performance of extruded parts compared to the bulk material. Modifying the printing parameters such as raster width, back pressure and velocity can eliminate the percentage of air voids. In material jetting, if the deposited droplets do not merge, pores will also be generated along the printed lines resulting in even more inferior mechanical properties. On the other hand, if the ink is very low viscous, the printing resolution will be jeopardized. Even if the printing parameters are optimized to produce fully dense layers with high surface qualities (as was shown for ink A in Chapter 4), the gradual build up of viscous solid-like inks around the nozzle intensified by the deflection of silicone droplets from the previous silicone layers as a result of electrostatic repulsion described in [73] deteriorates the surface quality of higher layers by generating air voids. Reducing the air gap volume in a jetted structure can be achieved by: (1) increasing the jetting frequency; (2) curing the structure after the print instead of curing each layer; and (3) tuning the rheological behavior of ink. The first two methods might not be practical in all cases, as increasing the jetting frequency results in wider lines (lower resolution) and more overspraying, while not curing the printed layers will cause structural collapse and deviation from target height. As a result, the silicone ink should be tailored to be adequately flowable so that coalescence happens at the contact point of droplets to form a uniform filament without risking the well defined resolution of lines. The results of oscillatory shear stress tests (5.5) showed that this can be obtained using the ink 45A-55B. The slightly higher G'' of this ink guarantees the slight slumping of ink under the effect of gravity upon exiting the nozzle, yet the ink does not slump too much so that the resolution of line is lost.

This conclusion is validated by studying the tomography results of parts fabricated using the viscous ink with solid-like behavior (A) and the ink with dominant liquid-like behavior (45A-55B). The CT scan results demonstrate a reduction in pore size and total pore volume for 2 orders of magnitude and 1 order of magnitude, respectively, by increasing

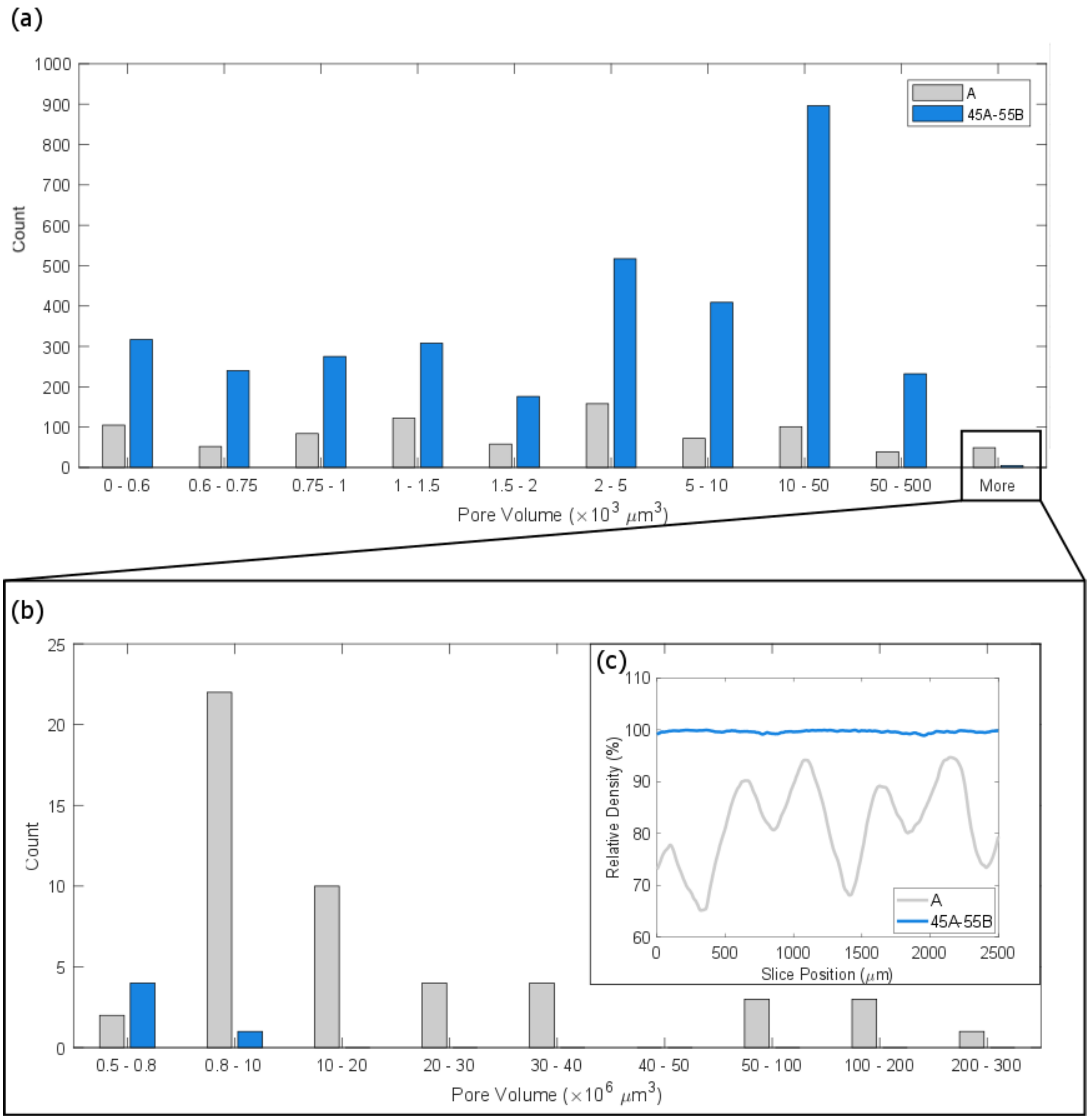

Figure 5.7: (a) Histogram of pore volumes obtained at 4 $\mu m/pixel$ for samples A and 45A-55B; (b) magnification of the histogram at higher volume size bins; (c) slice-wise relative density calculation at 4 $\mu m/pixel$ for samples A and 45A-55B.

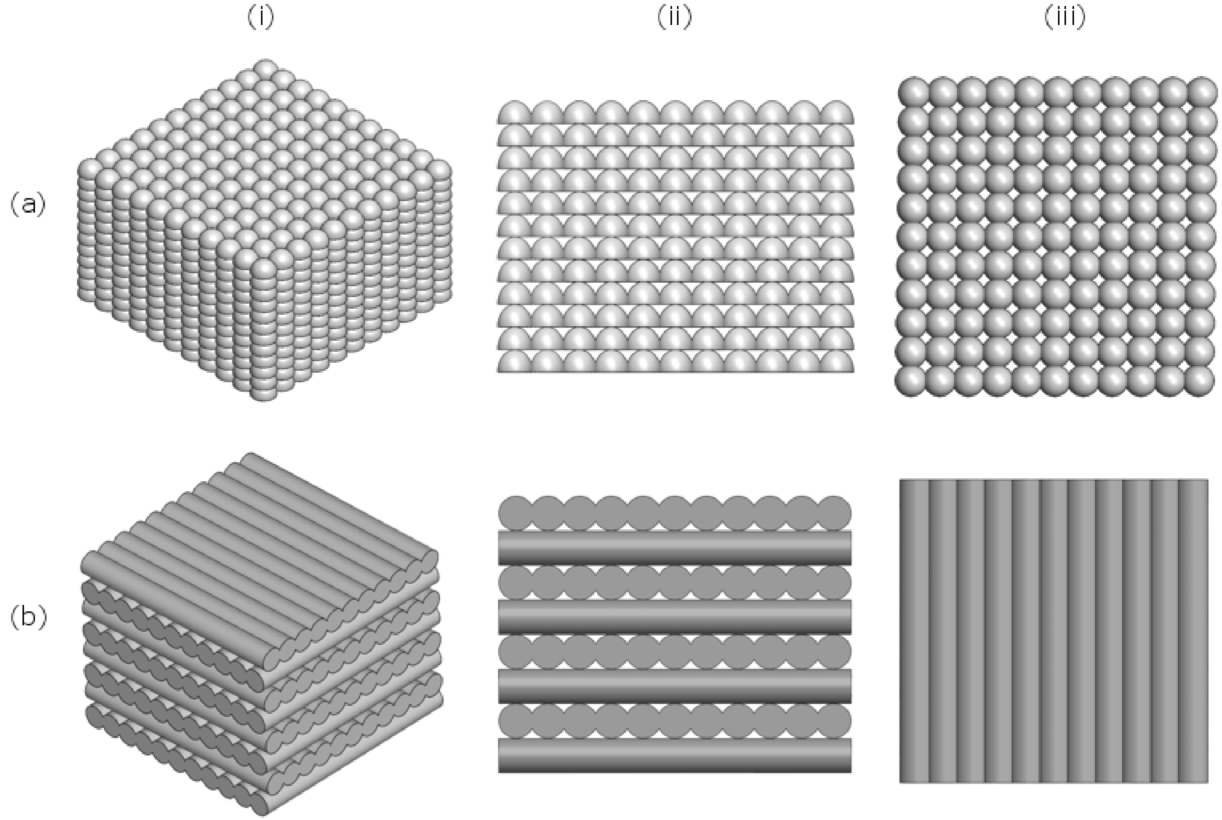

Figure 5.8: Schematic view of 3D structures made using (a) jetting and (b) extrusion. (a-i) 3D view; (a-ii) side view showing inter-layer pores; (a-iii) top view showing in-layer pores. (b-i) 3D view; (b-ii) side view showing inter-layer pores, (b-iii) no in-layer pore or air gap is visible if the strands overlap.

the amount of silicone B to 55 wt.%. However, this has increased the total number of pores by approximately 4 times, introducing many pores with sub-micron size diameter to the media. This has resulted in production of a structure with the least amount of pore volume (0.7×10^8 μm^3) and highest solid density (99.65%).

5.3.3 Effects of Porosity on Mechanical Performance of Parts

The uniaxial tensile test, tear resistance test, and durometry test have been carried out for inks A and 45A-55B (Fig. 5.9) for the parts made using PPJ (AM-made) as well as the molded bulk materials (cast).

Figure 5.9(a) shows 38.6% reduction in the average elongation at break (ϵ_f) for AM-made parts from ink A (381%) compared to its cast control sample (234%). For ink 45A-55B, the average ϵ_f was reduced to 97.3% and 85.1% for AM-made and cast specimens, respectively. As a result, the difference percentage for this parameter has been reduced to 12.6% for ink 45A-55B. Similar behavior can be observed in Fig. 5.9(b) for the tensile strength (σ_f). A significant 45.9% reduction in the value of σ_f from 1.35 MPa for cast to 0.73 MPa for AM-made specimens has been reduced to 2% difference between average σ_f of cast (0.49 MPa) and AM-made (0.5 MPa) samples.

The tearing resistance test results are demonstrated in Fig 5.9(c). For this property of the matter, the tear strength (T_s) of cast and AM-made samples are not significantly different for inks A (0.66%) and 45A-55B (2.4%). For ink A, the average tear force is 10.85 kN/m for cast specimens and 10.77 kN/m for AM-made specimens. These values have been dropped to 1.003 kN/m and 1.027 kN/m for cast and AM-made specimens of ink 45A-55B, respectively. Similarly, the hardness values, shown in Fig. 5.9(d), are not significantly different for the two different fabrication methods for both inks. The average hardness value for cast samples of ink A is 73.2 (Shore 00) as opposed to 70.1 (Shore 00) for AM-made samples. The hardness of parts manufactured from ink 45A-55B is slightly less (66.5 and 64.5 (Shore 00) for cast and AM-made samples, respectively). The details of measurements and statistical comparison of mean values are provided in Table E.1. The corresponding stress-strain curves and tearing force plots are provided in Fig. E.2.

The adverse effect of pores on the mechanical performance as well as improving the strength of the parts by reducing the porosity level through modification of printing parameters has been extensively studied for extrusion-based systems [143–148]. Moreover, the quality of the inter-layer bonds can determine the strength of parts as well. The creation of strong cohesive bonds between successive layers was obtained through the *in-situ*

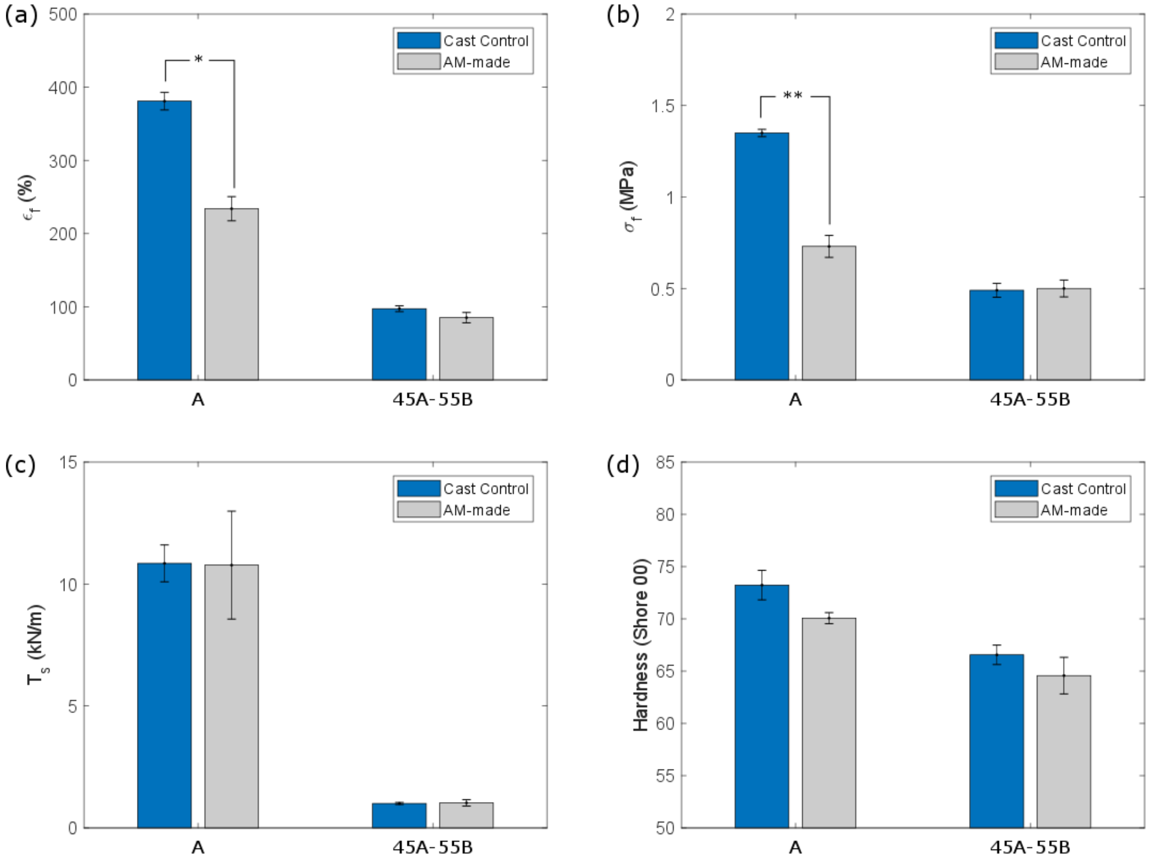

Figure 5.9: Comparing the mechanical characteristics of AM-made and cast samples made from inks A and 45A-55B ($\alpha = 0.05$): (a) Elongation at break (ϵ_f), (b) tensile strength (σ_f), (c) tear strength (T_s), and (d) Shore 00 hardness. The p-value for significant difference between the average of parameters under study: $*$ 0.001, $**$ 0.00. (a-d) n = 3.

partial curing mechanism explained in Section 5.3.1. Thus, the significant difference between the cast and AM-made parts for both ultimate stress and strain (σ_f and ϵ_f) can be justified through the difference in their porosity. Sample A is $\sim$ 19 times more porous than sample 45A-55B. Small pores ($< 0.5 \times 10^6$ μm^3) are visible in both samples with higher concentration is sample 45A-55B; however, sample A contains a significant number of large pores in the volume range $0.8 \times 10^6 - 300 \times 10^6$ μm^3 (more than 50 pores in 125 mm^3). The tomography results (Fig. 5.6) shows that the small voids of sample 45A-55B are introduced to the structure during the jetting process and scattered throughout the structure with no special pattern which is similar to what might be seen during the casting; however, the large air voids of sample A seem to be made as a result of failed merging of adjacent beaded lines. The weak bond between lines in one layer as well as the stress concentration zones generated by the large pores throughout the testing section of tensile specimens leads to their pre-mature failure compared to cast samples. The insignificant difference for sample 45A-55B shows that the small spherical pores ($< 0.5 \times 10^6$ μm^3) do not contribute much to lowering the tensile strength and elasticity of parts made via PPJ. The lower σ_f and ϵ_f of ink 45A-55B is due to the use of silicone B with short-chain monomers. Similar reduction in resilience and strength has been reported for a silicone composed of short- and long-chain monomers at similar ratio by Jindal et al. [105].

The adverse effect of porosity on the tensile properties was corroborated by studying the fracture surface of tensile specimens A (Fig. 5.10(a)) and 45A-55B (Fig. 5.10(b)). Pores observed on the fracture surface of specimen A are marked in Fig. 5.10(a-i). In comparison, the fracture surface of specimen 45A-55B only contains one pore (Fig. 5.10(b-i)). The initiation of cracks from the edge of the pores and their propagation through the surface can be observed in Fig. 5.10(a-iii). On the other hand, the brittle nature of silicone B has resulted in a clean flat rupture through parallel vertical and horizontal cracks covering the entire surface from edge to edge which can be observed in Figs. 5.10[(b-ii)-(b-iii)].

The manufacturing method seems to have no influence on the tearing strength for both inks. This can be attributed to the fact that in type C specimen of ASTM D 624 standard, the initiation of tear happens at the right-angled stress concentration apex. The effect of this apex on the initiation of rupture surpasses the effects of stress concentration zones of small pores. Similarly, the effect of manufacturing method on the hardness is minimal. This effect on the hardness, however, is slightly larger compared to tear strength. Even for ink A, there is a statistically significant difference between the average hardness of cast and AM-made parts; however, because the p-value (0.041) is close to the significance level, the difference is considered to be experimentally insignificant. Moreover, hardness is the only parameter which is not sensitive to the change in the ink composition. Meanwhile, adding 55 wt.% silicone B to the composition of ink has reduced the tear strength by a

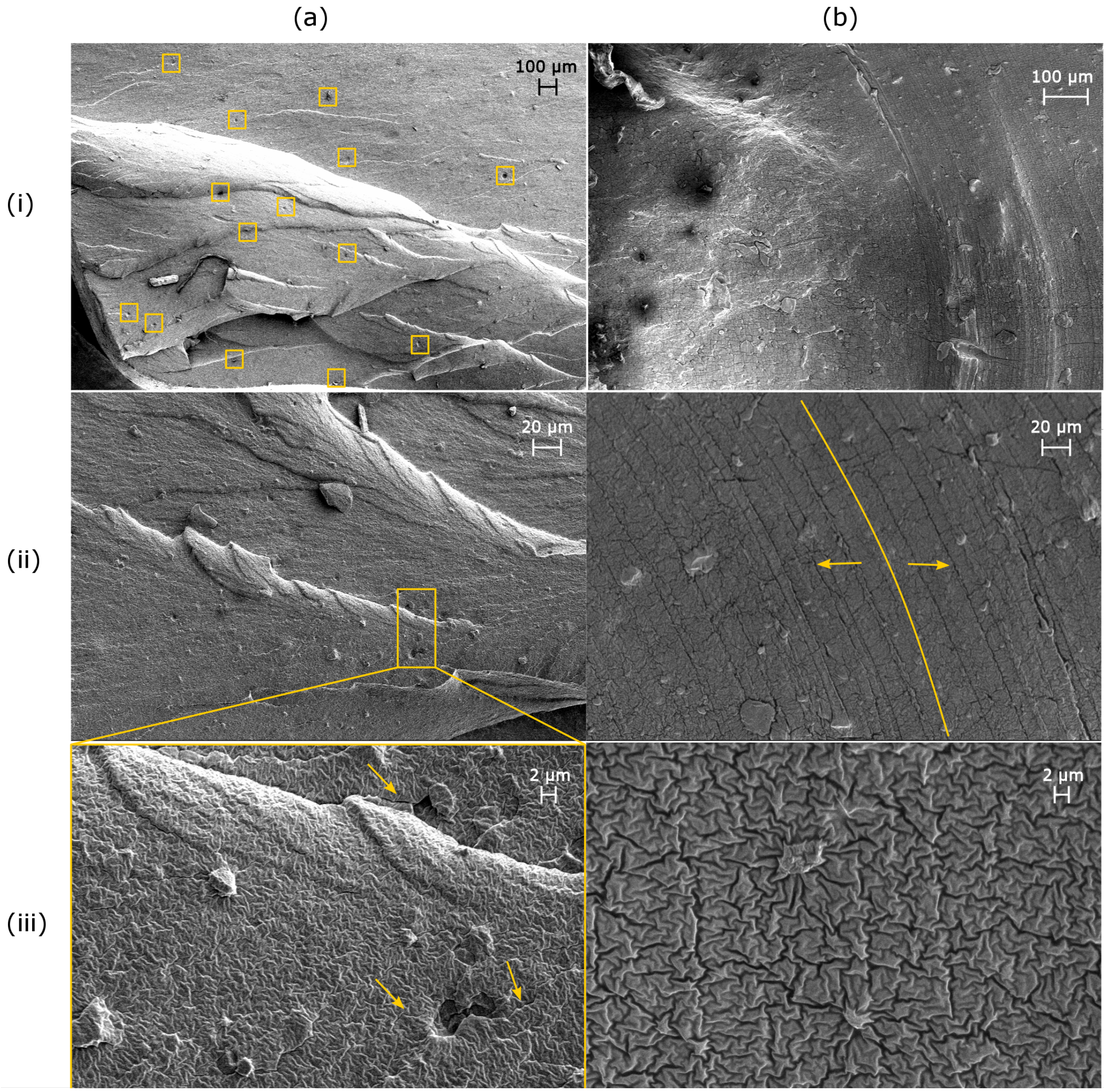

Figure 5.10: SEM of fracture surfaces of tensile specimens: (a) A, (b) 45A-55B. (a-i) Pores are visible on the fracture surface of the specimen A. The fracture surface is non-flat and irregular cracks are observed; (a-ii) and (a-iii) magnified view of fracture surface of specimen A. The failure cracks around pores are visible. (b-i) Non-porous flat fracture surface of specimen 45A-55B; (b-ii) The surface is covered with curved fracture lines parallel to the build direction. Shallower cracks are created perpendicular to the build direction. (b-iii) A magnified view of the fracture surface demonstrating the cracks propagation path.

factor of ten.

When considering the rheological properties of silicone ink for PPJ system, it is recommended that an ink with marginally higher loss modulus and low shear yield be used. This yields an almost fully dense structure with a mechanical performance similar to the bulk material.

5.4 Silicone-based Motion-Detector Sensor

The capability of the hybrid multi-nozzle AM method in fabrication of the heterogeneous bio-structures was investigated in the context of fabricating a wearable motion-detector sensor (Fig. 5.11). Motion-detector stretchable sensors can be attached to the skin or clothes in order to detect the motion (e.g. pulse). Thus, they can be used as health monitoring and rehabilitation assistance devices. The fabrication of stretchable sensors has been widely investigated using traditional methods such as casting which includes multiple time-consuming steps [149, 150]. Extrusion-based AM have been used to integrate dielectric and conductive inks into a 3D structure with a printing speed of $4-7.5\ mm/s$ as well [66, 67].

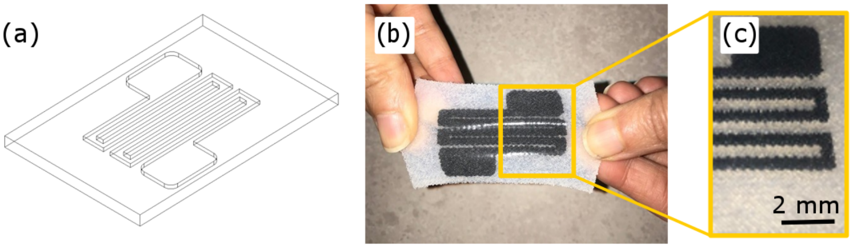

Figure 5.11: Flexible sensor printed using PPJ system: (a) CAD model of the sensor; (b) stretched sensor; (c) magnified view of the graphene-silicone pattern

We designed a sensor composed of a pattern of proprietary silicone-augmented graphene ink embedded within silicone. The CAD model of the sensor can be seen in Fig. 5.11(a). Silicone A has been used to improve the stretchability of graphene ink and 3D print the perimeter of each layer. The body of the silicone frame is made from the 45A-55B silicone ink with printing parameters introduced in Section 5.2.2. The printing parameters for the graphene-silicone ink are similar to those obtained in Section 4.3.2; however, the temperature of the ink was 25 °C. The stretchability and printing details are shown in

Fig. 5.11(b-c). The fabrication of this structure at 104 mm/s from three different materials with various electrical and mechanical properties simultaneously at a high spatial resolution demonstrates the capability of the proposed hybrid AM method in production of heterogeneous structures at a higher efficiency compared to casting and with a higher speed compared to extrusion AM.

5.5 Summary

A comprehensive study of the effect of the rheology of different blends of short- and long-chain silicones on their porosity and mechanical performance was presented in this chapter. An ink with 45:55 wt.% of short-chain and long-chain silicone polymers showed a slightly higher G'' than G' which resulted in the complete coalescence of jetted droplets without a significant loss of resolution. As a result, almost fully dense structures were produced. More importantly, it was established that the in-line porosity introduced to the part when using an ink with high yield stress leads to poor mechanical performance in terms of ϵ_f and σ_f compared to the bulk material. The effect of AM on the mechanical performance of the part was improved by using the fluid-like ink. No significant difference in the average T_s and hardness of the parts based on the level of porosity was observed. The fabrication of a multi-material stretchable bio-sensor was showcased.

Chapter 6

Additive Manufacturing of Silicone via Powder-Bed Binder-Jetting Technique

6.1 Introduction

Research and commercial efforts in AM of silicone materials have focused on material extrusion, vat photopolymerization, and material jetting, with various degrees of success and technology-specific limitations. PBBJ, also known as 3D printing [151]; however, has not been used prior for the fabrication of silicone structures. This method relies on AM of parts by converting a CAD model into layer-by-layer images that are sequentially printed onto thin layers of powder. The printed liquid acts as a binder, consolidating the powder into a so-called green part once the binder is cured. The thin layers of powder are spread using a counter-rotating roller or a blade mechanism from a douser or a feed bed. The green part is porous and typically undergoes a series of post-processing protocols, which may involve de-powdering, thermal treatments, or matrix infiltration. The materials used for PBBJ AM are mainly ceramics, metals, or their composites [58]. In a recent review of AM materials, PBBJ methods had not been introduced as a manufacturing method for any kind of thermoset polymer including silicone [152].

The PBBJ AM technique has shown great compatibility with bio-materials for multiple applications [153–158]. There are three main advantages for PBBJ manufacturing approaches: (1) the ability to use a wide range of materials [58, 159–162]; (2) the degree of freedom in manufacturing complex and scalable parts without the need for support structures [58, 163]; and (3) the high production speed with commercial systems performing often in the order of a few seconds per layer. In addition, PBBJ systems are capable of producing functionally graded structures [160, 164–167], with multi-material or multi-colour features [21, 51]. The versatility of this methodology is the driving factor in exploring PBBJ in manufacturing silicone structures. The most pressing drawbacks in manufacturing silicone parts via PBBJ is that the smallest feature size of conventional PBBJ equipment is limited by the size distribution of the powder [159, 162, 168, 169], the binder jetting resolution [159], and de-powdering constraints [159, 165, 169, 170]. For PBBJ, the minimum cavity feature size is typically considered at 500 μm for de-powdering considerations, with a layer thickness in the order of 25 – 200 μm. The powders used in PBBJ should comply with specific rheology and powder size distribution criteria to ensure uniform and defect-free layer properties in this layer thickness range. In addition, commercial PBBJ systems employ a single powder type during the build. The liquid binder is typically dispensed through a thermal or piezoelectric printhead, with a general limit in viscosity of less than 40 $mPa.s$ to ensure proper material jetting, as well as fast infiltration through the powder substrate. The parts are typically exposed to a post-processing protocol for de-powdering, followed by heat-annealing, chemical setting, irradiation or infiltration, depending on the material system used. These post-processing steps typically result in part shrinkage or swelling and reduce the overall geometrical accuracy of the final product. The dimensional deviation can be considered in the CAD design stage by applying dimensional compensation factors.

To overcome some of the limitations in PBBJ, a new hybrid PBBJ and micro-deposition system was developed [118, 163] to target manufacturing of functionally-graded parts with multi-material and custom variable porous structures. This new system employs multiple powder feed mechanisms to dynamically select and deploy up to three different powder compositions to each layer, thermal and piezoelectric printhead delivery systems for jetting of various liquid binders, a variable counter-rotating roller mechanism to control powder compaction, a solid material dispenser for embedding discrete pore-generating sacrificial materials (porogens), and a micro-dispensing head for deposition of liquids throughout the porous matrix of the part at select locations.

In this chapter, the hybrid PBBJ AM system is used for the direct production of silicone structures. The system employs a material system composed of silicone powder as the base material in the substrate, a water-based liquid binder (Zb®60) that is jetted through a thermal printhead onto the powder substrate to develop the wetted layer outline of the parts, and a thermoset silicone liquid binder to impart the necessary structural integrity of each layer. The thermoset silicone binder is heat cured after printing a fixed number of layers. Curing the thermoset silicone prevents any further permeation of subsequent silicone binder through previous layers, thus preserving the dimensions of the parts. The machine and material system is used to manufacture cylindrical shapes ($5\ mm\ D \times 3\ mm\ H$) as part of a DoE.

6.2 Materials and Methods

6.2.1 Powder Silicone Materials

Two hybrid organopolysiloxane powders consisting of spherical silicone rubbers were used as received in this research. These powder samples offer all of the unique properties of a regular PDMS rubber including high thermal resistance, weatherability, and biocompatibility. The first powder (powder A) consists of silicone rubbers covered with a silicone resin (KMP-602, Shin-Etsu Chemical, Tokyo, Japan). The resin cover provides high resistance to impact by relaxing the stress, and improves the lubricity property. The rubber part is responsible for the resistance to extreme temperatures and abrasion. The second silicone powder (powder B) is made of pure spherical silicone rubbers without the resin coating (KMP-598, Shin-Etsu Chemical, Tokyo, Japan).

Powder Size and Morphology Characterization

The particle size distribution of the silicone powder samples and their sphericity and symmetry were verified using a dynamic image processing system (CamSizer XT, Retsch-Technology, Germany). The shadow of dispersed silicone particles illuminated by two LED sources were captured as they passed through a free-fall feed shaft in front of two cameras. The system measured parameters corresponding to the particle size distribution, sphericity, and symmetry in real time.

Powder Dynamic Flowability, Shear Rate Sensitivity, and Bulk Properties Characterization

A powder rheometer (FT4, Freeman Technology, UK) was used to determine the rheological properties of the silicone powders in response to multiple external conditions such as flow rate, aeration, and consolidation, its bulk properties such as compressibility and permeability, and its shear rate sensitivity. Before conducting each test, a uniform initial state of stress was achieved at the conditioning stage by disturbing the particles gently through the helical movement of a blade.

6.2.2 Liquid Silicone Binder

The two-part thermal-curable liquid silicone rubber (JY-9010, Changzhou Juyou New Material Tech Co., China) was used with 100:1 main component to curing agent ratio. This silicone liquid is comprised of modified silica and Octamethylcyclotetrasiloxane which is a non-toxic organosilicon compound.

Viscosity Measurement

The viscosity of liquid silicone binder was measured at 25 ± 0.01 °C using a digital cone and plate rheometer (RST-CPS-P, Brookfield Engineering, MA, USA) at 200 – 2000 s^{-1} shear rate range by first increasing and then decreasing the shear rate value. The measurement data was collected at 15 points in 60 s for both ascendant and descendant curves.

Differential Scanning Calorimetry (DSC) Analysis

The analysis of the thermal behavior of liquid silicone binder was conducted using a DSC device (STA 449 F1, Netzsch, Germany) in the range of 25 - 160 °C with a heating rate of 5 °C/min. In order to measure the curing time, the isothermal test was carried out with a DSC device (MTDSC 2920, TA Instruments, DE, USA) at the equilibrium temperatures of 60 °C, 100 °C, and 110 °C. The curing behaviour was investigated in an inert atmosphere (Nitrogen), and each test was replicated three times.

6.2.3 Liquid Water-based Binder

An aqueous liquid binder (Zb®60, 3D systems, SC, USA) was inkjet printed onto the powder-bed to form the wetted precursor image of each layer. The Zb®60 includes 85 – 95% v/v of distilled water and 5 – 15% v/v of humectant and a proprietary polymer as a binding agent.

6.2.4 Experimental Setup

As the proof-of-concept, filled cylindrical structures (5 mm D × 3 mm H) were printed using the hybrid PBBJ AM system. The process of manufacturing the silicone structures starts with designing cylindrical CAD models and slicing the digital data into successive layers and execution steps for each layer. The hybrid PBBJ AM of a 3D object with both the structural powder material and the binder made from silicone has four stages as illustrated in Fig. 6.1 and described in detail as follows:

(1) A roller with a linear velocity of 20 mm/s and rotational velocity of 100 rpm spreads the silicone powder from a feeding bed (also called supply powder bed) to a build bed. This results in a flat layer of silicone powder with a fixed layer thickness (LT) (Fig. 6.1(a)).

(2) The thermal inkjet printhead jets the water-based Zb® 60 binder onto the powder surface based on the image corresponding to the layer being manufactured. The Zb® 60 liquid binder acts as a glue spread onto the silicone powder substrate to generate the structure by binding the silicone particles according to the geometry of the slice and to wet the substrate in preparation for the liquid silicone binder. Steps (1) and (2) are repeated a fixed number of times called dispensing frequency (Fr) before the deposition of liquid silicone is carried out (Fig. 6.1(b)) in step (3).

(3) The nozzle with inner diameter 100 μm is located above the center of the structure with 2 mm off-set. By applying 100 kPa air pressure through a micro-syringe extrusion system (Optimeter, Nordson EFD, RI, USA), a droplet of silicone is dispensed to infiltrate the binder-wetted porous media substrate (Fig. 6.1(c)).

(4) The structure is then exposed to a temperature of 100 - 120 °C supplied via a thermal lamp for 1 min to initiate and complete the polymerization of the two-part heat-curable silicone binder solution (Fig. 6.1(d)).

The four steps are repeated until the cylindrical structure is completed in a layer-by-layer fashion. The parts are left in the build bed for 2 – 3 hours. Finally, they are removed from the hybrid PBBJ system and air-heated at 85 °C to ensure the full curing.

6.2.5 Imaging

The liquid silicone binder droplet size at multiple pressure values were measured using a digital camera (AM7915MZT, Dino Lite, Taiwan) at 21× magnification. Images of the silicone binder droplets pendant from the needle tip were captured at 1 s intervals between the moment the pressure was applied, up to the separation of the droplet. The

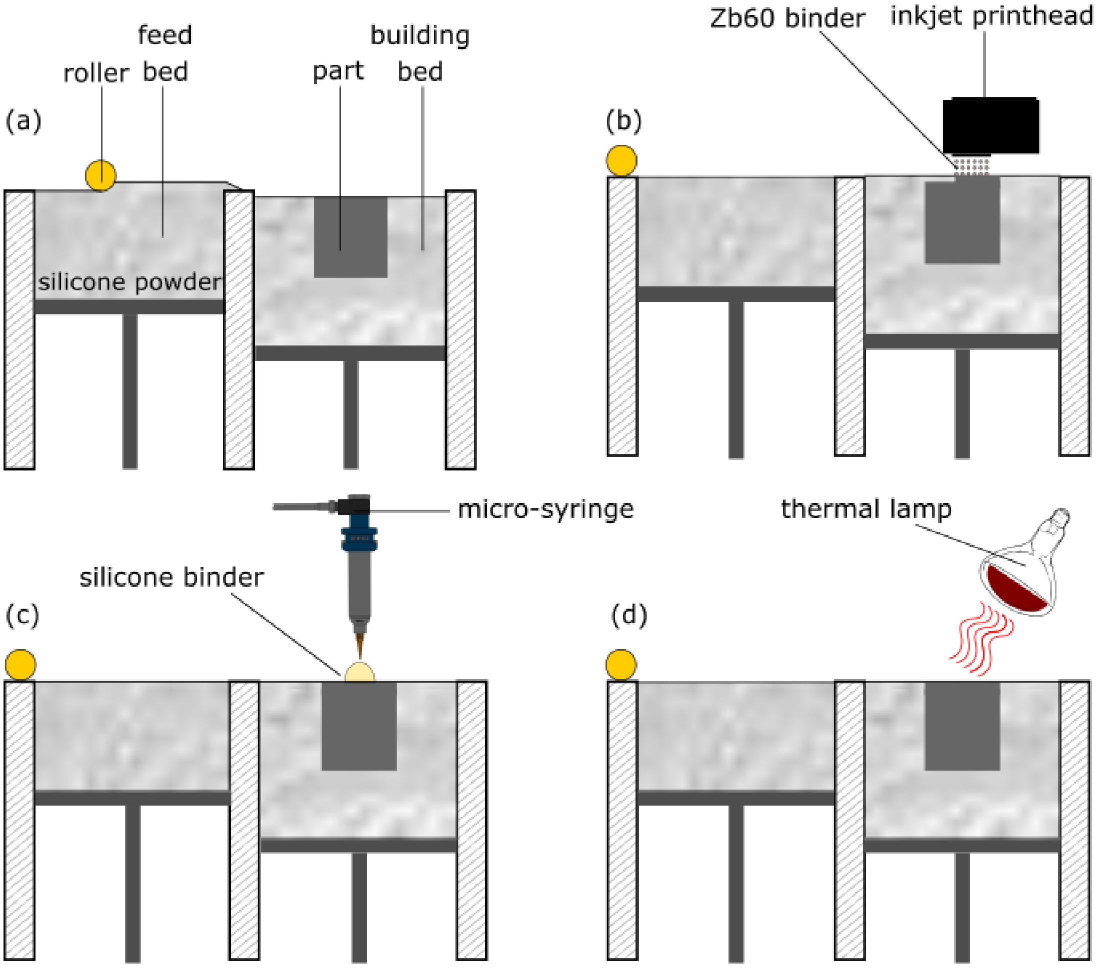

Figure 6.1: The schematic of hybrid PBBJ AM system. (a) spreading the silicone powder from feed bed onto the build bed; (b) wetting each layer by inkjet printing the water-based binder; (c) dispensing a droplet of silicone binder to fill up the silicone porous media using a pneumatic extrusion system; (d) partial curing of the silicone binder using a thermal lamp at 100 °C temperature.

maximum diameter of droplet before separation was measured using the image processing software DinoCapture (Dino Lite, Taiwan). The powder silicone particle morphology was investigated using SEM (Ultra Plus, Carl Zeiss AG, Germany) at accelerating voltages of 10 kV and 3 kV for powder A and powder B, respectively.

6.2.6 Part 3D Profilometry

Profiles of the additively manufactured samples were obtained using a laser confocal microscope (VK-X250, Keyence, Japan) at 100× magnification. The height and the diameter of the circles fitted to the cross-section of the cylindrical samples were measured using the software MultiFileAnalyzer (Keyence, Japan).

6.2.7 Part Computed Tomography (CT) Scan

The tomography of the entire printed structure was captured using a nano-CT scanner (Xradia 520 Versa, Carl Zeiss AG, Germany). The scanning parameters are provided in Table 6.1.

Table 6.1: CT scanning parameters

Parameters	Voxel size (μm)		
	4.05	1.4	0.727
Source Power (W)	3	3	3
X-ray Energy (kV)	40	40	40
Filter	LE2	LE1	LE1
X-ray Optic Lens	4×	20×	20×
Exposure Time (s)	1	1	10
Number of Projections	801	801	1601
Binning Level	4	4	2

In order to calculate the solid phase density for 4.05 μm resolution CT scan result, the original greyscale image was filtered with both a small kernel Gaussian filter, then with a larger kernel bilateral filter (2 voxel radius) which is an edge preserving Gaussian filter. A greyscale threshold was then determined manually to segment the dense particle phase from the void and silicone binder phases. The exterior regions were masked from the part, to not be included in the porosity calculations. The masking was performed by eroding the surface down by a localized porosity threshold until the mask closely tracked the part surface. Then, each voxel within the masked region was given a distance value from the central axis, and another distance value from the base of the domain. These distance values were used to group voxels into radial and vertical position bins for the respective porosity distributions.

For separating three different phases of silicone powder, silicone binder, and air voids in the nano-scale CT scan results, the original greyscale image was first adjusted with a normalizing gradient to correct for artifacts associated with the sample exceeding the scanning field of view. A bilateral filter with a spatial radius of 2 voxel lengths was then applied to remove noise. Finally, the three phases were separated from each other in a combination of manual greyscale threshold selection and morphological image processing steps, including opening, closing, and three dimensional median filters. The image processing routine had to be carefully performed due to the large overlap in the histograms of the porous and polymer phases.

6.2.8 Hardness

A Shore 00 handheld durometer (Shore S1, Shore Instruments-Instron, MA, USA) was used to measure the hardness of 3D printed samples as well as samples of the silicone binder cured in a mold for comparison (cast control samples). The rigid ball was located on the center of the cylindrical samples, and the hardness value was captured after 1 s dwell time. Each reading was repeated three times for two replicates of samples manufactured under similar printing conditions.

6.2.9 Statistical Analysis

In order to optimize the 3D printing parameters, a multi-level experimental design was formed with LT and Fr as the control factors. Table 6.2 shows the levels of each factor. The height (H), inner diameter (ID), and the diameter difference (DD) between the inner and outer circles fitted to the cross section of parts are the responses. The outer diameter (OD) is the diameter of the largest circle fitted to the cross-section of the cylindrical parts so that it covers the entire cross-section including the irregular edges. The diameter of the circle that only covers the central parts of the cross-section and not the irregularity caused by the lateral infiltration of silicone binder is *ID*. The difference between *ID* and *OD* is depicted in Fig. 6.2 and is the method used to calculate *DD*.

Table 6.2: Experimental design factor levels for PBBJ process.

Factor	Low Level (–1)	Center Level (0)	High Level (+1)
LT (μm)	50	-	100
Fr	1 drop per 100 μm	1 drop per 200 μm	1 drop per 300 μm

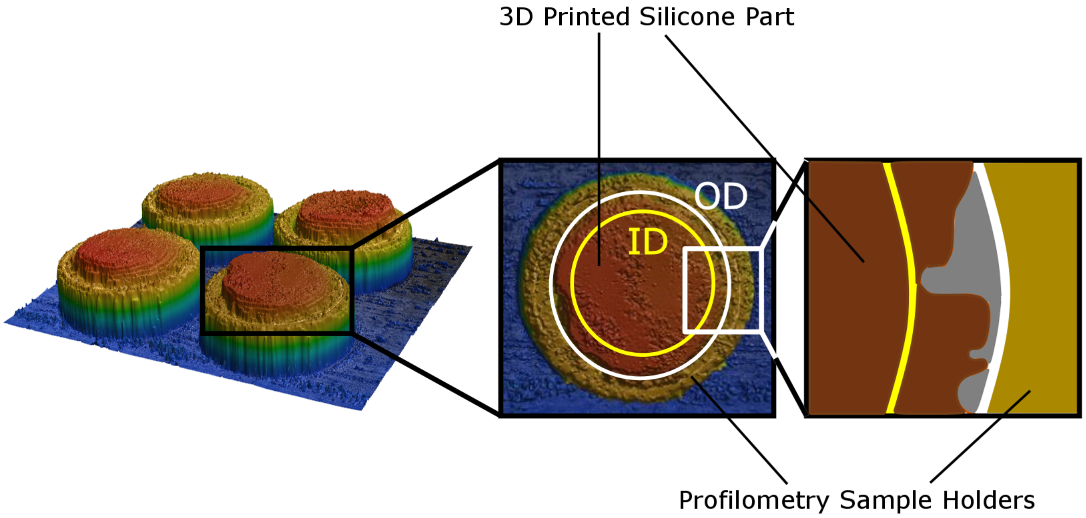

Figure 6.2: Sample of the 3D profile of the four replications of a part manufactured with similar printing parameters. The difference between the two circles fitted to the cross-section of each sample is shown in the magnified top view images.

The path to the optimized region for each parameter was found using RSM. Finally, all three responses were optimized simultaneously using desirability function technique (utility transfer function). The levels of significant factors were selected so that *DD* was minimized, and *H* and *ID* approached the target values of 3 mm and 5 mm, respectively.

A one-way Tukey ANOVA at 95% confidence level was employed to compare the hardness of parts manufactured under different 3D printing conditions.

6.3 Results and Discussion

6.3.1 Silicone Binder Viscosity and Droplet Size in Dispensing

Figure 6.3(a) shows the viscosity of silicone binder at the shear rate range of 200 - 2000 s^{-1}. The viscosity vs. shear rate plot shows a Newtonian behavior with the constant viscosity of 78 $mPa.s$ at room temperature. The ascendant and descendant plots coincide as well showing the independency of the rheological behavior of the fluid on the shearing history. For a fluid with the shown viscous behavior, the syringe dispensing was tested under various pressures. It was found that varying the dispensing air back-pressure did not affect the volume of the dispensed droplet, however, it changed the separation time (see Table 6.3). With a pressure of approximately 100 kPa, the droplet separated 8 s after the pressure was applied providing enough time for the control of dispensing mechanism. Figure 6.3(b) shows the image of a silicone droplet captured before its separation form the needle tip with the inner diameter of 100 μm. The diameter of the shown droplet is 1.54 mm.

Table 6.3: Dispensing duration for one droplet at different air pressure values.

P (kPa)	Dispensing Time (s)
30	15
50	10
100	8

The constant diameter of silicone binder droplet before separation from the needle tip under different pressure values allows the adjustment of the dispensing time by modifying the air pressure (Fig. 6.3a). The viscosity of silicone binder (78 $mPa.s$) is not very high so that it prevents the creation and separation of droplets, at the same time, it is not very low to cause fluid dripping (Fig. 6.3b). However, once dispensed on the dry powder bed, the infiltration process takes 10 - 20 s. Moreover, this long infiltration causes the disturbance of silicone powder particle distribution in the layer. In order to minimize this issue, the powder surface was pre-wetted with the water-based binder. The utilization of water-based binder helps the proposed hybrid AM technique by: (1) binding the silicone particles temporarily together; (2) speeding up the process of silicone binder infiltration by enhancing the wetting properties of silicone particles. The aqueous binder is used to wet the powder substrate in order to accelerate the progression of the silicone liquid droplet from primary to secondary liquid spread [171]. Primary spread occurs when the sessile

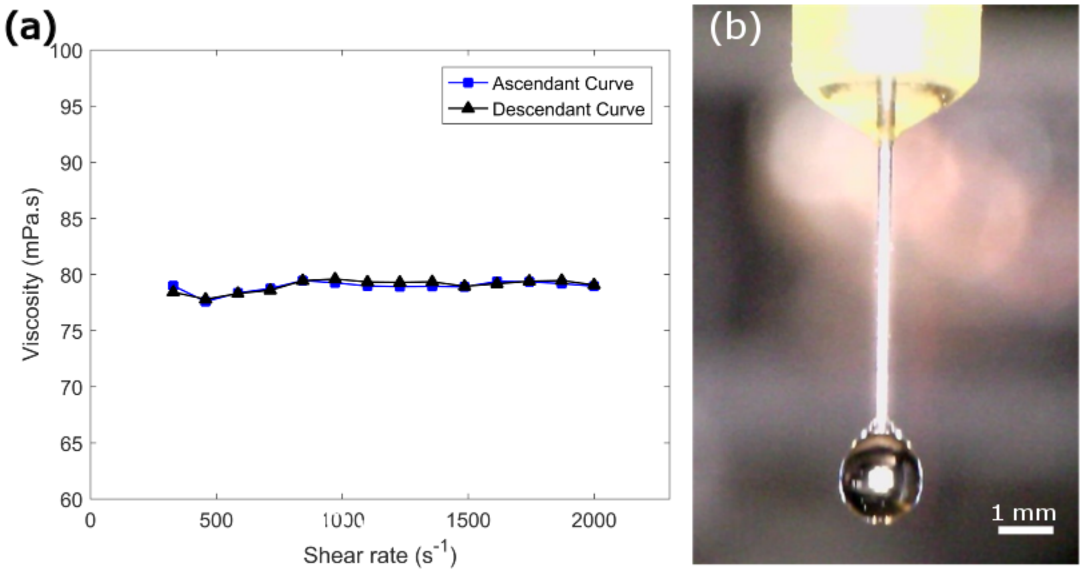

Figure 6.3: (a) The viscosity of silicone binder showing a Newtonian behavior at the shear rate range of 200 - 2000 s^{-1}; (b) The silicone binder droplet before separation from the needle with a maximum diameter of 1.54 mm.

droplet volume (volume above the powder) is not zero, where the secondary spread occurs within the porous substrate only. In the absence of the aqueous binder, the primary spread could take more than 10 s, while in the presence of the aqueous binder, the primary spread is reduced to approximately 1 s. The infiltration process is schematically illustrated in Fig. 6.4.

6.3.2 Thermal Analysis of Silicone Binder

The exothermic silicone cross-linking process for the samples of silicone binder at various hold temperatures are depicted in Fig. 6.5(a). For all three replications of the experiment, the positive peak appears in the range of 75 - 90 °C. Thus, the maximum temperature of three tests (90 °C) was selected for further investigation. The isothermal DSC results (Fig. 6.5(b)) at 90 °C show that the curing process is accelerated after 3 - 4 min at equilibrium and takes approximately 2 min to reach the maximum curing rate. Similar experiment conducted at 100 °C (Fig. 6.5(c)) shows that the curing happens right after the temperature equilibrium is reached. Increasing the temperature even further results in curing of the binder before reaching the target temperature (Fig. 6.5(d)).

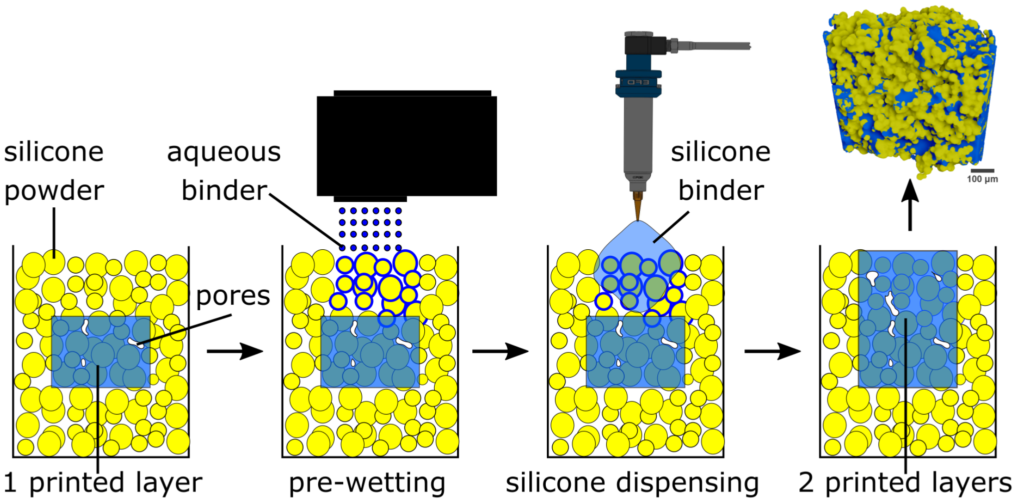

Figure 6.4: The infiltration of silicone binder in pre-wetted substrate.

Investigating the thermal behavior of the curing process of the liquid silicone binder is crucial in designing a curing mechanism that assures the geometrical accuracy of the parts is maintained by crosslinking the silicone binder after dispensing as fast as possible to prevent its penetration into the surrounding powder environment. The entire curing process for silicone binder at 90 °C takes approximately 6 *min* which can prolong the manufacturing process. As a result, the silicone binder was exposed to a curing temperature between 100 - 120 °C for 1 *min* using a thermal lamp. The changes in the powder surface temperature measured using a thermocouple (Fig. E.3) shows that the powder bed temperature reaches 100 °C after 50 *s* and 110 °C after 60 *s*. The isothermal plots at these two temperatures (Fig. 6.5(c-d)) demonstrate that curing happens immediately after reaching 100 °C, and a full cure takes less than 1 *min*. As a result, the employed curing policy of 1 *min* exposure to heat prevents both the unnecessary increase in the total manufacturing time and permeation of silicone binder outside the region of interest.

When considering the liquid silicone material and the rheological and thermal behavior during the curing, it is recommended that for manufacturing of such silicone structures, the following considerations should be met: (1) increasing the infiltration rate of liquid silicone binder by enhancing the wettability of particles through pre-wetting of the powder-bed; (2) preventing the permeation of silicone binder to the areas that are not supposed to be a part of final structure through instant curing; (3) tailoring the rheological properties of silicone binder (recommended viscosity range: 70 - 90 $mPa.s$) so that it is not too viscous for common direct write AM techniques, yet viscous enough so that it does not permeate too

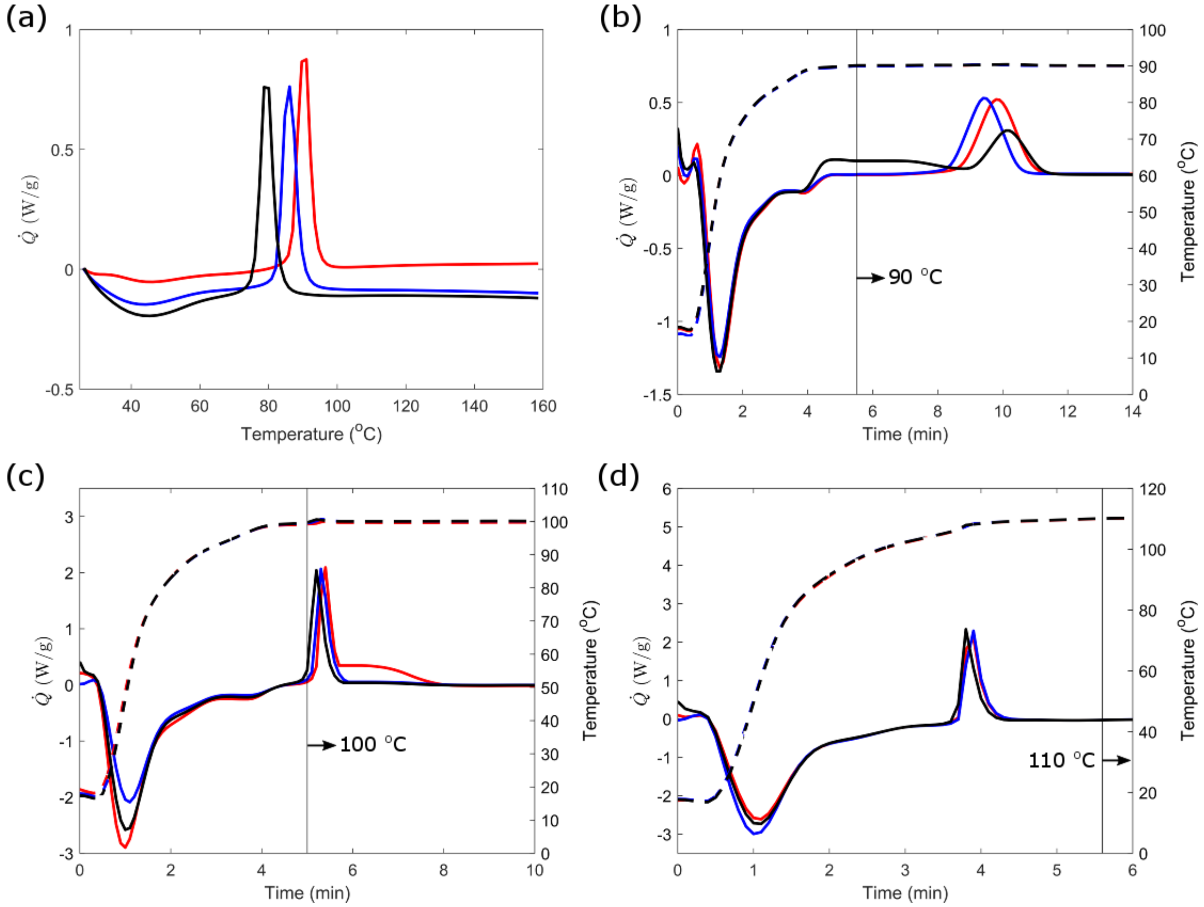

Figure 6.5: Thermal analysis results for silicone binder: (a) non-isothermal curves (heat flux vs. temperature); (b) isothermal curves at 90 °C; (c) isothermal curves at 100 °C; (d) isothermal curves at 110 °C; (a-d) $n = 3$, solid lines and dashed line corresponds to heat flux and temperature, respectively.

fast before crosslinking; and (4) increasing the resolution and accuracy of the technique by replacing the extrusion system with a DOD AM printhead in order to reduce the diameter of silicone binder droplets from 1.54 mm to less than 300 μm

6.3.3 Silicone Powder Size, Morphology, and Rheology

The deep understanding of the powder rheology and properties is important in powder-bed AM processes in order to obtain a consistent and uniformly spread layer and minimize the printing variability. Thus, investigating the rheological properties of a silicone powder with successful flowability for AM would be beneficial for future development of silicone powder customized for powder-bed systems.

The SEM images of powder A (Fig. 6.6(a-c) and powder B (Fig. 6.6(d-f)) show their effective spherical morphology. The particles of powder A appear segregated, while the particles of powder B have cohered together and produced large agglomeration of clusters surrounded by finer satellite particles. The powder particles in both powder A and B appear spherical in nature. Powder A had a fine coating in the as-purchased state, and this can be seen as surface flakes in Fig. 6.6(c). Powder B did not have any coating in the as-purchased state, and appears smooth in nature, as seen in Fig. 6.6(f).

The particle size distribution of powder A can be seen in Fig. 6.7 with an average particle size of 30 μm. The shape analysis test for powder A showed a high level of sphericity (average value of 0.842 for four test replications where 1 represents the perfect circle). The symmetry index for the powder A was 0.963 as well (with 1 representing the full symmetricity). Studying the particle size distribution and quantifying the sphericity of powder B was not possible due to its high degree of agglomeration and cohesiveness. However, the manufacturer reports particle size distribution of 2 - 30 μm with an average particle size of 13 μm for this powder.

The flow properties of silicone powders were measured based on their resistance to the movement of a blade which creates a flow pattern by its rotational and vertical movement. Guidelines provided in [172–174] have been used to interpret the powder rheology results. The energy required to establish this flow pattern for both powders is shown in Fig. 6.8(a). The first 8 repeated tests have been conducted at the same blade velocity, followed by the gradual decrease in the velocity in tests 9 - 12. At the fixed velocity region, the energy required for the flow is 15 mJ higher for the powder B. The same pattern with lower difference in the value of energy can be observed for the lower velocities. The lower energy for the powder A shows that it is a non-cohesive powder with better flow properties. This

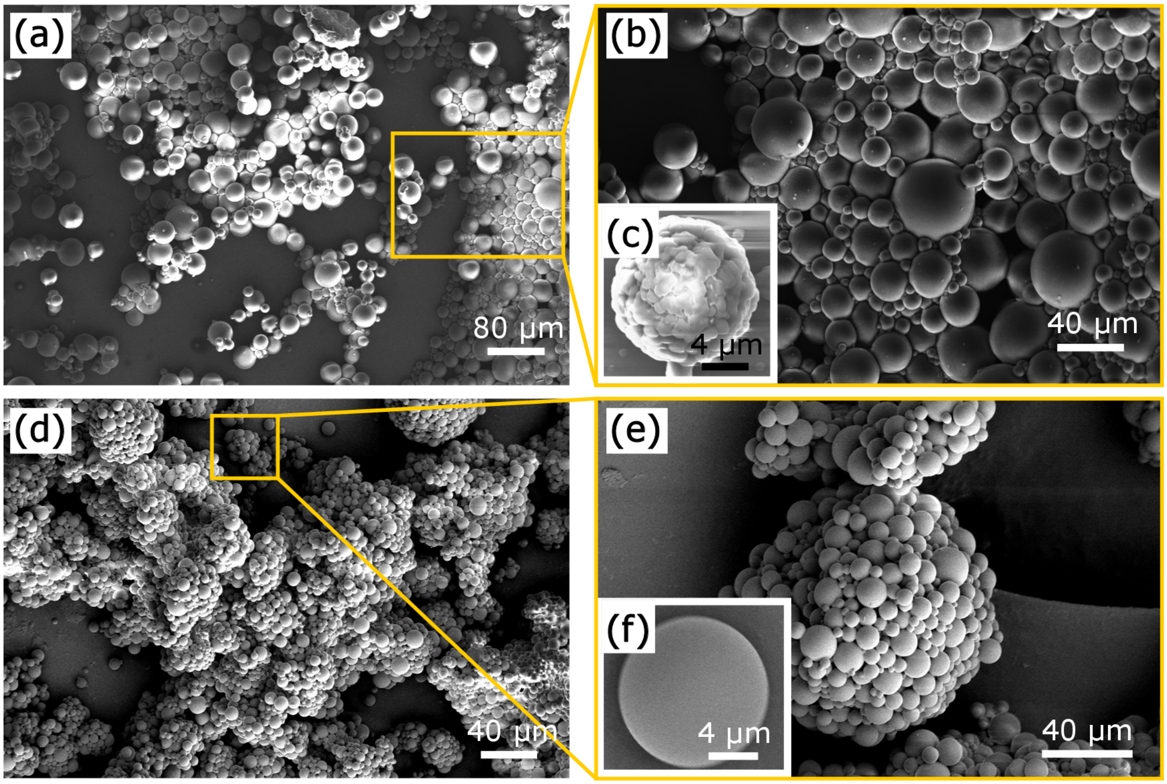

Figure 6.6: (a-c) SEM images for powder A shows spherical and symmetrical particles; (d-f) SEM images for powder B shows the creation of large clusters of particles due to cohesiveness of the powder.

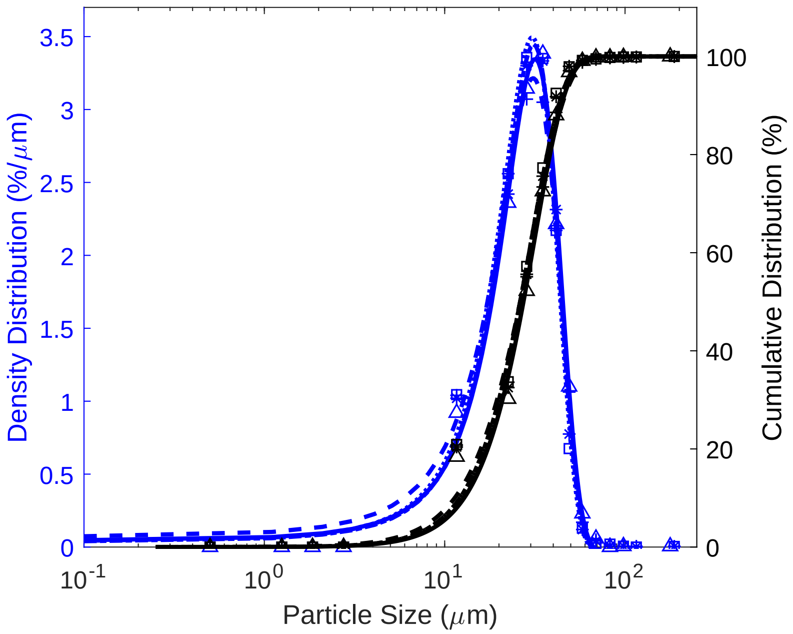

Figure 6.7: Particle size distribution for powder A ($n = 3$).

conclusion will be reaffirmed through other permeation, aeration, compression, and shear tests.

A similar test was conducted for both powder types while they were conditioned with the air flow with varying velocities. The aeration test for powder A (Fig. 6.8(b)) and powder B (Fig. 6.8(c)) demonstrate drastically different behaviors. The energy required for the flow of blade has been reduced to almost zero for powder A even at a low air velocity of 1 mm/s and remained near zero for the higher velocities (2 - 5 mm/s) as well. As for the powder B, the zero plateau was never achieved even with an air velocity as high as 150 mm/s. The zero energy indicates a virtually fluidized powder bed that makes the rotation of the blade through the powder bulk easier. The sharp decrease in the amount of energy for the hybrid powder and reaching the fluidization state confirms the non-cohesive behavior of powder A.

The compressibility and permeability test results are shown in Fig. 6.8(d-e). In these two tests a sample of pre-conditioned powder is compressed under certain normal stress values. The compressibility test measures the change in the powder volume when exposed to normal stress, and the permeation quantifies the ability of the bulk powder in passing a fluid through its porous structure by measuring the air pressure needed in order to maintain a constant air flow as the normal stress is increased. Figure 6.8(d) shows that powder B is 4 - 6 times more compressible than powder A at any given normal stress. Powders with lower compressibility have a more efficient packing of particles, and are less cohesive. On the other hand, the pressure drop for powder A is approximately 10 $mBar$ more than that of the powder B which makes the hybrid powder A highly permeable to air.

The shear strength was measured at 7, 6, 5, 4, and 3 kPa normal stresses after pre-shearing the powder at 9 kPa. The higher value of shear stress at any given normal stress indicates a more difficult flow due to cohesiveness, irregular shape of particles, void-free structure etc. Powder A demonstrates lower shear yield loci for any normal stress compared to powder B making it less resistant to the flow during the recoating process.

Comparison of the shape and size of powders A and B (Fig. 6.6(a-f)) suggests that powder A could be a viable candidate for powder-bed AM. Powders A and B both have a narrow particle size distribution range and spherical shape which are both favorable powder characteristics for AM. However, the smaller particle size of powder B (almost half the size of powder A) increases the free surface area and consequently the friction and static forces between the powder particles. This will result in the inefficient packing properties and difficulty in powder spreading and layer recoating process [175]. The lower flowability under static and aerated conditions, lower permeability, and higher compressibility of powder B confirm the conclusions inferred from particle shape and size analyses. A high degree of agglomeration was observed in the SEM image of powder B (Fig. 6.6(d)). The reason behind the low flowability and permeability of silicone B could be the formation of tightly packed structures as finer separated silicone particles interlock through static friction to form powder agglomerations. The high compressibility is an indicator of the cohesiveness of powder B which justifies the agglomeration. An important characteristic of the powder feedstock used in AM is their shear stress as the particles slide relative to each other when transferred from the feeding compartment to the building compartment by the roller, and the initiation of the flow is dependent on overcoming the resistance to the flow. The lower shear stress for the powder A shows its better flow properties and less cohesive behavior. The lubricating effect derived from the resin coated hybrid powder A also contributes to its overcoming of the inter-particular shear forces.

When considering the powder silicone material and the rheological and morphology of the powders, it is recommended that for manufacturing of such silicone structures, the following considerations should be met: (1) spherical and symmetric powder particles; (2) average particle size between 30 - 40 μm with a reasonably wide distribution range ($\sim \pm$ 30 μm) to provide an efficient particle packing in the powder-bed; (3) non-cohesive powder demonstrating limited compressibility (10 - 20 %) and high permeability to air; (4) powder with low shear yield (less than 2.5 kPa for normal pressure between 1 - 7 kPa) to decrease

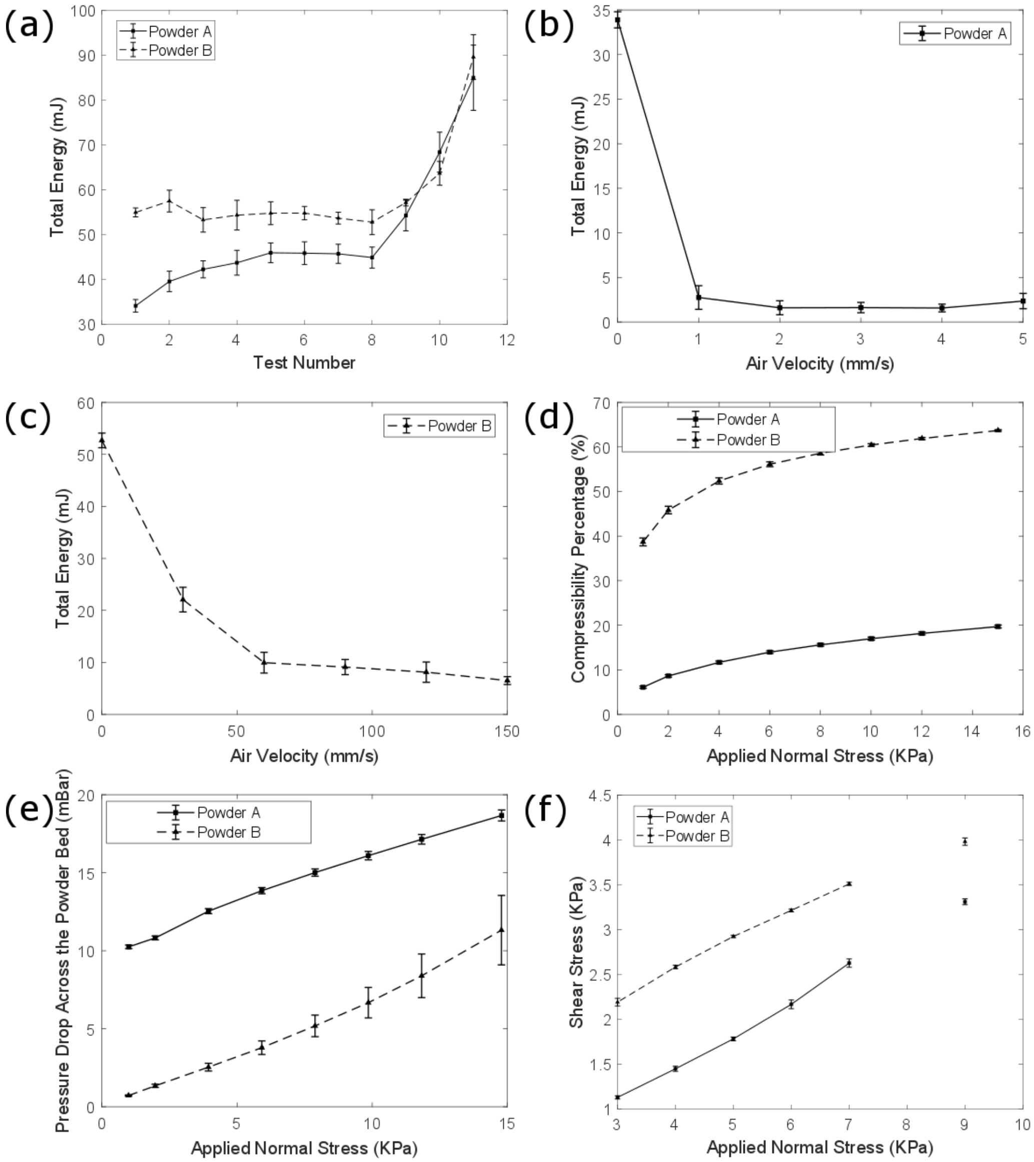

Figure 6.8: Silicone powder characterization results; (a) flow test for powders A and B; (b) aeration test for powder A; (c) aeration test for powder B; (d) compressibility results for powders A and B; (e) permeation results for powders A and B; (f) shearing test for powders A and B; (a-f) $n = 3$.

the resistance to flow during the recoating.

6.3.4 Part Shape Fidelity Characterization

The significance of *LT* and *Fr* on the dimensional accuracy of the 3D printed parts was evaluated using a multi-level experimental design. The details of design and the measured values for height and width can be found in Table D.1. The samples were manufactured in a completely randomized order according to the designed experiment. The responses were assumed to be independent.

The ANOVA results are shown in Tables D.2, D.3, and D.4 for *H*, *ID*, and *DD*, respectively. The results show that for *H* and *ID*, *Fr* has a significant effect at 95% confidence level. However, none of the parameters are significant at 95% confidence level for the *DD*. The response surface plots (Fig. 6.9([a-i]-[c-i]) demonstrate the path to the optimization for each of the responses. Marginal mean plots (Fig. 6.9([a-ii]-[c-ii]) confirm the ANOVA conclusions. The marginal mean plots for *H* and *ID* both show that the higher limit of *LT* (100 μm) yields dimensional values closer to the target. However, *Fr* of 1 drop per 200 μm and 1 drop per 300 μm produce the best results for *H* and *ID*, respectively. Thus, the desirability function technique was adopted to optimize the input parameters simultaneously (Table D.5). The simultaneous optimization of three responses showed that by setting *LT* and *Fr* both at their high level (100 μm and 1 drop per 300 μm, respectively), the optimum results will be achieved. At this condition, the average values of *ID*, *H*, and *DD* will be 5.45 mm, 3.77 mm, and 1.6 mm, respectively.

The investigation of part shape fidelity through the experimental design showed that at the optimum condition, *H* and *ID* of the sample parts are 0.45 mm and 0.75 mm larger than their target values, respectively. Moreover, the optimized *DD* value of 1.7 mm will reduce the geometrical accuracy of the shape. The results show that further work in this area must be done in order to obtain higher geometrical accuracy. To this end, the effect of surfactants on the surface properties and the size of silicone binder droplet and the effect of additives to the powder system for controlling its fluid permeability properties will be investigated in the future work.

6.3.5 Part Internal Features

The CT scanning results at 4.05 μm voxel resolution for the entire AM-made silicone structure manufactured using 100 μm *LT* and 1 droplet per 3 layers *Fr*. is shown in Fig. 6.10(a). A higher concentration of silicone powder is visible in the center of the

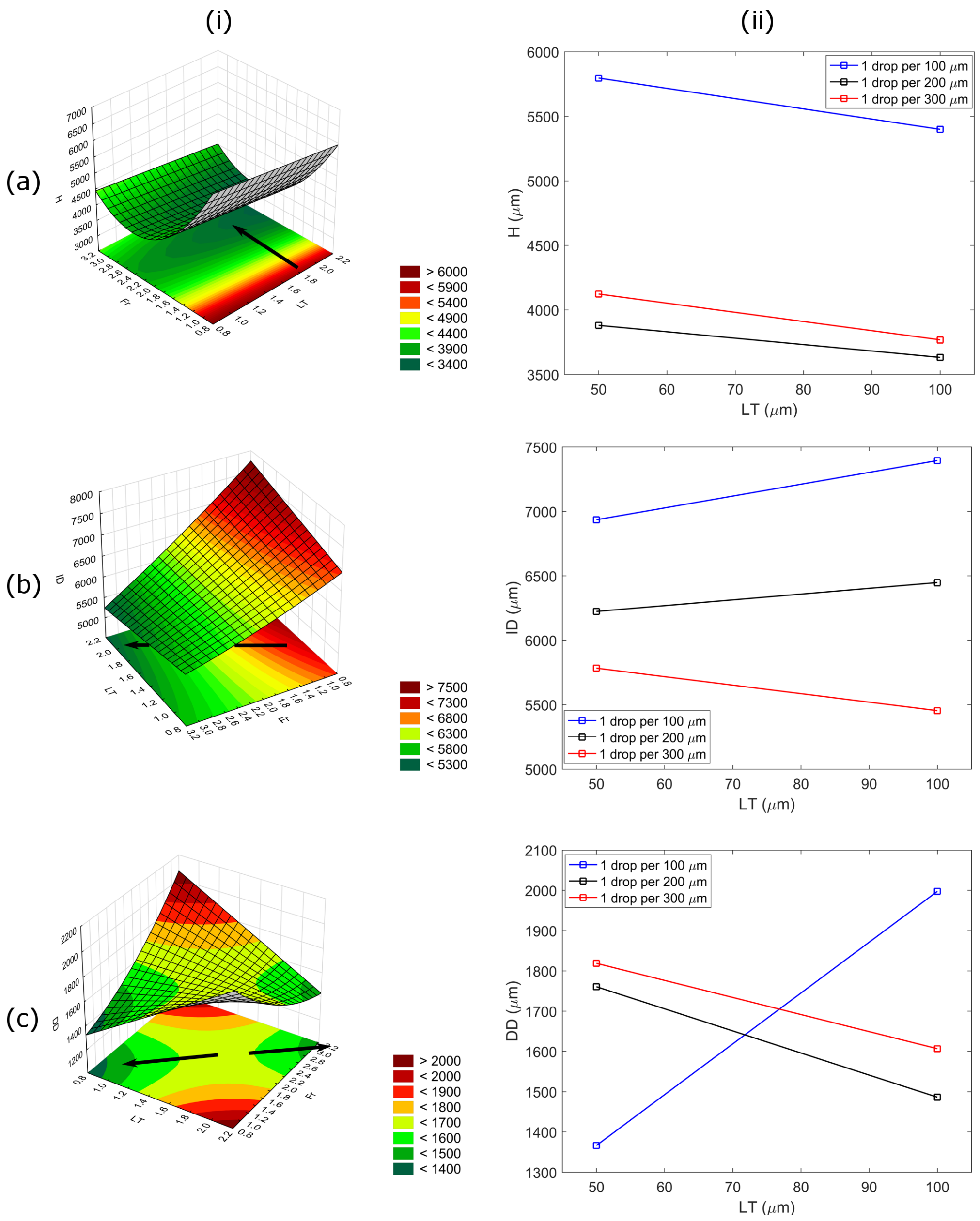

Figure 6.9: The optimization results for separate analysis of responses; (a-i) the contour plot and optimization path for H; (a-ii) the plot of marginal means for H; (b-i) the contour plot and optimization path for ID; (a-ii) the plot of marginal means for ID; (c-i) the contour plot and optimization path for DD; (c-ii) the plot of marginal means for DD. The arrows show the path to the optimized regions

structure as opposed to its shell. The quantified vertical and radial particle phase fraction for each slice are plotted in Fig. 6.11(a) and Fig. 6.11(b), respectively, demonstrate that the particle phase fraction is dropped from 75% at core to 55% at the edge. This change in the density of powder however is less variant along the height of the sample (55% – 65%). A magnified view of two regions of interest inside the structure at higher resolution helps in distinguishing between the particle and cured binder phases. Figure 6.10(b) shows a zone inside the structure with visibly higher concentration of silicone powder particles. Comparing these images with the CT scan results of a central section of the structure (Fig. 6.10(c)) reveals that the difference in concentration of particles is much higher in radial direction. The overall solid particle phase density for this cylindrical structure is 59.8%. The remaining 40.2% of the entire volume is comprised of silicone binder and pores.

In order to separate the silicone binder and air pores, image processing was conducted on the CT scanning data obtained for a small section of the AM-made part at nano-resolution (727 nm voxel resolution). Figure 6.12(a) shows the overall view of the scanned samples. Silicone binder and pores are isolated in Fig. 6.12(b) and Fig. 6.12(c), respectively. Based on the quantification results of image processing, the sample is made of 70.5% silicone powder, 21.3% silicone binder, and 8.2% pore. Five of the largest pores are shown in different colors in Fig. 6.12(d).

Based on the CT scan data, the silicone part fabricated at optimum printing condition using the hybrid method consists of approximately 8.2% air voids (Fig. 6.12) which are distributed unevenly throughout the structure (Fig. 6.11). Moreover, despite the presence of regional pore interconnectivity at multiple locations in the AM-made sample, the pores of larger volume are actually isolated and trapped inside the part (Fig. 6.12(d)). As a result, a new dispensing method using piezo-dispensing should be investigated to determine the feasibility of dispensing smaller liquid silicone droplet volumes throughout the layer of interest to increase shape fidelity and control over the internal porosity. Printing droplets with volumes in the order of pico- or micro-liter provides higher control and flexibility over the total silicone binder volume infiltrated in each layer, and makes it possible to fill a certain percentage of the air voids. In such drop-on-demand systems, adjusting the actuation parameters in combination with translational velocity of the printhead can change the volume of droplets as well as the deposition frequency. Thus, multiple patterns from continuous lines to separate droplets can be laid down on the powder substrate which in turn make controlling the overall density of the structure possible. This provides an apparatus for fabrication of silicone structures with variable density profile from fully dense to highly porous with interconnected channels.

The CT analysis results illustrated in Fig. 6.11 showed a variability in silicone powder volume fraction radially, with more particles clustering in the center compared to the pe-

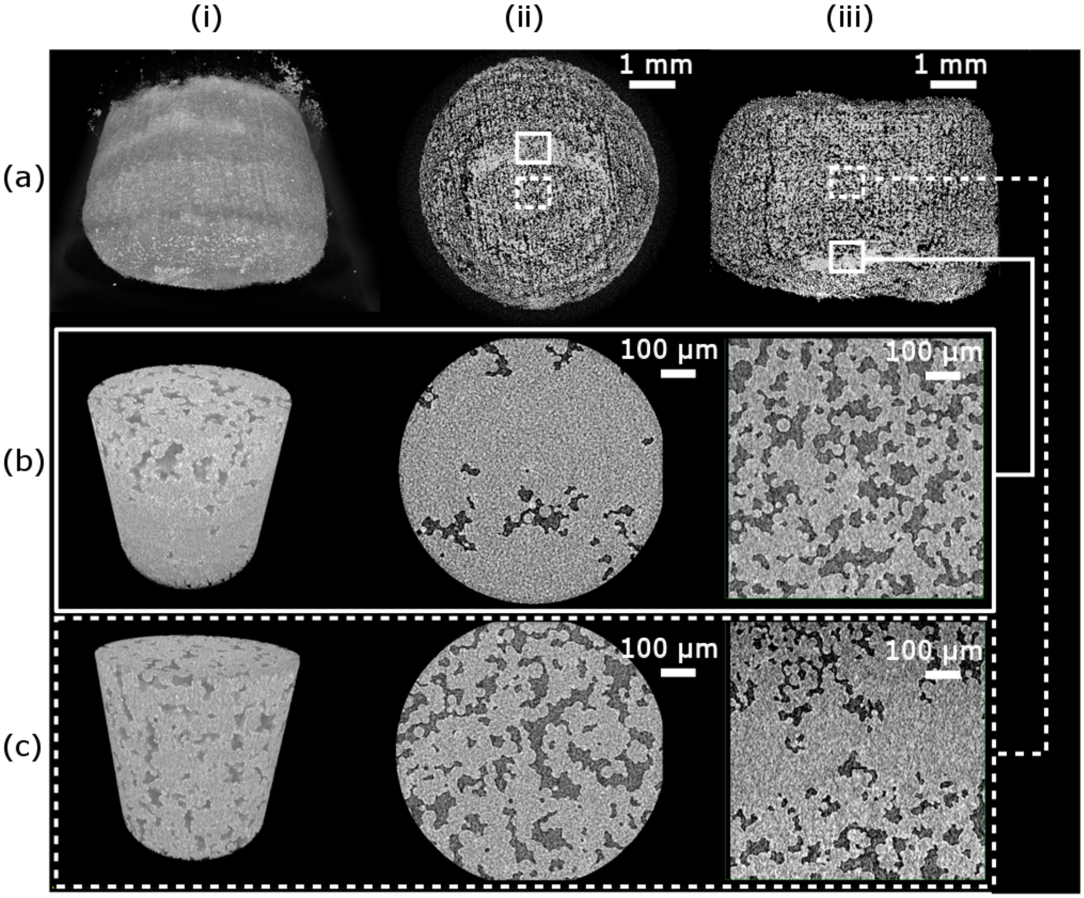

Figure 6.10: CT scan results for the silicone part made via hybrid PBBJ-extrusion system; (a) overall structure, (b) defect region with high particle density; (c) central region with regular particle density; (a-c) (i) 3D view, (ii) top view, (iii) front view; (a) CT scanning resolution: 4.05 μm; (b-c) CT scanning resolution: 1.4 μm.

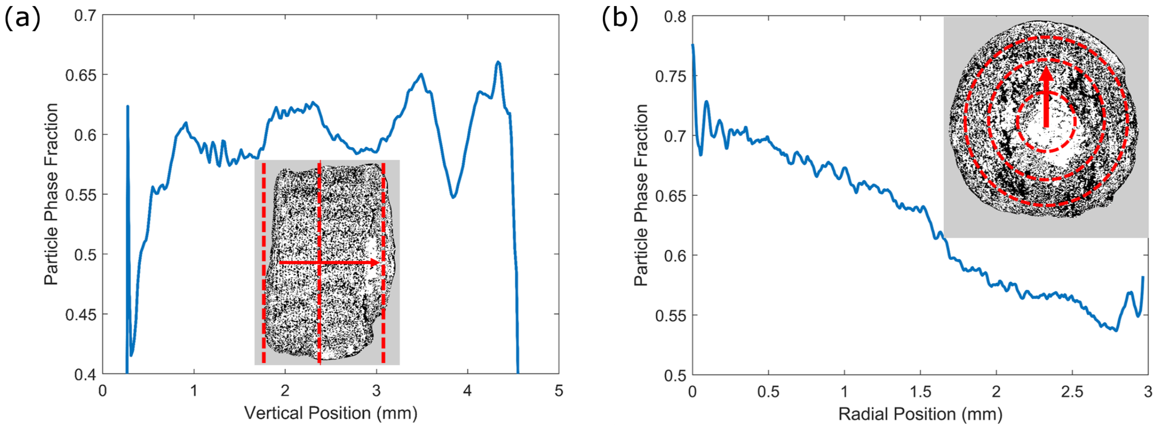

Figure 6.11: Silicone particle phase fraction vs. (a) vertical position and (b) radial position.

riphery of the parts. This is an artefact of the droplet deposition process. When infiltrating polymer solution droplets onto a porous substrate [176], the liquid permeation through the porous powder media is dependent on the droplet kinetics, porosity of the substrate, as well as the wetting angle of the powder material. Considering that the size of the liquid silicone droplet ($\sim 1.54\ mm$) is significantly larger than the average powder particle size used in this study (powder Type A, 30 μm), the dynamic impact kinetics of the traveling droplet and liquid spreading mechanisms of the sessile droplet through the porous media can play a significant role in disturbing the powder [171]. The impact kinetics of the falling droplet can explain the regions of higher powder particle concentration at the bottom of the parts, as particles are displaced vertically [176]. The difference in powder fraction radially, from 75% volume fraction of particles in the centre of the part to 55% at the periphery, can be explained by the theory of droplet primary and secondary liquid spread [171]. In the primary spread, the liquid droplet meets the substrate and starts to imbibe the powder. During this phase, there is an instantaneous flow rate initiated at the liquid-powder interface. This generates a net force acting at the inlet powder boundary, thus particles can be dislodged and can travel within the sessile droplet radially, which may explain the different concentration of particles in the centre of the parts. Overall, the theory seems to suggest that smaller liquid silicone droplets would reduce the powder displacement and likely result in a more uniform component, furthering the need for a better liquid silicone delivery method.

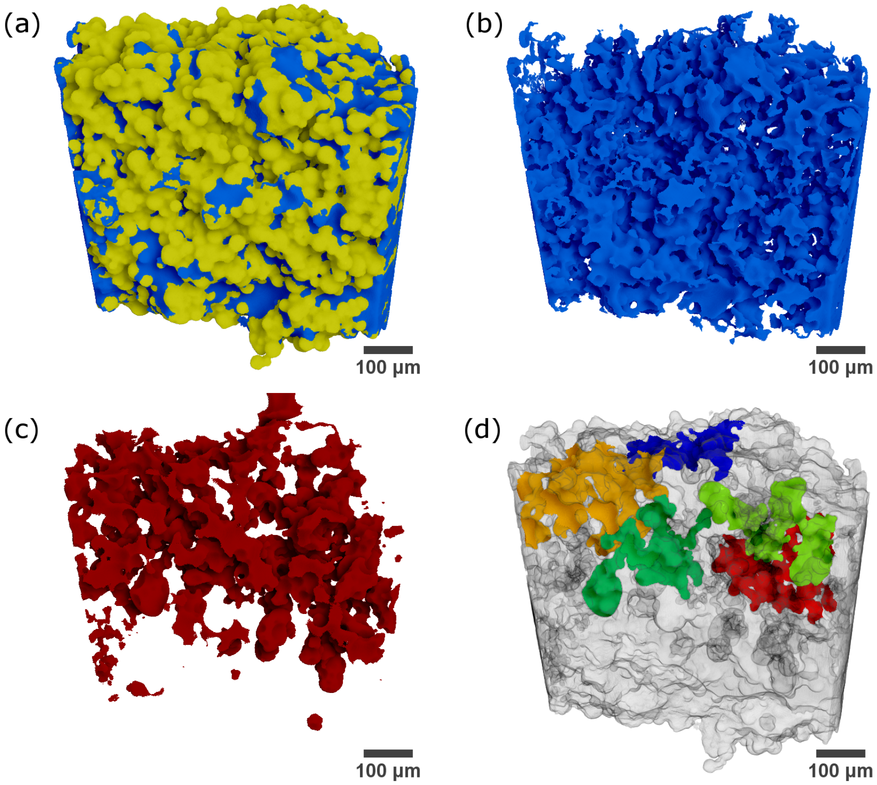

Figure 6.12: Separation of different phases of AM-made structure; (a) yellow: silicone powder, blue: cross-linked silicone binder; (b) isolated cross-linked silicone binder; (c) isolated pores; (d) largest air gaps in the pore network separated with different colors; (a-d) CT scanning resolution: 727 *nm*.

6.3.6 Part Durometry

Two sets of parts were 3D printed at optimized printing conditions (*LT* of 100 μm and *Fr* 1 drop per 300 μm). Three cylindrical parts from each batch were selected for the hardness test. The tests were replicated three times for each part. Similar testing approach was employed for the cured silicone binder molded based on ASTM D2240. The hardness test results are summarized in Table 6.4. The ANOVA study was used to compare the average hardness of AM-made cylinders, the results of which (Table 6.5) failed to show a significant difference between the hardness of the parts.

Table 6.4: The durometry results for the 3D printed cylinders and molded silicone binder ($n = 3$).

Sample	Hardness (Shore 00)			
	test 1	test 2	test 3	Average
Cylinder 1 (batch 1)	80.5	85.6	80.9	82.3
Cylinder 2 (batch 1)	87.3	85.2	82.8	85.1
Cylinder 3 (batch 1)	80.7	80.1	81.5	80.8
Cylinder 1 (batch 2)	81.5	85.3	86	84.3
Cylinder 2 (batch 2)	85.3	84.3	85.2	84.9
Cylinder 3 (batch 2)	80.9	87.8	84.7	84.5
Total average for cylindrical samples				**83.6**
Molded silicone binder 1	81.5	80.1	75.4	79
Molded silicone binder 2	81.2	81.2	79.6	80.7
Total average for molded silicone binder				**79.8**

Table 6.5: ANOVA results for the hardness test.

Source	DF	Adj SS	Adj MS	F-Value	P-Value
Measurements	5	55.49	11.098	2.54	0.086
Error	12	52.47	4.373		
Total	17	107.96			

Similarly, the comparison of average hardness values for the AM-made cylinders and the pure silicone binder using a t-test does not show a statistically significant difference at 95% confidence level (Table 6.6. The average hardness is approximately 83.6 (Shore A) for the 3D printed parts and 79.8 (Shore A) for the crosslinked silicone binder. The hardness of powder A, reported in the materials certificate, is 70 (Shore A).

Table 6.6: Comparing the hardness of 3D printed structures and molded silicone binder using t-test method.

	N	Mean	Std Dev	SE Mean
3D printed structures	6	83.64	1.72	0.7
Molded silicone binder	2	79.84	1.18	0.83

The durometry results for the AM-made samples show that different replicates of the same manufacturing process produce similar durometry results which indicate the reproducibility of the hybrid PBBJ-extrusion process. A full mechanical characterization will be carried out on the products of this AM method in the future. Specifically, the effect of the printing parameters on σ_f, T_s, and ϵ_f [103] should be investigated in order to make any required changes to the system of materials for each particular biomedical application.

6.4 Summary

In this chapter, a novel hybrid method combining PBBJ and deposition techniques for fabrication of 3D structures entirely made from silicone was introduced. Cylindrical samples optimized in terms of geometrical accuracy were showcased. The permeation of silicone binder in the powder bed was sped up by pre-wetting the surface with an aqueous binder. The rapid curing mechanism of the parts was designed based on the thermal analysis of the binder. Guidelines for efficient flowability of silicone powder were provided based on its rheological properties and shear sensitivity. The experimental results indicated that PBBJ technique is capable of processing thermoset powders. The main challenge remaining is integration of a multi-nozzle inkjet printhead compatible with medium to high viscous silicone binders to the system. Such a binder deposition system will increase the AM speed, improves the geometrical accuracy of the final products, and provides higher control over the properties of parts. Upon further improvement in the deposition of silicone binder, this hybrid method could be used for production of structures with the capability of controlled release of fluids for drug-delivery applications.

Chapter 7

Conclusions and Future Work

Development and characterization of additive manufacturing (AM) systems and the associated methodologies for fabrication of silicone structures has been pursued throughout this thesis. To this end, a custom multi-nozzle hybrid three-dimensional (3D) printer based on piezoelectric-pneumatic jetting (PPJ) was designed and developed that can deposit highly viscous silicone inks in a drop-on-demand fashion at high throughput rate, while the well-defined boundary of each layer is laid using a pneumatic micro-dispensing system. Moreover, a manufacturing methodology integrating direct write technologies with powder-bed binder-jetting (PBBJ) was introduced to shape form the silicone powder into a 3D structure for the first time. The effects of process parameters on the mechanical, surface, and internal properties of additively manufactured structures were investigated as well.

In PPJ, the entire structure is deposited in a drop-on-demand fashion. On the other hand, only a portion of structures volume is inkjet printed in PBBJ. Under normal conditions, the jetting of partial volume of the part and support-free fabrication technique should make PBBJ a faster method. However, we only obtained the objective of high speed silicone AM using PPJ method. In PBBJ, the time-consuming silicone binder deposition step using micro-dispensing slows down the process as the high speed of PBBJ process is mostly due to the use of inkjet printheads that have hundreds of orifices which can deposit a considerable volume of fluid as they pass over a large area. In thermal printheads, the evaporation of ink inside the reservoir is the source of energy for jetting. It is obvious that silicone with a high thermal stability (up to 300 °C) is not a good candidate for use in thermal inkjet printheads. Moreover, both piezoelectric and thermal inkjet printheads are limited by the viscosity of inks that can be printed. Silicone inks can be diluted using solvents such as toluene for use in piezoelectric printheads but other complications such as shrinkage might happen after solvent evaporation. The current PPJ printheads have only one orifice too and their high throughput is mainly because of their high translation speed. As a result, the printing speed of the PBBJ technique can be improved by multi-orifice inkjet printheads for materials that experience a viscosity larger than 40 $mPa.s$ at the nozzle. Similar technology can further improve the throughput of PPJ as well.

In terms of the capability of producing heterogeneous structures, the PPJ system is currently able to print up to three materials at a high spatial precision. The number of materials can be increased by addition of printheads. The production of truly material-graded parts with various property profiles; however, is only possible by employment of the multi-orifice systems. In general, material jetting performs better than regular PBBJ systems for production of material-graded structures as it is prohibitive to incorporate hundreds of powder feed chambers into the system but PBBJ excels in rapid fabrication of porous structures.

This thesis contributed to the field of advanced manufacturing by addressing some of the current limitations in 3D printing of soft elastomeric structures through introduction of two systems that can be used to control the internal features of products and fabricate material-graded structures. Moreover, the shortcomings of the proposed systems were pointed out and suggestions for improvement of their speed and flexibility were made.

A summary of the technical conclusions and some of the future work proposed as a continuation to this thesis are provided in this chapter.

7.1 Thesis Conclusions

The following conclusions can be drawn from this thesis:

1. The hybrid extrusion-PPJ system was used successfully to fabricate complex 3D structures composed of multiple materials with various properties. Both extrusion and PPJ systems were capable of depositing a silicone paste with a viscosity of approximately 1.6×10^6 $mPa.s$ (shear rate of 1 s^{-1}) at 25 °C.

2. Irradiance-curable silicones perform better in the context of AM due to their faster crosslinking rate (in the order of a few seconds) compared to heat- or moisture-curable silicones. The light irradiation systems can also be easily integrated into the AM system. Morever, the ink containers and printheads can be protected from the light irradiation much easier than the heat leading to a lower chance of nozzle clogging.

3. According to the statistical optimization conducted, a combination of 100 kPa pressure, 5 mm/s printhead velocity, and 0.2 mm nozzle working distance for a 250 μm nozzle results in dispensing of line features with an average width of 322.8 μm. At 2D level, pressure, working distance, their interaction, and raster width control the surface quality. A combination of higher pressure and lower raster width yields in a lower surface waviness, however, at a risk of increasing the layer thickness through overprinting. 0.1 mm raster width, 200 kPa pressure, and 2 mm working distance generate a surface with a waviness of 3 μm.

4. Among all the process parameters of PPJ system, pulse time, velocity, stroke, and close time have the highest effect on the quality of printed strands of silicone at the investigated region in Chapter 4. According to the statistical optimization conducted, pulse time of 0.4 ms, close time of 0.2 ms, stroke of 86%, and velocity of 97 mm/s result in a uniform line with an average width of 580 μm. Increasing the velocity to 104 mm/s with a raster width of 0.39 mm yields a minimum surface waviness of 8 μm.

5. Due to the lower surface waviness and higher width uniformity of extruded filaments compared to the jetted lines, the perimeter of each layer was printed using the pneumatic extrusion system so that the highest surface quality is obtained.

6. When printing a 3D silicone structure, even with the optimized process parameters, the quality of printed layers might differ as the height increases. This happens mainly due to the build up of the viscous material around the orifice after a certain time. This increases the level of porosity in the parts which leads to their deteriorated mechanical properties. This issue was resolved by tailoring the viscosity and rheology of ink.

7. Control over the internal porosity of parts was achieved by varying the rheology of silicone ink. The ink with a low shear yield stress obtained by mixing polysiloxsnes with short- and long-chain monomers at 45:55 wt.% ratio. This ink flew under the effect of gravity just enough to merge the separated droplets into a uniform line, and resulted in a structure with a relative solid density of 99.65%. This eliminated the porosity introduced to the system as a result of material build up at orifice, deflection of droplets caused by the repulse of like electric charges on the surface of droplets and previously laid layer, and unsuccessful coalesce of viscous droplets.

8. For a silicone ink with dominant solid-like behavior and relatively large shear yield stress, the high level of porosity results in 45.9% and 38.6% decrease in the tensile

strength and elongation at break of the parts made via PPJ, respectively, compared to those of the bulk material. This difference was drastically reduced to 2% for tensile strength and 12.6% for elongation at break by lowering the porosity level through increasing the flowability of ink. Other characteristics such as tear resistance and hardness were not sensitive to the porosity level of the manufactured parts.

9. The hybrid PBBJ-extrusion printing methodology was used successfully to fabricate 3D structures based on silicone powder for the first time. The products are made fully from two different phases of silicone (i.e., powder and crosslinked rubber) as well as a water-based binder which leaves a biocompatible residue after evaporation. Thus, the products of this system can be directly applied to different biomedical applications.
10. The use of a silicone binder with low viscosity ($< 100\ mPa.s$) leads to faster percolation of binder in the powder-bed, and consequently higher manufacturing speed in hybrid PBBJ-extrusion method. Moreover, the pre-wetting of powders with water-based binder helps to speed up this infiltration process even more.
11. The shape and size of silicone particles affects the flow of powder and consequently, the quality of final parts. The use of spherical powder with an average particle size of $30 - 40\ \mu m$ and standard deviation of approximately $30\ \mu m$ is expected to show low shear yield and high flowability.
12. It was established that the parts fabricated via the PBBJ-extrusion system contain 8.2 vol.% air void which are locally interconnected and distributed unevenly throughout the structure. Generally, the structure is more dense at regions of the sample closer to the dispensing point. It can be concluded that the adoption of a method with higher control over the delivery of silicone binder could lead to control of the porosity of products. As a result, the fabrication of parts with variable density profiles from highly porous to fully dense will be possible.

The backbone of both AM methods introduced in this thesis is jetting. There are advantages and disadvantages to both methods; however, the challenges faced by both of them can be resolved through development of a multi-orifice material jetting printhead which can process fluids with various rheological properties from water to paste-like silicone, and mix different materials to adjust the properties of the prepolymer(s) during the print.

7.2 Recommendations and Future Work

The research work described in this thesis was intended to study the feasibility of rapid manufacturing of soft heterogeneous parts made from different phases of silicone which have not been investigated before, namely high viscous paste and powder, through additive methods. To this end, two systems and methods were introduced and characterized. To achieve our intended vision of developing commercially ready systems for additive manufacturing of silicone bio-structures, further research on software, hardware, material systems, and applications should be conducted.

7.2.1 AM of Silicone Based on the PPJ System

1. The use of experimentally-obtained regression models for the prediction of the effect of process parameters on printing quality for every new material and ink seems prohibitive. Even though, the established models in Chapters 3 and 4 can be used for inks with similar behavior to our sample silicone with slight modifications, developing analytical models for prediction of the geometry of viscous non-Newtonian droplets in PPJ techniques is recommended.

2. The developed PPJ system prints silicone structures $10 - 20$ times faster than regular extrusion systems. However, in terms of the speed, it still falls behind the Poly-Jet systems with multi-orifice printheads. As a result, improving the scalibility of this system by redesigning the piezoelectric-pneumatic printheads to include an array of orifices instead of one single orifice increases the chance of industrial adoption of this technique. Furthermore, such a technology can make the fabrication of fully colored bio-structures possible.

3. Tailoring the mechanical properties of silicone for different bio-medical applications based on the rheological guidelines provided in Chapter 5 should be pursued. Moreover, given the fact that irradiance-curable silicones are highly compatible with additive manufacturing systems such as jetting, extrusion, and stereolithography, commercial biocompatible photoinitiators need to be developed.

7.2.2 AM of Silicone Based on the PBBJ System

1. The parts fabricated via the PBBJ-extrusion system, demonstrated overprinting even at optimized process parameters of 100 μm layer thickness, 1 silicone droplet per 300

μm of powder, 20 mm/s linear roller velocity, and 100 rpm rotational roller velocity. In order to improve the geometrical accuracy of parts made via this system the following changes are recommended:

   (a) Replacing the extrusion-based system with a piezoelectric drop-on-demand system for delivering the silicone binder. This facilitates the jetting of droplets at pico-liter order. Coupled with a fast *in-situ* curing system, the overprinting issue as a result of lateral permeation will be resolved. It will also increase the manufacturing speed drastically.

   (b) Mixing the silicone powder with solid additives such as polyvinyl alcohol (PVA) could restrain the overflow of silicone binder.

2. The investigation of the effect of process parameters on the mechanical characteristics and internal porosity of parts is recommended.

Letter of Copyright Permission

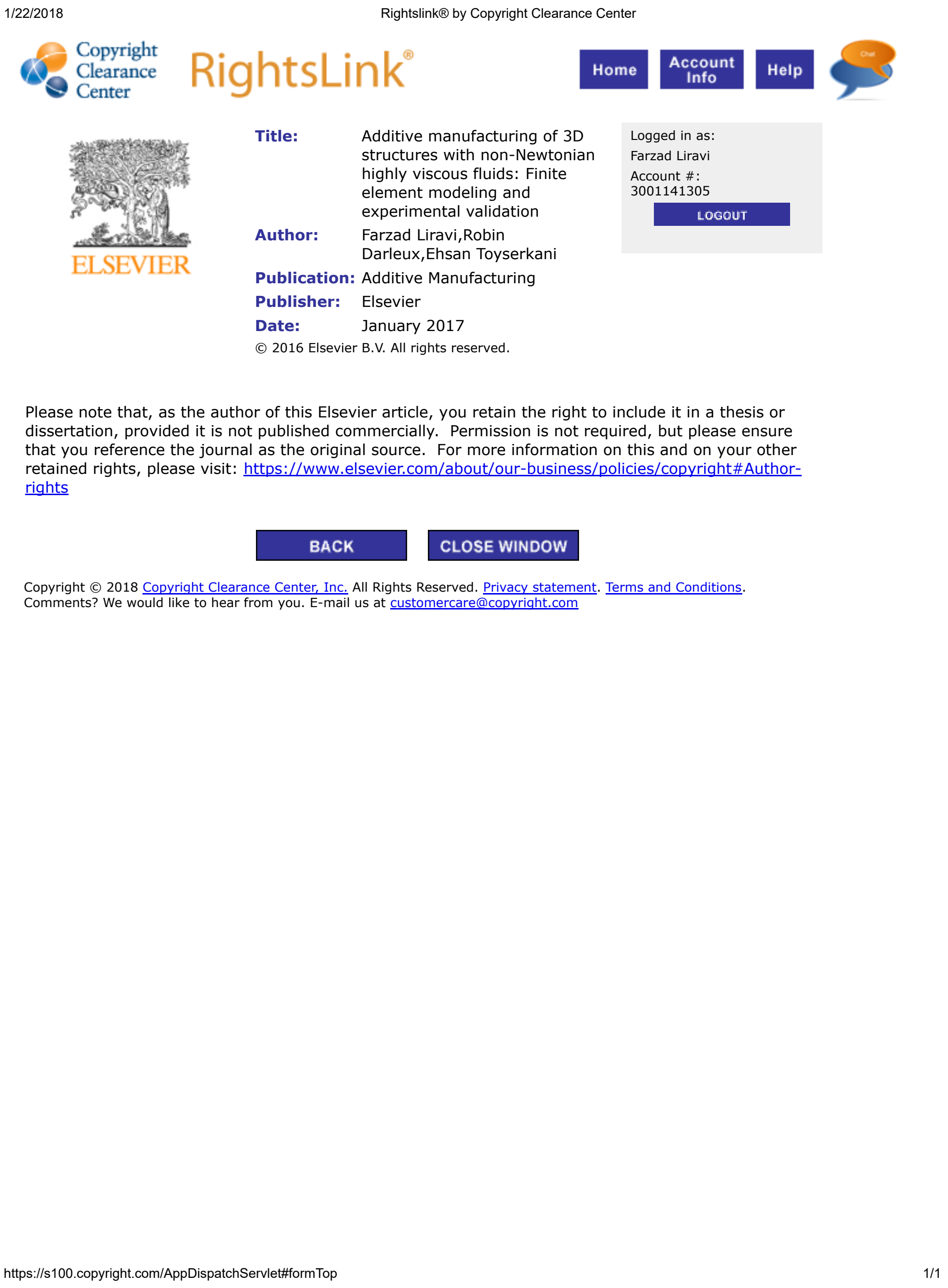

1/22/2018 Rightslink® by Copyright Clearance Center

Title: Additive manufacturing of 3D structures with non-Newtonian highly viscous fluids: Finite element modeling and experimental validation

Author: Farzad Liravi,Robin Darleux,Ehsan Toyserkani

Publication: Additive Manufacturing

Publisher: Elsevier

Date: January 2017

© 2016 Elsevier B.V. All rights reserved.

Logged in as:
Farzad Liravi
Account #:
3001141305

Please note that, as the author of this Elsevier article, you retain the right to include it in a thesis or dissertation, provided it is not published commercially. Permission is not required, but please ensure that you reference the journal as the original source. For more information on this and on your other retained rights, please visit: https://www.elsevier.com/about/our-business/policies/copyright#Author-rights

Copyright © 2018 Copyright Clearance Center, Inc. All Rights Reserved. Privacy statement. Terms and Conditions.
Comments? We would like to hear from you. E-mail us at customercare@copyright.com

https://s100.copyright.com/AppDispatchServlet#formTop 1/1

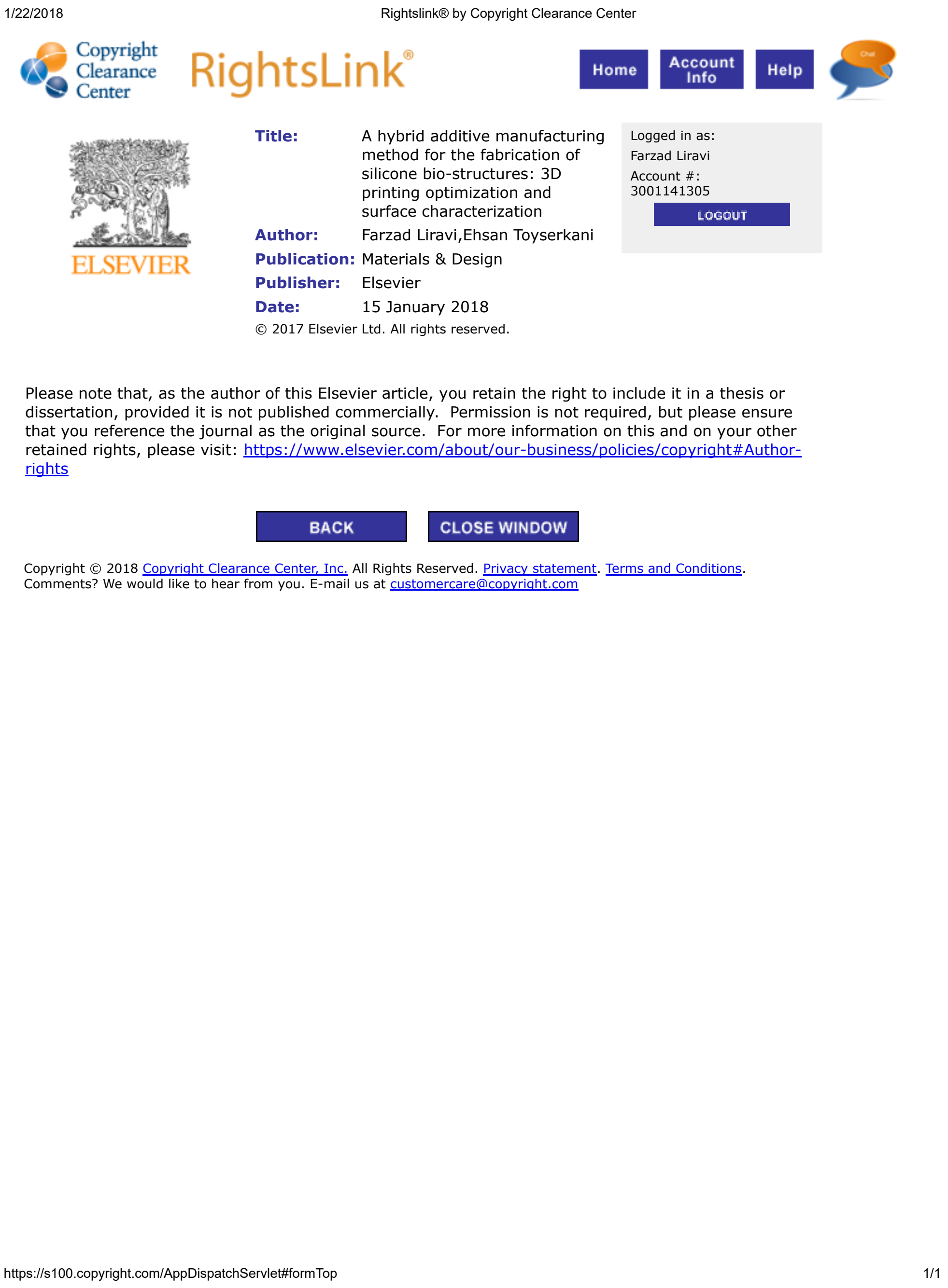

Title:	A hybrid additive manufacturing method for the fabrication of silicone bio-structures: 3D printing optimization and surface characterization
Author:	Farzad Liravi,Ehsan Toyserkani
Publication:	Materials & Design
Publisher:	Elsevier
Date:	15 January 2018

Logged in as:
Farzad Liravi
Account #:
3001141305

Please note that, as the author of this Elsevier article, you retain the right to include it in a thesis or dissertation, provided it is not published commercially. Permission is not required, but please ensure that you reference the journal as the original source. For more information on this and on your other retained rights, please visit: https://www.elsevier.com/about/our-business/policies/copyright#Author-rights

Copyright Clearance Center RightsLink®

Home | Account Info | Help

ACS Publications
Most Trusted. Most Cited. Most Read.

Title: 3D Printed Bionic Ears
Author: Manu S. Mannoor, Ziwen Jiang, Teena James, et al
Publication: Nano Letters
Publisher: American Chemical Society
Date: Jun 1, 2013

Logged in as:
Farzad Liravi
Account #:
3001141305
LOGOUT

PERMISSION/LICENSE IS GRANTED FOR YOUR ORDER AT NO CHARGE

This type of permission/license, instead of the standard Terms & Conditions, is sent to you because no fee is being charged for your order. Please note the following:

- Permission is granted for your request in both print and electronic formats, and translations.
- If figures and/or tables were requested, they may be adapted or used in part.
- Please print this page for your records and send a copy of it to your publisher/graduate school.
- Appropriate credit for the requested material should be given as follows: "Reprinted (adapted) with permission from (COMPLETE REFERENCE CITATION). Copyright (YEAR) American Chemical Society." Insert appropriate information in place of the capitalized words.
- One-time permission is granted only for the use specified in your request. No additional uses are granted (such as derivative works or other editions). For any other uses, please submit a new request.

If credit is given to another source for the material you requested, permission must be obtained from that source.

BACK | CLOSE WINDOW

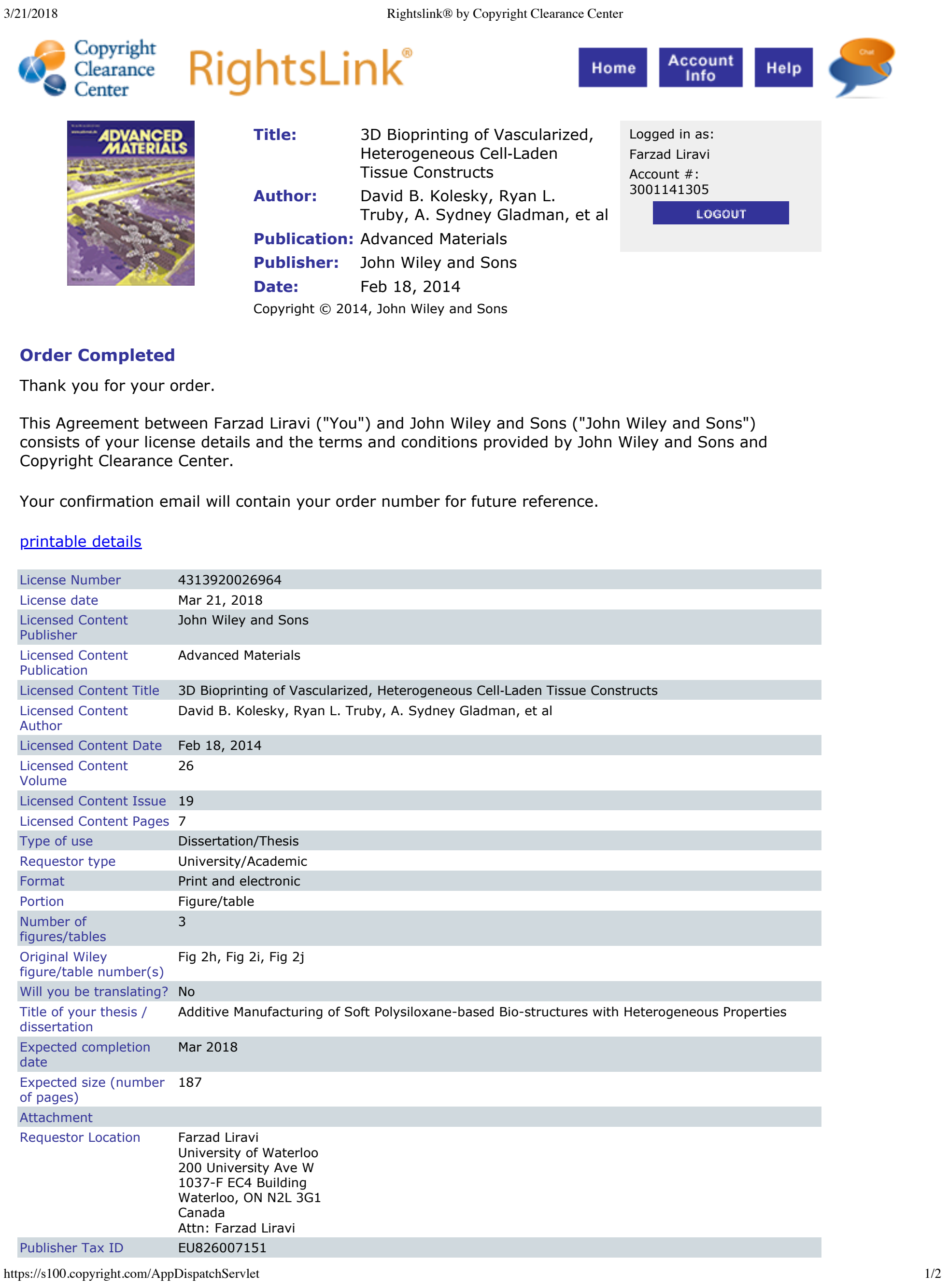

3/21/2018 Rightslink® by Copyright Clearance Center

Title: 3D Bioprinting of Vascularized, Heterogeneous Cell-Laden Tissue Constructs

Author: David B. Kolesky, Ryan L. Truby, A. Sydney Gladman, et al

Publication: Advanced Materials

Publisher: John Wiley and Sons

Date: Feb 18, 2014

Copyright © 2014, John Wiley and Sons

Logged in as:
Farzad Liravi
Account #:
3001141305

Order Completed

Thank you for your order.

This Agreement between Farzad Liravi ("You") and John Wiley and Sons ("John Wiley and Sons") consists of your license details and the terms and conditions provided by John Wiley and Sons and Copyright Clearance Center.

Your confirmation email will contain your order number for future reference.

printable details

License Number	4313920026964
License date	Mar 21, 2018
Licensed Content Publisher	John Wiley and Sons
Licensed Content Publication	Advanced Materials
Licensed Content Title	3D Bioprinting of Vascularized, Heterogeneous Cell-Laden Tissue Constructs
Licensed Content Author	David B. Kolesky, Ryan L. Truby, A. Sydney Gladman, et al
Licensed Content Date	Feb 18, 2014
Licensed Content Volume	26
Licensed Content Issue	19
Licensed Content Pages	7
Type of use	Dissertation/Thesis
Requestor type	University/Academic
Format	Print and electronic
Portion	Figure/table
Number of figures/tables	3
Original Wiley figure/table number(s)	Fig 2h, Fig 2i, Fig 2j
Will you be translating?	No
Title of your thesis / dissertation	Additive Manufacturing of Soft Polysiloxane-based Bio-structures with Heterogeneous Properties
Expected completion date	Mar 2018
Expected size (number of pages)	187
Attachment	
Requestor Location	Farzad Liravi University of Waterloo 200 University Ave W 1037-F EC4 Building Waterloo, ON N2L 3G1 Canada Attn: Farzad Liravi
Publisher Tax ID	EU826007151

https://s100.copyright.com/AppDispatchServlet 1/2

Home (https://www.omicsonline.org/)
Publications (https://www.omicsonline.org/open-access-journals-list.php)
Conferences (https://www.omicsonline.org/international-scientific-conferences/)
Register (https://www.omicsonline.org/register.php)
Contact (https://www.omicsonline.org/contact.php)

in
(https://www.linkedin.com/company/om
publishing
(https://

(https://www.omicsonline.org/anaplastology.php)

ISSN: 2161-1173

Reconstructive Surgery & Anaplastology

Search.. search

Like us on: Like 9.5K

Research Article Open Access

Investigation of Elastomer Infiltration into 3D Printed Facial Soft Tissue Prostheses

Faraedon M Zardawi[1,2], Kaida Xiao[2], Richard van Noort[2] and Julian M Yates[3]*

[1]Department of Periodontology, School of Dentistry, University of Sulaimani, Iraq

[2]Academic Unit of Restorative Dentistry, School of Clinical Dentistry, University of Sheffield, UK

[3]Dept of Oral & Maxillofacial Surgery, School of Dentistry, University of Manchester, UK

***Corresponding Author:**
Julian M Yates
Professor of Oral & Maxillofacial Surgery
The University of Manchester
Room 1.012 - School of Dentistry
Coupland III Building, Coupland Street
Manchester, M13 9PL, UK
Tel: 0044 (0)1612756865
Fax: 0044 (0)1613061565
E-mail: julian.yates@manchester.ac.uk

Received Date: June 04, 2014; **Accepted Date:** November 13, 2014; **Published Date:** November 18, 2014

Citation: Zardawi FM, Kaido X, Noort R, Yates JM (2015) Investigation of Elastomer Infiltration into 3D Printed Facial Soft Tissue Prostheses.Anaplastology 4:139. doi:10.4172/2161-1173.1000139

Visit for more related articles at Reconstructive Surgery & Anaplastology (https://www.omicsonline.org/archive-anaplastology-open-access.php)

3D Printing PDMS Elastomer in a Hydrophilic Support Bath via Freeform Reversible Embedding

Thomas J. Hinton[†], **Andrew Hudson**[†], **Kira Pusch**[‡], **Andrew Lee**[†], **and Adam W. Feinberg**[*][†‡]
[†]Department of Biomedical Engineering and [‡]Department of Materials Science and Engineering, Carnegie Mellon University, 5000 Forbes Avenue, Pittsburgh, Pennsylvania 15213 United States

ACS Biomater. Sci. Eng., **2016**, *2* (10), pp 1781–1786
DOI: 10.1021/acsbiomaterials.6b00170
Publication Date (Web): May 4, 2016
Copyright © 2016 American Chemical Society

*E-mail: feinberg@andrew.cmu.edu.

This article is part of the 3D Bioprinting special issue.

Article Views: 4,144 Times

Received 29 March 2016
Date accepted 4 May 2016
Published online 4 May 2016
Published in print 10 October 2016

Abstract

Polydimethylsiloxane (PDMS) elastomer is used in a wide range of biomaterial applications including microfluidics, cell culture substrates, flexible electronics, and medical devices. However, it has proved challenging to 3D print PDMS in complex structures due to its low elastic modulus and need for support during the printing process. Here we demonstrate the 3D printing of hydrophobic PDMS prepolymer resins within a hydrophilic Carbopol gel support via freeform reversible embedding (FRE). In the FRE printing process, the Carbopol support acts as a Bingham plastic that yields and fluidizes when the syringe tip of the 3D printer moves through it, but acts as a solid for the PDMS extruded within it. This, in combination with the immiscibility of hydrophobic PDMS in the hydrophilic Carbopol, confines the PDMS prepolymer within the support for curing times up to 72 h while maintaining dimensional stability. After printing and curing, the Carbopol support gel releases the embedded PDMS prints by using phosphate buffered saline solution to reduce the Carbopol yield stress. As proof-of-concept, we used Sylgard 184 PDMS to 3D print linear and helical filaments via continuous extrusion and cylindrical and helical tubes via layer-by-layer fabrication. Importantly, we show that the 3D printed tubes were manifold and perfusable. The results demonstrate that hydrophobic polymers with low viscosity and long cure times can be 3D printed using a hydrophilic support, expanding the range of biomaterials that can

Copyright Clearance Center RightsLink® Home Account Info Help

Title: Hydrostatic support-free fabrication of three-dimensional soft structures

Author: Dong Sung (Danny) Kim,Bruce L. Tai

Publication: Journal of Manufacturing Processes

Publisher: Elsevier

Date: October 2016

Logged in as:
Farzad Liravi
Account #:
3001141305
LOGOUT

Order Completed

Thank you for your order.

This Agreement between Farzad Liravi ("You") and Elsevier ("Elsevier") consists of your license details and the terms and conditions provided by Elsevier and Copyright Clearance Center.

Your confirmation email will contain your order number for future reference.

printable details

License Number	4313920330018
License date	Mar 21, 2018
Licensed Content Publisher	Elsevier
Licensed Content Publication	Journal of Manufacturing Processes
Licensed Content Title	Hydrostatic support-free fabrication of three-dimensional soft structures
Licensed Content Author	Dong Sung (Danny) Kim,Bruce L. Tai
Licensed Content Date	Oct 1, 2016
Licensed Content Volume	24
Licensed Content Issue	n/a
Licensed Content Pages	6
Type of Use	reuse in a thesis/dissertation
Portion	figures/tables/illustrations
Number of figures/tables/illustrations	3
Format	both print and electronic
Are you the author of this Elsevier article?	No
Will you be translating?	No
Original figure numbers	Fig 2a, Fig 2b, Fig 7
Title of your thesis/dissertation	Additive Manufacturing of Soft Polysiloxane-based Bio-structures with Heterogeneous Properties
Expected completion date	Mar 2018
Estimated size (number of pages)	187
Attachment	
Requestor Location	Farzad Liravi University of Waterloo 200 University Ave W 1037-F EC4 Building Waterloo, ON N2L 3G1 Canada Attn: Farzad Liravi
Publisher Tax ID	GB 494 6272 12
Total	0.00 CAD

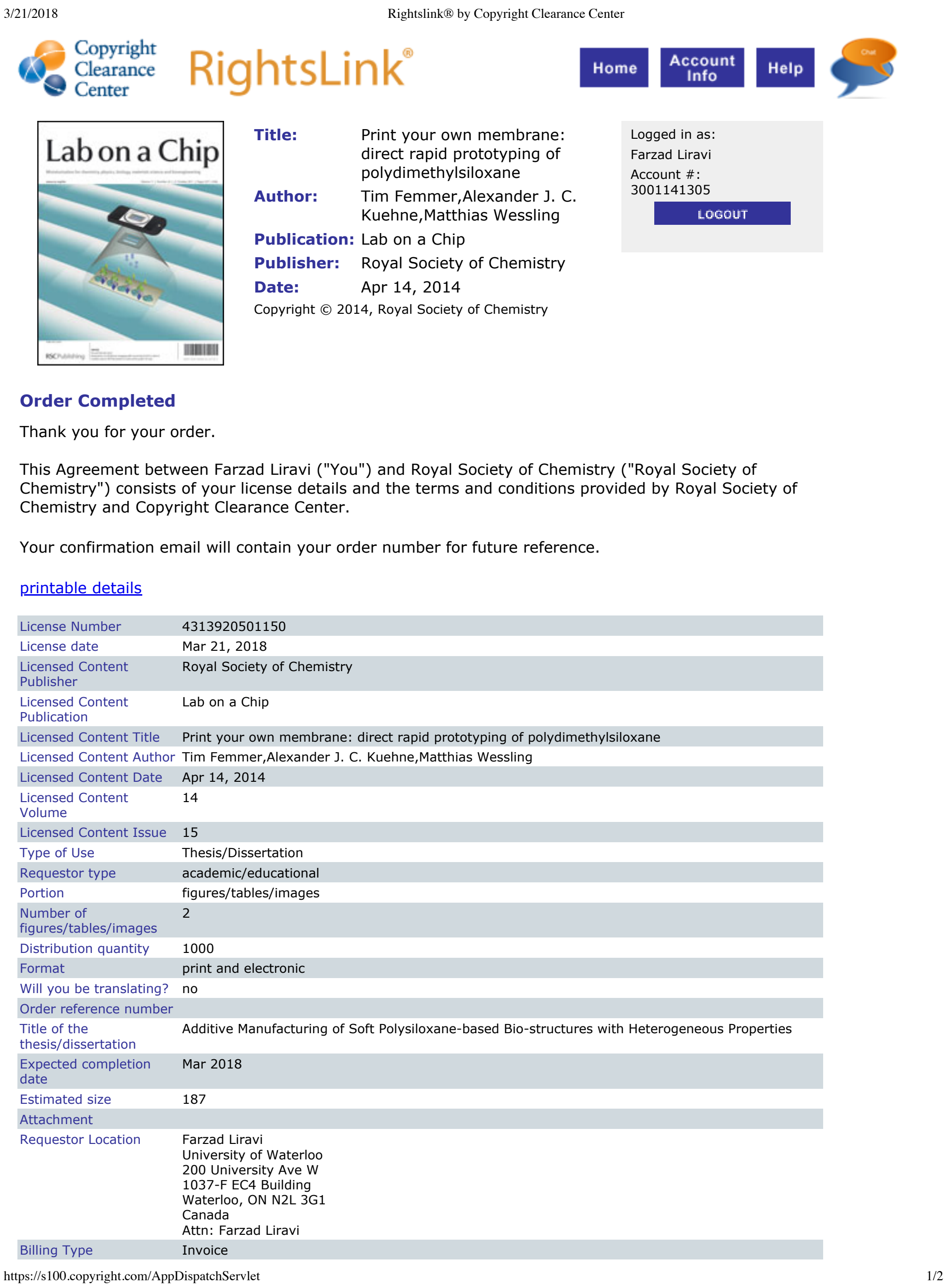

3/21/2018 Rightslink® by Copyright Clearance Center

Title: Print your own membrane: direct rapid prototyping of polydimethylsiloxane
Author: Tim Femmer,Alexander J. C. Kuehne,Matthias Wessling
Publication: Lab on a Chip
Publisher: Royal Society of Chemistry
Date: Apr 14, 2014
Copyright © 2014, Royal Society of Chemistry

Logged in as:
Farzad Liravi
Account #:
3001141305
LOGOUT

Order Completed

Thank you for your order.

This Agreement between Farzad Liravi ("You") and Royal Society of Chemistry ("Royal Society of Chemistry") consists of your license details and the terms and conditions provided by Royal Society of Chemistry and Copyright Clearance Center.

Your confirmation email will contain your order number for future reference.

printable details

License Number	4313920501150
License date	Mar 21, 2018
Licensed Content Publisher	Royal Society of Chemistry
Licensed Content Publication	Lab on a Chip
Licensed Content Title	Print your own membrane: direct rapid prototyping of polydimethylsiloxane
Licensed Content Author	Tim Femmer,Alexander J. C. Kuehne,Matthias Wessling
Licensed Content Date	Apr 14, 2014
Licensed Content Volume	14
Licensed Content Issue	15
Type of Use	Thesis/Dissertation
Requestor type	academic/educational
Portion	figures/tables/images
Number of figures/tables/images	2
Distribution quantity	1000
Format	print and electronic
Will you be translating?	no
Order reference number	
Title of the thesis/dissertation	Additive Manufacturing of Soft Polysiloxane-based Bio-structures with Heterogeneous Properties
Expected completion date	Mar 2018
Estimated size	187
Attachment	
Requestor Location	Farzad Liravi University of Waterloo 200 University Ave W 1037-F EC4 Building Waterloo, ON N2L 3G1 Canada Attn: Farzad Liravi
Billing Type	Invoice

https://s100.copyright.com/AppDispatchServlet 1/2

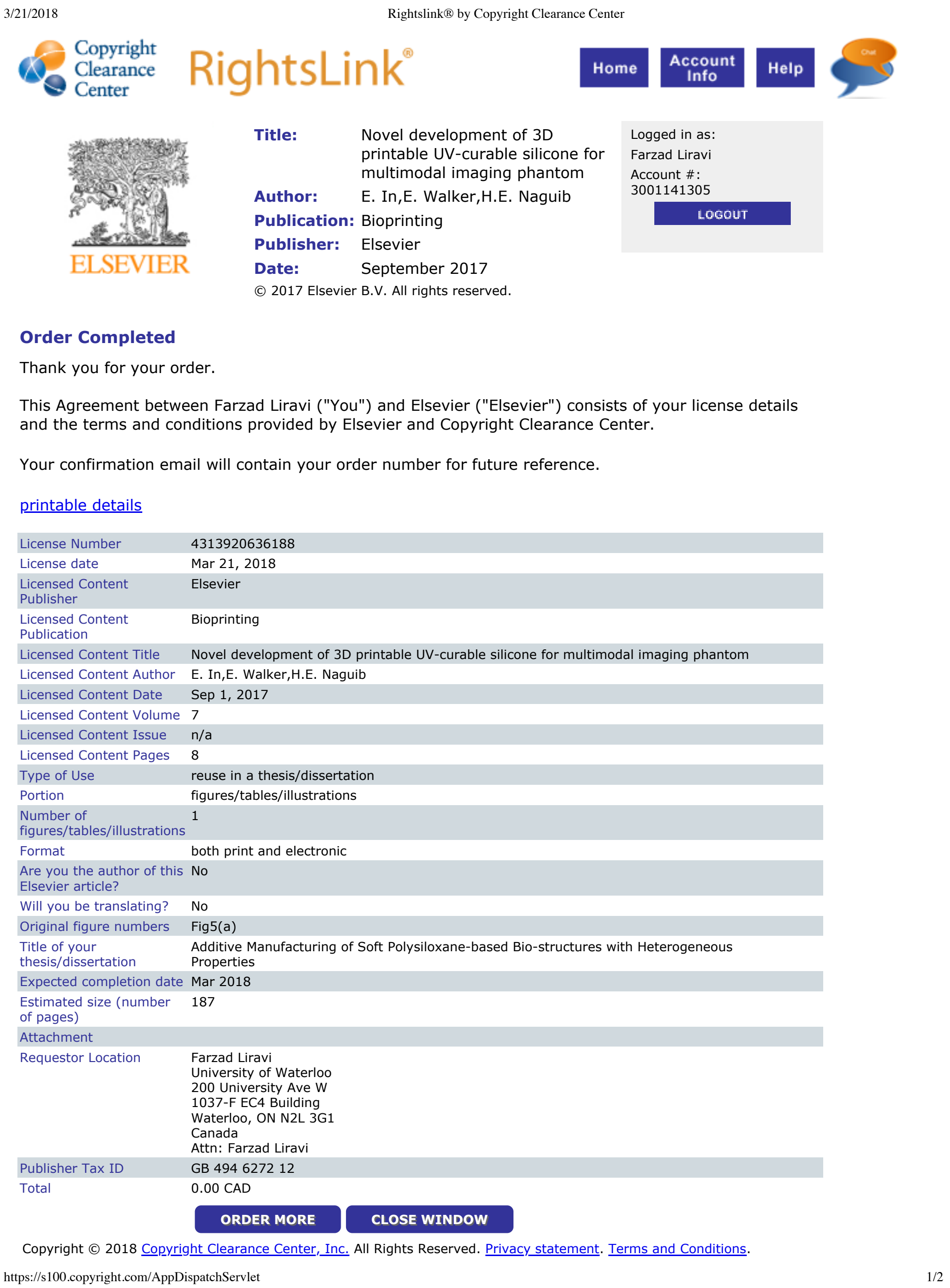

3/21/2018 Rightslink® by Copyright Clearance Center

Title: Novel development of 3D printable UV-curable silicone for multimodal imaging phantom
Author: E. In,E. Walker,H.E. Naguib
Publication: Bioprinting
Publisher: Elsevier
Date: September 2017

Logged in as:
Farzad Liravi
Account #:
3001141305

Order Completed

Thank you for your order.

This Agreement between Farzad Liravi ("You") and Elsevier ("Elsevier") consists of your license details and the terms and conditions provided by Elsevier and Copyright Clearance Center.

Your confirmation email will contain your order number for future reference.

printable details

License Number	4313920636188
License date	Mar 21, 2018
Licensed Content Publisher	Elsevier
Licensed Content Publication	Bioprinting
Licensed Content Title	Novel development of 3D printable UV-curable silicone for multimodal imaging phantom
Licensed Content Author	E. In,E. Walker,H.E. Naguib
Licensed Content Date	Sep 1, 2017
Licensed Content Volume	7
Licensed Content Issue	n/a
Licensed Content Pages	8
Type of Use	reuse in a thesis/dissertation
Portion	figures/tables/illustrations
Number of figures/tables/illustrations	1
Format	both print and electronic
Are you the author of this Elsevier article?	No
Will you be translating?	No
Original figure numbers	Fig5(a)
Title of your thesis/dissertation	Additive Manufacturing of Soft Polysiloxane-based Bio-structures with Heterogeneous Properties
Expected completion date	Mar 2018
Estimated size (number of pages)	187
Attachment	
Requestor Location	Farzad Liravi University of Waterloo 200 University Ave W 1037-F EC4 Building Waterloo, ON N2L 3G1 Canada Attn: Farzad Liravi
Publisher Tax ID	GB 494 6272 12
Total	0.00 CAD

https://s100.copyright.com/AppDispatchServlet 1/2

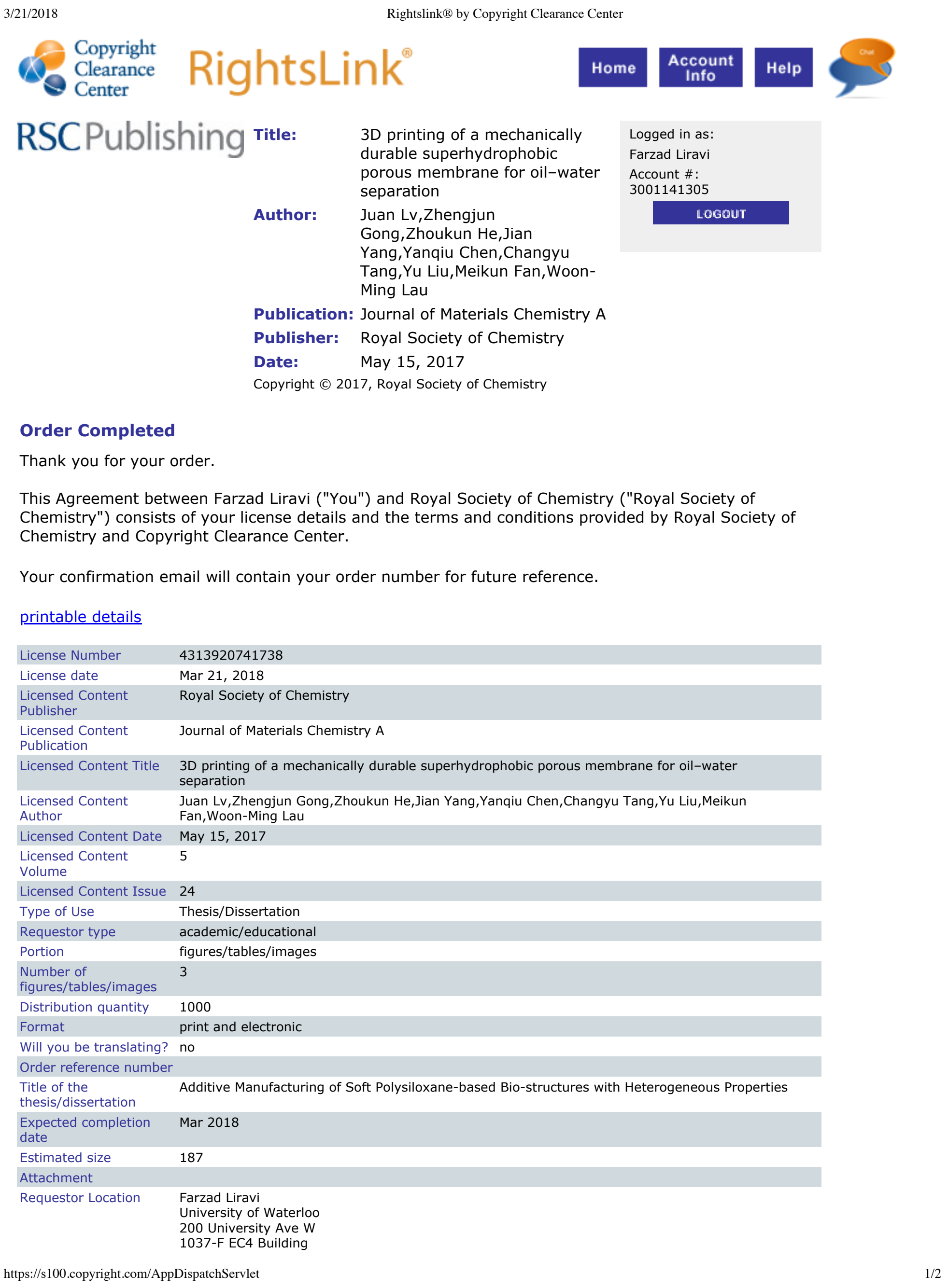

3/21/2018 Rightslink® by Copyright Clearance Center

Title:	3D printing of a mechanically durable superhydrophobic porous membrane for oil–water separation
Author:	Juan Lv,Zhengjun Gong,Zhoukun He,Jian Yang,Yanqiu Chen,Changyu Tang,Yu Liu,Meikun Fan,Woon-Ming Lau
Publication:	Journal of Materials Chemistry A
Publisher:	Royal Society of Chemistry
Date:	May 15, 2017

Copyright © 2017, Royal Society of Chemistry

Logged in as:
Farzad Liravi
Account #:
3001141305

Order Completed

Thank you for your order.

This Agreement between Farzad Liravi ("You") and Royal Society of Chemistry ("Royal Society of Chemistry") consists of your license details and the terms and conditions provided by Royal Society of Chemistry and Copyright Clearance Center.

Your confirmation email will contain your order number for future reference.

printable details

License Number	4313920741738
License date	Mar 21, 2018
Licensed Content Publisher	Royal Society of Chemistry
Licensed Content Publication	Journal of Materials Chemistry A
Licensed Content Title	3D printing of a mechanically durable superhydrophobic porous membrane for oil–water separation
Licensed Content Author	Juan Lv,Zhengjun Gong,Zhoukun He,Jian Yang,Yanqiu Chen,Changyu Tang,Yu Liu,Meikun Fan,Woon-Ming Lau
Licensed Content Date	May 15, 2017
Licensed Content Volume	5
Licensed Content Issue	24
Type of Use	Thesis/Dissertation
Requestor type	academic/educational
Portion	figures/tables/images
Number of figures/tables/images	3
Distribution quantity	1000
Format	print and electronic
Will you be translating?	no
Order reference number	
Title of the thesis/dissertation	Additive Manufacturing of Soft Polysiloxane-based Bio-structures with Heterogeneous Properties
Expected completion date	Mar 2018
Estimated size	187
Attachment	
Requestor Location	Farzad Liravi University of Waterloo 200 University Ave W 1037-F EC4 Building

https://s100.copyright.com/AppDispatchServlet 1/2

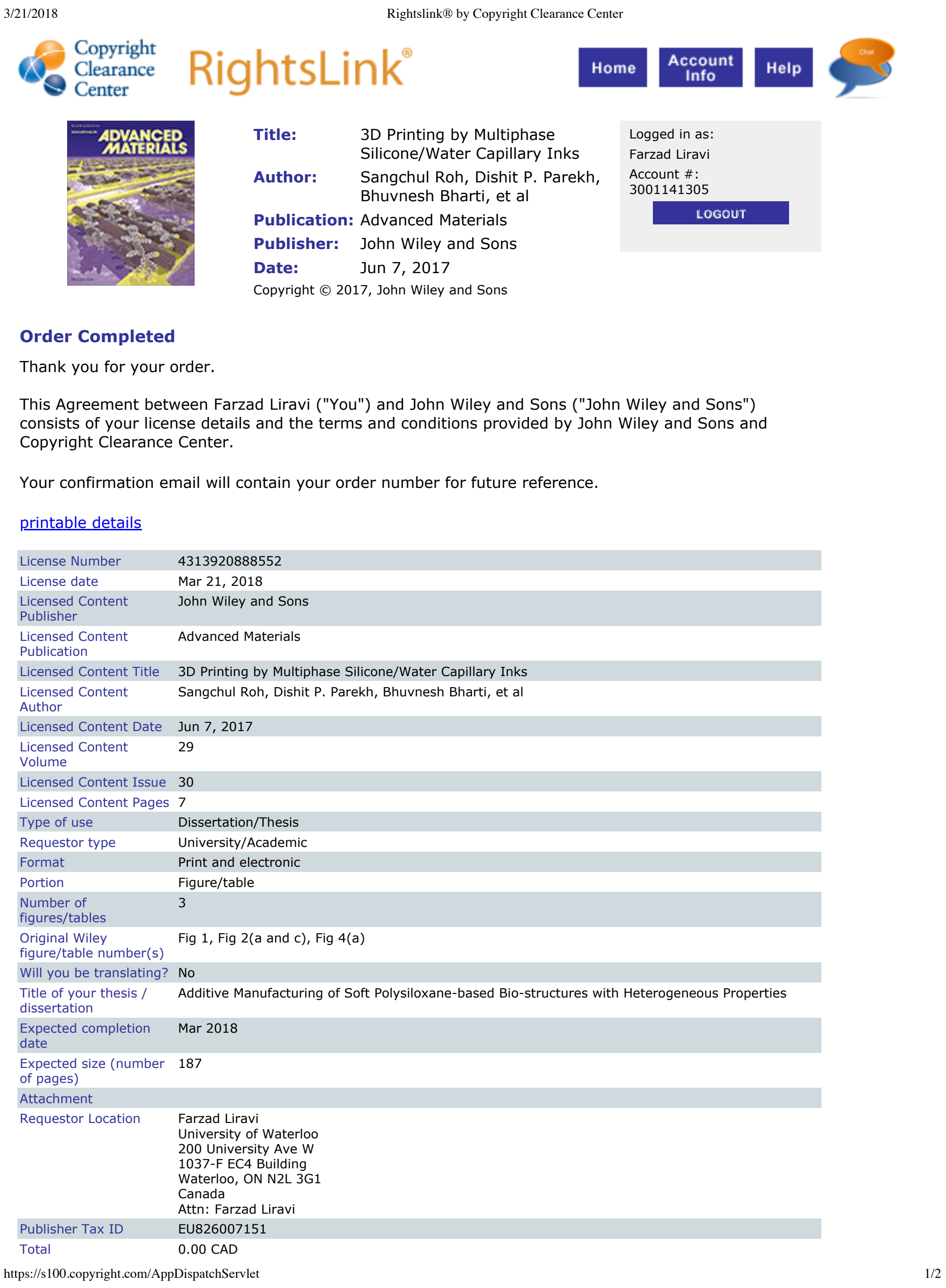

3/21/2018 Rightslink® by Copyright Clearance Center

Title: 3D Printing by Multiphase Silicone/Water Capillary Inks

Author: Sangchul Roh, Dishit P. Parekh, Bhuvnesh Bharti, et al

Publication: Advanced Materials

Publisher: John Wiley and Sons

Date: Jun 7, 2017

Copyright © 2017, John Wiley and Sons

Logged in as:
Farzad Liravi
Account #:
3001141305

Order Completed

Thank you for your order.

This Agreement between Farzad Liravi ("You") and John Wiley and Sons ("John Wiley and Sons") consists of your license details and the terms and conditions provided by John Wiley and Sons and Copyright Clearance Center.

Your confirmation email will contain your order number for future reference.

printable details

License Number	4313920888552
License date	Mar 21, 2018
Licensed Content Publisher	John Wiley and Sons
Licensed Content Publication	Advanced Materials
Licensed Content Title	3D Printing by Multiphase Silicone/Water Capillary Inks
Licensed Content Author	Sangchul Roh, Dishit P. Parekh, Bhuvnesh Bharti, et al
Licensed Content Date	Jun 7, 2017
Licensed Content Volume	29
Licensed Content Issue	30
Licensed Content Pages	7
Type of use	Dissertation/Thesis
Requestor type	University/Academic
Format	Print and electronic
Portion	Figure/table
Number of figures/tables	3
Original Wiley figure/table number(s)	Fig 1, Fig 2(a and c), Fig 4(a)
Will you be translating?	No
Title of your thesis / dissertation	Additive Manufacturing of Soft Polysiloxane-based Bio-structures with Heterogeneous Properties
Expected completion date	Mar 2018
Expected size (number of pages)	187
Attachment	
Requestor Location	Farzad Liravi University of Waterloo 200 University Ave W 1037-F EC4 Building Waterloo, ON N2L 3G1 Canada Attn: Farzad Liravi
Publisher Tax ID	EU826007151
Total	0.00 CAD

https://s100.copyright.com/AppDispatchServlet 1/2

Copyright Clearance Center RightsLink®

Home Account Info Help

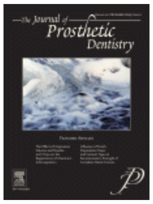

Title: Development of a 3D printable maxillofacial silicone: Part I. Optimization of polydimethylsiloxane chains and cross-linker concentration

Author: Swati K. Jindal,Martyn Sherriff,Mark G. Waters,Trevor J. Coward

Publication: The Journal of Prosthetic Dentistry

Publisher: Elsevier

Date: October 2016

Logged in as:
Farzad Liravi
Account #:
3001141305
LOGOUT

Order Completed

Thank you for your order.

This Agreement between Farzad Liravi ("You") and Elsevier ("Elsevier") consists of your license details and the terms and conditions provided by Elsevier and Copyright Clearance Center.

Your confirmation email will contain your order number for future reference.

printable details

License Number	4313920997021
License date	Mar 21, 2018
Licensed Content Publisher	Elsevier
Licensed Content Publication	The Journal of Prosthetic Dentistry
Licensed Content Title	Development of a 3D printable maxillofacial silicone: Part I. Optimization of polydimethylsiloxane chains and cross-linker concentration
Licensed Content Author	Swati K. Jindal,Martyn Sherriff,Mark G. Waters,Trevor J. Coward
Licensed Content Date	Oct 1, 2016
Licensed Content Volume	116
Licensed Content Issue	4
Licensed Content Pages	6
Type of Use	reuse in a thesis/dissertation
Portion	figures/tables/illustrations
Number of figures/tables/illustrations	2
Format	both print and electronic
Are you the author of this Elsevier article?	No
Will you be translating?	No
Original figure numbers	Table 2, Table 4
Title of your thesis/dissertation	Additive Manufacturing of Soft Polysiloxane-based Bio-structures with Heterogeneous Properties
Expected completion date	Mar 2018
Estimated size (number of pages)	187
Attachment	
Requestor Location	Farzad Liravi University of Waterloo 200 University Ave W 1037-F EC4 Building Waterloo, ON N2L 3G1

References

[1] W. Noll. *Chemistry and technology of silicones.* Elsevier, 2012.

[2] A. Cracchiolo, J. B. Weltmer Jr, G. Lian, T. Dalseth, and F. Dorey. Arthroplasty of the first metatarsophalangeal joint with a double-stem silicone implant. results in patients who have degenerative joint disease failure of previous operations, or rheumatoid arthritis. *The Journal of bone and joint surgery.American volume*, 74(4):552–563, Apr 1992.

[3] A. B. Swanson, S. H. Jaeger, and D. La Rochelle. Comminuted fractures of the radial head. the role of silicone-implant replacement arthroplasty. *The Journal of bone and joint surgery.American volume*, 63(7):1039–1049, Sep 1981.

[4] M. Belachew, M-J Legrand, TH Defechereux, M-P Burtheret, and N. Jacquet. Laparoscopic adjustable silicone gastric banding in the treatment of morbid obesity. *Surgical endoscopy*, 8(11):1354–1356, 1994.

[5] R. Carmen and S. C. Mutha. Lipid absorption by silicone heart valve poppetsinvivo and invitro results. *Journal of Biomedical Materials Research*, 6(5):327–346, 1972.

[6] M. A. Erlich and A. Parhiscar. Nasal dorsal augmentation with silicone implants. *Facial plastic surgery*, 19(04):325–330, 2003.

[7] D. P. Gorczyca, S. Sinha, C. Y. Ahn, N. D. DeBruhl, M. K. Hayes, V. R. Gausche, W. W. Shaw, and L. W. Bassett. Silicone breast implants in vivo: Mr imaging. *Radiology*, 185(2):407–410, Nov 1992.

[8] L. W. Luria. The role of medical grade silicones in surgery and its topical applications. *Operative Techniques in Plastic and Reconstructive Surgery*, 9(2):67–74, 2002.

[9] S. CN Chang, J. A. Rowley, G. Tobias, N. G. Genes, A. K. Roy, D. J. Mooney, C. A. Vacanti, and L. J. Bonassar. Injection molding of chondrocyte/alginate constructs in

the shape of facial implants. *Journal of Biomedical Materials Research*, 55(4):503–511, 2001.

[10] M. D. Timmer, C. Carter, C. G. Ambrose, and A. G. Mikos. Fabrication of poly (propylene fumarate)-based orthopaedic implants by photo-crosslinking through transparent silicone molds. *Biomaterials*, 24(25):4707–4714, 2003.

[11] R. Remmers, D. Cook, and V. Gervasi. Custom, integrated, pneumatic, rotary actuator for an active ankle-foot orthosis. In *2010 SFF Symposium Proceedings, Austin, TX*, pages 816–827, 2010.

[12] M. Salmi, K. Paloheimo, J. Tuomi, J. Wolff, and A. Makitie. Accuracy of medical models made by additive manufacturing (rapid manufacturing). *Journal of Cranio-Maxillofacial Surgery*, 41(7):603–609, 2013.

[13] D. Bourell, B. Stucker, D. Cook, V. Gervasi, R. Rizza, S. Kamara, and X. Liu. Additive fabrication of custom pedorthoses for clubfoot correction. *Rapid Prototyping Journal*, 16(3):189–193, 2010.

[14] I. Drstvensek, B. Valentan, T. Brajlih, T. Strojnik, and N. Ihan Hren. Direct digital manufacturing as communication and implantation tool in medicine. In *US-TURKEY Workshop On Rapid Technologies, September*, volume 24, pages 75–81, 2009.

[15] M. Salmi. Medical applications of additive manufacturing in surgery and dental care. 2013.

[16] P. Maguire and C. M. Parkes. Surgery and loss of body parts. *BMJ (Clinical research ed.)*, 316(7137):1086–1088, Apr 4 1998.

[17] C. M. Parkes. Psycho-social transitions: comparison between reactions to loss of a limb and loss of a spouse. *The British journal of psychiatry : the journal of mental science*, 127:204–210, Sep 1975.

[18] M. C. Goiato, A. A. Pesqueira, C. R. da Silva, H. G. Filho, and D. M. Dos Santos. Patient satisfaction with maxillofacial prosthesis. literature review. *Journal of Plastic, Reconstructive & Aesthetic Surgery*, 62(2):175–180, 2009.

[19] J. C. Lemon, S. Kiat-amnuay, L. Gettleman, J. W. Martin, and M. S. Chambers. Facial prosthetic rehabilitation: preprosthetic surgical techniques and biomaterials. *Current Opinion in Otolaryngology & Head and Neck Surgery*, 13(4):255–262, Aug 2005.

[20] T. Chang, N. Garrett, E. Roumanas, and J. Beumer. Treatment satisfaction with facial prostheses. *The Journal of prosthetic dentistry*, 94(3):275–280, 2005.

[21] K. Xiao, F. Zardawi, R. van Noort, and J. M. Yates. Developing a 3d colour image reproduction system for additive manufacturing of facial prostheses. *The International Journal of Advanced Manufacturing Technology*, 70(9-12):2043–2049, 2014.

[22] L. H. Chen, S. Tsutsumi, and T. Iizuka. A cad/cam technique for fabricating facial prostheses: a preliminary report. *The International journal of prosthodontics*, 10(5):467–472, Sep-Oct 1997.

[23] M. O. Karatas, E. D. Cifter, D. O. Ozenen, A. Balik, and E. B. Tuncer. Manufacturing implant supported auricular prostheses by rapid prototyping techniques. *European journal of dentistry*, 5(4):472–477, Aug 2011.

[24] M. Tsuji, N. Noguchi, K. Ihara, Y. Yamashita, M. Shikimori, and M. Goto. Fabrication of a maxillofacial prosthesis using a computeraided design and manufacturing system. *Journal of Prosthodontics*, 13(3):179–183, 2004.

[25] A. Chandra, J. Watson, J. E. Rowson, J. H., R. A. Harris, and D. J. Williams. Application of rapid manufacturing techniques in support of maxillofacial treatment: evidence of the requirements of clinical applications. *Proceedings of the Institution of Mechanical Engineers, Part B: Journal of Engineering Manufacture*, 219(6):469–475, 2005.

[26] F. Liravi, R. Darleux, and E. Toyserkani. Nozzle dispensing additive manufacturing of polysiloxane: dimensional control. *International Journal of Rapid Manufacturing*, 5(1):20–43, 2015.

[27] F. Liravi, R. Darleux, and E. Toyserkani. Additive manufacturing of 3d structures with non-newtonian highly viscous fluids: Finite element modeling and experimental validation. *Additive Manufacturing*, 13:113–123, 2017.

[28] F. Liravi and E. Toyserkani. A hybrid additive manufacturing method for the fabrication of silicone bio-structures: 3d printing optimization and surface characterization. *Materials & Design*, 138:46–61, 2017.

[29] F. Liravi and M. Vlasea. Powder bed binder jetting additive manufacturing of silicone structures. *Additive Manufacturing*, 2018.

[30] S. Braley. The chemistry and properties of the medical-grade silicones. *Journal of Macromolecular ScienceChemistry*, 4(3):529–544, 1970.

[31] S. J. Clarson and J. A. Semlyen. *Siloxane polymers*. Prentice Hall, 1993.

[32] R. G. Jones, W.u Ando, and J. Chojnowski. *Silicon-containing polymers: the science and technology of their synthesis and applications*. Springer Science & Business Media, 2013.

[33] S. J. Clarson. *Synthesis and properties of silicones and silicone-modified materials*. American Chemical Society, 2003.

[34] R. A. Rhein. *Thermally stable elastomers: A review*, 1983.

[35] D. Eggbeer, R. Bibb, P. Evans, and L. Ji. Evaluation of direct and indirect additive manufacture of maxillofacial prostheses. *Proceedings of the Institution of Mechanical Engineers.Part H, Journal of engineering in medicine*, 226(9):718–728, Sep 2012.

[36] D. Palousek, J. Rosicky, and D. Koutny. Use of digital technologies for nasal prosthesis manufacturing. *Prosthetics and orthotics international*, 38(2):171–175, Apr 2014.

[37] J. Sun and F. Zhang. The application of rapid prototyping in prosthodontics. *Journal of Prosthodontics*, 21(8):641–644, 2012.

[38] J. Abduo, K. Lyons, and M. Bennamoun. Trends in computer-aided manufacturing in prosthodontics: a review of the available streams. *International journal of dentistry*, 2014:783948, 2014.

[39] T. Jiao, C. Zhu, X. Dong, and X. Gu. Rehabilitation of maxillectomy defects with obturator prostheses fabricated using computer-aided design and rapid prototyping: a pilot study. *The International journal of prosthodontics*, 27(5):480–486, Sep-Oct 2014.

[40] A. A. Laghi. *Multi hardness silicone implants*, 1992.

[41] S. Bai, Z. Feng, R. Gao, Y. Dong, Y. Bi, G. Wu, and X. Chen. Development and application of a rapid rehabilitation system for reconstruction of maxillofacial soft-tissue defects related to war and traumatic injuries. *Military Medical Research*, 1(1):11, 2014.

[42] P. Liacouras, J. Garnes, N. Roman, A. Petrich, and G. T. Grant. Designing and manufacturing an auricular prosthesis using computed tomography, 3-dimensional photographic imaging, and additive manufacturing: a clinical report. *The Journal of prosthetic dentistry*, 105(2):78–82, 2011.

[43] C. L. Morris, R. F. Barber, and R. Day. Orofacial prosthesis design and fabrication using stereolithography. *Australian Dental Journal*, 45(4):250–253, 2000.

[44] G. Wu, B. Zhou, Y. Bi, and Y. Zhao. Selective laser sintering technology for customized fabrication of facial prostheses. *The Journal of prosthetic dentistry*, 100(1):56–60, 2008.

[45] F. Yoshioka, S. Ozawa, S. Okazaki, and Y. Tanaka. Fabrication of an orbital prosthesis using a noncontact threedimensional digitizer and rapidprototyping system. *Journal of Prosthodontics*, 19(8):598–600, 2010.

[46] M. Al Mardini, C. Ercoli, and G. N. Graser. A technique to produce a mirror-image wax pattern of an ear using rapid prototyping technology. *The Journal of prosthetic dentistry*, 94(2):195–198, 2005.

[47] N. H. Cohrs, A. Petrou, M. Loepfe, M. Yliruka, C. M. Schumacher, A. X. Kohll, C. T. Starck, M. Schmid Daners, M. Meboldt, and V. Falk. A soft total artificial heartfirst concept evaluation on a hybrid mock circulation. *Artificial Organs*, 2017.

[48] O. Ginty, J. Moore, T. Peters, and D. Bainbridge. Modelling patient-specific deformable mitral valves. *Journal of cardiothoracic and vascular anesthesia*, 2017.

[49] R. Bibb, D. Eggbeer, and P. Evans. Rapid prototyping technologies in soft tissue facial prosthetics: current state of the art. *Rapid Prototyping Journal*, 16(2):130–137, 2010.

[50] R. Van Noort, J. Yates, T. Fripp, and D. Wildgoose. Method and system for producing prostheses, 2012.

[51] F. M Zardawi. Characterisation of implant supported soft tissue prostheses produced with 3d colour printing technology. 2013.

[52] F. M. Zardawi, K. Xiao, R. Van Noort, and J. M. Yates. Investigation of elastomer infiltration into 3d printed facial soft tissue prostheses. *Anaplastology*, 4(139):2161–1173, 2015.

[53] S. V. Murphy and A. Atala. 3d bioprinting of tissues and organs. *Nature biotechnology*, 32(8):773–785, 2014.

[54] C. C. Chang, E. D. B., S. K. Williams, and J. B. Hoying. Directwrite bioprinting threedimensional biohybrid systems for future regenerative therapies. *Journal of Biomedical Materials Research Part B: Applied Biomaterials*, 98(1):160–170, 2011.

[55] M. G. Li, X. Y. Tian, and X. B. Chen. A brief review of dispensing-based rapid prototyping techniques in tissue scaffold fabrication: role of modeling on scaffold properties prediction. *Biofabrication*, 1(3):032001, 2009.

[56] F. P. Melchels, J. F., and D. W. Grijpma. A review on stereolithography and its applications in biomedical engineering. *Biomaterials*, 31(24):6121–6130, 2010.

[57] E. Selbertinger, F. Achenbach, and B. Pachaly. *Method for producing silicone elastomer parts*, 2015.

[58] I. Gibson, D. W. Rosen, and B. Stucker. *Additive manufacturing technologies.* Springer, 2010.

[59] M. Vaezi, H. Seitz, and S. Yang. A review on 3d micro-additive manufacturing technologies. *The International Journal of Advanced Manufacturing Technology*, 67(5-8):1721–1754, 2013.

[60] Y. Jin, J. Plott, and A. J. Shih. Extrusion-based additive manufacturing of the moisture-cured silicone elastomer. In *International Solid Freeform Fabrication Symposium.* Laboratory for Freeform Fabrication and the University of Texas Austin, TX, USA, 2015.

[61] M. S. Mannoor, Z. Jiang, T. James, Y. Lin Kong, Karen A. Malatesta, Winston O. Soboyejo, Naveen Verma, David H. Gracias, and Michael C. McAlpine. 3d printed bionic ears. *Nano letters*, 13(6):2634–2639, 2013.

[62] E. B. Duoss, T. H. Weisgraber, K. Hearon, C. Zhu, W. Small, T. R. Metz, J. J. Vericella, H. D. Barth, J. D. Kuntz, and R. S. Maxwell. Threedimensional printing of elastomeric, cellular architectures with negative stiffness. *Advanced Functional Materials*, 24(31):4905–4913, 2014.

[63] D. B. Kolesky, R. L. Truby, A. G., T. A. Busbee, K. A. Homan, and J. A. Lewis. 3d bioprinting of vascularized, heterogeneous cellladen tissue constructs. *Advanced Materials*, 26(19):3124–3130, 2014.

[64] D. B. Kolesky, K. A. Homan, M. A. Skylar-Scott, and J. A. Lewis. Three-dimensional bioprinting of thick vascularized tissues. *Proceedings of the National Academy of Sciences of the United States of America*, 113(12):3179–3184, Mar 22 2016.

[65] J. Hollander, R. Hakala, J. Suominen, N. Moritz, J. Yliruusi, and N. Sandler. 3d printed uv light cured polydimethylsiloxane devices for drug delivery. *International journal of pharmaceutics*, 2017.

[66] K. Tian, J. Bae, S. E. Bakarich, C. Yang, R. D. Gately, G. M. Spinks, Z. Suo, and J. J. Vlassak. 3d printing of transparent and conductive heterogeneous hydrogelelastomer systems. *Advanced Materials*, 2017.

[67] S. S. Robinson, K. W. OBrien, H. Zhao, B. N. Peele, C. M. Larson, B. C. Mac Murray, I. M. Van Meerbeek, S. N. Dunham, and R. F. Shepherd. Integrated soft sensors and elastomeric actuators for tactile machines with kinesthetic sense. *Extreme Mechanics Letters*, 5:47–53, 2015.

[68] J. Plott and A. Shih. The extrusion-based additive manufacturing of moisture-cured silicone elastomer with minimal void for pneumatic actuators. *Additive Manufacturing*, 17:1–14, 2017.

[69] X. Tian, J. Plott, H. Wang, B. Zhu, and A. J. Shih. Silicone foam additive manufacturing by liquid rope coiling. *Procedia CIRP*, 65:196–201, 2017.

[70] A. M. Schmalzer, C. M. Cady, D. Geller, D. Ortiz-Acosta, A. T. Zocco, J. Stull, and A. Labouriau. Gamma radiation effects on siloxane-based additive manufactured structures. *Radiation Physics and Chemistry*, 130:103–111, 2017.

[71] Z. He, Y. Chen, J. Yang, C. Tang, J. Lv, Yu L., J. Mei, W. Lau, and D. Hui. Fabrication of polydimethylsiloxane films with special surface wettability by 3d printing. *Composites Part B: Engineering*, 129:58–65, 2017.

[72] K. B. Putra, J. Plott, and A. J. Shih. Biaxial mooney-rivlin coefficient of silicone sheet by additive manufacturing. *Procedia CIRP*, 65:189–195, 2017.

[73] D. Porter, A. Cohen, P. Krueger, and D. Son. Additive manufacturing utilizing stock ultraviolet curable silicone. In *28th Annual International Solid Freeform Fabrication Symposium*, page 1771, 2017.

[74] T. J. Hinton, A. R. Hudson, K. Pusch, A. Lee, and A. W. Feinberg. 3d printing pdms elastomer in a hydrophilic support bath via freeform reversible embedding. *ACS Biomaterials Science & Engineering*, 2(10):1781–1786, 2016.

[75] C. S. OBryan, T. Bhattacharjee, S. Hart, C. P. Kabb, K. D. Schulze, I. Chilakala, B. S. Sumerlin, W. G. Sawyer, and T. E. Angelini. Self-assembled micro-organogels for 3d printing silicone structures. *Science Advances*, 3(5):e1602800, 2017.

[76] T. Fripp, N. Frewer, and L. Green. *Method and apparatus for additive manufacturing*, 2014.

[77] T. Femmer, A. J. Kuehne, and M. Wessling. Print your own membrane: direct rapid prototyping of polydimethylsiloxane. *Lab on a Chip*, 14(15):2610–2613, 2014.

[78] D. Kim and B. L. Tai. Hydrostatic support-free fabrication of three-dimensional soft structures. *Journal of Manufacturing Processes*, 24:391–396, 2016.

[79] D. Kim, Y. Kao, and B. L. Tai. Hydrostatic 3d-printing for soft material structures using low one-photon polymerization. *Manufacturing Letters*, 10:6–9, 2016.

[80] D. Kim, J. Suriboot, . Grunlan, and B. Tai. Modeling of low one-photon polymerization for 3d printing of uv-curable silicones. In *28th Annual International Solid Freeform Fabrication Symposium*, page 1750, 2017.

[81] Y. Tang, C. L. Henderson, J. Muzzy, and D. W. Rosen. Stereolithography cure process modeling using acrylate resin. In *Solid Freeform Fabrication Symposium*, 2004.

[82] A. K. Au, W. Lee, and A. Folch. Mail-order microfluidics: evaluation of stereolithography for the production of microfluidic devices. *Lab on a Chip*, 14(7):1294–1301, 2014.

[83] D. Han, H. Gu, J. Kim, and S. Yokota. A bio-inspired 3d-printed hybrid finger with integrated ecf (electro-conjugate fluid) micropumps. *Sensors and Actuators A: Physical*, 257:47–57, 2017.

[84] M. I. Mohammeda, J. Tatinenia, B. Caddb, G. Peartb, and I. Gibsona. Applications of 3d topography scanning and multi-material additive manufacturing for facial prosthesis development and production.

[85] D. K. Patel, A. Sakhaei, M. Layani, B. Zhang, Q., and S. Magdassi. Highly stretchable and uv curable elastomers for digital light processing based 3d printing. *Advanced Materials*, 2017.

[86] S. Reitelshfer, M. Gttler, P. Schmidt, P. Treffer, M. Landgraf, and J. Franke. Aerosol-jet-printing silicone layers and electrodes for stacked dielectric elastomer actuators in one processing device. In *SPIE Smart Structures and Materials Nondestructive Evaluation and Health Monitoring*, volume 9798, pages 97981Y–97981Y–9. International Society for Optics and Photonics, 2016.

[87] D. McCoul, S. Rosset, S. Schlatter, and H. Shea. Inkjet 3d printing of uv and thermal cure silicone elastomers for dielectric elastomer actuators. *Smart Materials and Structures*, 26(12):125022, 2017.

[88] H. Yang, Y. He, C. Tuck, R. Wildman, I. Ashcroft, P. Dickens, and R. Hague. High viscosity jetting system for 3d reactive inkjet printing. In *Annual international solid freeform fabrication symposium*, 2013.

[89] A. Foerster, R. Wildman, R. Hague, and C. Tuck. Reactive inkjet printing approach towards 3d silicone elastomeric structures fabrication. In *28th Annual International Solid Freeform Fabrication Symposium*, page 1795, 2017.

[90] J. Stampfl, H. E. Pettermann, and R. Liska. *Bioinspired Cellular Structures: Additive Manufacturing and Mechanical Properties*, pages 105–123. Biomimetics–Materials, Structures and Processes. Springer, 2011.

[91] J. Morrow, S. Hemleben, and Y. Menguc. Directly fabricating soft robotic actuators with an open-source 3-d printer. *IEEE Robotics and Automation Letters*, 2(1):277–281, 2017.

[92] E. In, E. Walker, and H. Naguib. Novel development of 3d printable uv-curable silicone for multimodal imaging phantom. *Bioprinting*, 2017.

[93] J. Lv, Z. Gong, Z. He, J. Yang, Y. Chen, C. Tang, Y. Liu, M. Fan, and L. Lau. 3d printing of mechanically durable superhydrophobic porous membrane for oil-water separation. *Journal of Materials Chemistry A*, 2017.

[94] M. M. Durban, J. M. Lenhardt, A. S. Wu, W. Small, T. M. Bryson, L. PerezPerez, D. T. Nguyen, S. Gammon, J. E. Smay, and E. B. Duoss. Custom 3d printable silicones with tunable stiffness. *Macromolecular rapid communications*, 2017.

[95] S. Roh, D. P. Parekh, B. Bharti, S. D. Stoyanov, and O. D. Velev. 3d printing by multiphase silicone/water capillary inks. *Advanced Materials*, 2017.

[96] Y. Han, A. D. Rogalsky, B. Zhao, and H. J. Kwon. The application of digital image techniques to determine the large stressstrain behaviors of soft materials. *Polymer Engineering & Science*, 52(4):826–834, 2012.

[97] M. C. Goiato, Al. A. Pesqueira, D. M. dos Santos, and S. F. de Carvalho Dekon. Evaluation of hardness and surface roughness of two maxillofacial silicones following disinfection. *Brazilian oral research*, 23(1):49–53, 2009.

[98] F. Schneider, T. Fellner, J. Wilde, and U. Wallrabe. Mechanical properties of silicones for mems. *Journal of Micromechanics and Microengineering*, 18(6):065008, 2008.

[99] F. Schneider, J. Draheim, R. Kamberger, and U. Wallrabe. Process and material properties of polydimethylsiloxane (pdms) for optical mems. *Sensors and Actuators A: Physical*, 151(2):95–99, 2009.

[100] I. D. Johnston, D. K. McCluskey, C. Tan, and M. C. Tracey. Mechanical characterization of bulk sylgard 184 for microfluidics and microengineering. *Journal of Micromechanics and Microengineering*, 24(3):035017, 2014.

[101] T. K. Kim, J. K. Kim, and O. C. Jeong. Measurement of nonlinear mechanical properties of pdms elastomer. *Microelectronic Engineering*, 88(8):1982–1985, 2011.

[102] M. Liu, J. Sun, Y. Sun, C. Bock, and Q. Chen. Thickness-dependent mechanical properties of polydimethylsiloxane membranes. *Journal of Micromechanics and Microengineering*, 19(3):035028, 2009.

[103] T. Aziz, M. Waters, and R. Jagger. Analysis of the properties of silicone rubber maxillofacial prosthetic materials. *Journal of dentistry*, 31(1):67–74, 2003.

[104] V. Ozbolat, M. Dey, B. Ayan, A. Povilianskas, M. C. Demirel, and I. Ozbolat. 3d printing of pdms improves its mechanical and cell adhesion properties. *ACS Biomaterials Science & Engineering*, 2017.

[105] S. K. Jindal, M. Sherriff, M. G. Waters, and T. J. Coward. Development of a 3d printable maxillofacial silicone: Part i. optimization of polydimethylsiloxane chains and cross-linker concentration. *The Journal of prosthetic dentistry*, 116(4):617–622, 2016.

[106] S. K. Jindal, M. Sherriff, M. G. Waters, J. E. Smay, and T. J. Coward. Development of a 3d printable maxillofacial silicone. part ii: Optimization of moderator and thixotropic agent. *The Journal of prosthetic dentistry*, 2017.

[107] H. Yuk and X. Zhao. A new 3d printing strategy by harnessing deformation, instability, and fracture of viscoelastic inks. *Advanced Materials*, 2017.

[108] ASTM Standard. F2792-12a.(2012).. *Standard Terminology for Additive Manufacturing Technologies, ASTM International, West Conshohocken, Pa.*

[109] Y. Gao, H. Li, and J. Liu. Direct writing of flexible electronics through room temperature liquid metal ink. 2012.

[110] A. J. Lopes, E. MacDonald, and R. B. Wicker. Integrating stereolithography and direct print technologies for 3d structural electronics fabrication. *Rapid Prototyping Journal*, 18(2):129–143, 2012.

[111] B. K. Park, D. Kim, S. Jeong, J. Moon, and J. Sub Kim. Direct writing of copper conductive patterns by ink-jet printing. *Thin Solid Films*, 515(19):7706–7711, 2007.

[112] K. Hon, L. Li, and I. M. Hutchings. Direct writing technologyadvances and developments. *CIRP Annals-Manufacturing Technology*, 57(2):601–620, 2008.

[113] Robert Chang, Jae Nam, and Wei Sun. Effects of dispensing pressure and nozzle diameter on cell survival from solid freeform fabrication-based direct cell writing. *Tissue Engineering Part A*, 14(1):41–48, 2008.

[114] S. Khalil, J. Nam, and W. Sun. Multi-nozzle deposition for construction of 3d biopolymer tissue scaffolds. *Rapid Prototyping Journal*, 11(1):9–17, 2005.

[115] L. Geng, W. Feng, D. W. Hutmacher, Y. S. Wong, H. T. Loh, and J.. Y. Fuh. Direct writing of chitosan scaffolds using a robotic system. *Rapid Prototyping Journal*, 11(2):90–97, 2005.

[116] L. Mortara, J. Hughes, P. S. Ramsundar, F. Livesey, and D. R. Probert. Proposed classification scheme for direct writing technologies. *Rapid Prototyping Journal*, 15(4):299–309, 2009.

[117] G. Vozzi, A. Previti, D. De Rossi, and A. Ahluwalia. Microsyringe-based deposition of two-dimensional and three-dimensional polymer scaffolds with a well-defined geometry for application to tissue engineering. *Tissue engineering*, 8(6):1089–1098, 2002.

[118] M. Vlasea and E. Toyserkani. Experimental characterization and numerical modeling of a micro-syringe deposition system for dispensing sacrificial photopolymers

on particulate ceramic substrates. *Journal of Materials Processing Technology*, 213(11):1970–1977, 2013.

[119] J. H. Oh and S. Y. Lim. Precise size control of inkjet-printed droplets on a flexible polymer substrate using plasma surface treatment. *Journal of Micromechanics and Microengineering*, 20(1):015030, 2010.

[120] L. M. Galantucci, F. Lavecchia, and G. Percoco. Quantitative analysis of a chemical treatment to reduce roughness of parts fabricated using fused deposition modeling. *CIRP Annals-manufacturing technology*, 59(1):247–250, 2010.

[121] G. Pyka, G. Kerckhofs, I. Papantoniou, M. Speirs, J. Schrooten, and M. Wevers. Surface roughness and morphology customization of additive manufactured open porous ti6al4v structures. *Materials*, 6(10):4737–4757, 2013.

[122] S. Barr and A. Bayat. Breast implant surface development: perspectives on development and manufacture. *Aesthetic Surgery Journal*, 31(1):56–67, 2011.

[123] V. Lazenco and A. Alicia. Breast implant surface development. 2015.

[124] H. J. Subramani, H. K. Yeoh, R. Suryo, Q. Xu, B. Ambravaneswaran, and O. A. Basaran. Simplicity and complexity in a dripping faucet. *Physics of Fluids (1994-present)*, 18(3):032106, 2006.

[125] B. Ambravaneswaran, H. J. Subramani, S. D. Phillips, and O. A. Basaran. Dripping-jetting transitions in a dripping faucet. *Physical Review Letters*, 93(3):034501, 2004.

[126] Q. Xu and O. A. Basaran. Computational analysis of drop-on-demand drop formation. *Physics of Fluids (1994-present)*, 19(10):102111, 2007.

[127] B. Derby. Inkjet printing of functional and structural materials: fluid property requirements, feature stability, and resolution. *Annual Review of Materials Research*, 40:395–414, 2010.

[128] E. Toyserkani, M. Vlasea, and Y. Shanjani. Systems and methods for additive manufacturing of heterogeneous porous structures and structures made therefrom, 2014.

[129] J. Kechagias. Investigation of lom process quality using design of experiments approach. *Rapid Prototyping Journal*, 13(5):316–323, 2007.

[130] H. Bikas, P. Stavropoulos, and G. Chryssolouris. Additive manufacturing methods and modelling approaches: a critical review. *The International Journal of Advanced Manufacturing Technology*, pages 1–17, 2015.

[131] F. Kaji and A. Barari. Evaluation of the surface roughness of additive manufacturing parts based on the modelling of cusp geometry. *IFAC-PapersOnLine*, 48(3):658–663, 2015.

[132] K. Kumar and G. S. Kumar. An experimental and theoretical investigation of surface roughness of poly-jet printed parts: This paper explains how local surface orientation affects surface roughness in a poly-jet process. *Virtual and Physical Prototyping*, 10(1):23–34, 2015.

[133] V. Tirtaatmadja, G. H. McKinley, and J. J. Cooper-White. Drop formation and breakup of low viscosity elastic fluids: Effects of molecular weight and concentration. *Physics of Fluids (1994-present)*, 18(4):043101, 2006.

[134] E. D. Wilkes, S. D. Phillips, and O. A. Basaran. Computational and experimental analysis of dynamics of drop formation. *Physics of Fluids (1994-present)*, 11(12):3577–3598, 1999.

[135] S. Cruz Aguilar, M. Ahmadi, S. R. Des Jardins, E. Fiske, M. Meier, H. Quinones, T. L. Ratledge, and R. J. Wright. *Modular jetting devices*, 2017.

[136] G. E. Box and N. R. Draper. *Empirical model-building and response surfaces*, volume 424. Wiley New York, 1987.

[137] T. Kim, H. Song, J. Ha, S. Kim, D. Kim, S. Chung, J. Lee, and Y. Hong. Inkjet-printed stretchable single-walled carbon nanotube electrodes with excellent mechanical properties. *Applied Physics Letters*, 104(11):113103, 2014.

[138] U. Caglar, K. Kaija, and P. Mansikkamaki. Analysis of mechanical performance of silver inkjet-printed structures. In *Nanoelectronics Conference, 2008. INEC 2008. 2nd IEEE International*, pages 851–856. IEEE, 2008.

[139] I. Kim, Y. A. Song, H. C. Jung, J. W. Joung, S. Ryu, and J. Kim. Effect of microstructural development on mechanical and electrical properties of inkjet-printed ag films. *Journal of Electronic Materials*, 37(12):1863–1868, 2008.

[140] T. Zhang, B. Jiang, and Y. Huang. Uv-curable photosensitive silicone resins based on a novel polymerizable photoinitiator and go-modified tio 2 nanoparticles. *Composites Part B: Engineering*, 2017.

[141] B. R. Chambers, S. L. Hannah, and R. J. Raleigh Jr. *Dual-cure silicone compounds exhibiting elastomeric properties*, 2006.

[142] P. Tingaut, R. Hauert, and T. Zimmermann. Highly efficient and straightforward functionalization of cellulose films with thiol-ene click chemistry. *Journal of Materials Chemistry*, 21(40):16066–16076, 2011.

[143] M. Milosevic, D. Stoof, and K. Pickering. Characterizing the mechanical properties of fused deposition modelling natural fiber recycled polypropylene composites. *Journal of Composites Science*, 1(1):7, 2017.

[144] S. N. Cerda-Avila, H. I. Medelln-Castillo, and D. F. de Lange. Analysis and numerical simulation of the mechanical performance of fdm samples with variable infill values. In *ASME 2017 International Mechanical Engineering Congress and Exposition*, pages V002T02A034–V002T02A034. American Society of Mechanical Engineers, 2017.

[145] A. K. Sood, R. K. Ohdar, and S. S. Mahapatra. Parametric appraisal of mechanical property of fused deposition modelling processed parts. *Materials & Design*, 31(1):287–295, 2010.

[146] M. S. Hossain, J. Ramos, D. Espalin, M. Perez, and R. Wicker. Improving tensile mechanical properties of fdm-manufactured specimens via modifying build parameters. In *International Solid Freeform Fabrication Symposium: An Additive Manufacturing Conference. Austin, TX*, volume 2013, pages 380–392, 2013.

[147] M. Domingos, F. Chiellini, A. Gloria, L. Ambrosio, P. Bartolo, and E. Chiellini. Effect of process parameters on the morphological and mechanical properties of 3d bioextruded poly (-caprolactone) scaffolds. *Rapid Prototyping Journal*, 18(1):56–67, 2012.

[148] S. J. Kalita, S. Bose, H. L. Hosick, and A. Bandyopadhyay. Development of controlled porosity polymer-ceramic composite scaffolds via fused deposition modeling. *Materials Science and Engineering: C*, 23(5):611–620, 2003.

[149] C. H. Yang, B. Chen, J. J. Lu, J. H. Yang, J. Zhou, Y. M. Chen, and Z. Suo. Ionic cable. *Extreme Mechanics Letters*, 3:59–65, 2015.

[150] J. Sun, C. Keplinger, G. M. Whitesides, and Z. Suo. Ionic skin. *Advanced Materials*, 26(45):7608–7614, 2014.

[151] E. M. Sachs, J. S. Haggerty, M. J. Cima, and P. A. Williams. *Three-dimensional printing techniques*, 1993.

[152] D. Bourell, J. P. Kruth, M. Leu, G. Levy, D. Rosen, A. M. Beese, and A. Clare. Materials for additive manufacturing. *CIRP Annals-Manufacturing Technology*, 2017.

[153] S. B. Hong, N. Eliaz, G. G. Leisk, E. M. Sach, R. M. Latanision, and S. M. Allen. A new ti-5ag alloy for customized prostheses by three-dimensional printing (3dp). *Journal of dental research*, 80(3):860–863, Mar 2001.

[154] Y. Shanjani, Y. Hu, R. M. Pilliar, and E. Toyserkani. Mechanical characteristics of solid-freeform-fabricated porous calcium polyphosphate structures with oriented stacked layers. *Acta biomaterialia*, 7(4):1788–1796, 2011.

[155] P. Habibovic, U. Gbureck, C. J. Doillon, D. C. Bassett, C. A. van Blitterswijk, and J. E. Barralet. Osteoconduction and osteoinduction of low-temperature 3d printed bioceramic implants. *Biomaterials*, 29(7):944–953, 2008.

[156] U. Gbureck, E. Vorndran, F. A. Muller, and J. E. Barralet. Low temperature direct 3d printed bioceramics and biocomposites as drug release matrices. *Journal of Controlled Release*, 122(2):173–180, 2007.

[157] A. Khalyfa, S. Vogt, J. Weisser, G. Grimm, A. Rechtenbach, W. Meyer, and M. Schnabelrauch. Development of a new calcium phosphate powder-binder system for the 3d printing of patient specific implants. *Journal of Materials Science: Materials in Medicine*, 18(5):909–916, 2007.

[158] K. Igawa, M. Mochizuki, O. Sugimori, K. Shimizu, K. Yamazawa, H. Kawaguchi, K. Nakamura, T. Takato, R. Nishimura, and S. Suzuki. Tailor-made tricalcium phosphate bone implant directly fabricated by a three-dimensional ink-jet printer. *Journal of Artificial Organs*, 9(4):234–240, 2006.

[159] A. Butscher, M. Bohner, S. Hofmann, L. Gauckler, and R. Mller. Structural and material approaches to bone tissue engineering in powder-based three-dimensional printing. *Acta biomaterialia*, 7(3):907–920, 2011.

[160] B. Stevens, Y. Yang, A. Mohandas, B. Stucker, and K. T. Nguyen. A review of materials, fabrication methods, and strategies used to enhance bone regeneration in engineered bone tissues. *Journal of biomedical materials research Part B: applied biomaterials*, 85(2):573–582, 2008.

[161] M. Castilho, I. Pires, B. Gouveia, and J. Rodrigues. Structural evaluation of scaffolds prototypes produced by three-dimensional printing. *The International Journal of Advanced Manufacturing Technology*, 56(5-8):561–569, 2011.

[162] S. Yang, K. Leong, Z. Du, and C. Chua. The design of scaffolds for use in tissue engineering. part ii. rapid prototyping techniques. *Tissue engineering*, 8(1):1–11, 2002.

[163] M. Vlasea, E. Toyserkani, and R. Pilliar. Effect of gray scale binder levels on additive manufacturing of porous scaffolds with heterogeneous properties. *International Journal of Applied Ceramic Technology*, 12(1):62–70, 2015.

[164] D. W. Hutmacher. Scaffolds in tissue engineering bone and cartilage. *Biomaterials*, 21(24):2529–2543, 2000.

[165] D. W. Hutmacher, M. Sittinger, and M. V. Risbud. Scaffold-based tissue engineering: rationale for computer-aided design and solid free-form fabrication systems. *Trends in biotechnology*, 22(7):354–362, 2004.

[166] M. Castilho, M. Dias, U. Gbureck, J. Groll, P. Fernandes, I. Pires, B. Gouveia, J. Rodrigues, and E. Vorndran. Fabrication of computationally designed scaffolds by low temperature 3d printing. *Biofabrication*, 5(3):035012, 2013.

[167] P. H. Warnke, H. Seitz, F. Warnke, S. T. Becker, S. Sivananthan, E. Sherry, Q. Liu, J. Wiltfang, and T. Douglas. Ceramic scaffolds produced by computerassisted 3d printing and sintering: Characterization and biocompatibility investigations. *Journal of Biomedical Materials Research Part B: Applied Biomaterials*, 93(1):212–217, 2010.

[168] S. Yang, K. Leong, Z. Du, and C. Chua. The design of scaffolds for use in tissue engineering. part i. traditional factors. *Tissue engineering*, 7(6):679–689, 2001.

[169] K. F. Leong, C. M. Cheah, and C. K. Chua. Solid freeform fabrication of three-dimensional scaffolds for engineering replacement tissues and organs. *Biomaterials*, 24(13):2363–2378, 2003.

[170] W. K. Chiu and K. M. Yu. Direct digital manufacturing of three-dimensional functionally graded material objects. *Computer-Aided Design*, 40(12):1080–1093, 2008.

[171] B. Markicevic, T. G. DOnofrio, and H. K. Navaz. On spread extent of sessile droplet into porous medium: Numerical solution and comparisons with experiments. *Physics of Fluids*, 22(1):012103, 2010.

[172] R. Freeman and X. Fu. Characterisation of powder bulk, dynamic flow and shear properties in relation to die filling. *Powder Metallurgy*, 51(3):196–201, 2008.

[173] R. Freeman. Measuring the flow properties of consolidated, conditioned and aerated powdersa comparative study using a powder rheometer and a rotational shear cell. *Powder Technology*, 174(1):25–33, 2007.

[174] X. Fu, D. Huck, L. Makein, B. Armstrong, U. Willen, and T. Freeman. Effect of particle shape and size on flow properties of lactose powders. *Particuology*, 10(2):203–208, 2012.

[175] S. Hatami, O. Lyckfeldt, L. Tonnang, and K. Fransson. Flow properties of tool steel powders for selective laser meltinginfluence of thermal and mechanical powder treatments. *Powder Metallurgy*, 60(5):353–362, 2017.

[176] R. K. Holman, M. J. Cima, S. A. Uhland, and E. Sachs. Spreading and infiltration of inkjet-printed polymer solution droplets on a porous substrate. *Journal of colloid and interface science*, 249(2):432–440, 2002.

[177] E. Brandl, U. Heckenberger, V. Holzinger, and D. Buchbinder. Additive manufactured alsi10mg samples using selective laser melting (slm): Microstructure, high cycle fatigue, and fracture behavior. *Materials & Design*, 34:159–169, 2012.

[178] H. Liao and J. Shie. Optimization on selective laser sintering of metallic powder via design of experiments method. *Rapid Prototyping Journal*, 13(3):156–162, 2007.

[179] R. L. Mason, R. F. Gunst, and J. L. Hess. *Statistical design and analysis of experiments: with applications to engineering and science*, volume 474. John Wiley & Sons, 2003.

[180] D. C. Montgomery. *Design and analysis of experiments*, volume 7. Wiley New York, 1984.

[181] H. Pasandideh and T. Akhavan Niaki. Multi-response simulation optimization using genetic algorithm within desirability function framework. *Applied Mathematics and Computation*, 175(1):366–382, 2006.

[182] S. Sen, V. D. Veeranki, and B. Mandal. Effect of physical parameters, carbon and nitrogen sources on the production of alkaline protease from a newly isolatedbacillus pseudofirmus svb1. *Annals of microbiology*, 59(3):531–538, 2009.

[183] O. E. Yildirim and O. A. Basaran. Dynamics of formation and dripping of drops of deformation-rate-thinning and-thickening liquids from capillary tubes. *Journal of Non-Newtonian Fluid Mechanics*, 136(1):17–37, 2006.

[184] K. Sarikhani, K. Jeddi, R. B. Thompson, C. B. Park, and P. Chen. Effect of pressure and temperature on interfacial tension of poly lactic acid melt in supercritical carbon dioxide. *Thermochimica Acta*, 609:1–6, 2015.

[185] Y. Suh and G. Son. A level-set method for simulation of a thermal inkjet process. *Numerical Heat Transfer, Part B: Fundamentals*, 54(2):138–156, 2008.

[186] J. Hu, R. Jia, K. Wan, and X. Xiong. Simulation of droplet impingement on a solid surface by the level set method.

[187] S. Granick, Y. Zhu, and H. Lee. Slippery questions about complex fluids flowing past solids. *Nature Materials*, 2(4):221–227, 2003.

[188] B. P. Cahill, A. T. Giannitsis, G. Gastrock, M. Min, and D. Beckmann. A dynamic electrowetting simulation using the level-set method. *Proc.of the COMSOL coference*, 2008.

Appendices

Appendix A

Scientific Background

A.1 Design of Experiments (DoE)

A systematic way to find the optimum combination of factors is to study the effect of each factor and interaction of different factors on the response. Design of experiments has been adopted by many research groups to investigate and optimize the quality of additive manufacturing processes [119, 129, 177, 178]. The screening experiment was performed to find out which factors have significant effects on width of the printed lines. As only three factors needed to be studied, a full factorial experiment was chosen. Factorial designs make it possible to simultaneously study the effects of different parameters and their interaction on response(s). It is also possible to find out how the effect of one factor changes when other factors are not constant. This simultaneous study of factor effects in DOE is done using analysis of variance (ANOVA) and hypothesis testing. Equations underlying the ANOVA procedure are from Montgomery (1984) and Mason (2003) books. Suppose a general experiment with three factors A, B, and C needs to be screened to find significant factors. Factor A has i levels (i = 1, 2, ..., a), factor B has j levels (j = 1, 2, ..., b), factor C has k levels (k = 1, 2, , c) and l represents the number of experiment replicates (l = 1, 2, ..., n). A total of abcn observations will be measured in a full factorial design. In order to conduct ANOVA, every observation will be decomposed into different components. The decomposed observations can be written as [179, 180]:

$$\mu_{ijkl} = \mu + \tau_i + \beta_j + \gamma_k + (\tau\beta)_{ij} + (\tau\gamma)_{ik} + (\beta\gamma)_{jk} + (\tau\beta\gamma)_{ijk} + \epsilon_{ijkl} \tag{A.1}$$

where μ is the overall main effect, τ_i is the effect of i^{th} level of factor A, β_j is the effect of j^{th} level of factor B, γ_k is the k^{th} level effect of factor C, $(\tau\beta)_{ij}$ is the effect of the interaction between τ and β, $(\tau\gamma)_{ik}$ is the effect of the interaction between τ and γ, $(\beta\gamma)_{jk}$ is the effect of the interaction between β and γ, $(\tau\beta\gamma)_{ijk}$ is the effect of the interaction between τ , β and γ, ϵ_{ijkl} is the experimental error. The purpose of factorial design is to see if any of main effects, their second order combinations, and their third order combinations are significant. For doing so, following null hypotheses should be defined:

$$\begin{cases} H_0 : \tau_i = 0 \text{ for all } i;\; H_0 : \beta_j = 0 \text{ for all } j;\; H_0 : \gamma_k = 0 \text{ for all } k \\ H_0 : (\tau\beta)_{ij} = 0 \text{ for all } i,\; j;\; H_0 : (\tau\gamma)_{ik} = 0 \text{ for all } i,\; k;\; H_0 : (\beta\gamma)_{jk} = 0 \text{ for all } j,\; k \\ H_0 : (\tau\beta\gamma)_{ijk} = 0 \text{ for all } i,\; j,\; k \end{cases} \tag{A.2}$$

The alternative hypotheses for all of the terms in Eq. A.2 would be at least one effect, e.g. , is not equal to zero (Montgomery et al., 1984). Let $y_{....}$ be the total of all observations, $y_{i...}$ be the total of all observations under the i^{th} level etc., $y_{ij..}$ be the total of all observations under the ij_{th} level etc., and $y_{ijk.}$ be the total of all observations under the ijk^{th} level. The average of these values will be calculated by dividing them by their number and will be shown as $(\bar{y_{....}})$ etc. Their total corrected sum of squares can be written as:

$$SS_T = \sum_{i=1}^{a}\sum_{j=1}^{b}\sum_{k=1}^{c}\sum_{l=1}^{n}(y_{ijkl} - \bar{y_{....}})^2 \tag{A.3}$$

where SS_T is the total corrected sum of squares. Solving for Eq. A.3 and simplifying results we get:

$$SS_T = SS_A + SS_B + SS_C + SS_{AB} + SS_{AC} + SS_{BC} + SS_{ABC} + SS_E \tag{A.4}$$

The means squares SS_is is calculated by dividing them by their degrees of freedom (DF) as follows:

$$MS_i = \frac{SS_i}{DF_i} \tag{A.5}$$

Division of mean squares of factors and their combinations over the mean square of error will be distributed as F probability distribution. As a result, if this F-value is smaller than the critical F, the hypothesis will be rejected i.e. that factor is significant. Equation A.6 shows how F-value is calculated:

$$F_i = \frac{MS_i}{MS_E} \tag{A.6}$$

Design of experiments fits a regression model to the three factors and their interactions that can be written as:

$$y = \beta_0 + \beta_1 x_1 + \beta_2 x_2 + \beta_3 x_3 + \beta_{12} x_{12} + \beta_{13} x_{13} + \beta_{23} x_{23} + \beta_{123} x_{123} \tag{A.7}$$

where Y is the response, the ${\beta_i}^{'}$s are process parameter coefficients, and ${x_i}^{'}$s are the process parameter values.

A.2 Desirability Function Method

Where there is a need for optimization of more than one response, the desirability function method (also known as utility transfer function) is widely used. To this end, the value of every response will be converted to a number between zero and one which is called desirability. Desirability values closer to one demonstrate better results. The optimization algorithm chooses factor levels that maximize the overall desirability value [181, 182]. In this study, the minimization function will be used to calculate the individual desirabilities first. Considering $d(y_i)$ (i=1, 2, and 3) as the desirability of response y_i, the minimization function will be:

$$d(y_i) = \begin{cases} 1 & \text{for } y_i < t_i \\ (\frac{u_i - y_i}{u_i - t_i})^r & \text{for } t_i \leq y_i \leq u_i \\ 0 & \text{for } y_i \geq u_i \end{cases} \tag{A.8}$$

where r determines the shape of the function; linear, convex, and concave for $r = 1$, $r < 1$, and $r > 1$, respectively. u_i is the upper limit of the response y_i , and t_i is the target value of response y_i , i.e. the maximum value it can accept in this case. Then, the overall desirability function can be calculated as follows:

$$d_{total} = (d(y_1)d(y_2)...d(y_i))^{\frac{1}{i}} \tag{A.9}$$

A.3 Level-set Model

Level-set method was introduced by Osher and Sethian [183] in 80s to capture the interface of two fluids and the changes that interface goes through due to motion. This Eulerian method is applicable to analysis of the motion of interfaces e.g., the merging of two droplets in two or three dimensions.

In this method the curve is defined by a level-set equation ϕ (in 2D space). The boundary between two fluids is represented by contour 0.5. The transition area with ϕ less than 0.5 is air and ϕ more than 0.5 represents silicone.

$$\begin{cases} 0 \leq \phi \leq 0 & \text{air} \\ \phi = 0.5 & \text{boundary} \\ 0.5 \leq \phi \leq 1 & \text{silicone} \end{cases} \tag{A.10}$$

Density and viscosity of the two fluids change in the transition area according to the following equations using level-set function:

$$\rho = \rho_{air} + (\rho_{silicone} - \rho_{air})\phi \tag{A.11}$$

$$\mu = \mu_{air} + (\mu_{silicone} - \mu_{air})\phi \tag{A.12}$$

where ρ denotes the density and μ denotes the viscosity.

The movement of the fluids interface under velocity field (ν) is described by Eq. A.13:

$$\frac{\partial \phi}{\partial t} + \nu \cdot \nabla \phi = 0 \tag{A.13}$$

In the level-set method, the interface is considered to move normal to itself. Hence, only the normal component of the velocity field (ν_n) is important [184]. Replacing $\nu_n = \nu \cdot \hat{n} = \nu \cdot \frac{\nabla \phi}{|\nabla \phi|}$ with ν in above equation results in the level-set equation:

$$\frac{\partial \phi}{\partial t} + \nu_n |\nabla \phi| = 0 \tag{A.14}$$

The level-set function should remain as a distance function ($|\nabla \phi| = 1$) throughout the simulation process in order to depict the changes of interface accurately. In order to solve this problem, numerical reinitialization and stabilization terms are added to level-set equation so that it is set back to distance function from the boundary after each time step [134, 185]. Following equation presents the non-conservative reinitialized level-set function and is solved in COMSOL multiphysics:

$$\rho(\frac{\partial\phi}{\partial t}+\nu\cdot\nabla\phi)=\Gamma[\epsilon\nabla\cdot\nabla\phi-\nabla\cdot(\phi(1-\phi)\frac{\nabla\phi}{|\nabla\phi|})] \tag{A.15}$$

where ϵ is the thickness of the transition layer. Half of the size of the typical mesh size in the region passed by the droplet [186] is suggested for ϵ. $\mathit{\Gamma}$ is the reinitialization factor and is approximately equal to the maximum value of the velocity field.

A.4 Fluid Flow Governing Equations

The flow of silicone in nozzle dispensing system is incompressible and laminar. Non-conservative time-dependent Navier-Stokes equations are solved for this model to demonstrate the transport of mass and momentum [185]:

$$\nabla\cdot\nu=0 \tag{A.16}$$

$$\rho\frac{\partial\nu}{\partial t}+\rho(\nu\cdot\nabla)\nu=\nabla\cdot[-PI+\mu(\nabla u+(\nabla u)^T)]+\rho g+F_{st} \tag{A.17}$$

where ρ is the density, ν is the velocity field, P is the pressure of silicone, I is the identity matrix, μ is the dynamic viscosity, g is the acceleration of gravity, F_{st} denotes the surface tension force. Eq. A.18 is used to calculate the value of surface tension force.

$$F_{st}=\nabla\cdot[(\gamma(I-NN^T))\delta] \tag{A.18}$$

where γ is the surface tension. Also, N denotes the normal to the interface and δ is the Dirac delta function, which is formulized as following:

$$n=\frac{\nabla\Phi}{|\nabla\Phi|} \tag{A.19}$$

$$\delta=6|\Phi(1-\Phi)||\nabla\Phi| \tag{A.20}$$

Droplet generation on the surface is modeled by definition of wetted wall boundary condition parametrized with contact angle and slip length for the substrate. The slip length, i.e. the distance behind the substrate at which the velocity can be extrapolated to zero [187] is required for modeling the movement of the boundary between two fluids and to prevent singularity. The recommended slip length is equal to mesh size [188]. The wetted wall boundary condition is described using friction force (F_f) in Eq. A.21:

$$\gamma(n - n_{int} \cos\theta)\delta = -F_f = \frac{\mu}{\beta}\nu \tag{A.21}$$

where β is the slip length, Θ_c is the contact angle and F_f is the friction force.

Appendix B

Experimental Design for Material Extrusion

B.1 Line Features

Table B.1: 2^3 full factorial design and measurements

	Variables			Coded Variables			Response		
Run	Pressure	Velocity	Working Distance	Pressure	Velocity	Working Distance	Average Width	Uniformity	Surface Quality
1	200	10	0.5	1	1	1	367.6	2.06	171.5
2	100	5	0.2	-1	-1	-1	289.3	4.27	65.8
3	200	10	0.2	1	1	-1	492	1.9	290.3
4	200	10	0.2	1	1	-1	675.6	0.8	83.6
5	100	5	0.2	-1	1	-1	266.6	1.96	140.2
6	100	5	0.5	-1	1	1	42.4	18.91	39.7
7	100	5	0.5	-1	-1	1	90.2	29.5	8
8	200	10	0.5	1	-1	1	541.8	2.79	125.9
9	100	5	0.2	-1	1	-1	338.2	6.4	155.6
10	200	10	0.5	1	1	1	321.6	2.24	26.1
11	100	5	0.2	-1	-1	-1	237.8	2.48	21.3
12	100	5	0.5	-1	-1	1	191.8	32.75	102
13	200	10	0.2	1	-1	-1	870.6	0.49	34.3
14	200	10	0.2	1	-1	-1	859.6	2.33	37.9
15	150	7.5	0.35	0	0	0	253.2	3.12	140.3
16	150	7.5	0.35	0	0	0	274.8	4.83	87.2
17	200	10	0.5	1	-1	1	488.4	4.27	37.6
18	100	5	0.5	-1	1	1	56.6	30.63	57.8

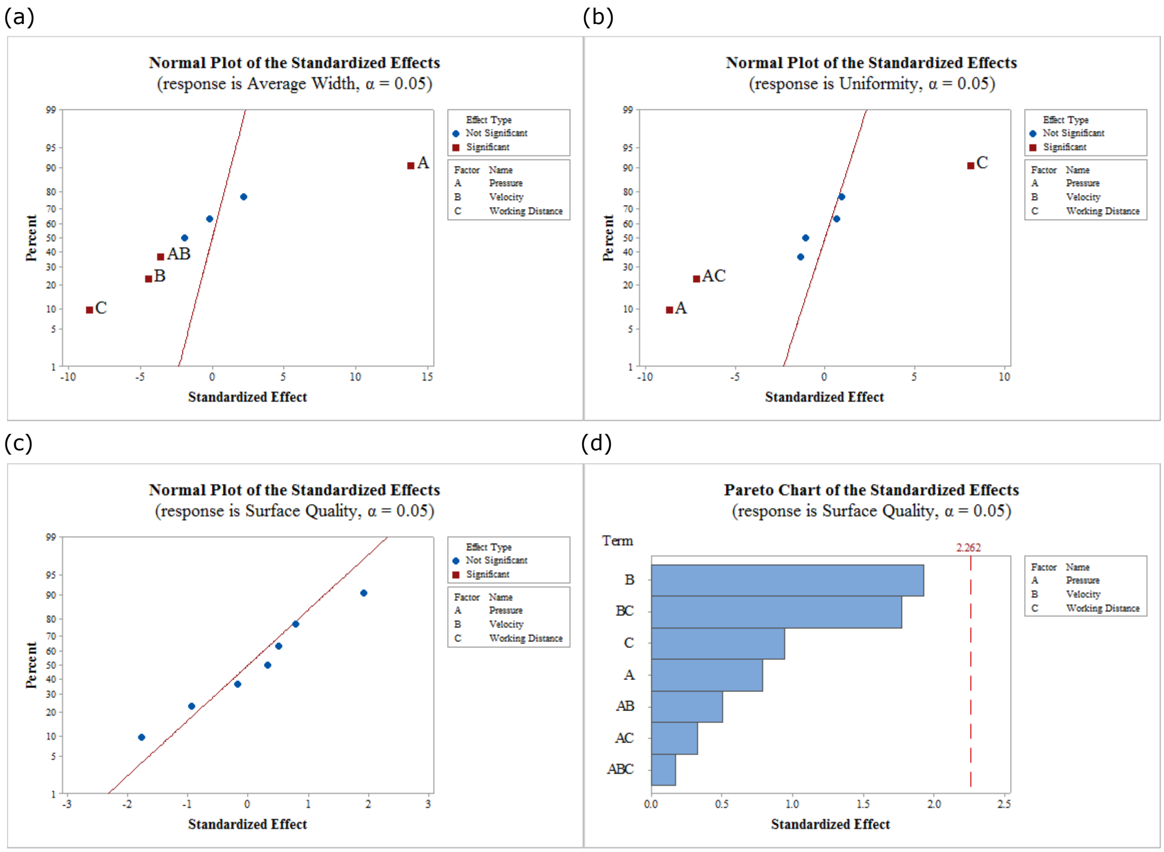

Figure B.1: Significant process parameters; (a) Normal plot for W_{avg}; (b) Normal plot for $W_{s.d.}$; (c) Normal plot for W_q; (d) Pareto chart for surface quality.

Table B.2: Process parameter coefficients in regression equation

	β_0	β_1	β_2	β_3	β_{12}	β_{13}	β_{23}	β_{123}
W_{avg}	383.1	194	-63.1	-120.6	-49.9	0	0	-119.1
$W_{s.d.}$	8.986	-6.876	0	6.407	0	-5.677	0	-5.01
W_q	87.3	13.6	33.3	-16.3	8.7	5.7	-30.6	-2.9

Table B.3: ANOVA and model summary

	DF	Adj SS	Adj MS	P-Value
W_{avg}				
Main Factors	3	602292	299516	0
P	1	898547	602292	0
v	1	63617	63617	0.003
WD	1	232637	232637	0
Second order interactions	1	39830	39830	0.012
$P{*}v$	1	39830	39830	0.012
Curvature	1	25231	25231	0.205
R-squared	94.62%			
Adj R-squared	92.37%			
$W_{s.d.}$				
Main Factors	2	1413.3	706.65	0
P	1	756.48	756.48	0
WD	1	656.81	656.81	0
Second order interactions	1	515.65	515.65	0
$P{*}WD$	1	515.65	515.65	0
Curvature	1	44.58	44.58	0.057
R-squared	93.67%			
Adj R-squared	91.73%			

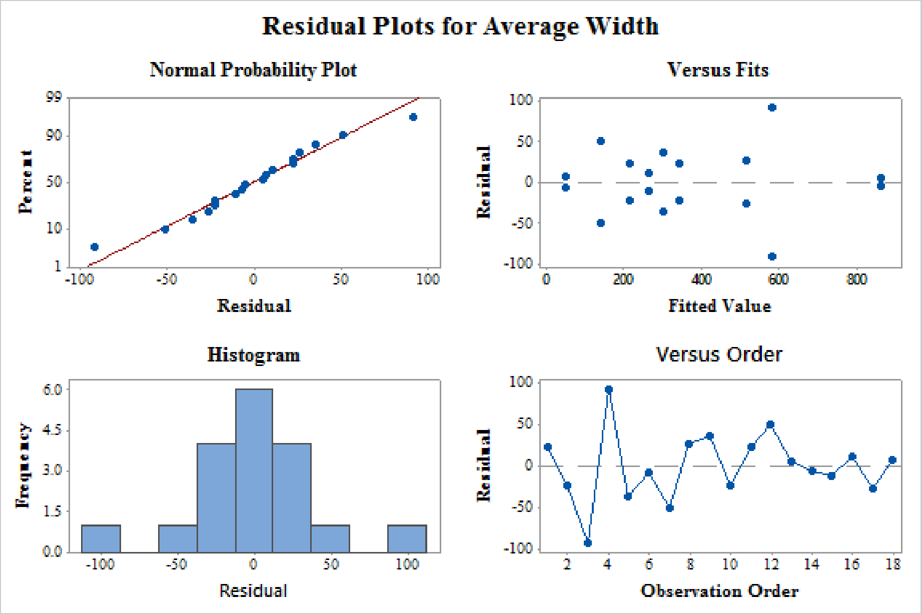

Figure B.2: Residual plots for W_{avg} show normality and independence assumptions are valid.

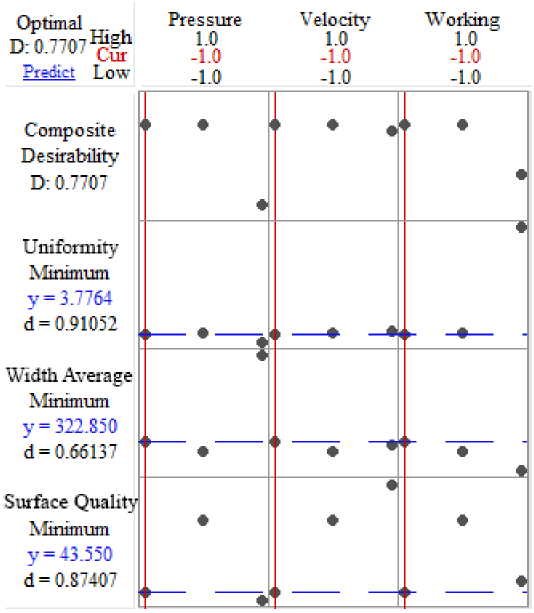

Figure B.3: Optimization plot: -1, -1, -1 level set treatment combination for P, V and WD, respectively, gives the optimal results.

B.2 Plane Features

Table B.4: 2^4 design and the response values

No.	P	v	RW	WD	W_q
9	150	10	0.1	0.2	2.571
11	150	20	0.1	0.2	11.53
4	200	20	0.1	0.1	2.129
8	200	20	0.2	0.1	5.531
12	200	20	0.1	0.2	1.98
31	200	10	0.2	0.2	6.098
5	150	10	0.2	0.1	4.087
23	200	10	0.2	0.1	4.547
34 (C)	Center	Center	Center	Center	3.942
3	150	20	0.1	0.1	4.248
6	200	10	0.2	0.1	4.906
20	150	20	0.1	0.1	2.239
32	150	20	0.2	0.2	13.905
13	150	10	0.2	0.2	8.838
21	200	20	0.1	0.1	1.498
18	150	10	0.1	0.1	2.25
2	200	10	0.1	0.1	3.095
33	200	20	0.2	0.2	7.183
14	200	10	0.2	0.2	5.211
27	200	10	0.1	0.2	3.145
28	150	20	0.1	0.2	6.063
7	150	20	0.2	0.1	5.172
24	150	20	0.2	0.1	4.516
26	150	10	0.1	0.2	2.645
16	200	20	0.2	0.2	5.108
17 (C)	Center	Center	Center	Center	3.097
22	150	10	0.2	0.1	3.004
10	200	10	0.1	0.2	1.977
29	200	20	0.1	0.2	1.599

Table B.5: ANOVA for W_q in 2^4 design

Factor	SS	DF	MS	F-observe	P-Value
P	117.2134	1	117.2134	10.19629	0.004044*
v	6.4064	1	6.4064	0.55729	0.462918
RW	156.2647	1	156.2647	13.59334	0.00122*
WD	102.1235	1	102.1235	8.88364	0.006689*
$P \times v$	5.4022	1	5.4022	0.46993	0.49987
$P \times RW$	7.3344	1	7.3344	0.63802	0.432601
$P \times WD$	87.7415	1	87.7415	7.63256	0.011078*
$v \times RW$	0.6992	1	0.6992	0.06082	0.807394
$v \times WD$	8.006	1	8.006	0.69644	0.412568
$RW \times WD$	68.1003	1	68.1003	5.92399	0.023114*
Error	264.4007	23	11.4957		
Total	823.6922	33			

Table B.6: ANOVA for W_q for the extruded planar features after removing the insignificant factors.

Factor	SS	DF	MS	F-observe	P-Value
P	117.2134	1	117.2134	11.23006	0.002316
RW	156.2647	1	156.2647	14.97152	0.000596
WD	102.1235	1	102.1235	9.78432	0.004083
$P \times WD$	87.7415	1	87.7415	8.4064	0.007194
$RW \times WD$	68.1003	1	68.1003	6.5246	0.016366
Error	292.2489	28	10.4375		
Total	823.6922	33			

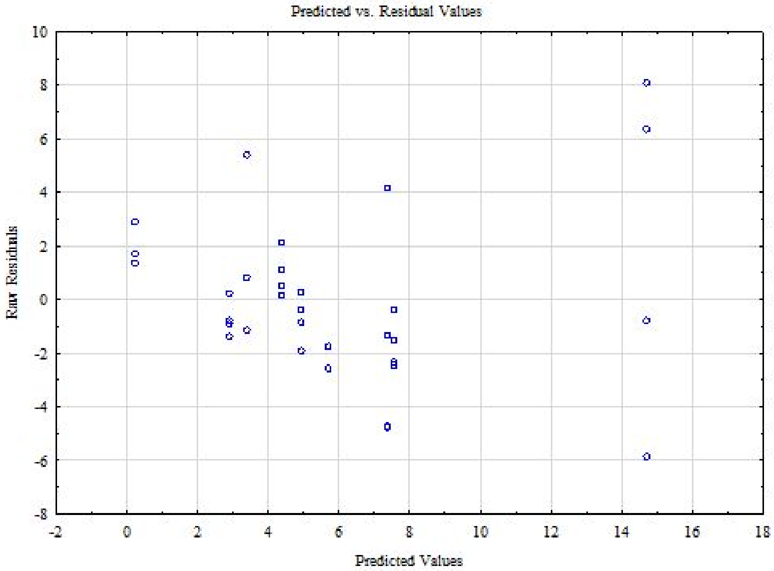

Figure B.4: NPP of residuals for the 2^4 design shows that the residuals fall along a straight line when ignoring the values at extremes, as a result, the normality assumption is valid.

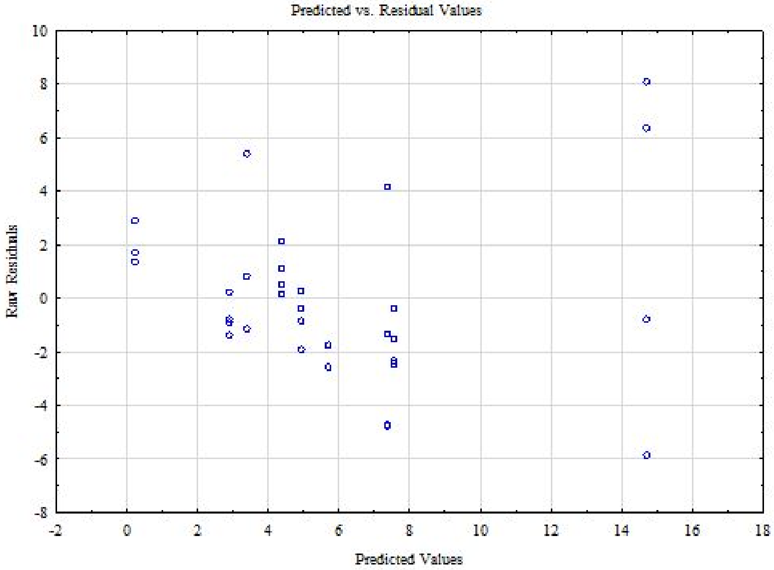

Figure B.5: Plot of residuals vs. predicted values is structureless and there is no tendency toward negative or positive residuals.

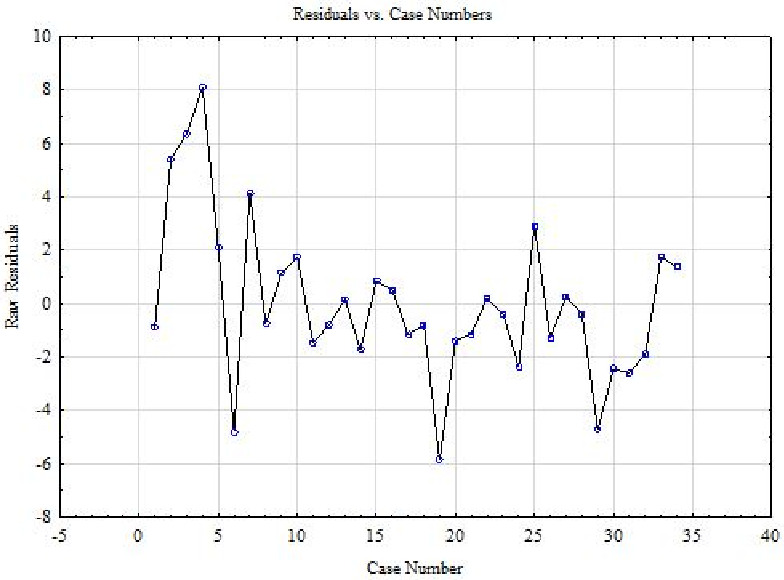

Figure B.6: The plot of residuals vs. time does not show any special pattern.

Appendix C

Experimental Design for Material Jetting

C.1 Line Features: Screening

Given the fact that we are dealing with ten factors at the screening stage, running a full factorial design becomes prohibitive. Moreover, at this point we are only interested in identifying the significant factors, not their higher-order interactions. As a result, a $2^{10\text{-}5}$ design with resolution V was selected for the purpose of factor screening. The design was replicated in order to estimate the sum of squares of errors. Two center points were added to the model as well. Hence, 66 independent experiments were run in a random order and the average and standard deviation values were measured for the width of the printed samples. The first and second replicates were run at different days in order to minimize the effect of the nuisance factors.

Table C.1: $2^{10\text{-}5}{}_{\mathrm{V}}$ design and the response values.

No.	PT	CyT	T	V	$Str\%$	OT	CT	v	WD	P	$W_{s.d.}$	W_{avg}
1	0.37	3.5	90	85	80	0.2	0.2	60	3	600	*	*
2	0.43	3.5	90	85	80	0.15	0.15	50	2	600	0.10	0.81
3	0.37	4	90	85	80	0.15	0.15	50	3	500	0.03	0.67
4	0.43	4	90	85	80	0.2	0.2	60	2	500	0.18	0.66
5	0.37	3.5	100	85	80	0.15	0.15	60	2	500	0.01	0.67

Continued on next page

No.	PT	CyT	T	V	$Str\%$	OT	CT	v	WD	P	$W_{s.d.}$	W_{avg}
6	0.43	3.5	100	85	80	0.2	0.2	50	3	500	0.23	1.08
7	0.37	4	100	85	80	0.2	0.2	50	2	600	0.07	0.85
8	0.43	4	100	85	80	0.15	0.15	60	3	600	0.12	0.65
9	0.37	3.5	90	95	80	0.15	0.2	50	2	500	0.05	0.50
10	0.43	3.5	90	95	80	0.2	0.15	60	3	500	0.03	0.54
11	0.37	4	90	95	80	0.2	0.15	60	2	600	0.03	0.77
12	0.43	4	90	95	80	0.15	0.2	50	3	600	0.15	0.57
13	0.37	3.5	100	95	80	0.2	0.15	50	3	600	0.08	0.88
14	0.43	3.5	100	95	80	0.15	0.2	60	2	600	0.06	0.59
15	0.37	4	100	95	80	0.15	0.2	60	3	500	0.01	0.49
16	0.43	4	100	95	80	0.2	0.15	50	2	500	0.01	0.69
17	0.37	3.5	90	85	90	0.2	0.15	50	2	500	0.08	0.88
18	0.43	3.5	90	85	90	0.15	0.2	60	3	500	0.15	0.72
19	0.37	4	90	85	90	0.15	0.2	60	2	600	*	*
20	0.43	4	90	85	90	0.2	0.15	50	3	600	0.03	0.76
21	0.37	3.5	100	85	90	0.15	0.2	50	3	600	0.18	0.93
22	0.43	3.5	100	85	90	0.2	0.15	60	2	600	0.08	0.86
23	0.37	4	100	85	90	0.2	0.15	60	3	500	0.01	0.81
24	0.43	4	100	85	90	0.15	0.2	50	2	500	*	*
25	0.37	3.5	90	95	90	0.15	0.15	60	3	600	0.02	0.91
26	0.43	3.5	90	95	90	0.2	0.2	50	2	600	0.08	0.74
27	0.37	4	90	95	90	0.2	0.2	50	3	500	0.02	0.75
28	0.43	4	90	95	90	0.15	0.15	60	2	500	0.04	0.60
29	0.37	3.5	100	95	90	0.2	0.2	60	2	500	0.02	0.80
30	0.43	3.5	100	95	90	0.15	0.15	50	3	500	0.02	0.71
31	0.37	4	100	95	90	0.15	0.15	50	2	600	0.01	0.90
32	0.43	4	100	95	90	0.2	0.2	60	3	600	0.04	0.57
33	C	C	C	C	C	C	C	C	C	C	0.05	0.64
34	0.37	3.5	90	85	80	0.2	0.2	60	3	600	0.08	0.52
35	0.43	3.5	90	85	80	0.15	0.15	50	2	600	0.05	0.54
36	0.37	4	90	85	80	0.15	0.15	50	3	500	0.05	0.56
37	0.43	4	90	85	80	0.2	0.2	60	2	500	0.24	0.51
38	0.37	3.5	100	85	80	0.15	0.15	60	2	500	0.03	0.57
39	0.43	3.5	100	85	80	0.2	0.2	50	3	500	*	*
40	0.37	4	100	85	80	0.2	0.2	50	2	600	*	*
41	0.43	4	100	85	80	0.15	0.15	60	3	600	*	*
42	0.37	3.5	90	95	80	0.15	0.2	50	2	500	0.07	0.64

Continued on next page

No.	PT	CyT	T	V	$Str\%$	OT	CT	v	WD	P	$W_{s.d.}$	W_{avg}
43	0.43	3.5	90	95	80	0.2	0.15	60	3	500	0.08	0.58
44	0.37	4	90	95	80	0.2	0.15	60	2	600	0.01	0.65
45	0.43	4	90	95	80	0.15	0.2	50	3	600	0.19	0.75
46	0.37	3.5	100	95	80	0.2	0.15	50	3	600	0.01	0.80
47	0.43	3.5	100	95	80	0.15	0.2	60	2	600	0.07	0.54
48	0.37	4	100	95	80	0.15	0.2	60	3	500	0.12	0.61
49	0.43	4	100	95	80	0.2	0.15	50	2	500	0.04	0.60
50	0.37	3.5	90	85	90	0.2	0.15	50	2	500	0.03	0.79
51	0.43	3.5	90	85	90	0.15	0.2	60	3	500	*	*
52	0.37	4	90	85	90	0.15	0.2	60	2	600	*	*
53	0.43	4	90	85	90	0.2	0.15	50	3	600	0.12	0.61
54	0.37	3.5	100	85	90	0.15	0.2	50	3	600	*	*
55	0.43	3.5	100	85	90	0.2	0.15	60	2	600	*	*
56	0.37	4	100	85	90	0.2	0.15	60	3	500	0.01	0.64
57	0.43	4	100	85	90	0.15	0.2	50	2	500	*	*
58	0.37	3.5	90	95	90	0.15	0.15	60	3	600	0.01	0.66
59	0.43	3.5	90	95	90	0.2	0.2	50	2	600	0.07	0.66
60	0.37	4	90	95	90	0.2	0.2	50	3	500	0.01	0.60
61	0.43	4	90	95	90	0.15	0.15	60	2	500	0.03	0.47
62	0.37	3.5	100	95	90	0.2	0.2	60	2	500	0.01	0.64
63	0.43	3.5	100	95	90	0.15	0.15	50	3	500	0.05	0.63
64	0.37	4	100	95	90	0.15	0.15	50	2	600	0.01	0.70
65	0.43	4	100	95	90	0.2	0.2	60	3	600	0.10	0.54
66	C	C	C	C	C	C	C	C	C	C	0.09	0.60

Table C.2: ANOVA for $W_{s.d.}$ in $2^{10\text{-}5}$ design

Factor	SS	DF	MS	F-observe	P-Value
PT	0.0277	1.0000	0.0277	17.6418	0.000128*
CyT	0.0000	1.0000	0.0000	0.0001	0.9934
T	0.0008	1.0000	0.0008	0.4816	0.4913
V	0.0310	1.0000	0.0310	19.7556	0.000059*
$Str\%$	0.0066	1.0000	0.0066	4.1995	0.046427*
OT	0.0004	1.0000	0.0004	0.2578	0.6142
CT	0.0429	1.0000	0.0429	27.3297	0.000005*
v	0.0008	1.0000	0.0008	0.5217	0.4739
WD	0.0031	1.0000	0.0031	2.0024	0.1641
P	0.0009	1.0000	0.0009	0.5470	0.4635
Error	0.0690	44.0000	0.0016		
Total	0.1844	54.0000			

Table C.3: ANOVA for $W_{s.d.}$ for the jetted line features after removing the insignificant factors.

Factor	SS	DF	MS	F-observe	P-Value
PT	0.0301	1.0000	0.0301	19.9138	0.0000
V	0.0318	1.0000	0.0318	21.0422	0.0000
$Str\%$	0.0063	1.0000	0.0063	4.1638	0.0466
CT	0.0428	1.0000	0.0428	28.2725	0.0000
Error	0.0757	50.0000	0.0015		
Total	0.1844	54.0000			

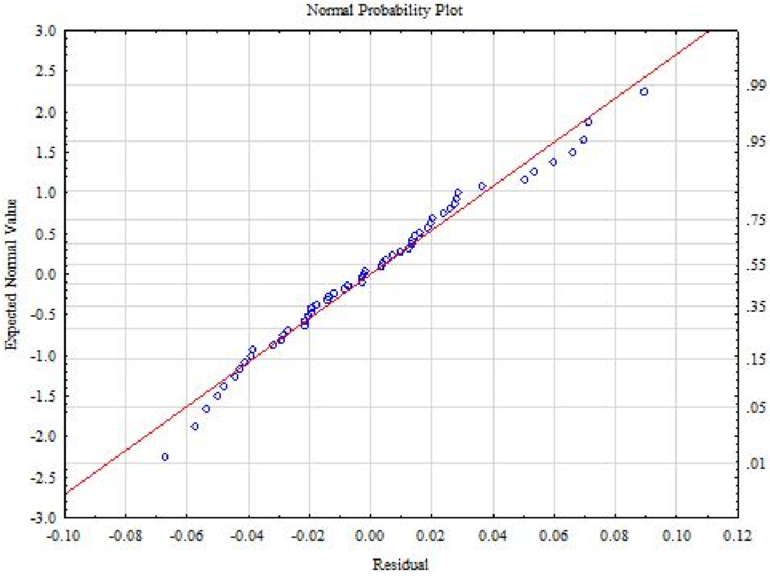

Figure C.1: NPP of residuals for the $2^{10\text{-}5}$ design shows that the residuals fall along a straight line, as a result, the normality assumption is valid.

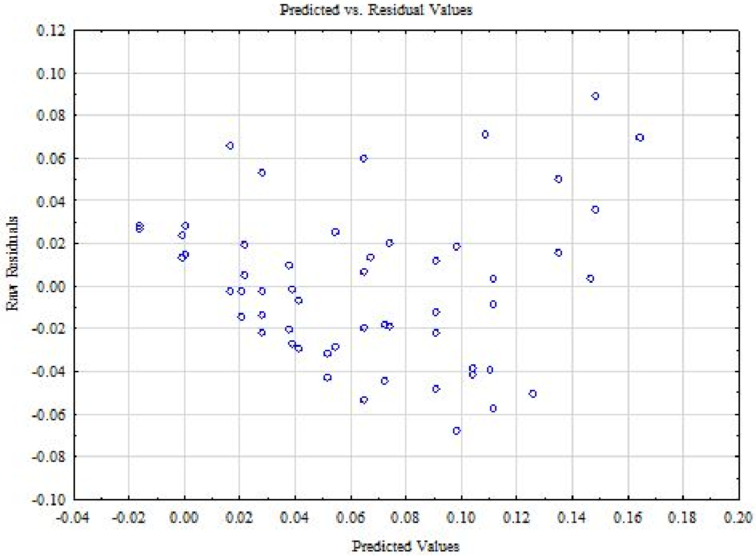

Figure C.2: Plot of residuals vs. predicted values is structureless and there is no tendency towards negative or positive residuals.

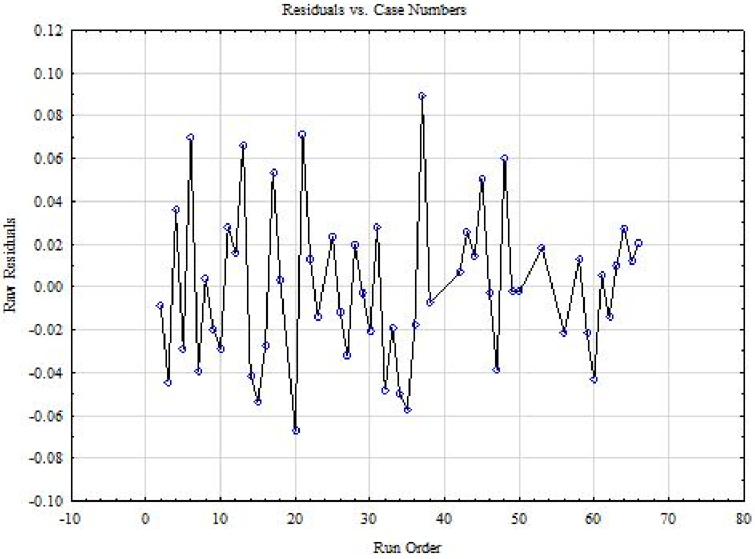

Figure C.3: The plot of residuals vs. time does not show any special pattern.

C.2 Line Features: Optimization

Table C.4: $3^{4\text{-}1}{}_{IV}$ design and the response values

No.	PT	CT	V	$Str\%$	W_{avg}
1	0.35	0.15	93	86	0.875
2	0.35	0.15	95	90	0.919
3	0.35	0.15	97	88	0.904
4	0.35	0.17	93	90	0.819
5	0.35	0.17	95	88	0.807
6	0.35	0.17	97	86	0.790
7	0.35	0.19	93	88	0.750
8	0.35	0.19	95	86	0.859
9	0.35	0.19	97	90	0.925
10	0.37	0.15	93	90	0.860
11	0.37	0.15	95	88	0.846
12	0.37	0.15	97	86	0.871
13	0.37	0.17	93	88	0.789
14	0.37	0.17	95	86	0.827
15	0.37	0.17	97	90	0.829
16	0.37	0.19	93	86	0.725
17	0.37	0.19	95	90	0.799
18	0.37	0.19	97	88	0.812
19	0.39	0.15	93	88	0.835
20	0.39	0.15	95	86	0.836
21	0.39	0.15	97	90	0.866
22	0.39	0.17	93	86	0.718
23	0.39	0.17	95	90	0.811
24	0.39	0.17	97	88	0.775
25	0.39	0.19	93	90	0.727
26	0.39	0.19	95	88	0.706
27	0.39	0.19	97	86	0.653
28	0.37	0.17	95	88	0.818
29	0.37	0.17	95	88	0.846

Table C.5: ANOVA for W_{avg} in $3^{4\text{-}1}{}_{IV}$ design

Factor	SS	DF	MS	F-observe	P-Value
PT	0.028736	1	0.028736	30.23031	0.0000784*
PT^2	0.000932	1	0.000932	0.98068	0.338839
CT	0.040708	1	0.040708	42.82435	0.000013*
CT^2	0.002732	1	0.002732	2.87429	0.11212
V	0.005962	1	0.005962	6.27236	0.02524*
V^2	0.002749	1	0.002749	2.89188	0.111124
$Str\%$	0.008916	1	0.008916	9.37919	0.00843*
$Str\%^2$	0.00074	1	0.00074	0.77873	0.392429
$PT \times CT$	0.004813	1	0.004813	5.06356	0.04103*
$PT \times V$	0.00136	1	0.00136	1.43088	0.251488
$PT \times Str\%$	0.000678	1	0.000678	0.71349	0.41249
$CT \times V$	0.001564	1	0.001564	1.64542	0.220414
$CT \times Str\%$	0.001114	1	0.001114	1.17196	0.297294
$V \times Str\%$	0.0019	1	0.0019	1.99875	0.179279
Error	0.013308	14	0.000951		
Total	0.11806	28			

Table C.6: ANOVA for W_{avg} for the jetted line features after removing the insignificant factors.

Factor	SS	DF	MS	F-observe	P-Value
PT	0.028736	1	0.028736	24.60158	0.000052
CT	0.040708	1	0.040708	34.85067	0.000005
V	0.005962	1	0.005962	5.10448	0.033647
$Str\%$	0.008916	1	0.008916	7.63283	0.011076
$PT \times CT$	0.006874	1	0.006874	5.88469	0.023525
Error	0.026865	23	0.001168		
Total	0.11806	28			

Table C.7: Regression coefficients of the reduced model for jetting of line features.

Factor	Reg. Coeff.	SE	P-Value
Mean	0.813717	0.006346	0
PT	-0.039956	0.008056	0.000052
CT	-0.047556	0.008056	0.000005
V	0.0182	0.008056	0.033647
$Str\%$	0.022256	0.008056	0.011076
$PT \times CT$	-0.023933	0.009866	0.023525

In this resolution IV design, the main factors are confounded with the third order interaction factors. Also, the second order interactions are confounded with each other. Assuming that the third or higher order interactions are not significant, no further investigation is required for the significant main factors. The second order interaction $PT \times CT$ is confounded with $V \times Str\%$ interaction. There is no straightforward method to associate the calculated sum of squares (0.00069) to one of these second order interactions or both. However, based on the smaller P-values for the pulse time and close time factors and the experience gained while running the experiments, we can conclude that $PT \times CT$ has a larger impact on the output compared to $V \times Str\%$.

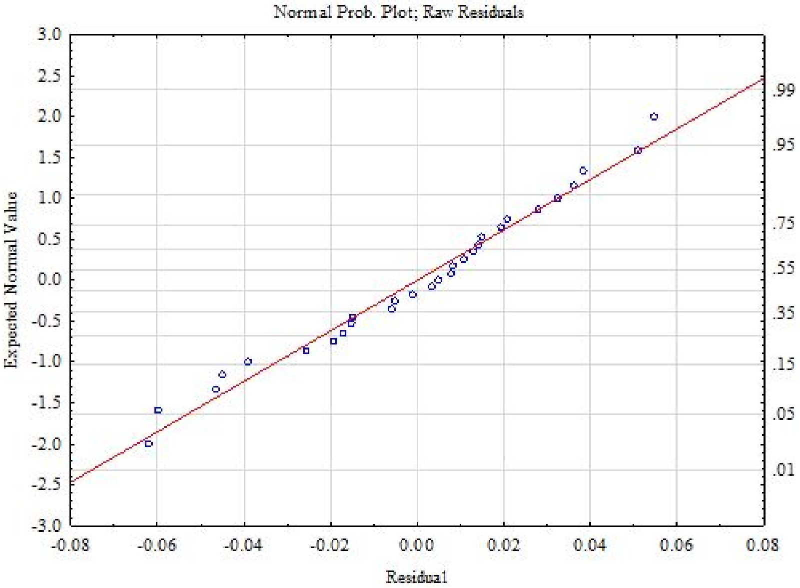

Figure C.4: NPP of residuals for the $3^{4\text{-}1}{}_{IV}$ design shows that the residuals fall along a straight line, as a result, the normality assumption is valid.

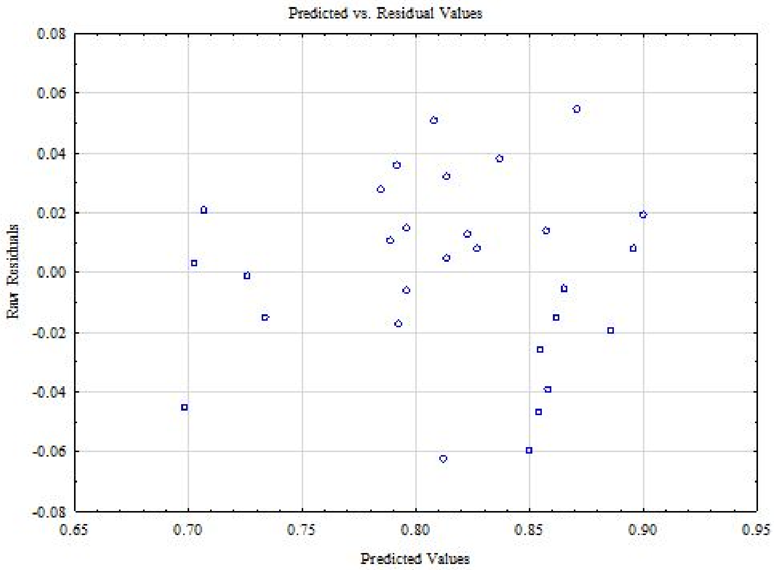

Figure C.5: Plot of residuals vs. predicted values is structureless and there is no tendency towards negative or positive residuals; however, there is slight indication of inconsistent variance which is negligible.

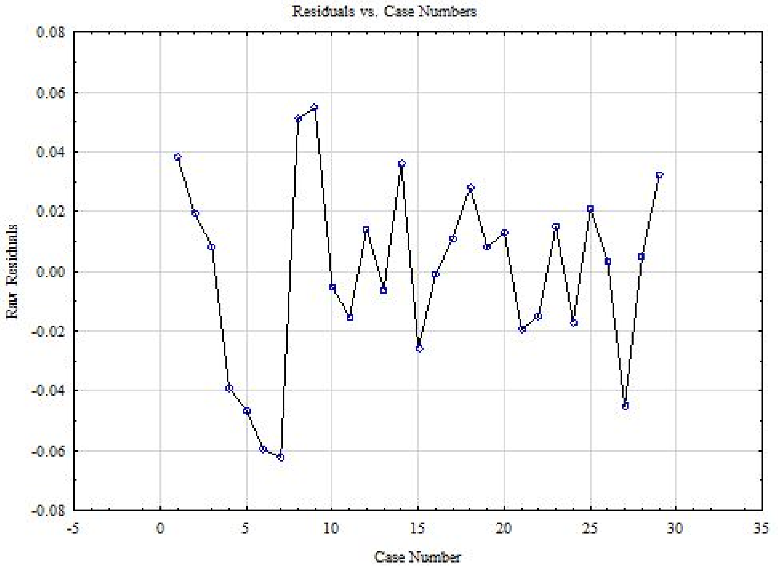

Figure C.6: The plot of residuals vs. time does not show any special pattern.

Table C.8: ANOVA for W_{avg} in CCD

Factor	SS	DF	MS	F-observe	P-Value
PT	0.001636	1	0.001636	3.01424	0.101749
PT^2	0.003088	1	0.003088	5.69153	0.029754*
CT	0.000427	1	0.000427	0.78728	0.388068
CT^2	0.002678	1	0.002678	4.93473	0.0411*
$PT \times CT$	0.006012	1	0.006012	11.07822	0.004257*
Error	0.008682	16	0.000543		
Total	0.024616	21			

Table C.9: Regression coefficients of the CCD model.

Factor	Reg. Coeff.	SE	P-Value
Mean	0.5929	0.0085	0.0000
PT	-0.0117	0.0067	0.1017
PT^2	0.0247	0.0103	0.0298
CT	-0.0060	0.0067	0.3881
CT^2	0.0230	0.0103	0.0411
$PT \times CT$	0.0274	0.0082	0.0043

C.3 Plane Features: Optimization

Table C.10: 2^2 design and the response values.

No.	v	RW	W_q
2	100	0.4	22.609
10 (C)	80	0.45	40.308
7	100	0.4	22.275
8	60	0.5	51.943
3	60	0.5	50.614
9	100	0.5	40.151
5 (C)	80	0.45	46.611
6	60	0.4	49.197
4	100	0.5	38.31
1	60	0.4	54.195

Table C.11: ANOVA for W_q for the jetted planar features.

Factor	SS	DF	NS	F-observe	P-Value
v	852.928	1	852.9276	117.8215	0.000036
RW	134.005	1	134.0048	18.5111	0.005079
$v \times RW$	148.023	1	148.0232	20.4476	0.004009
Error	43.435	6	7.2391		
Total	1178.391	9			

Table C.12: Regression coefficients for the jetting of the planar features model.

Factor	Regr. Coeff.	SE	P-Value
Mean	41.6213	0.850832	0
v	-10.3255	0.951259	0.000036
RW	4.0928	0.951259	0.005079
$v \times RW$	4.3015	0.951259	0.004009

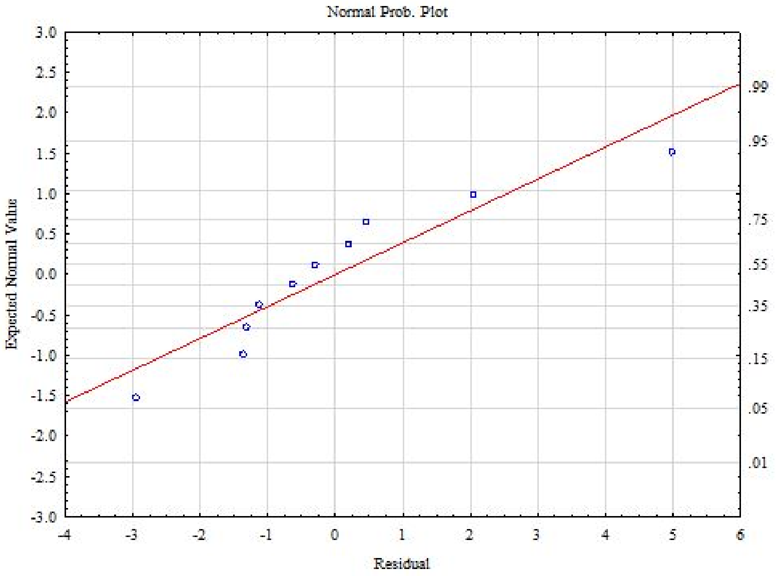

Figure C.7: NPP for the 2^2 design shows that the residuals fall along a straight line when ignoring the values at extremes, as a result, the normality assumption is valid.

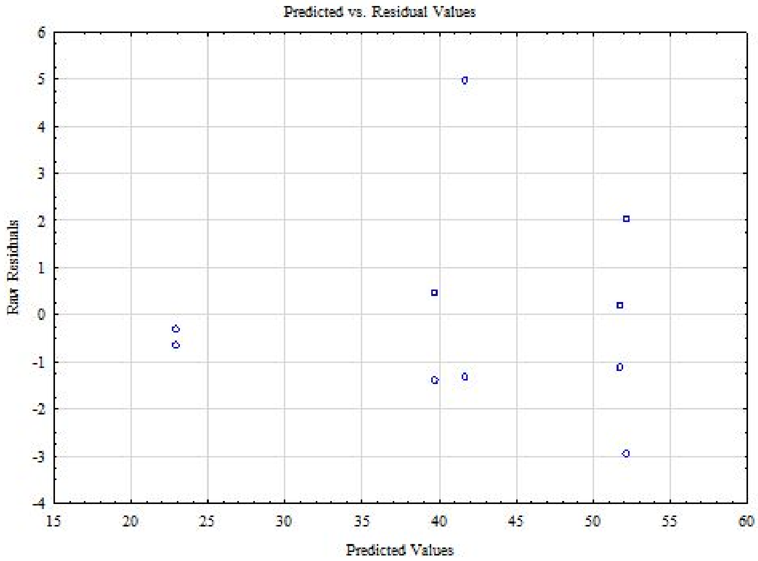

Figure C.8: Plot of residuals vs. predicted values is structureless and there is no tendency toward negative or positive residuals; however, there is slight indication of inconsistent variance which is negligible.

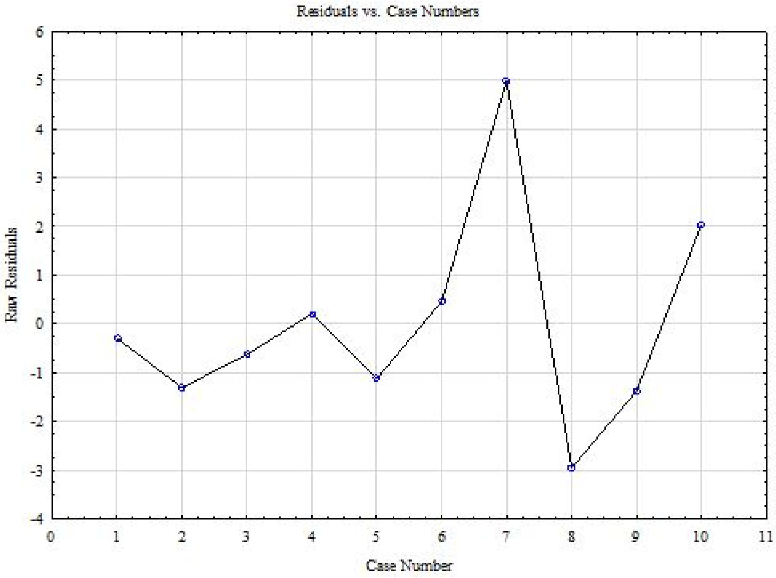

Figure C.9: The plot of residuals vs. time does not show any special pattern.

Appendix D

Experimental Design for PBBJ

D.1 Screening

Table D.1: The measured values for H, ID, and OD.

No.	LT (μm)	Fr	h (μm)	ID (μm)	DD (μm)
1	50	3	4130.676	5407.209	1563.818
2	50	1	5685.574	6966.943	1476.194
3	50	1	5907.289	6904.469	1256.984
4	100	3	3673.833	5579.145	1283.139
5	100	3	3863.966	5329.552	1930.681
6	50	2	3852.614	5685.995	1905.692
7	100	1	4894.481	7436.54	2126.095
8	50	3	4116.611	6160.803	2074.107
9	50	2	3909.257	6762.391	1615.955
10	100	2	3619.815	6588.914	1835.162
11	100	2	3645.568	6307.557	1137.825
12	100	1	5904.6	7353.762	1869.109

Table D.2: ANOVA results for H.

Source	DF	Adj SS	Adj MS	F-Value	P-Value
Model	5	8550286	1710057	18.49	0.001
Linear	3	8538548	2846183	30.78	0
LT	1	333253	333253	3.6	0.106
Fr	2	8205295	4102648	44.36	0
2-Way Interaction	2	11738	5869	0.06	0.939
$LT \times Fr$	2	11738	5869	0.06	0.939
Error	6	554859	92476		
Total	11	9105145			

Table D.3: ANOVA results for ID.

Source	DF	Adj SS	Adj MS	F-Value	P-Value
Model	5	5160132	1032026	6.59	0.02
Linear	3	4831906	1610635	10.29	0.009
LT	1	41732	41732	0.27	0.624
Fr	2	4790174	2395087	15.3	0.004
2-Way Interaction	2	328226	164113	1.05	0.407
$LT \times Fr$	2	328226	164113	1.05	0.407
Error	6	939373	156562		
Total	11	6099505			

Table D.4: ANOVA results for OD.

Source	DF	Adj SS	Adj MS	F-Value	P-Value
Model	5	534849	106970	0.94	0.516
Linear	3	23421	7807	0.07	0.975
LT	1	6973	6973	0.06	0.813
Fr	2	16449	8224	0.07	0.931
2-Way Interaction	2	511428	255714	2.25	0.187
$LT \times Fr$	2	511428	255714	2.25	0.187
Error	6	682013	113669		
Total	11	1216862			

D.2 Optimization

Table D.5: Desirability function response optimization.

Response	Goal	Lower	Target	Upper	Weight
DD	Minimum	*	1137.82	2126.09	1
ID	Target	4500	5000	7436.54	1
h	Target	2700	3000	5907.29	1

Appendix E

Supporting Experiments

E.1 Experiments of Chapter 5

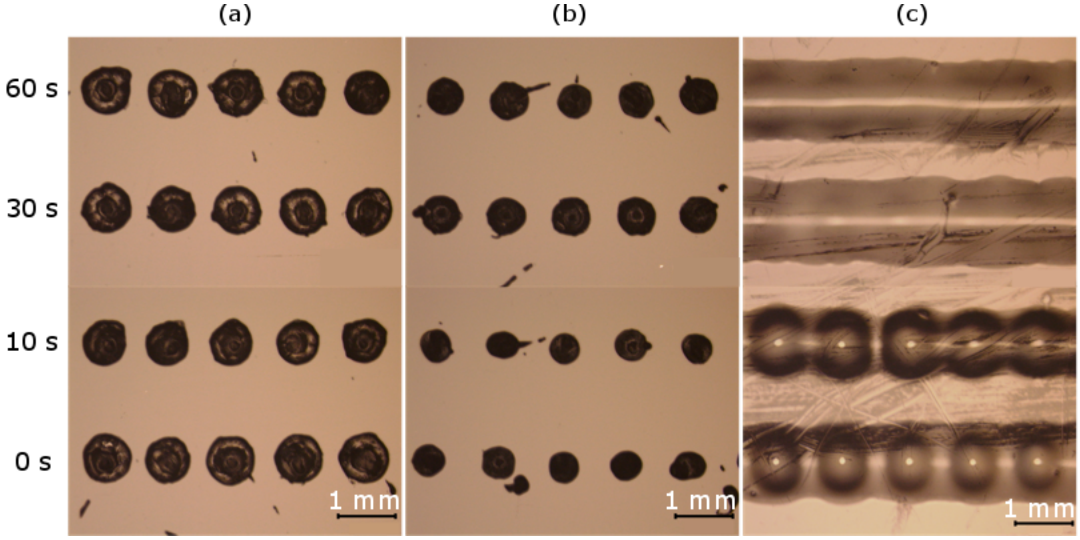

Figure E.1: Jetted droplets of inks (a) A, (b) 70A-30B, and (c) 45A-55B cured 0s, 10s, 30s, and 60 s after deposition. The slumping of ink 45A-55B has made the coalesce of droplets possible.

Table E.1: Measurement of mechanical properties and t-test comparisons.

Ink	Method		ϵ_f (%)	σ_f (MPa)	T_s (kN/m)	Hardness (00)
A	Cast	Sample 1	389	1.38	10.26	75.1
		Sample 2	390	1.33	10.58	72.9
		Sample 3	364	1.35	11.7	71.7
		Avg.	381.000	1.353	10.847	73.233
		Std. Dev.	12.028	0.021	0.756	1.408
	AM-made	Sample 1	226	0.72	13.25	69.4
		Sample 2	257	0.81	8.99	70.7
		Sample 3	219	0.67	10.085	70.1
		Avg.	234.000	0.733	10.775	70.067
		Std. Dev.	16.513	0.058	2.212	0.531
	Percentage Change		38.58%	45.92%	0.66%	4.33%
	P-value		0.001	0	0.96	0.041
45A-55B	Cast	Sample 1	96.9	0.48	0.97	65.3
		Sample 2	92.7	0.46	0.99	66.9
		Sample 3	102.47	0.55	1.05	67.5
		Avg.	97.357	0.497	1.003	66.567
		Std. Dev.	4.002	0.039	0.042	0.929
	AM-made	Sample 1	76.28	0.44	0.91	63.7
		Sample 2	85.58	0.52	1.17	67
		Sample 3	93.55	0.55	1	63
		Avg.	85.137	0.503	1.027	64.567
		Std. Dev.	7.057	0.046	0.132	1.744
	Percentage Change		12.55%	2.04%	2.40%	3.01%
	P-value		0.1	0.883	0.785	0.226

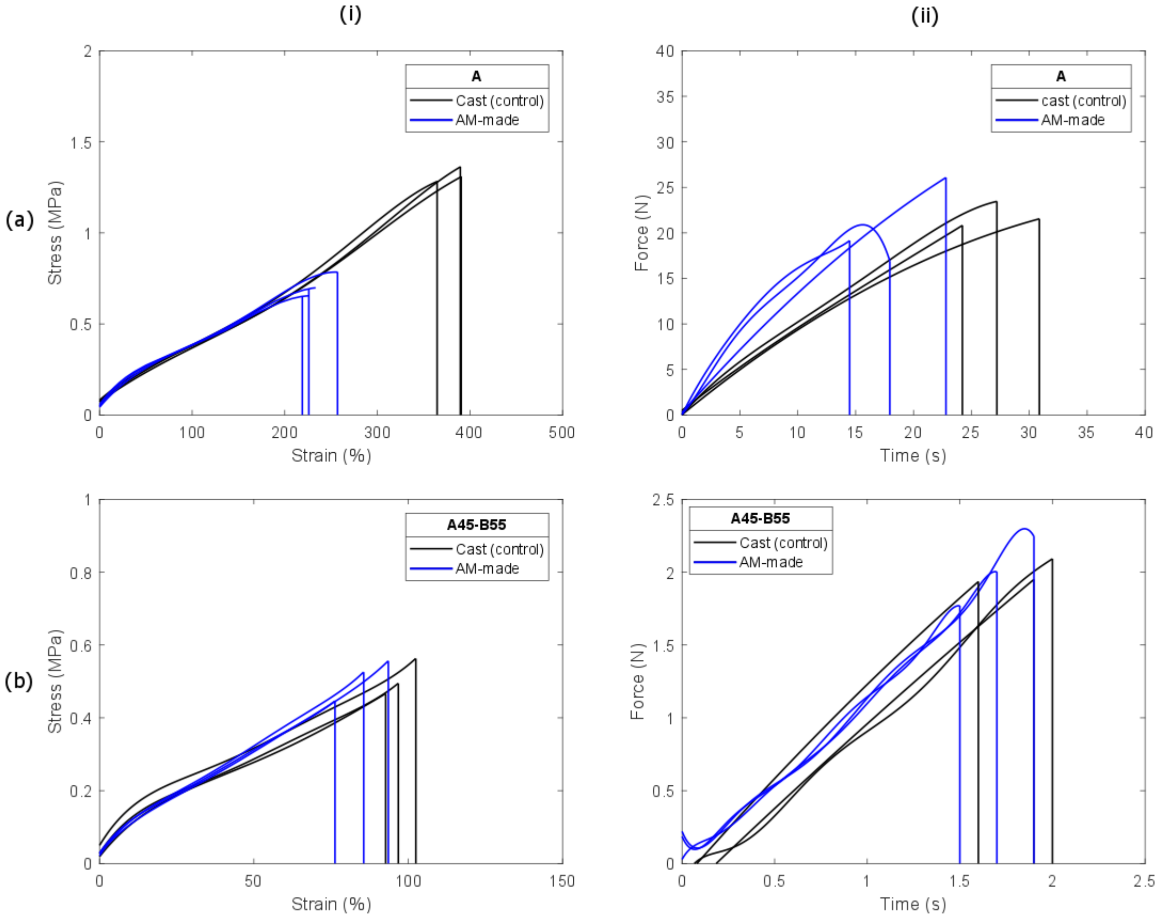

Figure E.2: (a-i) Tensile test and (a-ii) tearing test curves for ink A. (b-i) Tensile test and (b-ii) tearing test curves for ink 45A-55B.

E.2 Experiments of Chapter 6

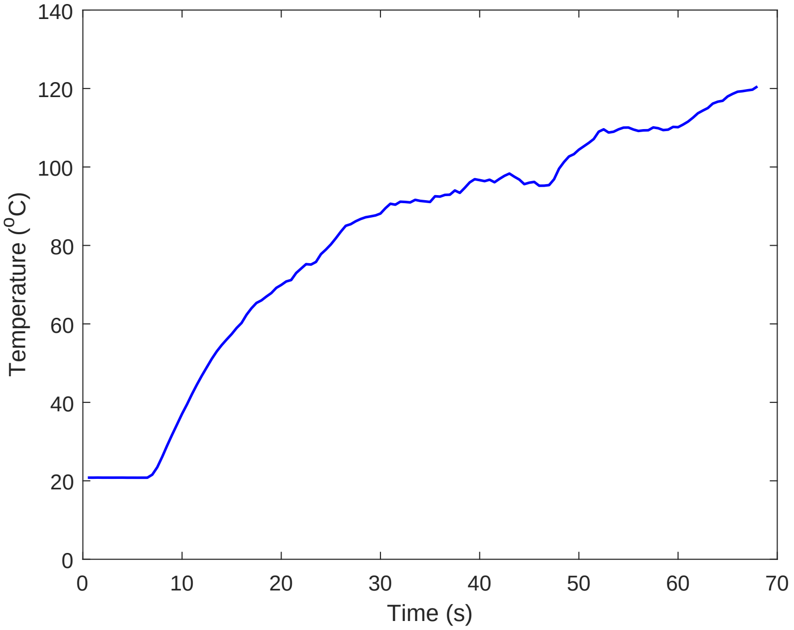

Figure E.3: Temperature of the powder bed vs. time.